SYSTEMS ANALYSIS OF CARDIAC β-ADRENERGIC SIGNALING REGULATION

A Dissertation Presented to the Faculty of
The School of Engineering and Applied Science
University of Virginia

In Partial Fulfillment
of the Requirements for the Degree of
Doctor of Philosophy in Biomedical Engineering

by

JASON HUNG-YING YANG
MAY 2012

APPROVAL SHEET

This dissertation is submitted in partial fulfillment of the requirements for the degree of Doctor of Philosophy in Biomedical Engineering

Jason Hung-Ying Yang, *Author*

This dissertation has been read and approved by the Examining Committee:

Jeffrey J. Saucerman, Ph.D., *Dissertation Advisor*

Brent A. French, Ph.D., *Committee Chair*

Ian G. Macara, Ph.D., *Minor Mentor*

Frederick H. Epstein, Ph.D.

Jeffrey W. Holmes, Ph.D.

Jason A. Papin, Ph.D.

Accepted for the School of Engineering and Applied Science:

Dean, School of Engineering and Applied Science

MAY 2012

For Jeff, Monica, Ashley, Dana, Stacey and the gentlemen of the
Virginia Rugby Football Club

Only those who dare to fail greatly can ever achieve greatly.
– Robert F. Kennedy

Friendship is precious, not only in the shade, but in the sunshine of life;
and thanks to a benevolent arrangement of things,
the greater part of life is sunshine.
– Thomas Jefferson

Abstract

Cardiovascular diseases constitute a significant global health burden and are the leading cause of death in the United States. By 2020, it is estimated that cardiovascular disease will be the leading cause of death worldwide, accounting for an estimated 25 million deaths annually. The contemporary view of heart failure states the development of the failing heart is driven in large part by circulating neurohormones and catecholamines which can stimulate pathologic remodeling events such as cardiac hypertrophy and fibrosis. However, these circulating factors also act on signaling pathways important for regulating normal cardiac function, such as the β-adrenergic signaling pathway, which regulates contractility in the *fight-or-flight* response. The overall goal of this dissertation is to investigate mechanisms which differentially regulate β-adrenergic signaling-stimulated contractility and β-adrenergic signaling-stimulated hypertrophy.

Like most signaling pathways, the β-adrenergic signaling pathway is a complex network of signaling species that interact to elicit diverse cellular functions in response to receptor stimulation. An open challenge therefore remains in understanding how certain cardiac functions are selectively activated or silenced in the presence of a common biochemical stress. Traditional reductionist approaches have proven very successful for identifying components of the β-adrenergic signaling pathway, but the complexity of this network

renders intuitive understanding of signaling responses difficult. These challenges provide opportunities for quantitative engineering methods, such as computational modeling, to provide insight into cardiac biology and potential therapies. In this dissertation, we take a multidisciplinary approach, integrating computational modeling with analysis of published experimental data and novel live-cell imaging strategies to interrogate the mechanisms regulating β-adrenergic signaling dynamics.

Complex signaling networks contain many topological network motifs that may be important for regulating signaling flow through the network. In the present work, we develop highly mechanistic and carefully constrained models of cardiac β-adrenergic signaling to test the hypothesis that topological features in this network may be important for regulating contractile responses. By this approach, we show an incoherent feed-forward loop formed by two protein kinase A substrates accelerates and induces adaptation in cardiac contractility responses. Moreover, extending these methods to Angiotensin II signaling, we show this network motif is also an important regulator of cardiac fibrosis. Together, these results implicate an important role of *network topology* in regulating β-adrenergic signaling.

Recent studies from our lab and by others indicate β-adrenergic signaling is spatially and temporally heterogeneous in the cardiac myocyte. Because the protein kinase A substrates regulating cardiac contractility and hypertrophy reside in different subcellular compartments of the cardiac myocyte, we have hypothesized that such compartmentation may be important for regulating stimulated hypertrophic responses. In the present work,

we have used computational models as a hypothesis-generating inference tool to inspire experiments investigating the regulation of nuclear protein kinase A activity its downstream effects on cardiac myocytes. With this approach, we show that in contrast to HEK 293 cells, where nuclear protein kinase A activity is regulated by a subnuclear A-kinase anchoring protein signaling complex, nuclear protein kinase A activity in cardiac myocytes is directly regulated by *catalytic subunit compartmentation*.

Together, this body of work provides insight into how β-adrenergic signaling responses are selectively manipulated. These findings are important as the current therapeutic strategy for treating heart disease is antagonism of the entire β-adrenergic signaling pathway, which leaves patients vulnerable to electrophysiological and mechanical deficiencies. The present work provides evidence suggesting these therapies may be improved with a therapeutic strategy which more directly inhibits nuclear protein kinase A activity, while preserving or enhancing cytosolic protein kinase A activity.

Acknowledgments

It is a privilege, that in science we have the opportunity to work on interesting problems and experience the pleasure of finding things out. But I think what makes science special is the richness of colleagues, friends, mentors with whom we journey. Any success of which I could claim credit is built upon a long history of knowledge, hard work and mentorship from those who have come before me. It truly takes a whole village to raise a child. I regret I have so few pages to acknowledge those giants upon whose shoulders I have stood. It would take volumes to adequately honor everyone who has touched my life these past years. But there are a few whom have really challenged my views on science, society and the human experience and have powerfully shaped the person I am today.

I am indebted to my advisor and friend Jeff Saucerman. Jeff has been constant and supportive of me through my most difficult times in Charlottesville and did not give up on me when I wanted to give up on myself. He regarded me scientifically as a colleague, but challenged me in frankness with the areas in which I needed to grow. Jeff gave me latitude to stroll off the beaten path and encouraged me to investigate different facets of the scientific profession. It has only been through his encouragement that I have been able to grow in self-awareness and find my scientific identity.

It has been a pleasure to work alongside many members of the Saucerman lab, past and present. Robert Amanfu, Karen Ryall and Eric Greenwald have shared in these early years of our young lab and Renata Polanowska-Grabowska and Lindsay McLellan have been tremendously helpful in helping me complete my experiments. I am fortunate to have worked closely with many undergraduates. Special acknowledgments go to Lulu Chu, Brooks Taylor, Anthony Soltis, Greg Bass, Jeff Smith and Wyatt Shields.

Many other faculty at UVA have profoundly shaped my views on science and academics. My committee members (Brent French, Fred Epstein, Ian Macara, Jeff Holmes and Jason Papin) have all been both supportive and constructively critical. I have truly appreciated their fair, but firm perspectives. Tom Skalak has been an amazing advocate who has consistently challenged me to expand my vision and take risks. I have enjoyed my many conversations with Brian Duling and Gary Owens, who have challenged my views on science philosophy, scientific career strategy and scientific mentorship. Erik Fernandez has given me a separate perspective on mentorship – as an expression of moral duty and faithfulness – and Bill Petri has helped me consider how our work can intersect with global challenges. Timothy Allen, Shayn Peirce-Cottler, Michael Palmer and Deandra Little have helped me cultivate my views on undergraduate teaching. I am particularly grateful for the Tomorrow's Professors Today program for giving me unique perspective on the university as an institution. Kevin Janes, Kim Kelly and Gordon Laurie have been both good friends and helpful in developing my philosophy toward basic science and scientific translation.

I am grateful for the Biotechnology Training Program for introducing me to new friends from other departments and giving me an opportunity to chair a very successful symposium and do an internship at AstraZeneca Pharmaceuticals in Götenborg, Sweden. Many thanks go to Carl Whatling and Willie McPheat for helping me carve a self-directed and unique experience. Many more thanks go to Jane McPheat, Linda Sundström and Lisbeth Kristensson for guiding my work at AstraZeneca. I have made many friends in my time there, but special thanks go to Annika Dronge, Daniel Klamer and Rami Avidan for sharing their life stories with me and helping me process and overcome some of the major personal and professional challenges in my life at the time.

I am grateful for my mentors at Johns Hopkins who helped me see the stars in one of the darkest and most uncertain periods of my life. Rai Winslow taught me to think quantitatively about biology, take responsibility for my career and think independently as a researcher. Pat Helm taught me MATLAB and helped me cultivate my passion for asking and answering interesting questions. David Yue inspired me by his humble scientific curiosity and faithfulness in finding an intersection between his science and his faith. Feilim MacGabhann has been another great friend and example to look toward. Ergin Atalar gave me my first opportunity to do research. Rob Susil and Christopher Yeung inspired me with their brilliant thinking and passion for solving difficult puzzles.

I am lucky to cross paths with many special people during graduate school. Matt Oberhardt, Moriel Vandsburger, Keith Moored, Kelly Benedict, Ernie Perez, Netta Gurari, Avinash Ravichandran, Shikha Mishra and Matt Alexander were great friends in

both my personal and professional lives. We will write papers together someday. Vi Nguyen, Phil Yang, Christina Viau Haden, Jackie Ripollone Keller, James Keller, Jenny Hodges and Anna Blazier have been faithful friends these past 6 years and are some of the people who know me the best in the world. Monica Lee catalyzed one of the most important growth phases in my life. Ashley Camhi opened my eyes to global development and inspired me to change the world. Dana Ainsworth helped me distill the things I want from life and challenged me to take responsibility for my circumstances. Stacey Gorski challenged me to change the things I cannot accept and accept the things I cannot change. I love all of you.

I am indebted to the gentlemen of the Virginia Rugby Football Club, who have been tremendous in helping me figure out many different areas of my life and finding confidence in being myself. Special thanks go to Jason Gaviria, Eric Greenwald and Brian Carver for being real with me and helping me get swole. Thanks also go to Aaron Franke for introducing me to this sport and to Mark ‘Pappy’ Strickland, Tracy Burge, Mike Bischoff, Shawn ‘Larry’ Johnson, ‘Drunk’ Sean Mackintosh, Anthony ‘Mongo’ Montgomery, Marc ‘Lebou’ Breton, Ben Call, Damien Blanchon, Lucien ‘Lulu’ Dimani, Christian Wakeman, Johnny McNulty, Matthieu Finot and ‘Ginger’ Matt Burkett for welcoming me. Luis Lucas challenged me to play confidently and aggressively on the pitch. Special thanks go to Matt Staples, Todd Applebaum, Kevin Crookes, Tom Oxenham, Terry Whelan, Neil Livett, Rhynhardt Rademeyer and Darryl Cross for helping me develop as a player. You guys are family to me.

Finally, to my family who have supported me in my many years away from home. My parents Eric and Mimi have made life and humanity very real experiences to engage. My sister Judy will forever be my devil's advocate. My brother Sunny will forever be the rawest expression of the things I value. Uncle Phil and Aunt Winny have been constants in my life and have given me tremendous perspective in many of my difficult times. They have truly saved my life many times over.

It is a very unusual sensation to hold in one's hand the culmination of 6 years of work. But these past 6 years have meant so much more to me than this single volume. I am indebted to everyone who walked with me, through both beautiful and ugly times. It has truly been a rollercoaster journey and I am truly lucky for having not ridden it alone. I am blessed for this rich Charlottesville community that has helped me forget what lies behind, press on toward the goal for the prize and fight the good fight, to finish the course. Thanks be to God for walking with me in spite of my wretchedness, for the grace by which I am saved and the stripes by which I am healed.

Jason Yang
Charlottesville, May 2012

This work has been made possible by generous support from the University of Virginia, the National Institutes of Health (R01 HL094476 to Jeffrey J. Saucerman), the American Heart Association (0715283U to Jason H. Yang and 0830470N to Jeffrey J. Saucerman) and the Biotechnology Training Program (NIH T32 GM08715 to Jason H. Yang).

Table of Contents

Figures

Abbreviations

β-AR	β-adrenergic receptor
β_1-AR	β_1-adrenergic receptor
β_2-AR	β_2-adrenergic receptor
Ang II	angiotensin II
AC	adenylyl cyclase
ACE	angiotensin converting enzyme
AIC	Akaike Information Criterion
AKAP	A-kinase anchoring protein
AKAR	A-kinase activity reporter
ARB	angiotensin II receptor blocker
AT_1	angiotensin II type 1
AT_1R	angiotensin II type 1 receptor
AT_2	angiotensin II type 2
AT_2R	angiotensin II type 2 receptor
BAD	Bcl2-associated death promoter
CaM	calmodulin
CaMKII	Ca^{2+}/calmodulin protein kinase II
cAMP	cyclic adenosine monophosphate
CFP	cyan fluorescent protein
CICR	Ca^{2+}-induced Ca^{2+}-release
CREB	cAMP response element binding protein
CREM	cAMP response element modulator
CTL	control
DAD	delayed after depolarization
EAD	early after depolarization
EC	excitation-contraction
ECC	excitation-contraction coupling
ECM	extracellular matrix
ERK	extracellular signal-regulated kinase
Epac	exchange protein directly activated by cAMP
ET-1	endothelin-1
FDAR	frequency-dependent acceleration of recovery

FRET	Förster resonance energy transfer
FSK	forskolin
G_s	G_α stimulatory protein
GFP	green fluorescent protein
GPCR	G-protein coupled receptor
GYS	glycogen synthase
IBMX	3-isobytl-1-methylxanthine
ICUE	indicator for cAMP using Epac
ISO	isoproterenol
IUPS	International Union of Physiological Science
JNK	c-Jun N-terminal kinase
LCC	L-type Ca^{2+} channel
LQT	long QT
LQTS	long QT syndrome
LVAD	left ventricular assist device
M_2R	M_2 muscarinic receptor
MAPK	mitogen-activated protein kinase
MIL	milrinone
MKP	MAPK phosphatase
MLC	myosin light chain
MMP	matrix metalloproteinase
NCX	Na^+/ Ca^{2+}-ATPase
NES	nuclear export signal
NKA	Na^+/ K^+-ATPase
NLS	nuclear localization signa
PDE	phosphodiesterase
PKA	cAMP-dependent protein kinase
PLB	phospholamban
PLM	phospholemman
PM	plasma membrane
PP2A	phosphatase 2A
PPI	protein-protein interaction
RFP	red fluorescent protein
RP	rolipram
RyR	ryanodine receptor
sAC	soluble adenylyl cyclase
SERCA	sarco-/endoplasmic reticulum Ca^{2+}-ATPase
SHP	Src-homology phosphatase
SR	sarcoplasmic reticulum
TAC	transverse aortic constriction

tmAC	transmembrane adenylyl cyclase
TnI	troponin I
WGA	wheat germ agglutinin
WT	wild-type
YFP	yellow fluorescent protein

Chapter 1

Dissertation Aims

1.1 Introduction

β-adrenergic receptor signaling is well recognized in the heart for its acute actions in enhancing cardiac contractility during the *fight-or-flight* response[1]. However, during cardiac disease, sympathetic activity is elevated, chronically stimulating this pathway to drive pathologic remodeling processes such as hypertrophy and fibrosis[2]. Reductionist approaches have independently identified how contractility and hypertrophy may each be stimulated during β-adrenergic stimulation. However, the common regulation of these pathways by protein kinase A (PKA) makes it unclear how β-adrenergic signaling can sometimes elicit some responses of this network, but not all[3].

Recent studies from our lab indicate β-adrenergic signaling is spatially and temporally heterogeneous in the cardiac myocyte[4]. We have also used a computational model of the β-adrenergic signaling network to show how phospholamban (PLB) acts in concert with other PKA substrates to enhance Ca^{2+} transients during β-adrenergic stimulation[5-6]. These results have led us to hypothesize that β-adrenergic receptor-stimulated enhancements to contractility and myocyte hypertrophy are regulated by *topological features* of the β-adrenergic-PKA signaling network and by nuclear PKA *compartmentation*. Here, we have coupled computational modeling with fluorescence cell microscopy to test this hypothesis. Specific aims for this dissertation are

1.2 Dissertation Aims

Aim 1. Test the hypothesis that *incoherent feed-forward signaling* accelerates and causes adaptation in β-adrenergic receptor-stimulated contractility. The β-adrenergic signaling network contains many feedback and feed-forward motifs which may be important for directing phosphorylation of contractile PKA substrates. We have

A. *developed an integrated computational model of β-adrenergic signaling in the mouse cardiac myocyte and compared the actions of receptor-desensitization negative feedback and PLB-phospholemman (PLM) incoherent feed-forward signaling on stimulated Ca^{2+} transients*. We have tested the hypothesis that PLM uses incoherent feed-forward signaling to accelerate contractile Ca^{2+} responses faster than cAMP/PKA dynamics and cause adaptations in Ca^{2+} transients.
B. *further tested the hypothesis that incoherent feed-forward signaling also regulates G-protein coupled receptor-stimulated cardiac fibrosis* using a computational model of Angiotensin II signaling. We have shown the importance of incoherent feed-forward signaling is not limited to the β-adrenergic signaling network.

Aim 2. Test the hypothesis that *PKA catalytic subunit compartmentation* underlies differences in cytosolic and nuclear PKA dynamics and regulates β-adrenergic receptor-stimulated myocyte hypertrophy. We have previously found that nuclear PKA activity significantly differs from cytosolic PKA activity in dynamics and sensitivity to β-adrenergic agonists. However, it remains unclear if and how PKA directly stimulates hypertrophy during β-adrenergic signaling. We have

A. *identified regulators of nuclear PKA activity* by combining fluorescence microscopy of local cAMP and PKA dynamics in HEK 293 cells with computational modeling of cAMP and PKA activity. We have clarified the mechanisms giving rise to differences in cytosolic and nuclear PKA signaling dynamics.
B. *determined that nuclear PKA activity may elicit hypertrophic responses to β-adrenergic signaling* by combining fluorescence microscopy of Ca^{2+}, cell size and PKA dynamics with computational modeling of cytosolic and nuclear PKA activity and targeted PKA over-expression. We show that because nuclear PKA indeed selectively regulates myocyte hypertrophy, these results identify a novel form of cardiac β-adrenergic signaling compartmentation.

We expected these aims to elucidate mechanisms for how β-adrenergic signaling specifically regulates cardiac contractility and hypertrophy. Together, these aims prompt the targeting of nuclear PKA inhibition and cytosolic PKA enhancement and as a novel and specific therapeutic strategy for managing cardiac disease.

Chapter 2

Background and Significance

2.1 Cardiovascular Disease

Cardiovascular diseases constitute a significant disease burden in the western world, accounting for 34.3% of all deaths in the US and carrying a health care cost burden of $503.2 billion in 2010[7] (Figure 2.1). The failing heart is characterized by deficient cardiac output and is accompanied by significant tissue remodeling, resulting in myocardial hypertrophy and fibrosis in late stage congestive heart failure[8]. The onset of cardiac remodeling further drives progressive deterioration of the failing heart and may directly give rise to clinical arrhythmias[9] or sudden cardiac death in the absence of intervention[1]. Understanding the regulation of cardiac remodeling is therefore important for developing effective heart failure interventions and therapeutics.

Historically, heart failure was first understood to be a cardiorenal disorder in the 1940s and 1950s[10], in which circulatory abnormalities were explained by sodium retention and blood volume expansion. By the 1970s and 1980s, heart failure became regarded as a hemodynamic disorder of both the heart and peripheral circulation, in which the heart suffered abnormalities in pumping capacity and the circulation experienced excessive vasoconstriction[11]. This prompted the favor of positive inotropes[12-13] and vasodilators[14-15] for treating congestive heart failure. However, controlled clinical trials raised concerns that these strategies surprisingly increased the risk of worsening heart failure by exacerbating arrhythmia, provoking ischemia and accelerating cardiac remodeling[16-17].

By the 1980s and 1990s, heart failure was recognized as both a hemodynamic and a neurohormonal disorder: the *neurohormonal hypothesis*[18], which states cardiac

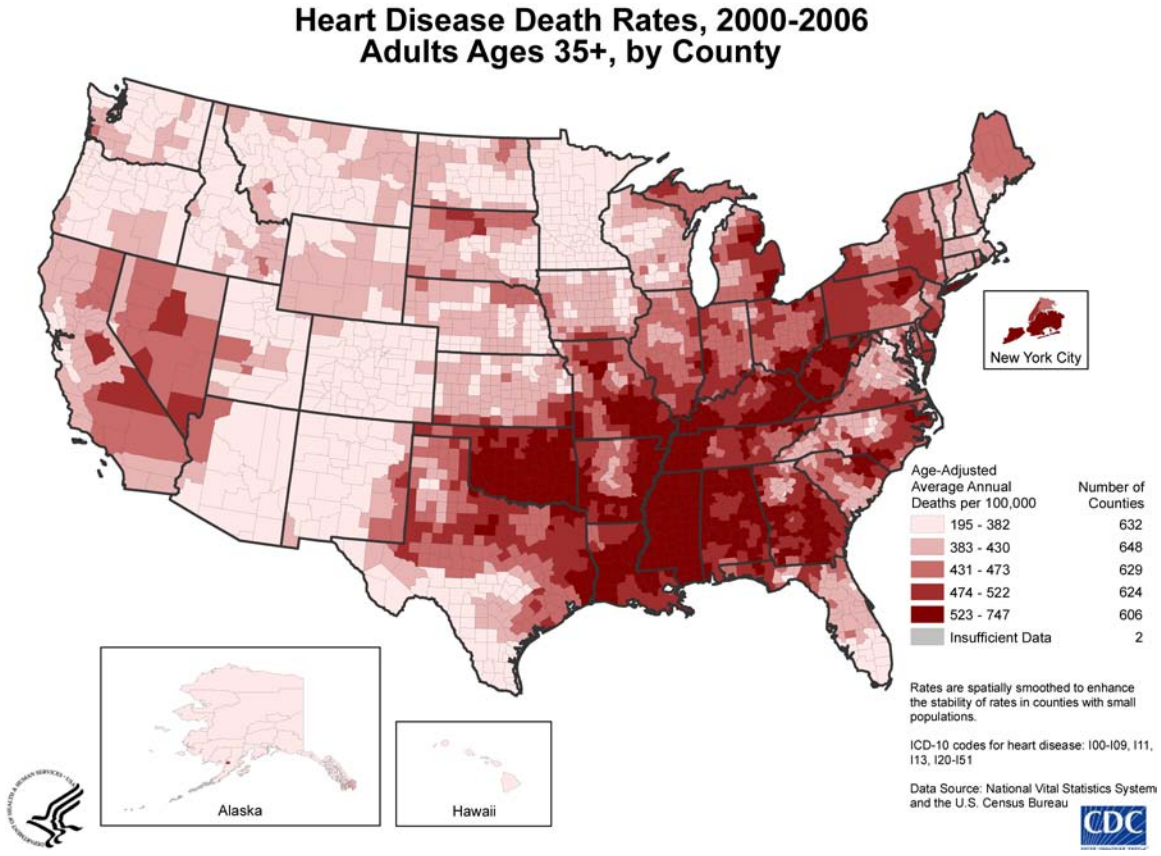

Figure 2.1 Cardiovascular disease incidence in the United States. Cardiovascular diseases are the leading cause of death in the U.S., accounting for 34.3% of all deaths and carrying a total health care cost burden of $503.2 billion in 2010[7]. Image adapted from the Centers for Disease Control[19].

remodeling is driven by the expression of circulating factors (Figure 2.2). This view was supported by the clinical efficacy of β-adrenergic receptor antagonists (β-blockers)[20-21] and angiotensin converting enzyme inhibitors (ACE inhibitors)[22-23] in treating heart failure patients. Today, these two classes of pharmaceutics constitute first-line therapeutics for managing cardiac disease[24-26]. This view revolutionized cardiac research and directed attention towards cardiac cell signaling as an important driver for heart failure progression.

2.2 β-Adrenergic Signaling in Cardiac Physiology

Of the many signaling pathways stimulated by sympathetic activation, the β-adrenergic signaling pathway is best recognized for its acute actions on enhancing cardiac contractility[1] (Figure 2.3). The β-adrenergic signaling pathway is a classic example of stimulatory G-protein coupled receptor (GPCR) signaling, in which binding of the β-adrenergic receptor (β-AR) by ligands such as epinephrine stimulates the dissociation of stimulatory G_α subunit (G_s) to activate transmembrane adenylyl cyclase (AC)[3]. In turn, AC drives the conversion of ATP to cAMP, which freely diffuses across the myocyte to bind protein kinase A (PKA) holoenzyme. Such binding elicits the dissociation of PKA catalytic subunits from PKA regulatory subunits, freeing PKA to phosphorylate substrates important for Ca^{2+} dynamics (*e.g.*, LCC: L-type Ca^{2+} channel, PLB: phospholamban), contractility (*e.g.*, MLC: myosin light chain, TnI: troponin I), ion homeostasis (*e.g.*, PLM: phospholemman), metabolism (*e.g.*, GYS: glycogen synthase), apoptosis/survival (*e.g.*, BAD: Bcl2-associated death promoter) and transcription (*e.g.*, CREB: cAMP response element binding protein, CREM: cAMP response element

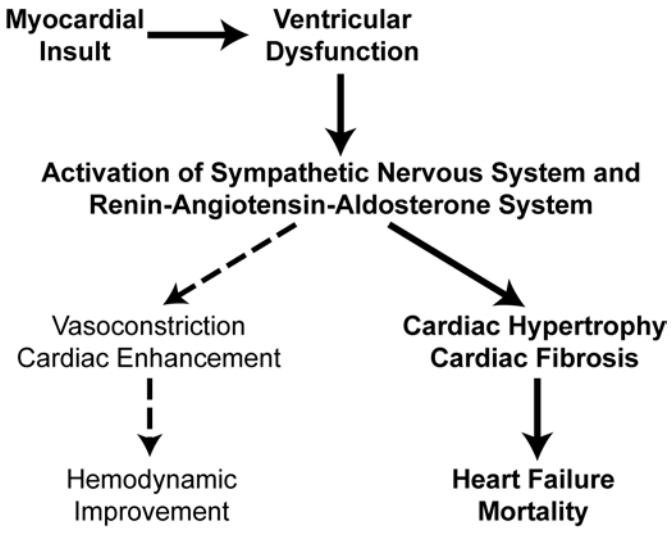

Figure 2.2 The neurohormonal hypothesis. Myocardial insults decrease cardiac contractile performance, stimulating release of catecholamines and neurohormones. Long-term sympathetic nervous system and renin-angiotensin-aldosterone system activation stimulates pathologic remodeling, eventually causing heart failure and mortality.

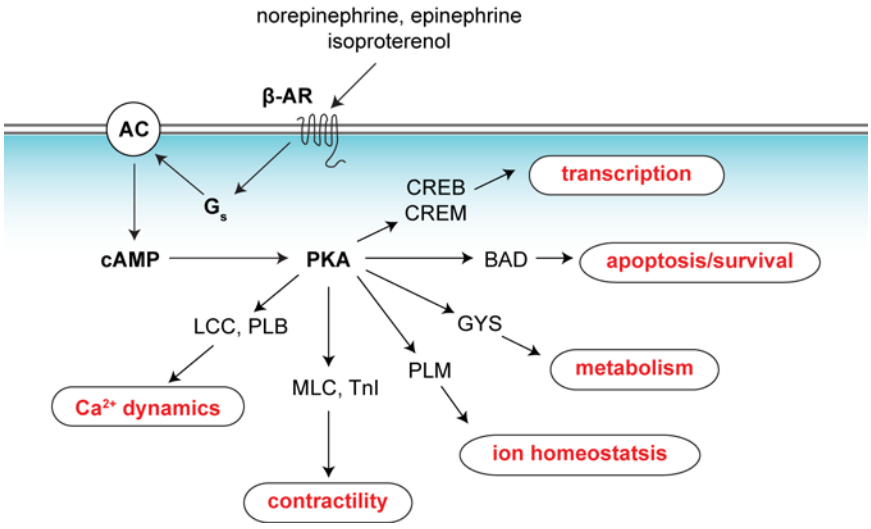

Figure 2.3 β-adrenergic signaling in cardiac physiology. Circulating catecholamines bind β-adrenergic receptors (β-AR), stimulating adenylyl cyclase activation (AC) by G_s and cyclic adenosine monophosphate (cAMP) generation by AC. cAMP binds and activates protein kinase A (PKA) holoenzyme, inducing dissociation of PKA catalytic subunits from regulatory subunits. PKA catalytic subunits phosphorylate substrates regulating Ca^{2+} (LCC: L-type Ca^{2+} channel, PLB: phospholamban), contractility (MLC: myosin light chain, TnI: troponin I), ion homeostasis (PLM: phospholemman), metabolism (GYS: glycogen synthase), apoptosis/cell survival (BAD: Bcl2-associated death promoter) and hypertrophy (CREB: cAMP response element binding protein, CREM: cAMP response element modulator).

modulator). The connectivity of the β-adrenergic signaling pathway to this diverse array of cardiac cell behaviors prompts many questions on how β-adrenergic signaling responses are coordinated and the role of β-adrenergic signaling in the development of cardiac disease.

2.3 β-Adrenergic Signaling in Heart Failure

During heart failure, sympathetic activity is globally enhanced by the elevation of circulating catecholamines[27]. Chronic catecholaminergic stimulation of the β-adrenergic signaling pathway[28-29] and transgenic over-expression of the β_1-adrenergic receptor (β_1-AR)[30], G_s[31] or PKA[32] are all sufficient to induce cardiac disease *in vivo*. These studies, together with the clinical efficacy for β-blockers, collectively implicate an important role for PKA-mediated β-adrenergic signaling in perpetuating heart failure.

However, the direct mechanism for heart failure induction by β-adrenergic signaling remains unclear, as this pathway itself undergoes significant remodeling during heart failure[33]. It is also unresolved whether the overall alterations to β-adrenergic signaling in heart failure are beneficial or detrimental[34-35]. In particular, expression of β_1-ARs decreases as much as 50%[36-37], with remaining β_1-ARs desensitized by enhanced G-protein coupled receptor kinase (GRK) expression[38-39]. G_s[40] and ACs[41] are also downregulated, resulting in decreased levels of cAMP in denervated preparations of the human heart[42-43]. However, the global enhancement in circulating sympathetic activity maintains the heart at a heighted state of adrenergic activation. These changes

collectively reduce β-adrenergic signaling reserve as the entire pathway is maximally engaged in the failing heart.

Thus, in chronic heart failure, β-adrenergic signaling is locked in a vicious cycle whereby elevated sympathetic stress stimulates transcriptional desensitization of β-adrenergic signaling, resulting in decreased contractile performance (Figure 2.4). To maintain myocardial function within physiologically sustainable bounds, adrenergic activation is further increased, fueling pathologic remodeling and driving heart failure progression.

2.4 Compartmentation in β-Adrenergic Signaling

The diversity of cardiac behaviors regulated by β-adrenergic signaling prompts many questions on how the cardiac myocyte makes context-dependent decisions in coordinating β-adrenergic-stimulated responses. One compelling hypothesis at the center of many recent studies is that subcellular localization of β-adrenergic signaling species into various functional 'compartments' of the myocyte may give rise to highly specific β-adrenergic signaling interactions, which may be important for helping the β-adrenergic signaling pathway navigate dynamic myocardial microenvironments in physiology and disease (*compartmentation*)[44-45].

Of the various mechanisms which may give rise to spatiotemporal heterogeneities in cardiac β-adrenergic signaling, three mechanisms have prominently featured in recent compartmentation studies: β-AR compartmentation by lipid rafts[46-47], cAMP compartmentation by phosphodiesterases (PDEs)[48-49] and PKA compartmentation by

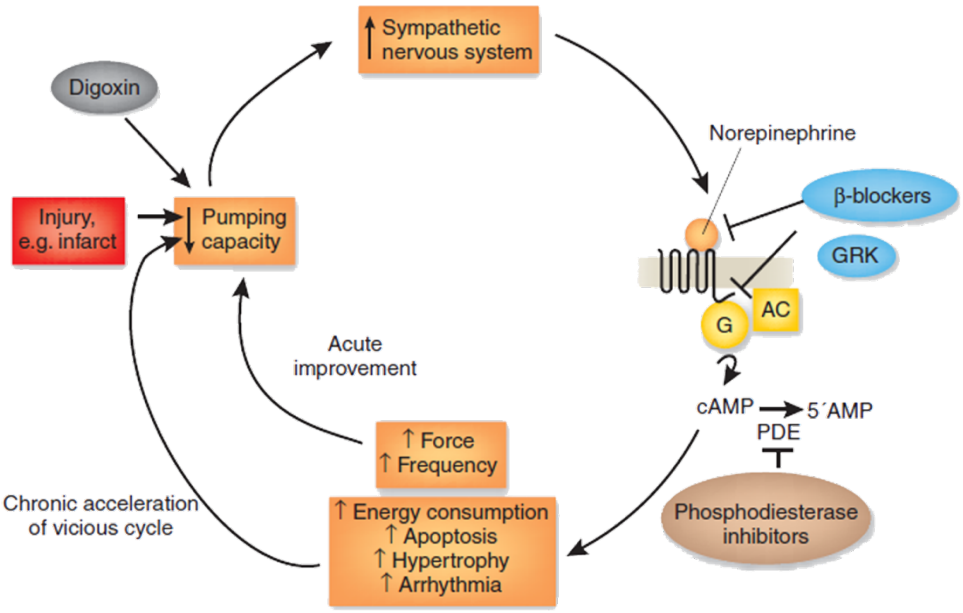

Figure 2.4 β-adrenergic signaling in heart failure[35]. Impaired cardiac performance induces compensatory β-adrenergic stimulation. Sustained β-adrenergic stimulation drives pathologic cardiac remodeling, weakening long-term contractility and inducing further β-adrenergic stimulation. Image by Eschenhagen, et al.[35].

A-kinase anchoring proteins (AKAPs)[50-51]. The importance of receptor compartmentation was highlighted by observations that in healthy myocytes, stimulation of β_1-AR s and β_2-ARs produce distinct subcellular cAMP gradients[52], but these distinctions are lost in heart failure myocytes due to receptor redistribution[53]. PDEs are also thought to importantly regulate cAMP gradients by restricting cAMP diffusion and cAMP access to PKA holoenzyme, deemed significant by observations that PDEs are often expressed in close proximity to PKA (*e.g.*, localized to PKA by some AKAPs[54]). AKAPs powerfully regulate PKA-mediated signaling responses by localizing other signaling species into a common signaling microdomain. This not only improves signaling specificity, but may also accelerate and amplify signaling responses[51].

Together, these compartmentation mechanisms organize the flow of cardiac β-adrenergic signaling. While β-blockers have been overwhelmingly successful as therapeutic agents for improving mortality and morbidity[21], they are often limited by risk of hypotension due to their negative inotropic effects on contractility[55]. These observations have prompted the suggestion of β-adrenergic signaling compartmentation mechanisms as novel therapeutic strategies[56-58]. The ideal therapy would preserve myocardial function and contractile reserve, while maximally inhibiting cardiac remodeling. Identification of mechanisms separating β-adrenergic contractile responses from transcriptional responses is therefore important for the development of next-generation therapeutics.

Chapter 3

Computational Models of Cardiac Signaling Networks

Work from this chapter is published in *Computational models reduce complexity and accelerate insight into cardiac signaling networks*. Yang, J.H., Saucerman, J.J. Circ. Res. 2011; 108(01):85-97.

3.1 Foreword

Cell signaling networks are key regulators of biological functions, but are intrinsically complex, exhibiting massive spatial and temporal heterogeneity within and across cells[59]. Traditional reductionist methods have been very successful in identifying the protein-protein interactions which form the foundation for reconstructing cell signaling networks. However, the interconnectivity and cross-talk of individual pathways challenges intuition for how flow through signaling networks is regulated. In recent decades, computational models have risen to this challenge to help accelerate insight to the regulation and consequences of cell signaling. In this chapter, we review contributions computational models have made toward the understanding of cardiac cell signaling.

3.2 Introduction

In the early 1990s, a major shift occurred in the understanding of heart failure as more than just a hemodynamic dysfunction. This paradigm shift (the *neurohormonal hypothesis*) states that persistent cell signaling by circulating factors is a key driver of pathological cardiac remodeling and helps perpetuate the heart failure phenotype[8,11,18]. This view guides the current therapeutic strategy for managing heart failure and many other cardiac diseases: use of β-blockers, angiotensin converting enzyme (ACE) inhibitors and angiotensin II receptor blockers (ARBs) to block the signaling pathways most strongly activated in disease first, treat other symptoms later. Indeed, 60% of all FDA-approved drugs target membrane-bound proteins; two-thirds of these are receptors for cell signaling[60].

This paradigm underscores the central role of cell signaling pathways in regulating cardiac physiology (*e.g.*, contractility, metabolism) and pathophysiology (*e.g.*, hypertrophy, fibrosis). These pathways comprise an intricate network of biochemical interactions between signaling proteins and exhibit considerate complexity. Tremendous effort has been exerted in the past two decades to understand how cardiac signaling pathways are regulated, how these pathways interface with core functions of the heart and which pathway components are best suited for drug targeting. However, the sheer complexity of these networks often stump experimental intuition and motivate new approaches to study cell signaling.

Still, two decades of experimental studies have yielded a wealth of insight into the biochemistry of signaling proteins, delineation of signaling pathways, and consequences on *in vivo* cardiac function[61-63]. Experimental studies have also empirically explained some of the fundamental mechanisms for cell signaling control, including pathway cross-talk[49,64], transcriptional feedback[65] and spatial compartmentation[44]. These studies collectively form large bodies of evidence that require new frameworks to organize and interpret data as they are generated.

While biologists who study cardiac signaling networks use different methods to probe their respective research interests, the questions they ask are often similar. In general, these questions can be distilled into three fundamental questions:

i.) What are the key *mechanisms* regulating my biological research interest?

ii.) What are the *multi-scale/multi-functional* consequences of my findings?

iii.) How can I extract the most useful biological information from *large data sets*?

These three issues of identifying mechanism, determining consequence and interpreting complex data are challenges well suited for computational modeling and analysis.

3.3 Computational Modeling

By definition, a model is a simplified representation of a complex system. Every experimentalist uses conceptual models to make predictions about how two species may be causally related. Conceptual models help contextualize data, build intuition, generate new hypotheses and facilitate experimental design. Computational models formalize these representations by using mathematical equations to describe the relationships between species.

Computational models take on a diversity of forms. The choice of model structure should be determined by the type of questions being asked, level of quantitative detail desired and quality of experimental data available to constrain model equations and parameters. Mechanistic models are frequently used as *in silico* workbenches for integrating diverse observations into common frameworks and for performing computational experiments to test hypotheses with high throughput. Statistical models are commonly used to identify correlations between species in more complex data sets where causal relationships may be unclear (such as high throughput '–omics' data).

The gold standard for evaluating the quality of a computational model is the extent to which its predictions are validated against experimental data not used in model formulation. A typical workflow for a modeling study starts with a well-defined biological question, iterates through cycles of model testing and refinement, and ends with an experimentally testable answer to that question (Figure 3.1). Modeling studies integrate well with experimental studies to build support for a common hypothesis. Models can complement experiments by making predictions that limit the breadth of experiments performed (thus avoiding unnecessary experiments), revealing candidate biochemical mechanisms that may regulate biological dynamics (thus building intuition) and identifying key participants of a biological phenomena (thus focusing on the most important players). Models also permit unique *in silico* experiments that may not yet be physically possible (*e.g.*, due to instrument resolution/dynamic range or specific and quantitative up-/down-regulation of single or combinations of biological species).

Computational models have enjoyed a long history in studies of cardiovascular physiology, with more depth than any other organ system[66-68]. These models have contributed significantly to the understanding of cardiac physiology and disease, giving insight into important behaviors such as cardiac pacemaking in the sino-atrial node[69], excitation-contraction coupling[70-71], cross-bridge cycling[72], and arrhythmogenesis in the ventricles[73]. Such computational modeling work in the heart played an important role in the development of systems biology[74], giving rise to global efforts such as the International Union of Physiological Science (IUPS) Physiome Project[75-76]. The Physiome Project aims to understand total human cell, tissue and whole-organism

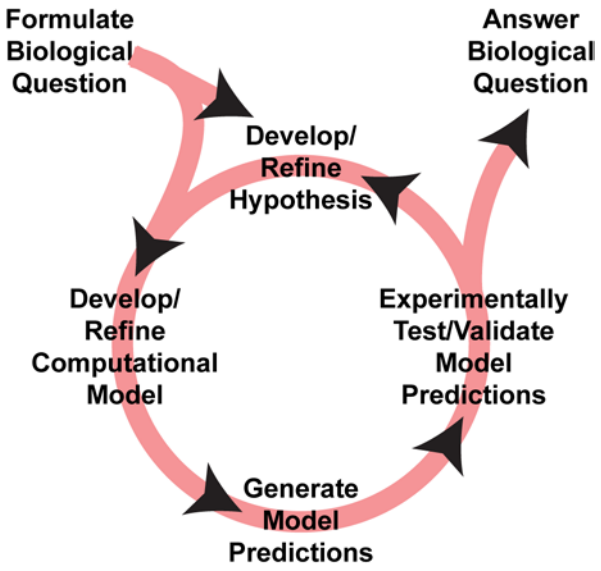

Figure 3.1. Typical workflow for a computational modeling study. Specific biological questions motivate the development of an appropriate modeling approach. Model prediction, validation and refinement is iteratively cycled until an experimentally testable answer is generated to answer the original biological question. These answers can sometimes motivate new hypotheses or new biological questions.

physiology via the integration of databases and computational models. Here, we specifically review the contributions computational modeling approaches have made toward understanding the regulation of cardiac signaling pathways and how these pathways interface with cardiac physiology.

3.4 Mechanistic Models of Cardiac Cell Signaling

The most common forms of computational models used to study cell signaling networks are those constructed with biochemical and biophysical mechanistic detail. These take a 'bottom-up' approach, using laws of mass action and Michaelis-Menten enzyme kinetics to mechanistically represent individual biochemical reactions in a cell signaling network. These models are frequently developed to predict the time-varying relationships between the components being modeled[77]. This approach assumes that the individual biochemical reactions represented are *sufficient* to describe the overall signaling network dynamics and its predictions can be sensitive to missing reactions. While these models require a large number of parameters to be appropriately constrained, the detailed representation of biochemical and biophysical mechanisms enables these models to perform predictive computational experiments, which can later be validated experimentally.

Bhalla, *et al.*, pioneered the use of large signaling network models, integrating many signaling pathways such as PKA, PKC, MAPK, IP3, CaMKII and Ca^{2+} signaling in neurons[78]. In this work, the authors demonstrated how intersecting signaling pathways, as whole networks, can give rise to emergent behaviors such as signal integration across time scales, bistability and feedback. Mechanistic models are also useful for

understanding the fundamental design principles underlying biological networks. Alon, *et al.,* combined modeling and experimental studies to demonstrate how common network motifs found in signaling networks can give rise to a diverse spectrum of systems properties such as network robustness, signaling acceleration/deceleration and memory[79-80]. Taken together, biochemically and biophysically mechanistic models of cell signaling are useful for understanding the mechanisms for cell signaling regulation and the relationships between cell signaling networks and the functions they regulate.

β-adrenergic signaling in the cardiac myocyte

β-adrenergic signaling centrally regulates cardiac contractility and the progression of heart failure (Figure 3.2)[3,34,81]. Under normal sympathetic activity, catecholamines bind β-adrenergic G-protein coupled receptors, signaling through G_s to activate protein kinase A (PKA). PKA can then elicit enhanced contractile (inotropy), relaxation (lusitropy), growth (hypertrophy) and death (apoptosis) responses to adapt to altered circulatory demands. While acute β-adrenergic signaling is important for the *fight-or-flight* response, persistent β-adrenergic signaling induces hypertrophy, fibrosis and heart failure[30,82]. In failing hearts, expression for multiple β-adrenergic signaling proteins decreases significantly[83-84] and drugs which directly inhibit β-adrenergic signaling (β-blockers) are effective first line therapies prescribed in the management of cardiac disease[24-26,85], though the primary mechanisms of action are still unknown.

Saucerman, *et al.,* used this mechanistic modeling approach to investigate the β-adrenergic signaling pathway in the cardiac myocyte[5]. Model simulations were used to

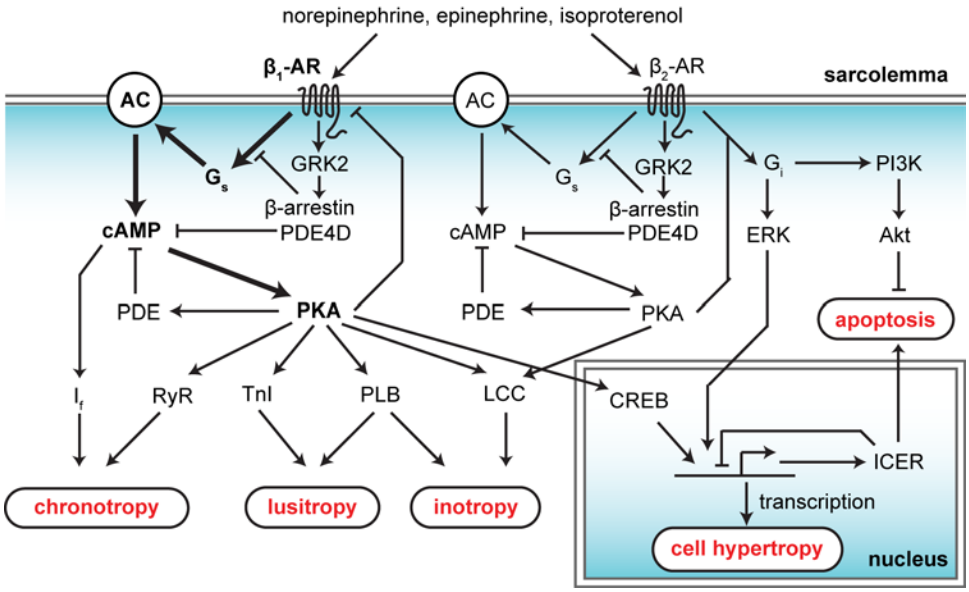

Figure 3.2. β-adrenergic signaling in the cardiac myocyte. Activation of β_1- and β_2-adrenergic receptors (β_1-AR, β_2-AR) by catecholamines initiates a signaling cascade of G-protein activation, adenylyl cyclase production of cAMP and PKA activation by cAMP. Phosphorylation of PKA substrates may elicit a number of cardiac behaviors such as inotropy, lusitropy, chronotropy, hypertrophy and apoptosis.

compare gene therapy strategies and show how protein kinase inhibitor (PKI) can make PKA act as an ultrasensitive switch. Another key aim of this study was to understand which intracellular targets for β-adrenergic signaling were most important for regulating cardiac inotropy. Model analysis demonstrated that most of the inotropic changes due to β_1-adrenergic signaling could be explained by PKA-mediated phosphorylation of the L-type Ca^{2+} channel (LCC) and phospholamban (PLB). In a subsequent study[6], the authors extended this model to show how PKA substrates perform specialized tasks in β_1-adrenergic receptor (β_1-AR)-stimulated inotropy: PLB phosphorylation increases sarcoplasmic reticulum (SR) Ca^{2+} load and accelerates relaxation; LCC and PLB phosphorylation together contribute to increased systolic Ca^{2+}. Moreover, while PKA phosphorylation of the ryanodine receptors (RyR) increased the Ca^{2+} sensitivity for SR Ca^{2+} release[86], its impact on steady-state Ca^{2+} transients was limited, consistent with the Ca^{2+} autoregulation hypothesis[87]. Collectively, these studies were the first to show how molecular perturbations in a cardiac signaling network could be interpreted in the context of cell physiology using computational models.

Other groups continued to explore the effects of β-adrenergic signaling on cardiac electrophysiology. Using a stochastic model of EC coupling in the canine ventricular myocyte, Greenstein, *et al.,* showed how increases in EC coupling gain observed in β-adrenergic stimulation may be explained by increased SR Ca^{2+} load rather than alterations to LCC gating[88]. Moreover, the authors showed how a shift in LCC gating towards higher activity can generate stochastic early after depolarizations (EADs) with implications for arrhythmogenesis under β-adrenergic stimulation. This study highlights

the importance of selecting an appropriate model structure to specifically answer a biological question: by using a stochastic (instead of deterministic) approach, the authors were able to detect rare, probabilistic arrhythmic events generated by β-adrenergic signaling that are otherwise non-intuitive and difficult to observe.

Kuzumoto, *et al.,* adapted the Saucerman model to study the effects of β_1-AR signaling on Na^+ regulation in a guinea pig EC coupling model, demonstrating the necessary role of phospholemman for limiting the increase in Na^+ concentration under β_1-AR stimulation[89]. This model prediction was later validated experimentally by Despa, *et al.*[90]. Himeno, *et al.*, adapted the Kuzumoto model to analyze the role of β_1-AR stimulation in inducing positive chronotropy[91]. They showed how increased firing frequency is driven by a combination of changes to the LCC current (I_{CaL}), sustained inward (Na^+ and K^+) current (I_{st}) and hyperpolarization-activated nonselective cation (Na^+ and K^+) current (I_{ha}). Moreover, the authors made the interesting observation that while the slow delayed rectifier K^+ current (I_{Ks}) contributes weakly to overall K^+ conductance, I_{Ks} plays an important role in counterbalancing increases in I_{CaL} and Na^+/Ca^{2+} exchanger current (I_{NaCa}) during β_1-AR stimulation, which would otherwise prolong the action potential and compromise positive chronotropy. These studies demonstrate how computational models can help reduce the complexity of signaling interactions with cell physiology. Using these models, the authors were able to isolate the actions of β_1-AR signaling on different ion channels to better understand how they act together in concert to regulate Na^+ concentration or cell pacemaking (a feat that could be experimentally intractable).

Mechanistic models of cardiac signaling networks can also be integrated with experimental studies to probe mechanisms for cell signaling kinetics and localization. In a later study, Saucerman, *et al.*, combined their β_1-AR signaling model with live-cell imaging to examine the role of cAMP compartmentation in regulating PKA activity[4]. The authors integrated a spatially explicit implementation of their existing β_1-AR signaling model with live cell Förster resonance energy transfer (FRET) imaging experiments in neonatal rat ventricular myocytes. Using the model, the authors showed how spatial PKA gradients detected in the FRET experiments could be explained by restricted cAMP diffusion, phosphodiesterase (PDE)-mediated cAMP degradation or PKA-mediated cAMP buffering and concluded that cAMP compartmentation is a candidate mechanism for rate limiting PKA activation. Such compartmentation can be an important mechanism for cell signaling specificity[59,92].

Iancu, *et al.*, also took a combined modeling/FRET approach to investigate cAMP compartmentation in cardiac myocytes. The authors first developed a computational model to investigate how the M_2 muscarinic receptor (M_2R) can both stimulate and inhibit cAMP-dependent responses to β_1-AR stimulation[93]. Using their model, the authors showed how the subcellular localization of adenylyl cyclase isoforms stimulated (AC4/7) or inhibited (AC5/6) by the G_i G-protein is sufficient for eliciting seemingly opposite cAMP responses to acetylcholine (ACh). Moreover, their model predicted a rebounding cAMP response following a transient ACh stimulus, which the authors validated using a PKA-based FRET sensor for cAMP. In a later study, the authors combined their model simulations with experiments using an Epac2-based FRET sensor for cAMP to

quantitatively estimate time-varying changes in cAMP concentration[94]. The authors showed cAMP concentrations were significantly higher in the bulk cytosol than near the PKA-based FRET sensor and suggested that these differences may explain how cAMP can differentially regulate PKA and Epac responses to β-adrenergic signaling. Together, these studies illustrate how modeling approaches can be used in concert with live-cell experimental studies to explain mechanisms for cell signaling regulation.

CaMKII signaling in the cardiac myocyte

Ca^{2+}/Calmodulin-dependent protein kinase II (CaMKII) manages another central signaling arm in the cardiac myocyte (Figure 3.3)[81,95]. Ca^{2+}-bound calmodulin (CaM) activates CaMKII, which phosphorylates many Ca^{2+}, Na^{2+} and K^{+} channels to regulate EC coupling and cardiac excitability[96-97]. CaMKII is an important integrator of many signaling pathways in the heart (Ca^{2+}, IP3, G_q-) and contributes to the heart failure phenotype by inducing hypertrophy, apoptosis and aberrant Ca^{2+} handling, which can trigger arrhythmias[98-99]. CaMKII also synergizes with PKA during β-adrenergic signaling[100] and growing evidence suggests CaMKII inhibition may have a beneficial impact on the development of heart failure[101]. These observations have made CaMKII a potentially attractive target for treating cardiac diseases[102].

Hund, *et al.,* implemented the first model of CaMKII signaling in an EC coupling model of the canine ventricular myocyte[103]. The authors showed that while CaMKII contributes to the positive Ca^{2+}-frequency relation by increasing EC coupling gain, action potential duration adaptation at higher frequencies is best explained by the effects of transient

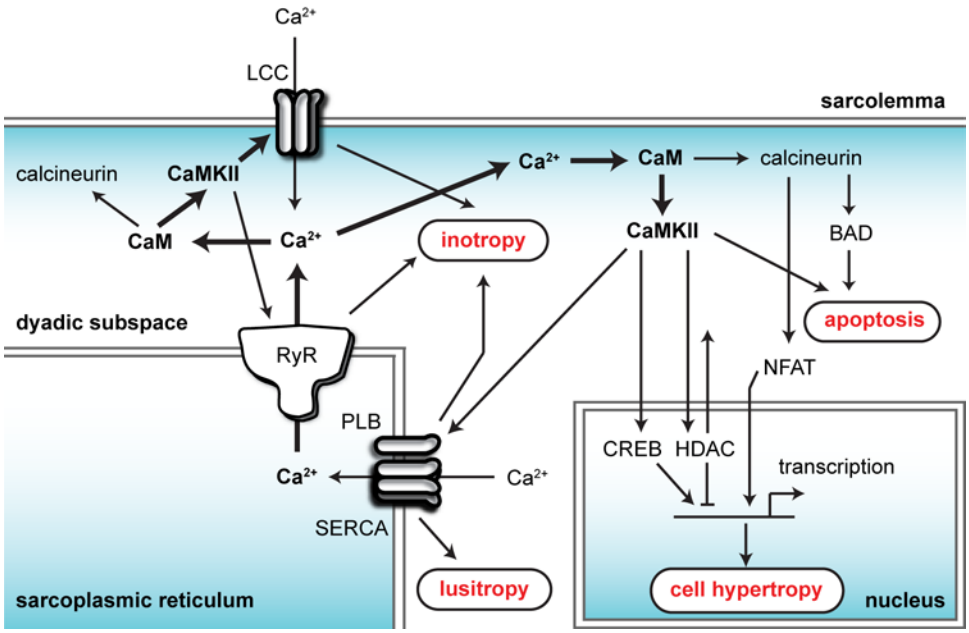

Figure 3.3. CaMKII signaling in the cardiac myocyte. Cardiomyocyte depolarization triggers Ca^{2+} influx through the L-type Ca^{2+} channels (LCCs) and Ca^{2+} release through the ryanodine receptors (RyRs). Free Ca^{2+} binds calmodulin (CaM), which activates CaMKII and calcineurin to elicit a number of cardiac behaviors such as inotropy, lusitropy, hypertrophy and apoptosis.

outward K^+ current (I_{to1}) on repolarization rather than CaMKII. Similarly, Grandi, *et al.*, modeled CaMKII's actions on I_{CaL}, I_{to1} and the fast Na^+ current (I_{Na}) in a rabbit EC coupling model, showing that while the individual effects of CaMKII on I_{Na} or I_{to1} may prolong the action potential, the combined effect on all three contribute to action potential shortening[104]. Moreover, the authors showed how transmural variations in I_{to1} expression may enhance CaMKII-induced arrhythmia in heart failure. The findings from these two studies could only be achieved by separating the individual contributions of CaMKII phosphorylation to the overall action potential, a task made tractable by the use of computational models.

Hashambhoy, *et al.,* also examined the consequences of CaMKII activity on cardiomyocyte electrophysiology. Using a stochastic EC coupling model of the canine ventricular myocyte, the authors showed that CaMKII-dependent shifts in LCC gating can explain LCC facilitation and the apparent faster recovery from LCC inactivation independent of changes to LCC inactivation kinetics[105]. In a subsequent study, the authors showed how LCC phosphorylation by CaMKII decreases EC coupling gain with a greater effect on RyR Ca^{2+} release than RyR phosphorylation itself[106]. Moreover, the authors show LCC hyperphosphorylation is sufficient to induce EADs. Soltis, *et al.,* used a similar approach to show CaMKII is required for the rapid adaptation that underlies frequency-dependent acceleration of recovery (FDAR)[107]. Integrating the Saucerman/McCulloch β_1-AR signaling model into their work, the authors also show that CaMKII and PKA synergize to potentiate a positive feedback loop of CaMKII-Ca^{2+}-CaMKII regeneration. Finally, the authors demonstrate that CaMKII

hyperphosphorylation of RyRs can trigger delayed after depolarizations (DADs), adding support to the hypothesis that CaMKII is responsible for inducing arrhythmias via leaky RyRs. Together, the above modeling studies demonstrate how CaMKII signaling controls the positive Ca^{2+}-frequency relation, LCC facilitation, FDAR and triggers for arrhythmogenesis, illustrating the utility of computational models for linking molecular signaling activities to emergent behaviors in the cardiac myocyte.

Computational models have also examined the role of CaMKII after myocardial infarction. Hund, *et al.*, experimentally measured increased CaMKII autophosphorylation in the border zone and used a model to explain how this can abnormally decrease Ca^{2+} transients by increasing Ca^{2+} leak from the SR[108]. Hyperactive CaMKII also reduced action potential upstroke velocity by altering I_{Na} gating kinetics, a potential mechanism for slow conduction and arrhythmogenesis at the myocardial infarct. Similarly, Christensen, *et al.*, measured increased CaMKII oxidation at the border zone of a canine infarct, and used a model to show how oxidized CaMKII can act on I_{Na} to prolong the action potential refractory period, slow border zone conduction and increase the vulnerability to conduction block at a canine myocardial infarct[109]. Taken together, these studies illustrate the use of models for interpreting the pathophysiological consequences of experimentally measured alterations to cardiac signaling in a disease condition.

Other modeling studies have focused on the biochemical mechanisms for CaMKII activation. In a combined experimental and modeling study, Song, *et al.*, first showed experimentally that CaM-dependent proteins (analogous to CaMKII and calcineurin)

differentially process beat-to-beat Ca^{2+} signals based on their affinity for CaM[110]. The authors used a simple computational model to explain how these differences in CaM affinity can give rise to qualitatively different downstream signaling by these targets. Moreover, deactivation kinetics of CaM targets was driven by Ca^{2+} dissociation from the Ca^{2+}-CaM-target complex rather than dissociation of Ca^{2+}-CaM. Saucerman, *et al.*, extended this modeling work to evaluate local CaMKII and calcineurin dynamics in the rabbit ventricular myocyte[111]. The authors showed how low-CaM affinity CaMKII and high-CaM affinity calcineurin can have different activity profiles and sensitivities to Ca^{2+} oscillations in the cytosol and dyadic cleft (where Ca^{2+} concentrations are considerably larger). By switching the CaMKII and calcineurin affinities for CaM, the local CaMKII and calcineurin responses were switched, leading the authors to conclude that CaMKII's low affinity for CaM is what permitted CaMKII to be highly sensitive to Ca^{2+} in the dyad, but not in the cytosol. This was in contrast to calcineurin, which is highly sensitive to Ca^{2+} in the cytosol but not in the dyad. Chiba, *et al.*, evaluated the role of phosphatases in regulating CaMKII[112]. The authors found that phosphatases limited CaMKII autophosphorylation and were important for regulating frequency-dependent activation of CaMKII. Collectively, these studies exemplify how models can be used to perform *in silico* experiments that are not otherwise tractable, (*e.g.*, manipulation of binding affinities or tracking local CaMKII activity) to identify mechanisms for the regulation of cardiac signaling pathways. These studies also highlight the need for quantitative experiments of localized kinase activities in myocytes.

In addition to activating kinase (CaMKII) and phosphatase (calcineurin) activities, CaM also has direct effects in managing other aspects of EC coupling. For instance, Ca^{2+}-CaM is known to directly regulate Ca^{2+}-dependent inactivation of LCCs[113-114]. While this is typically modeled implicitly as a property of LCC gating, Tanskanen, *et al.*, explicitly represented Ca^{2+}-CaM binding activities in a stochastic model of the cardiac dyad. The authors showed how protein size and arrangement in these microdomains spatially restricts Ca^{2+} movement and influences the macroscopic properties of Ca^{2+}-induced Ca^{2+}-release[115]. Tadross, *et al.*, used a computational model to further investigate how CaM can surprisingly confer sensitivity to small global Ca^{2+} signals in the presence of large local (Ca^{2+}-dependent inactivating) signals to Ca^{2+} channels in neurons[116]. The authors find these behaviors are managed by rapid Ca^{2+} dissociation from Ca^{2+}-CaM and preferential binding by Ca^{2+} channels to free CaM over Ca^{2+}-CaM. These studies illustrate how models can be used to identify new mechanisms for how protein complexes can contribute over many scales to regulate overall cell function.

Other signaling networks

Biochemically mechanistic models have been used to study a limited number of other cardiac signaling pathways as well. Cooling, *et al.*, modeled hypertrophic IP3 transients in response to endothelin 1 (ET-1) and angiotensin II (Ang II)[117]. Using a global sensitivity analysis to comprehensively test the role of every model parameter, the authors determined IP3 transients were primarily driven by dynamics at the receptor level. In particular, the authors showed how the more transient IP3 responses to Ang II than those generated by ET-1 could be explained by differences in receptor kinetics and

density. This global sensitivity analysis exemplifies the type of comprehensive *in silico* experiments that can bring focus on key mechanisms of cell signaling regulation and prioritize future experiments.

Shin, *et al.,* explored the counter-intuitive observation that MCIP can inhibit cardiac hypertrophy by blocking calcineurin, but can also stimulate hypertrophy in response to isoproterenol infusion or transverse aortic constriction (TAC)[118]. Using a computational model, the authors showed the biphasic behavior could be explained by a transcriptional negative feedback loop that includes a large NFAT threshold for MCIP expression. At low or moderate NFAT activity, MCIP expression is low and calcineurin inhibition is small, permitting hypertrophy. However, when NFAT activity crosses this threshold, MCIP expression increases and calcineurin inhibition is large, attenuating hypertrophy. Cooling, *et al.,* used models of NFAT translocation to examine how NFAT activity can be sensitive to both the magnitude and frequency of Ca^{2+} oscillations[119].

Niederer, *et al.,* investigated the role of stretch-induced nitric oxide (NO) generation on Ca^{2+} cycling and force generation in the rat ventricular myocyte[120]. The authors represented the effects of NO on regulating RyR function by making one of the RyR gating variables a function of cardiac myocyte strain, which is thought to increase RyR deactivation via local NO generation. This model predicted a steady-state decrease in Ca^{2+} transients in response to NO's actions on RyRs alone. The authors conclude that this mechanism does not fully explain the slow increased force response of cardiac myocytes

engaged in sustained tension. This study demonstrates how models can identify gaps in understanding and draw attention to areas which require more experimental investigation.

Summary

While biochemically and biophysically mechanistic models require significant data for model validation, their detailed representations can be useful for identifying the key biological mechanisms regulating cardiac signaling pathways. These approaches help reduce the complexity of a signaling network by permitting comprehensive *in silico* assays that dissect the simultaneous effects of multiple interacting signaling mechanisms. These approaches can also help understand how small changes to a signaling network's activity in a disease setting can produce large changes in phenotype. Moreover, these models have significant predictive value and integrate well with experimental studies to complement experimental findings with mechanistic understanding.

3.5 Multi-Scale / Integrated Models of Cardiac Signaling Networks

Cardiac cell-signaling research is motivated by the need to understand how signaling networks regulate human cardiac physiology and disease. Extrapolating molecular signaling events to organ-level phenotypes introduces inherent complexity across spatial, temporal and functional scales. As described above, mechanistic models of cell signaling pathways have tremendous *deductive* value for investigating biological mechanisms. However, other approaches are required for *inductive* extrapolation of the consequences of cell signaling on heart function. A second class of computational models are models

that integrate distinct cardiac functions into a common framework. In practice, model integration is modular in nature and usually involves linking common variables across computational models of different cardiac behaviors. For example, Cortassa, *et al.*, developed an integrated model of the guinea pig cardiomyocyte, linking cell electrophysiology, force generation and mitochondrial energy generation to investigate phenomena such as oxidative stress-induced action potential shortening[121]. By combining these different units into a cohesive framework, integrated models clarify nonintuitive relationships between sub-systems without obvious mechanistic links.

Multi-scale models of cardiac function

This integrative approach is used most extensively in modeling multi-scale aspects of cardiac electromechanics and hemodynamics[122]. Some multi-scale models combine EC coupling models with detailed representations of ventricular anatomies to analyze cellular mechanisms for arrhythmia[123]. Other models integrate descriptions for circulatory resistance to model cardiac hemodynamics[124-125]. Saucerman, *et al.*, used this approach to analyze the arrhythmogenic effects of a point mutation (KCQN1-G589D), which disrupts yotiao-mediated targeting of PKA and PP1 to the I_{Ks} channel[126]. The authors integrated their β-adrenergic signaling model with a rabbit EC coupling model and showed how this mutation would lead to a prolonged action potential only under β-adrenergic stimulation. Coupling this model with a three-dimensional rabbit ventricular wedge model, the authors showed how these cellular long QT events can amplify ventricular heterogeneities in electrical propagation to give rise to arrhythmias. Using this integrated

approach, the authors identified mechanisms for arrhythmia that were not obvious from the cellular or molecular phenotypes.

Nakamura, *et al.*, used a similar approach for investigating progesterone-dependent mechanisms for changes in LQT risk during female menstruation and pregnancy[127]. Taking a combined experimental and computational approach, the authors analyzed the effects of progesterone on the cardiomyocyte action potential and ECG. The authors first experimentally showed progesterone's actions were managed by increased nitric oxide (NO) production by eNOS. The authors then used a computational model to simulate shortened action potentials in conditions with elevated NO, which were consistent with their electrophysiologic measurements in intact myocytes. The authors combined this model with a single-fiber representation of ventricular tissue to simulate ECG responses to progesterone administration in a form of congenital LQT syndrome (KCNE1-D76N), showing progesterone may protect against arrhythmias by regulating cardiac repolarization. This study exemplifies a novel use of combining an integrated computational model with experimental studies to examine the molecular mechanisms behind gender differences in risk for cardiac disease.

Summary

Multi-scale, integrative modeling approaches are helpful for understanding the consequences of molecular signaling events on overall cardiac physiology and pathophysiology. These models integrate detailed descriptions of many cardiac functions into a consistent framework and can identify biological mechanisms that emerge from the

coupling between cells or the heterogeneities in cardiac tissue. These models are also useful for clarifying the relationship between cell signaling and global cardiac behaviors (*e.g.*, contractility, hemodynamics, electrophysiology, metabolism). Current multi-scale models including cell signaling have not yet incorporated tissue-level heterogeneity in cell signaling itself (*e.g.*, variation in neural density, paracrine factors, expression levels); this is an important future direction.

3.6 Large Data Sets

Recent advancements in high-throughput methods for characterizing genomic, transcriptomic, proteomic and metabolomic states allow one to view the global consequences of molecular perturbations rather than just the “usual suspects”. However, this wealth of *–omics* data creates new challenges in data interpretation, as most of the measurements lack a biological context for interpreting the biological relevance to the experimental perturbation. Statistical modeling techniques help reduce the complexity of these data sets by identifying clusters of signaling species that may either be co-regulated or that can similarly regulate other species in a signaling network.

Statistical modeling approaches draw upon information theory and computer science to identify features in the data that may globally represent the entire data set (*e.g.*, principal components). One advantage to these ‘top-down’ techniques is that they make few assumptions about the data and can provide unbiased identification of unexpected correlations. However, statistical models produce different types of information than mechanistic models. While mechanistic models can predict the time-varying dynamics

and spatial localization of individual species in a cell signaling network, statistical models predict correlations between species in a network. While these correlations do not always explain the causality between correlated species, the correlations can be useful for identifying non-intuitive patterns in the data and guide future experiments. These techniques can tremendously reduce the complexity of a high-throughput data set by three to four orders of magnitude and are most useful for screening a large number of observations or generating new hypotheses to explore experimentally. In the context of cardiac signaling networks, these approaches have been used most frequently to examine changes in co-regulated gene/protein expression and changes in the activity of co-regulated protein-protein interactions.

Statistical analysis of high-throughput genomic data

Some of the earliest applications of statistical modeling approaches to cardiac signaling networks involved efforts to interpret DNA microarray datasets. These studies drew from machine learning to identify possible mechanisms regulating the gene or protein expression changes observed between normal and diseased (or transgenic) cardiac tissue. In one group of studies, Hall, *et al.,* examined gene expression profiles associated with reverse remodeling in human hearts following left ventricular assist device (LVAD) treatment[128-129]. These studies revealed a number of important changes to cardiac vascular organization, cytoskeleton organization and integrin and cAMP signaling, suggesting these pathways may be relevant to cardiac remodeling. Hong, *et al.,* took a similar approach to analyze transcriptional profiles corresponding to 17 mouse cardiac phenotypes[130]. In that study, the authors used spectral graph clustering and identified 31

groups of cardiac-specific genes with co-regulated expression. The authors validated the differential expression of some of these genes in a TAC mouse by RT-PCR. These studies illustrate efforts to identify candidate genetic regulators of cardiac remodeling.

Other efforts have specifically focused on understanding experimental models of heart failure. Gao, *et al.,* compared the gene expression profiles from canine tachycardia-induced heart failure against gene expression profiles from heart failure in two other species[131]: 1.) human idiopathic and ischemic heart failure and 2.) mouse TNFα over-expression and MLP knockout heart failure. The authors discovered a number of gene expression changes common between these different heart failure models, including up-regulation of nucleic acid metabolism and transcription pathways and down-regulation of biosynthesis/metabolism and muscle development/contraction pathways. In a later study, the authors took a novel approach, combining microarray analysis with biochemically mechanistic modeling and *in vivo* hemodynamical and electrophysiogical measurements to examine longitudinal cardiac remodeling in canine tachycardia-induced heart failure[132]. They found significant gene expression changes to metabolism, cell signaling and extracellular matrix pathways early in the remodeling process and coincident with left ventricular dysfunction and action potential prolongation. Focusing on genes whose expression correlated with changes in action potential duration, the authors identified a number of candidate proteins that may regulate action potential duration, including the SERCA2 gene. The change in SERCA2 expression was validated by Western blot and a computational model was used to show that SERCA2 downregulation is a sufficient mechanism for prolonging the cardiac action potential. Taken together, the authors

demonstrate how these bioinformatics algorithms can be combined with experimental and computational validation to bring focus to specific molecular targets that manage the heart failure phenotype.

Statistical analysis of high-throughput proteomic data

Statistical modeling methods have also been used to characterize and analyze the cardiac proteome. Differential proteomic expression has significant diagnostic value in identifying patients with human heart failure[133-134]. Early work by Kislinger, *et al.*, combined statistical modeling methods with mass spectrometry characterization of the mouse proteome to classify the organ (brain, heart, kidney, liver, lung, placenta) and subcellular localization (cytosol, cell membrane, mitochondria, nucleus) of all detectable proteins in the mouse proteome[135]. In a later study, the authors made a more comprehensive attempt to characterize the mouse *cardiac* proteome, classifying proteins by subcellular localization and relative abundance and validating many proteins by immunoblotting[136]. Comparing this proteome with various cardiac transcriptomes, the authors showed nearly 50% of expressed proteins had a linear correlation between mRNA and protein expression (Pearson's correlation coefficient $r = 0.915$). Moreover, the majority of the 'outlier' proteins with low mRNA/protein expression correlation ($r = 0.147$) were involved in pathways regulating mitochondrial energy metabolism or ribosome assembly. From this body of work, the authors generated a reference profile of the wild-type mouse cardiac proteome.

These reference proteomes are useful for identifying biomarkers for cardiac disease[133,137]. As an example, Gramolini, *et al.,* focused on a specific heart failure model by comparing protein expression profiles from cardiomyopathic phospholamban mutant mice (PLN-R9C) against those from wild-type littermates[138]. The authors identified changes in protein expression in signaling pathways related to Ca^{2+} signaling, ER stress, cytoskeletal remodeling and apoptosis. These protein expression changes also included known biomarkers for heart failure (AT2A2, ANF, BNP, FABHP, and β-MHC). The authors validated these identified proteins against human cardiac PLN-R9C explants and found correlations in 27 of the 40 highest ranking candidates from the transgenic mouse tissue. Collectively, these studies illustrate how statistical learning methods can be used to simplify complex proteomic datasets to predict unique protein signatures corresponding to different cardiac phenotypes.

Protein-protein interaction networks

An alternative approach to analyzing large data sets is to use a protein-protein interaction (PPI) network to understand how changes in expression may correspond to changes in the regulation of specific signaling pathways and cardiac phenotypes. For example, Berger, *et al.*, used a human PPI network to predict SNPs and FDA approved drugs that may induce long QT syndrome (LQTS) and increase susceptibility for arrhythmias[139]. The authors first curated a human PPI network and then used methods from machine learning to identify a LQTS subnetwork based on 13 genes corresponding to 12 different long QT (LQT) phenotypes or reduced LQT susceptibility. The authors validated this subnetwork against genes, SNPs and drugs known to trigger LQTS and then used the LQTS

subnetwork to predict FDA approved drugs that were not classified as QT prolonging drugs but were associated with reports of QT prolongation. Using their PPI network, the authors hypothesized mechanisms linking the drug targets to the LQT phenotype.

Using a similar approach, Lage, *et al.*, recently examined the PPI subnetworks underlying cardiac morphogenesis in early development[140]. The authors manually curated 255 cardiac development-related genes and computationally classified these genes into 19 functional PPI subnetworks. These 19 subnetworks were then manually annotated by their role in cardiac development, revealing recycling of functional subnetworks during heart development. The authors note increased anatomical complexity correlated with increased signaling complexity, marked by increases in PPI subnetwork activation, transcriptional activity and protein expression. The authors experimentally validated these predictions in 19 human hearts at various stages of development and 14 embryonic human hearts, confirming the regional and temporal activation of these different subnetworks. These studies powerfully show how PPI networks can be used to give mechanistic information on proteins whose expression or activity may altered in human cardiac disease and development. More generally, these studies illustrate how statistical modeling approaches can clarify interpretation of complex data sets to gain insight into how specific signaling networks may regulate organ-level phenotypes.

Summary

Statistical modeling techniques are useful for reducing the dimensionality of complex data sets and identifying key changes in a disease or transgenic cardiac phenotype. These

approaches can identify groups of signaling proteins that are correlated with specific phenotypes or have correlated activity. These groups can be useful for identifying biomarkers for cardiac disease or generating new experimental leads for the regulation of heart failure progression. Protein-protein interaction networks can help facilitate mechanistic understanding of large data sets by identifying how signaling proteins may be connected to each other. Together, these approaches can draw attention to non-obvious relationships between different parts of a signaling network and bring focus to the most important players in a complex phenotype.

3.7 Future Directions

While the cardiovascular system has a rich history of using computational models to study its cellular physiology, the use of computational models to study cardiac signaling networks is still young. To accompany our growing appreciation of cell signaling complexity, there is a great need for new statistical and mechanistic modeling approaches that are scalable to larger signaling networks. At the same time, there are many areas of cardiac signaling that have not yet benefitted from computational modeling.

New statistical approaches to characterizing cardiac signaling networks

Next generation sequencing technologies are now rapidly generating a wealth of data, providing comprehensive profiles for cardiac gene expression[141]. In recent years, researchers studying other systems have developed powerful new statistical modeling techniques to deal with these growing data sets[142-143]. These techniques aim to reduce the dimensionality of large-scale data sets into a more limited number of principal

components that may be more directly associated with a specific phenotype or cell behavior. For example, Janes, *et al.*, examined the signaling network regulating cytokine-induced apoptosis in HT-29 cells, obtaining 7980 measurements of protein activation[144]. The authors used principal components analysis to identify groups of signaling proteins that correspond to stress-apoptosis or cell-survival behaviors. Performing regression analysis on these principal components, the authors generated a model capable of predicting apoptosis responses to TNF, EGF and insulin treatment, which they validated experimentally. The authors also identified certain situations that caused the model to fail in predicting experimental outcomes. By analyzing and reconciling these context-specific 'model breakpoints', the authors identified a number of new mechanisms regulating TNF-induced apoptosis, including an unexpected role for TGFα in PI3K-Akt signaling and a counterintuitive loss of ERK-mediated survival under IL-1a blockade. The authors also evaluated more general properties of cell signaling networks, demonstrating how the overall signaling network is more sensitive to the dynamic range of signaling species than the absolute strength of their signaling activation. This study exemplifies how new statistical modeling techniques can be used to help identify mechanisms for signaling network regulation. As the size of cardiac-specific genomic and proteomic data grows, similar techniques will be important for reducing the complexity of these data sets and for investigating the relationships between signaling species.

Large-scale mechanistic modeling of cardiac signaling networks

The biggest challenge implementing biochemically mechanistic models is the requirement for appropriate biochemical parameters to constrain all reactions in a

signaling network. As these parameters can be difficult to estimate, detailed kinetic models of signaling pathways are typically limited to 10-20 protein species. However, the signaling networks for regulating some cardiac behaviors (*e.g.*, cardiac hypertrophy) involve significantly more signaling molecules with considerably more complexity in network connectivity[64]. Thus, the field needs to identify modeling approaches that can "do more with less". One approach for analyzing a signaling network using its topology alone is to use Boolean or Bayesian analysis, as has been used to study signaling associated with inflammation[145-146]. But these approaches provide only qualitative steady-state information about a system and have difficulty with common network motifs such as feedback loops. Recent efforts have attempted to bridge the gap between network topology and signaling dynamics without requiring the full set of biochemical parameters[147-148]. As more information is known about the diverse signaling pathways that regulate complicated processes such as apoptosis, hypertrophy and metabolism, new progress must be made in the development of computational tools that can integrate these pathways into a consistent framework and make predictions about how they cross-talk to regulate cardiac behaviors.

Opportunities in cardiac cell-based therapies

Cell-based therapies for cardiac diseases are an exciting new research area[149-150]. However, the complexity of signaling pathways that regulate differentiation of cardiac progenitor cells into mature adult cardiac myocytes is a significant obstacle toward forward progress in translating these therapies to the clinic. Computational models can be useful in this context for understanding the relationship between the local environment

and differentiated state of cardiac progenitor cells[151]. In an elegant study combining computational and experimental work, Kirouac, *et al.*, showed how inter-cell paracrine signaling regulated the differentiation of hematopoietic stem and progenitor cells into cells that express blood lineage-associated cell surface antigens[152]. The authors developed a computational model and estimated parameters based on their experiments of stem and progenitor cell differentiation under different selection and media exchange conditions. Using a sensitivity analysis, the authors determined that differentiation of these cells was primarily regulated by secreted inhibitory factors, comprising a paracrine negative feedback loop. Using their model, the authors showed how experimental heterogeneity in long term cell cultures could be explained by stochastic variations in the secretion rates of inhibitory factors. Moreover, they showed how loss of responsiveness to these secreted inhibitory factors was sufficient to explain pathologic transformation of progenitor cells into leukemic stem cells (*in vitro* data published by Warner, *et al.*[153]). This study illustrates how mechanistic signaling models are currently being used to understand and guide experimental differentiation of stem and progenitor cells into desired phenotypes. As cell-based therapies become more attractive treatment options for cardiac diseases, computational models can help accelerate mechanistic understanding of the differentiation processes for cardiac progenitor cells.

Opportunities in mechanotransduction

Cardiac biomechanics play a central role in shaping cardiac development and pathophysiology[154-155]. However, the signaling pathways converting ventricular stresses and strains to signaling cues for cardiac remodeling remain poorly understood. While it is

clear that focal adhesion and integrin-mediated signaling pathways are important for regulating cardiac growth, contractility and repair[156-158], these pathways have received significantly less attention than those stimulated by circulating factors. Moreover, mechanical stretch alone is sufficient for inducing hypertrophy[159-161], arrhythmia[162-164] and changes to G-protein signaling[165-166] and mechanical unloading of failing hearts can reverse cardiac hypertrophy[167-168]. Computational models are already being used to explore the role of mechanical stretch in regulating myocyte electrophysiology[169-171], electromechanics[120,172] and ventricular arrhythmogenesis[173-174]. As cardiac mechanotransduction signaling pathways are better understood, computational models will be important for mechanistically understanding how mechanotransduction interfaces with other signaling pathways to control cardiac contractility and remodeling. Understanding these relationships will be an important step toward reconciling the strengths and weaknesses of the neurohormonal and biomechanical hypotheses for human heart failure[8,11,18] and may help generate new leads for better therapeutic options.

3.8 Conclusions

Computational models are important research tools that can complement experimental studies to reduce the complexity of cardiac signaling networks. Modeling approaches can accelerate mechanistic insight into how signaling networks are regulated and help extrapolate the consequences of these signaling pathways on cardiac physiology. To date, computational models have contributed significantly toward understanding β-adrenergic and CaMKII signaling. There are tremendous opportunities for these approaches to be extended to both well-studied signaling pathways (*e.g.*, α-adrenergic signaling, MAPKs)

and emerging signaling-related fields (*e.g.*, cardiac stem cells, mechanotransduction). Models can help integrate different aspects of cardiac function into coherent frameworks and help understand the actions of cardiac signaling networks on both homeostatic maintenance of cardiac physiology and pathologic progression into heart failure. Modeling studies can also complement experimental studies to both provide mechanistic understanding and generate new experimental leads. These approaches powerfully reduce the complexity of large data sets and bring focus to the most important signaling species or signaling mechanisms regulate cardiac behaviors. As the appreciation for cardiac signaling network complexity and the size/quantity of experimental data sets grow, computational models are becoming necessary for addressing these challenges in a quantitative, mechanistic and methodical manner. Such efforts will prove increasingly important for elucidating mechanisms underlying the *neurohormonal hypothesis* and understanding the pathogenesis of heart failure.

Chapter 4

Regulation of β-Adrenergic Receptor-Stimulated Contractility by Incoherent Feed-Forward Signaling

---

Work from this chapter is published in *Phospholemman is a incoherent feed-forward regulator of Ca^{2+} in β-adrenergic signaling, accelerating β-adrenergic inotropy*. Yang, J.H., Saucerman, J.J. J. Mol. Cell. Cardiol. 2012; 52(5):1048-55.

4.1 Foreword

β-adrenergic signaling is best recognized for its effects on managing the *fight-or-flight* response and stimulating acute enhancements to cardiac contractility. Though the fundamental mechanisms regulating contraction are now well-studied[175], a number of open questions remain regarding how contractile function in normal physiology is maintained. For instance, the sympathetic *fight-or-flight* response elicits a nearly instantaneous enhancement in heart function, while biochemical signaling events are thought to occur over the time scales of minutes. In this chapter, we test the hypothesis that topological features of the β-adrenergic signaling network, such as incoherent feed-forward signaling, play a very important role in regulating cardiac contractility.

4.2 Introduction

During the sympathetic *fight-or-flight* response, β-adrenergic receptor (β-AR) stimulation activates protein kinase A (PKA) to enhance cardiac inotropy and lusitropy[3]. The main PKA substrates responsible for these responses are the L-type Ca^{2+} channels (LCCs) and phospholamban (PLB), which regulate excitation-contraction (EC) coupling by increasing Ca^{2+} influx and increasing sarcoplasmic reticulum (SR) Ca^{2+} reloading, respectively[175]. PKA phosphorylates LCCs on both α and β subunits to both increase total current density and prolong LCC opening (Mode 2 gating). PLB phosphorylation releases inhibition of the SR Ca^{2+}-ATPase (SERCA), increasing the rate of Ca^{2+} uptake into the SR during relaxation.

Recently, phospholemman (PLM) emerged as another PKA substrate capable of regulating cardiomyocyte Ca^{2+} during β-AR stimulation[176]. In the heart, PLM directly inhibits the Na^+/K^+-ATPase (NKA)[177]. PLM phosphorylation by PKA releases this inhibition, driving Na^+ extrusion and indirectly augmenting Na^+/ Ca^{2+}-ATPase (NCX) function via $[Na^+]_i$[90]. This is itself a clinically relevant element of β-adrenergic signaling as $[Na^+]_i$ is elevated in heart failure[178] and PLM is phosphorylated during ischemia[179], identifying PLM as a candidate drug target[180]. Moreover, PLM is hypothesized to serve a protective role against arrhythmia by limiting the rise of intracellular Na^+ and Ca^{2+}[90]. However, it remains unclear if PLM phosphorylation is central to β-adrenergic inotropy.

To quantitatively investigate the role of PLM in β-adrenergic regulation of Ca^{2+} handling and contractility, we constructed a novel mechanistically detailed computational model of the mouse ventricular myocyte. Because PLM is already identified as a key integrator of Na^+ and Ca^{2+} in normal and failing cardiomyocytes[181], we hypothesized that PLM phosphorylation is critically important for the β-adrenergic signaling response. We asked the question, "How does PLM phosphorylation contribute to β-AR enhanced contractility?" Using the model, we show PLM forms an incoherent feed-forward loop with PLB and is necessary for producing rapid *fight-or-flight* responses.

4.3 Models

WT mouse ventricular myocyte model

During the cardiac action potential, membrane depolarization triggers the opening of

L-type Ca^{2+} channels (LCCs), which in turn trigger Ca^{2+} release from the SR through the ryanodine receptors (RyRs). Following this Ca^{2+}-induced Ca^{2+}-release (CICR), Ca^{2+} is resequestered by the SR Ca^{2+}-ATPase (SERCA) and extruded from the myocyte by NCX[81]. CICR is a tightly regulated process, requiring local control and luminal Ca^{2+} sensitivity for maintaining graded Ca^{2+} release with high gain and rapid RyR refractoriness[182-183]. β-adrenergic signaling regulates CICR primarily through protein kinase A (PKA) phosphorylation of the LCCs (increasing Ca^{2+} influx) and PLB (releasing basal SERCA inhibition to further load the SR).

In order to quantitatively describe Ca^{2+} dynamics in the mouse ventricular myocyte accurately, we updated the Bondarenko, *et al*., model of mouse myocyte electrophysiology[184] with new descriptions for locally controlled CICR[185-187], luminal Ca^{2+} dependence of RyR gating[188], reversible SERCA activity[189-190] and cytosolic and SR Ca^{2+} buffering[189,191] (*Appendix A*). In order to investigate β-adrenergic regulation of mouse EC coupling, we fully integrated a model of β_1-adrenergic signaling[5-6] (Figure 4.1). This included PKA-mediated phosphorylation of LCC (increasing peak LCC current and prolonging LCC openings), PLB (increasing SERCA affinity for cytosolic Ca^{2+}), PLM (increasing NKA affinity for cytosolic Na^{+}) and troponin I (increasing troponin C affinity for cytosolic Ca^{2+}). We also updated the NCX model[189] to better capture the interplay between Na^{+} dynamics and Ca^{2+} handling. Because EC coupling dynamics and β-adrenergic signaling dynamics vary over very different time scales (ms vs. min), we imposed ionic charge conservation on the stimulus current to overcome drift and help the model achieve stable steady-state behavior[192].

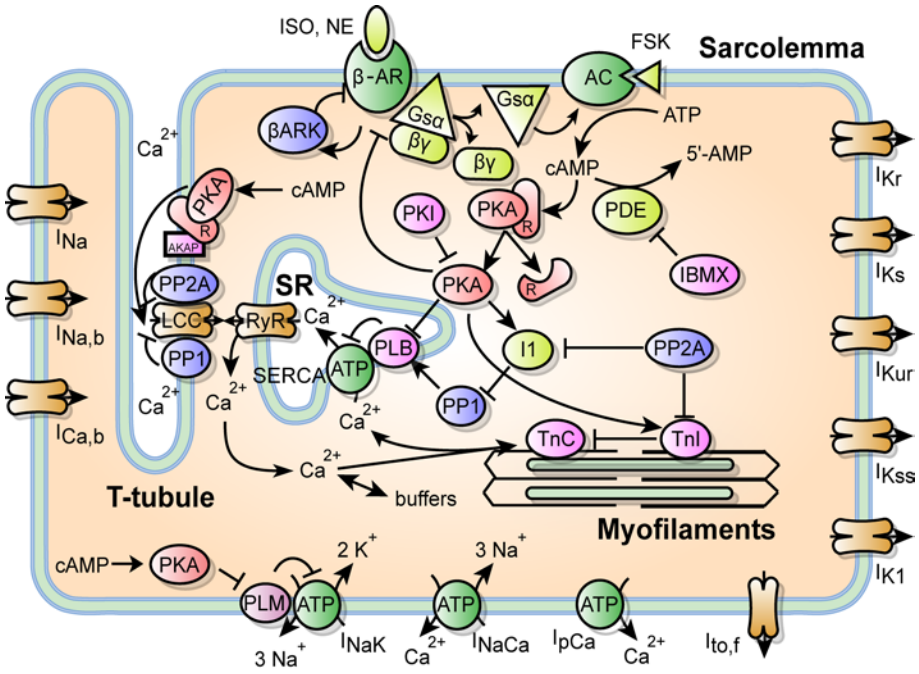

Figure 4.1 Model schematic for integrated β-adrenergic signaling/excitation-contraction coupling model. Beat-to-beat Ca^{2+} dynamics are driven by membrane depolarization, triggering voltage-gated ion channels. Ca^{2+} influx via L-type Ca^{2+} channels (LCCs) trigger Ca^{2+}-induced Ca^{2+}-release from the ryanodine receptors (RyRs). Activation of β-adrenergic receptors (β-AR) stimulates protein kinase A (PKA) activation by cAMP. PKA phosphorylates LCCs and phospholamban (PLB) to enhance Ca^{2+} dynamics. PKA also regulates Na^{+} and K^{+} homeostasis by phosphorylating phospholemman (PLM).

Transgenic mouse myocyte models

In order to simulate Ca^{2+} dynamics in PLM knockout (PLM-KO) and PLB knockout (PLB-KO) myocytes, we modified the WT model by eliminating the inhibitory effects of PLM and PLB on NKA and SERCA, respectively. We further included relevant changes in gene expression to Na^{+} or Ca^{2+} handling proteins. For the PLM-KO case, this meant a 20% reduction in NKA expression[177]. For the PLB-KO case, this meant a 25% reduction in RyR expression[193]. In the case of the PLB/PLM double knockout, we applied both sets of modifications to the WT model.

4.4 Results

PLM confers adaptation to β-AR-stimulated Ca^{2+} transients

During the sympathetic *fight-or-flight* response, intracellular [Na^{+}] is elevated by both increased Na^{+} channel firing frequency and enhanced Ca^{2+}-driven Na^{+} influx via NCX[194]. Simultaneously, β-AR stimulation enhances Na^{+} efflux via PKA-mediated PLM phosphorylation. PLM phosphorylation stimulates NKA Na^{+} extrusion in a manner analogous to PLB enhancement of SERCA function – by releasing basal inhibition and decreasing the K_m for intracellular Na^{+}[177]. In order to examine how β-AR stimulation coincidentally regulates Na^{+} and Ca^{2+}, we derived new expressions for PKA phosphorylation of PLM and incorporated the effects of PLM phosphorylation on NKA into the integrated model. We then modeled the PLM-KO by eliminating PLM-mediated regulation of NKA from the model.

To validate the model, we simulated Na^+ responses to the β-adrenergic agonist isoproterenol (ISO) in both resting (Figure 4.2A) and 2 Hz paced wild-type (WT) and PLM-KO cells. Treatment with 1 μM ISO reduced resting $[Na^+]_i$ in WT cells, but not in PLM-KO cells (Figure 4.2A; WT: 10.5 mM control to 7.8 mM ISO-stimulated $[Na^+]_I$, PLM-KO: 10.4 mM control to 10.4 mM ISO-stimulated $[Na^+]_i$)[177]. Under 2 Hz pacing, $[Na^+]_i$ increased for both WT and PLM-KO myocytes, but 1 μM ISO reversed this Na^+ accumulation in WT cells only (WT: 10.5 mM resting to 14.8 mM paced to 12.4 mM ISO-stimulated $[Na^+]_i$, PLM-KO: 10.4 mM resting to 13.8 mM paced to 15.5 mM ISO-stimulated $[Na^+]_i$)[90]. These results are consistent with the cited experimental data, demonstrating that the model accurately described Na^+ dynamics.

Dynamically, we observed a $[Ca^{2+}]_i$ adaptation (the property of returning to a sub-maximal response following persistent biochemical stimulation) concurrent with the decline in $[Na^+]_i$ in simulated WT cells, but not in PLM-KO cells (Figure 4.2B). This indicates a necessary role for PLM in conferring intracellular Ca^{2+} adaptation consistent with prior experiments[90]. Individual Ca^{2+} transients from unstimulated (*), 2 min early ISO-stimulated (†) and 30 min steady-state ISO-stimulated (‡) agreed with experimental measurements in both shape (Figure 4.2C) and relative change in magnitude (Figure 4.2D; WT: 253 nM control to 887 nM early ISO to 714 nM steady-state ISO twitch Ca^{2+} amplitude, PLM-KO: 223 nM control to 897 nM early ISO to 928 nM steady-state ISO twitch Ca^{2+} amplitude) for WT and PLM-KO myocytes[90]. Moreover, we also found similar increases in SR load to experimental observations (Figures 4.2E and 4.2F; WT: 1242 μM control to 1435 μM steady-state ISO $[Ca^{2+}]_{SR}$, PLM-KO: 1136 μM control to

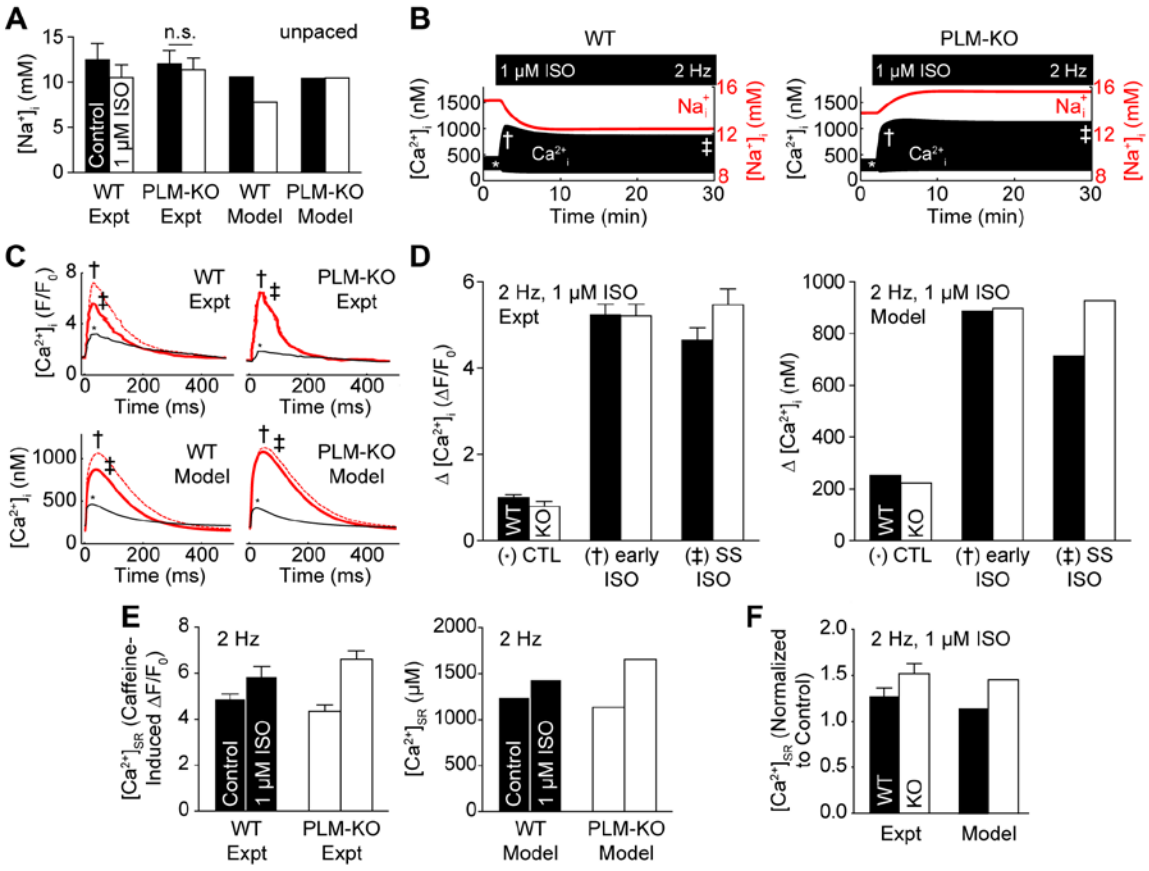

Figure 4.2 Model validation of PLM-KO cardiomyocyte model. A, ISO stimulation reduces $[Na^+]_i$ in resting WT, but not PLM-KO myocytes[177]. B, Cytosolic Ca^{2+} adaptation is uniquely present in the WT myocyte and coincides with the drop in intracellular Na^{+}[90]. C, Model Ca^{2+} transients from control (*), 2 min. early ISO stimulation (†) and 30 min. steady-state ISO stimulation (‡) are consistent with experimental findings[90]. D, Twitch Ca^{2+} amplitude decreases in the WT myocyte at steady-state, indicating Ca^{2+} adaptation[90]. E, ISO-stimulated SR load is larger in PLM-KO myocytes than WT myocytes[90]. F, ISO-stimulated SR loading is similar between model and experiment[90].

1655 μM steady-state ISO $[Ca^{2+}]_{SR}$)[90]. Thus, the model accurately predicts numerous aspects of Na^+/Ca^{2+} handling and β-adrenergic regulation in both WT and PLM-KO cardiac myocytes.

Na^+ manages β-AR-stimulated Ca^{2+} adaptation

Confident that the integrated model faithfully captured Na^+ and Ca^{2+} dynamics, we interrogated the role of Na^+ in managing Ca^{2+} adaptation by performing simulated intracellular Na^+ clamp experiments (Figure 4.3). First, we recorded the simulated normal Na^+ transients from both WT and PLM-KO myocytes (Figure 4.3A). We then repeated the 2 Hz pacing with 1 μM ISO simulations with WT and PLM-KO $[Na^+]_i$ clamped to the recordings from the opposite cell type. Switching the Na^+ transients between WT and PLM-KO myocytes switched the ability of intracellular Ca^{2+} transients to adapt to ISO stimulation (Figure 4.3B), giving direct evidence that PLM-mediated Ca^{2+} adaptation is managed via Na^+. Clamping $[Na^+]_i$ to control concentrations (Figure 4.3A; an intermediate between both ISO-stimulated conditions) prescribed an equivalent insignificant adaptation response (Figure 4.3B). Together, these indicate that the PLM-mediated drop in intracellular Na^+ is both sufficient and necessary to produce the Ca^{2+} adaptation observed in WT cells.

Na^+ regulates cytosolic Ca^{2+} by unloading SR Ca^{2+}

To further understand how Na^+ may regulate cytosolic Ca^{2+} dynamics, we investigated the effects of Na^+ dynamics on SR load (Figure 4.4). Concurrent with the adaptation in cytosolic Ca^{2+} transients, the model predicted an adaptation in SR Ca^{2+} in WT, but not

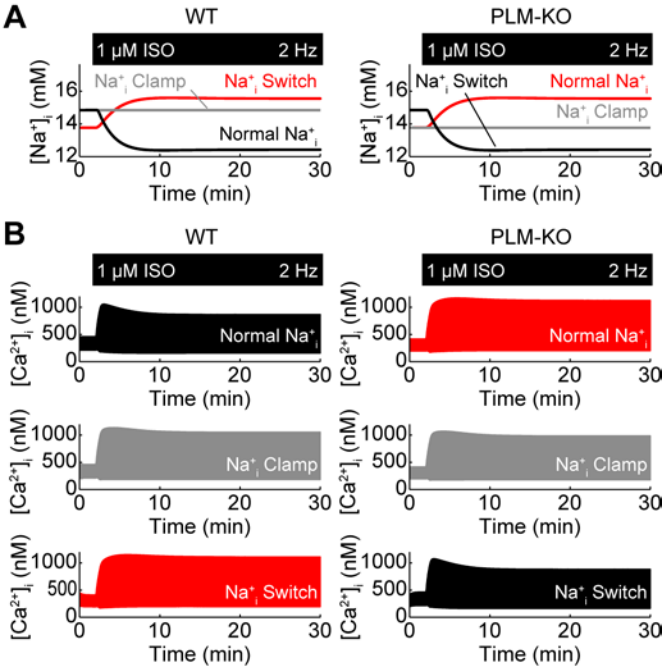

Figure 4.3 Role of Na^+ in managing PLM-mediated Ca^{2+} adaptation. A, Na^+ responses from simulated Na^+ clamp experiments – ISO causes Na^+ to decrease in WT myocytes but increase in PLM-KO myocytes. B, Clamping Na^+ in WT and PLM-KO myocytes to different Na^+ transients indicate a sufficient and necessary role for Na^+ in conferring Ca^{2+} adaptation, evidenced by switching of the Ca^{2+} adaptation phenomena between WT and PLM-KO myocytes.

PLM-KO cells (Figure 4.4A). However, the correlation between adaptive cytosolic Ca^{2+} transients and SR Ca^{2+} alone does not indicate the direction of causality. Recording these SR Ca^{2+} dynamics and performing SR load switch-clamp simulations, we again observed switching of the cytosolic Ca^{2+} adaptation responses (Figure 4.4B). These results give evidence that PLM-mediated Ca^{2+} adaptation to β-AR stimulation may be explained by Na^{+} indirectly unloading the SR.

PLM opposes PLB-mediated SR Ca^{2+} loading

To further explore the role of SR unloading, we sought a system by which one could directly manipulate SR load. PLB-KO mice are one experimentally tractable way of achieving this. We therefore developed a PLB-KO version of our model (Figure 4.5; see *Methods*). We validated this model by quantifying properties of SR load and cytosolic Ca^{2+} transients at rest and under 0.5 Hz pacing. At rest, PLB-KO myocytes had an SR load of 142 μM cytosol (vs. experimental 140 μM cytosol[195]). At 0.5 Hz pacing, cytosolic Ca^{2+} transients had similar amplitudes between WT and PLB-KO myocytes (Figures 4.5A and 4.5B; WT: 136 nM twitch Ca^{2+} amplitude, PLB-KO: 183 nM twitch Ca^{2+} amplitude)[195-196]. We also observed faster relaxation in PLB-KO myocytes than WT control (Figure 4.5C; WT: τ_{WT} = 139.3 ms, PLB-KO: τ_{KO} = 95.3 ms, 0.68 simulated τ_{KO}/ τ_{WT} vs. 0.60 experimental τ_{KO}/ τ_{WT})[195]. Correspondingly, we also observed increased SR loads in PLB-KO myocytes (Figure 4.5D; WT: 719 nM $[Ca^{2+}]_{SR}$, PLB-KO: 1306 nM $[Ca^{2+}]_{SR}$)[195]. Moreover, the simulated fraction of Ca^{2+} relaxation extruded by SERCA, NCX and I_{pCa} was 94.0%, 5.7% and 0.3%, respectively, similarly biased to SERCA as in

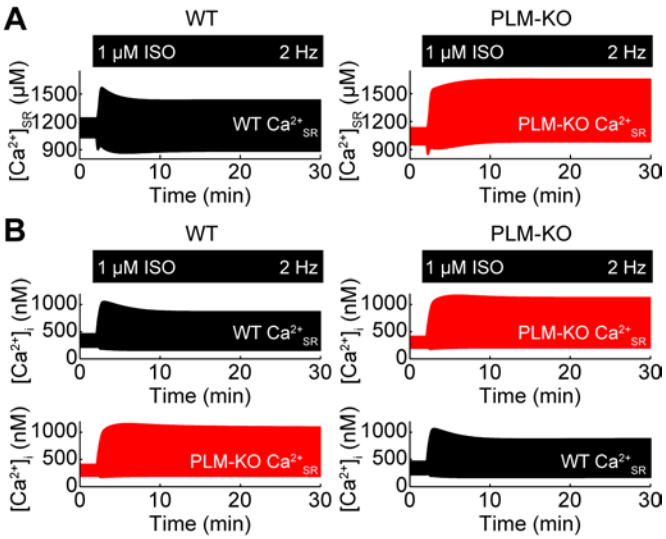

Figure 4.4 Role of SR Ca^{2+} load in managing PLM-mediated Ca^{2+} adaptation. A, SR Ca^{2+} loads for WT and PLM-KO myocytes. B, Switching SR load between WT and PLM-KO myocytes, switches the Ca^{2+} adaptation phenomena between WT and PLM-KO myocytes.

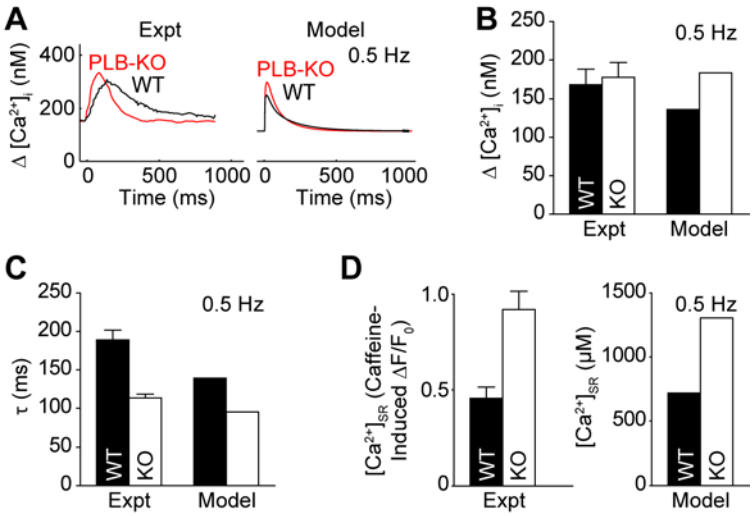

Figure 4.5 Model validation of PLB-KO cardiomyocyte model. A, Model Ca^{2+} transients from WT and PLB-KO myocytes are qualitatively similar to experimental findings[196]. B, WT and PLB-KO Ca^{2+} transients have similar amplitudes[195]. C, PLB knockout accelerates relaxation[195]. D, PLB knockout significantly enhances SR load[195].

experimental measurements (96.4% SERCA, 3.4% NCX, 0.1% other[195]). Thus, the model captured fundamental features of Ca^{2+} handling in PLB-KO myocytes.

At 2 Hz pacing and under 1 μM ISO, the PLB-KO myocyte exhibited an adaptive response in the cytosolic Ca^{2+} transients in spite of the significantly elevated SR load (Figure 4.6A, top). Upon further examination, we detected a decrease in SR load in PLB-KO myocytes when stimulated with ISO (Figure 4.6A, bottom). This surprising result identified a hidden component of the β-adrenergic signaling response normally masked by PLB phosphorylation: SR unloading. To test if PLM phosphorylation was responsible for this SR unloading, we crossed the PLB-KO model with the PLM-KO model to derive a PLB-KO/PLM-KO mouse model. In this double knockout simulation, cytosolic Ca^{2+} transients did not exhibit adaptation and SR Ca^{2+} content stayed elevated, indicating PLM phosphorylation underlied SR unloading (Figure 4.6B).

To further investigate the individual contributions of PLB and PLM to SR load under ISO stimulation, we simulated 2 Hz pacing, 1 μM ISO-stimulated responses in WT myocytes where PKA could only phosphorylate either PLB alone, PLM alone or both PLB and PLM only (Figure 4.6C). When PLB alone was phosphorylated, the τ for $[Ca^{2+}]_i$ decline decreased to 113 ms (from 124 ms in unstimulated WT myocytes) and SR load increased to 1802 μM $[Ca^{2+}]_{SR}$ (from 1242 μM $[Ca^{2+}]_{SR}$ in unstimulated WT myocytes). This exceeded the steady-state SR load in fully stimulated WT myocytes (1435 μM $[Ca^{2+}]_{SR}$). PLM phosphorylation alone also decreased the τ for $[Ca^{2+}]_i$ decline (to 118 ms), but in contrast to PLB phosphorylation alone, SR load decreased to 894 μM $[Ca^{2+}]_{SR}$. When

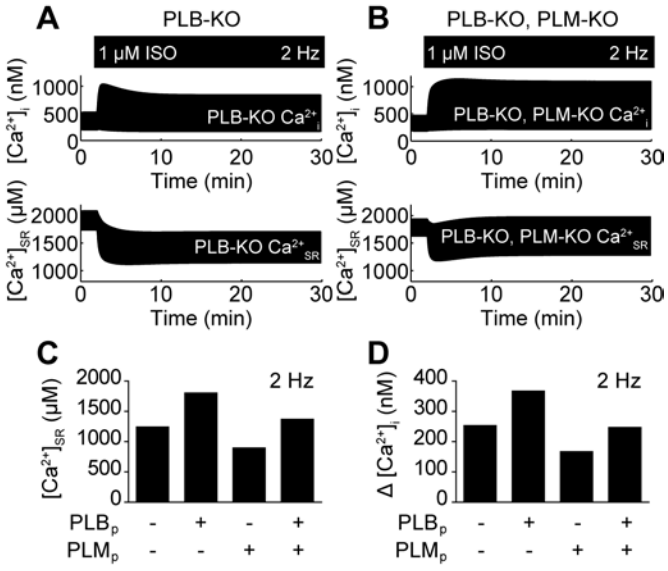

Figure 4.6 Opposing actions of PLB and PLM on EC coupling. A, PLB-KO myocytes also exhibit Ca^{2+} adaptation in spite of elevated SR load. SR load decreases with sustained β-AR stimulation. B, PLB-KO, PLM-KO myocytes do not exhibit Ca^{2+} adaptation. SR load does not decrease with sustained β-AR stimulation. C, PLB phosphorylation and PLM phosphorylation exert opposite effects on SR load. D, PLB phosphorylation and PLM phosphorylation exert opposite effects on cytosolic Ca^{2+} transients.

both PLB and PLM are phosphorylated (in the absence of LCC phosphorylation), the τ for $[Ca^{2+}]_i$ decline decreased to 100 ms and SR load reached 1369 μM $[Ca^{2+}]_{SR}$. Looking at Ca^{2+} transient amplitudes, we observe similar relationships between these different PLB and PLM phosphorylation conditions (Figure 4.5D), implying that cytosolic Ca^{2+} responses track with SR load. Together, these results demonstrate that while PLB and PLM both contribute to enhanced Ca^{2+} relaxation, PLB and PLM elicit opposite effects on both SR load and Ca^{2+} adaptation.

Ca^{2+} adaptation is a incoherent feed-forward property of β-adrenergic signaling

In principle, only two network motifs are capable of giving rise to adaptation responses in a cell signaling network: negative feedback loops and incoherent feed-forward loops[197-198]. In the β-AR signaling pathway, both motifs are present (Figure 4.1). First, β-ARs can be directly desensitized by both GRKs and PKA in a negative feedback loop[199] with significant implications for cardiac physiology[200]. Second, PKA phosphorylates both PLB and PLM, simultaneously increasing and decreasing total Ca^{2+} content. Both network motifs offer reasonable explanations for β-AR-stimulated Ca^{2+} adaptation.

To determine if the ISO-stimulated Ca^{2+} adaptation is a consequence of β-AR desensitization or PLM incoherent feed-forward control, we simulated 2 Hz pacing, 1 μM ISO-stimulated responses in WT myocytes with either PLM phosphorylation or β_1-AR desensitization blocked, or both. Removing PLM phosphorylation by PKA significantly inhibited Ca^{2+} adaptation in both SR load (Figure 4.7A) and cytosolic Ca^{2+} transients (Figure 4.7B). Steady-state twitch Ca^{2+} amplitudes reached 988 nM $[Ca^{2+}]_i$ from 714 nM

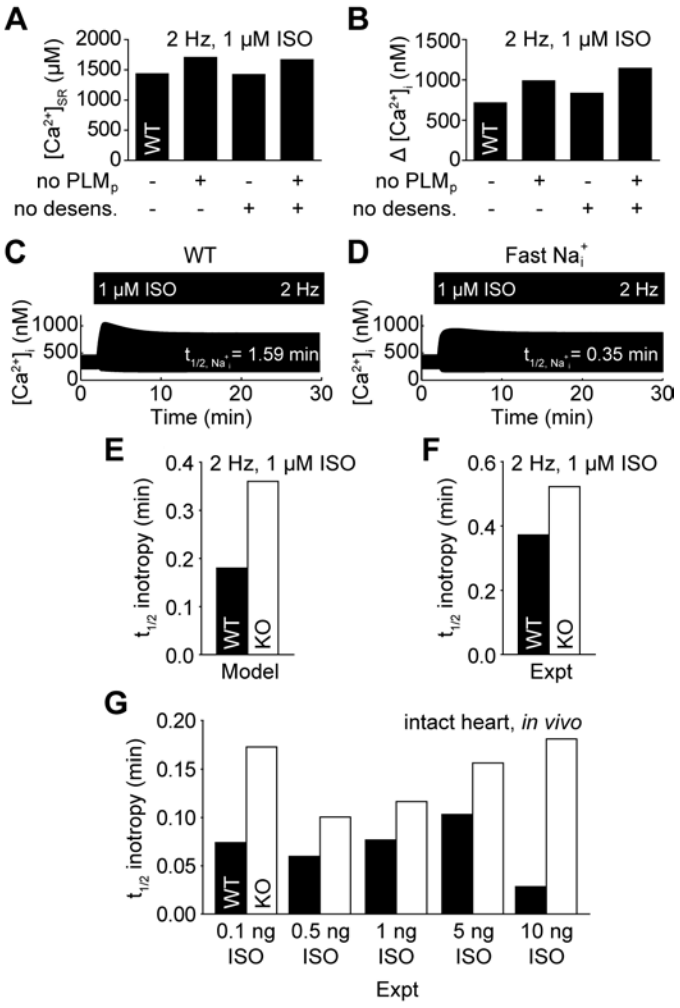

Figure 4.7 Ca^{2+} adaptation is explained by an incoherent feed-forward loop. A, Steady-state SR load is better explained by PLM phosphorylation than β-AR desensitization. B, PLM phosphorylation contributes more strongly to limit cytosolic Ca^{2+} transients than β-AR desensitization. C, WT Ca^{2+} adaptation is associated with slow intracellular Na^{+} dynamics. D, Acceleration of intracellular Na^{+} dynamics blocks Ca^{2+} adaptation in WT myocytes, indicating an incoherent feed-forward regulatory motif. E, The model predicts accelerated inotropic responses to ISO in WT myocytes over PLM-KO myocytes. F, Published experimental data validates this model prediction in cardiac myocytes[90] and G, also indicates this acceleration occurs in the intact heart[201].

$[Ca^{2+}]_I$ in WT cells. Blocking β_1-AR desensitization inhibited Ca^{2+} adaptation more weakly, with a steady-state twitch Ca^{2+} amplitude of 833 nM $[Ca^{2+}]_i$. Blocking both PLM phosphorylation and β_1-AR desensitization fully inhibited Ca^{2+} adaptation with a steady-state twitch Ca^{2+} amplitude of 1144 nM $[Ca^{2+}]_i$. These results indicate that PLM phosphorylation accounts for most of the cytosolic Ca^{2+} adaptation.

Adaptation in incoherent feed-forward loops requires a time delay between the fast positive signal transduction cascade and slow negative signal transduction cascade[198]. We therefore hypothesized that if the observed cytosolic Ca^{2+} adaptation is indeed a consequence of PLM-mediated incoherent feed-forward inhibition, then SR Ca^{2+} loading by SERCA (via PLB phosphorylation) must be fast with respect to Na^+ extrusion by NKA (via PLM phosphorylation). Indeed, the t_{50} for SR Ca^{2+} loading was 0.36 min while t_{50} for Na^+ extrusion was 1.59 min in ISO-stimulated WT cells (Figure 4.7C). We then tested the hypothesis that accelerating Na^+ extrusion (and therefore breaking the time delay between PLB- and PLM-mediated effects) would block the cytosolic Ca^{2+} adaptation. Indeed, increasing NKA activity to accelerate Na^+ extrusion to the same rate as SR Ca^{2+} loading (t_{50} = 0.35 min) blocked Ca^{2+} adaptation to ISO stimulation (Figure 4.7D). Together, these results offer strong evidence that Ca^{2+} adaptation is a incoherent feed-forward property of β-AR signaling, managed by PLM.

PLM phosphorylation accelerates β-adrenergic inotropy

In addition to providing mechanisms for adaptation, incoherent feed-forward loops are capable of accelerating cell signaling responses[202]. We hypothesized that PLM

phosphorylation may be important for accelerating β-AR-stimulated inotropy. We measured the t_{50} for steady-state Ca^{2+} transient enhancement in the simulated WT and PLM-KO myocytes (Figure 4.7E). Indeed, β-AR-stimulated inotropy was accelerated by 100% in WT myocytes over PLM-KO myocytes (WT: t_{50} = 0.18 min, PLM-KO: t_{50} = 0.36 min). We have not encountered any published reports of PLM-mediated acceleration of β-adrenergic inotropy, so we decided to experimentally validate this model prediction by reanalyzing published data. Digitizing and reanalyzing the work by Despa, *et al.*[90], we find 41% acceleration in their representative experiments of Ca^{2+} transients in isolated myocytes exposed to ISO (Figure 4.7F; WT: t_{50} = 0.37 min, PLM-KO: t_{50} = 0.52 min). We further reanalyzed *in vivo* data from Wang, *et al.*[201], which measured the timecourse of left ventricular pressure in live WT and PLM-KO mice following serial injections of ISO. This analysis revealed an average 168% acceleration of left ventricular pressure inotropy in WT mice over PLM-KO mice across a 2-order of magnitude range of ISO concentrations (Figure 4.7G). These results strongly support our hypothesis that PLM phosphorylation plays a central role in β-adrenergic signaling by accelerating steady-state inotropy *in vitro* and *in vivo*.

4.5 Discussion

In this chapter, we model the role of PLM phosphorylation in regulating cytosolic Ca^{2+} transients during β-adrenergic signaling. Extensive experimental work has demonstrated that PLM is important for managing intracellular Na^{+} and modulating EC coupling in normal and failing myocytes[90,177-178]. Here, we use a model to test our understanding of

how PLM may regulate EC coupling. Model simulations indicate a necessary and sufficient role for Na^+ to parlay PLM phosphorylation signals to the SR to confer long-term cytosolic Ca^{2+} adaptation to β-AR stimulation. The magnitude of this adaptation response cannot be explained by receptor-level negative feedback via β-AR desensitization, identifying PLM as an important incoherent feed-forward regulator of cytosolic Ca^{2+}.

PLM-mediated protection against spontaneous Ca^{2+} release

In the intact heart, β-adrenergic signaling simultaneously coordinates a number of events during the sympathetic *fight-or-flight* response[3]. While the net effect of these events is to enhance contractile function (via increased chronotropy, inotropy, lusitropy), persistent β-AR stimulation can itself drive cardiac pathologies. In addition to activating cardiac remodeling transcriptional programs, β-AR stimulation-induced chronotropy drives intracellular Na^+ loading by accelerating Na^+ entry with the increased frequency of myocyte depolarizations. Indeed, intracellular Na^+ is elevated in the failing heart and may have important consequences on NCX function[178]. Despa, *et al*., hypothesized that PLM phosphorylation may play a protective role in the sympathetic *fight-or-flight* response by limiting the rise of intracellular Na^+, thereby preventing Ca^{2+} overload and arrhythmic Ca^{2+} release[90]. Our results support this hypothesis, evidenced by the elevated $[Na^+]_i$ and reduced $[Ca^{2+}]_{SR}$ in our PLM-KO myocyte simulations (Figure 4.2).

Interestingly, Despa, *et al*., observed an increased propensity for spontaneous ISO-stimulated Ca^{2+} transients in their PLM-KO experiments[90]. However, our model did not

predict after-depolarizations in spite of the inclusion of a luminal RyR gating mechanism. There are a few possible explanations for this discrepancy. First, some evidence suggests that early after-depolarizations may be driven by stochastic LCC openings during β-AR stimulation[203], while our model is deterministic. Other evidence suggests RyR phosphorylation may lower the threshold for store overload-induced Ca^{2+}-release by sensitizing luminal Ca^{2+} dependence for RyR gating[204]. But this mechanism is unclear as other evidence suggests luminal RyR gating may be protective against spontaneous Ca^{2+} release by accelerating Ca^{2+} regulation[188]. Our recent models have predicted that CaMKII-mediated RyR phosphorylation can play a key role in β-AR-induced delayed after-depolarizations[107]. However, these effects are not included here as we limited our study to focus on PKA substrate phosphorylation.

Systems understanding of PLM in β-adrenergic regulation of contractility

In the conventional understanding of β-adrenergic regulation of EC coupling, PKA phosphorylates many targets to collectively enhance cardiac inotropy and lusitropy. It is proposed that PLM may act as a cardiac stress protein that minimizes the risk of arrhythmogenesis at the expense of reduced inotropy[176]. Consistent with this proposition is our model prediction that PLB and PLM phosphorylation elicit opposite effects on SR load (Figure 4.6C). Though these effects are similar in magnitude, release of PLB inhibition of SERCA overtakes release of PLM inhibition of NKA in regulating SR load, masking the PLM response. Simulations with PLB and PLM phosphorylation alone also unmask the relative effect of LCC phosphorylation. PLB and PLM are able to recapitulate most of the SR loading in ISO-stimulated WT cells (WT: 1435 μM $[Ca^{2+}]_{SR}$,

PLB/PLM phosphorylation: 1369 μM $[Ca^{2+}]_{SR}$), but are unable to recapitulate the enhanced Ca^{2+} transients (WT: 725 nM $\Delta[Ca^{2+}]_i$, PLB/PLM phosphorylation: 247 nM $\Delta[Ca^{2+}]_i$).

From this perspective, the roles of LCC, PLB and PLM are more clearly defined. While Ca^{2+} influx through LCCs is thought to be the primary mechanism for regulating total cellular Ca^{2+}[205], our model suggests β-adrenergic increases in the total Ca^{2+} content in mouse are primarily explained by enhanced Ca^{2+} retention (via PLB phosphorylation and increased SERCA Ca^{2+} uptake), rather than enhanced Ca^{2+} influx. Moreover, enhancements to β-adrenergic Ca^{2+} transients are better explained by increased CICR (via LCC phosphorylation, increasing trigger Ca^{2+} flux to enhance RyR release), than by mere enhancements to sarcolemmal Ca^{2+} influx or global $[Ca^{2+}]$. Indeed at 2 Hz pacing, 1 μM ISO increased steady-state RyR fractional release from 29.1% to 59.0%. However, when LCC phosphorylation was ablated, steady-state RyR fractional release only increased to 31.8%, highlighting the significance of high EC coupling gain under normal CICR and supporting the observation that β-adrenergic signaling enhances CICR by a local saturation of LCC trigger Ca^{2+} rather than an enhancement to SR load[206]. PLM moderates Ca^{2+} transients indirectly by enhancing NCX Ca^{2+} efflux, which reduces SR Ca^{2+} load and thus the extent of CICR.

If PLM acts to directly oppose PLB, what evolutionary advantage is gained by conserving this inefficient process? We show PLB and PLM form a negative (incoherent) feed-forward network motif[79], accelerating steady-state β-adrenergic inotropy (Figure

4.7). This PLM-mediated acceleration was substantial in our model (100%) and reanalysis of published *in vitro* data by Despa, *et al.*[90] and *in vivo* data by Wang, *et al.*[201] validate this model prediction (Figure 4.7). cAMP accumulation was previously shown to be a rate-limiting step in the β-adrenergic signaling response[4,207]. The current findings further elaborate this concept of pathway kinetics, showing that the downstream PLM feed-forward loop causes Ca^{2+} inotropy to reach steady state (t_{50} = 0.18 min) faster than the upstream cAMP (t_{50} = 0.41 min) and PKA (t_{50} = 0.33 min) signals. Thus paradoxically the β-adrenergic signaling pathway accelerates as the inotropic signal propagates downstream.

Moreover, the t_{50} for the WT myocyte in our model was 0.18 min shorter than the PLM-KO myocyte, implying these myocytes reach steady-state inotropy ~40 beats faster at the cost of minor reductions in inotropy. This model prediction is only a lower-bound estimate since PKA also phosphorylates troponin I and myosin binding protein C to sensitize myofilaments to Ca^{2+} and accelerate stretch activation[208-209]. Together these indicate that in addition to its role in protecting against arrhythmia, PLM critically accelerates β-adrenergic signaling responses, overcoming slow cAMP and PKA dynamics to ensure a rapid *fight-or-flight* response. PLM simultaneously mediates both this acceleration and its antiARrhythmic effects by adapting SR Ca^{2+} load.

Relevance to other species

Mouse EC coupling differs from EC coupling in other species with an increased heart rate and a more significant dependence on SERCA for Ca^{2+} relaxation. Mouse resting

$[Na^+]_i$ is also typically higher (10-15 mM) than that of other mammalian species (4-8 mM)[194], due to enhanced Na^+ influx. In contrast, NKA function is similar across species and PLM phosphorylation induces similar enhancements to NKA activity[210]. While there are few published studies of PLM phosphorylation-mediated effects on Ca^{2+} handling in other species, it stands to reason that the results presented here would generalize to other species since NKA is the primary mechanism for Na^+ extrusion in the cardiac myocyte. Because NCX more prominently regulates Ca^{2+} in human and other mammalian myocytes[175], PLM phosphorylation is expected to drive greater cytosolic Ca^{2+} unloading and greater Ca^{2+} adaptation in human than mouse, enhancing PLM-driven acceleration of β-adrenergic inotropy. Moreover, PLM phosphorylation may also have a stronger anti-arrhythmic role in human than mouse. New experimental work is needed to clarify the role of PLM in human cardiac Ca^{2+} handling.

Computational modeling of mouse EC coupling

Computational models have emerged as useful tools for interrogating cardiac signaling[211] and EC coupling[66]. There are now several published computational models of the mouse ventricular myocyte[184,212-216]. The model presented here improves upon existing mouse models by including mechanisms central to EC coupling and fully integrated descriptions of β-adrenergic signaling. Moreover, as Na^+ dynamics are relevant to cardiac disease, our model is the first to explicitly represent Na^+ regulation of Ca^{2+} transients. While this model is limited by variability in mouse strains and experimental data sources, this model captures many core components of cardiac Ca^{2+} handling, as evidenced by the ability to

faithfully reproduce quantitative data from WT and two non-trivial transgenic knockout mouse conditions.

One important component missing from this model is CaMKII regulation of EC coupling and frequency-dependent acceleration of relaxation (though the mechanism remains unknown[217]). However, for the purposes of this study we bounded the model at the level of PKA activation, as any model can always be improved without end. Indeed, the current model is already consistent with a wide range of experimental data. Modeling transgenic knockouts is also subject to gaps in knowledge of all the expression differences between knockout and WT – here we could only incorporate the primary known adaptive gene expression changes in PLM- and PLB-KO mice.

4.6 Conclusions

In summary, we have developed a new computational model of the mouse ventricular myocyte to investigate the role of PLM in regulating EC coupling responses to β-adrenergic signaling. Using this model, we have shown that PLM comprises a incoherent feed-forward loop with PLB, conferring both adaptation to cytosolic Ca^{2+} transients via Na^{+} effects on SR load and acceleration to β-AR-stimulated inotropy. In this way, PLM critically regulates the sympathetic *fight-or-flight* response.

Chapter 5

Regulation of Angiotensin II Receptor-Stimulated Fibrosis by Incoherent Feed-Forward Signaling

---

Work from this chapter is published in *Systems analysis of bounded signaling modules generates experimental roadmap for eight major diseases*. Benedict, K.F., Mac Gabhann, F.*, Amanfu, R.K.*, Chavali, A.K.*, Gianchandani, E.P.*, Glaw, L.S.*, Oberhardt, M.A.*, Thorne, B.C.*, Yang, J.H.**, Papin, J.A., Peirce, S.M., Saucerman, J.J., Skalak, T.C. Ann. Biomed. Eng. 2011; 39(2):621-35.

(*) denotes equal contribution

5.1 Foreword

In the previous chapter, we showed how incoherent feed-forward signaling can accelerate and confer adaptation to β-adrenergic receptor-stimulated contractility. These incoherent feed-forward signaling motifs are common in cell signaling, prompting us to hypothesize that these motifs may also be relevant to other aspects of cardiac disease. One such example is in Angiotensin II (Ang II) signaling, in which type 2 Ang II receptors directly antagonize type 1 Ang II receptors at multiple nodes. Similar to chronic β-adrenergic signaling, persistent Ang II signaling is implicated in cardiac remodeling events such as fibrosis. In this chapter, we test the hypothesis that incoherent feed-forward signaling acts as a controller for cardiac extracellular matrix remodeling, which becomes overwhelmed in elevated Ang II signaling.

5.2 Introduction

In addition to cardiac hypertrophy, fibrosis is a hallmark characteristic remodeling process implicated in cardiac disease[218]. Cardiac fibroblasts, which account for approximately 90% of non-contractile cells (>50% of all cells) in the heart, are thought to play a critical role in maintaining extracellular matrix (ECM) homeostasis and preventing fibrosis via the secretion and degradation of ECM proteins. However, during heart failure, expression of secreted matrix metalloproteinases (MMPs) is significantly altered, prompting MMPs to become candidate therapeutic targets[219-221]. Changes in MMP expression are in part stimulated by angiotensin II (Ang II) signaling. Consequently, angiotensin converting enzyme (ACE) inhibitors, which limit tissue Ang II

concentrations, have been shown effective for attenuating fibrotic remodeling in the heart and reducing the risk for atrial fibrillation, which may trigger heart attacks[222-223].

Mitogen-activated protein kinases (MAPKs) are particularly important signal transducers in Ang II-induced fibrosis[224-225] and are regulated by the G_q-coupled Ang II type 1 (AT_1) and type 2 (AT_2) receptors[226]. However, while Ang II is clearly linked to fibrotic remodeling, a number of significant questions remain in understanding how Ang II signals through AT_1Rs and AT_2Rs to stimulate cardiac fibrosis. First, there is extensive evidence suggesting AT_1R signaling is pro-fibrotic, but evidence for the role of AT_2Rs is contradictory[224,227]. One key question lies in understanding if AT_2Rs elicit a pro- or anti-fibrotic response and if the Ang II-induced remodeling phenotype is sensitive to perturbations by AT_2Rs over physiological ranges. This is important because AT_1R and AT_2R expression levels change significantly in heart failure[228-230].

Lack of quantitative detail about intermediate Ang II signaling steps is a significant hurdle in developing more efficacious treatment strategies. A second challenge lies in characterizing the key interventional targets for treating heart disease. ACE inhibitors are effective for globally reducing Ang II production, but tissue Ang II concentrations may remain elevated in some patients[231]. These indicate a need to better identify treatment strategies which may account for genetic variations between patients. Downstream signaling proteins which may more directly control the fibrotic response have not yet been quantitatively identified. Consequently, current treatments act only on either global Ang II or AT_1Rs. Finally, it remains poorly understood how Ang II signaling is

terminated. Such deactivation mechanisms are fundamentally important for both gaining understanding at a basic science level and for strategizing therapeutic development for fibrosis. Such strategies may curb side effects in the circulatory system by minimizing actions on non-cardiac cells. These strategies may also protect endogenous pro-survival Ang II signaling mechanisms in cardiac myocytes.

To address these challenges, we constructed a model of Ang II-stimulated MMP expression in the cardiac fibroblast. Using this model, we clarified the role of AT_2R signaling and identified highly sensitive signaling nodes in the Ang II signaling pathway. Moreover, we showed how an incoherent feed-forward signaling motif formed by AT_1Rs and AT_2Rs may limit the effectiveness of therapeutic strategies proposed in the literature.

5.3 Model

To quantitatively assess Ang II signaling dynamics, we constructed a mechanistic model of Ang II signaling in cardiac fibroblasts using ordinary differential equations based on Michaelis-Menten kinetics (Figure 5.1, *Appendix B*). In this model, stimulation of the AT_1Rs and AT_2Rs modulate the activity of c-Jun N-terminal kinase (JNK) and extracellular signal-regulated kinase (ERK) MAPKs, which directly phosphorylate multiple transcription factors to alter MMP expression. Parameters for this model were either derived from primary literature or fitted to data. To identify key interactions in this pathway, we performed a sensitivity analysis, computing ERK and JNK activities after varying each model parameter over 7 orders of magnitude (from 0.001x to 1000x). This dynamic model simulated ERK and JNK regulation by upstream kinases and

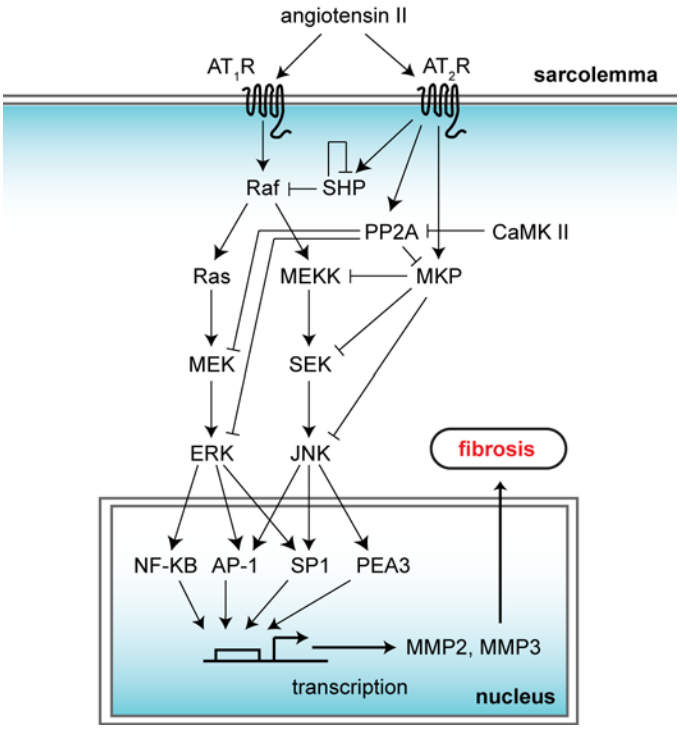

Figure 5.1 Model schematic for Ang II-stimulated fibrosis. Ang II binds the AT_1 and AT_2 receptors, which signals through mitogen-activated protein kinases (MAPKs) to stimulate transcription factors (NF-KB, AP-1, SP1 and PEA3) which regulate MMP2 and MMP3 expression.

phosphatases in response to Ang II stimulation of the AT_1 and AT_2 receptors. Changes in MMP expression were estimated as a linear combination of ERK and JNK activities, with the assumption that the total number of available MMP promoter regions is greater than the number of transcription factors activated by ERK and JNK. Together, this model mechanistically describes Ang II-induced ECM remodeling via changes in MMP expression.

5.4 Results and Discussion

Model Validations of Predicted ERK and JNK Activities

Our model accurately represented MAPK signaling dynamics and changes in MMP expression in response to Ang II stimulation. Where model parameters were absent in the literature, we fitted the model so that JNK, ERK, Src-homology phosphatase (SHP), phosphatase 2A (PP2A) and MAPK phosphatase (MKP) responses were constrained to measurements by independent labs (Figures 5.2 and 5.3). Model fits for ERK and JNK dynamics agreed well with experimental measurements. 1 μM Ang II induced a transient increase in ERK activity, peaking at 8 min and returning to basal levels[232] (Figure 5.2A). In contrast, JNK activity peaked at 20 minutes and reached equilibrium at half the peak activity[233] (Figure 5.2B). Simulated phosphatase dynamics also agreed well with experimentally measured activities. 100 nM Ang II increased SHP activity by 1.5-fold, reaching equilibrium within 5 minutes[234-235] (Figures 5.3A and 5.3B). At similar Ang II concentrations, PP2A and MKP activity increased 2-fold[236-237] (Figures 5.3C and 5.3D).

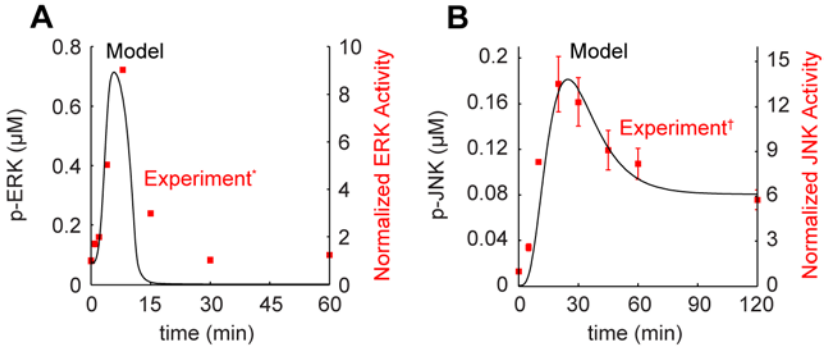

Figure 5.2 ERK and JNK activation by Ang II. A, ERK is transiently activated, with peak activity occurring 8 min after stimulation[232]. B, JNK is also transiently activated, with peak activity 20 min after stimulation[233].

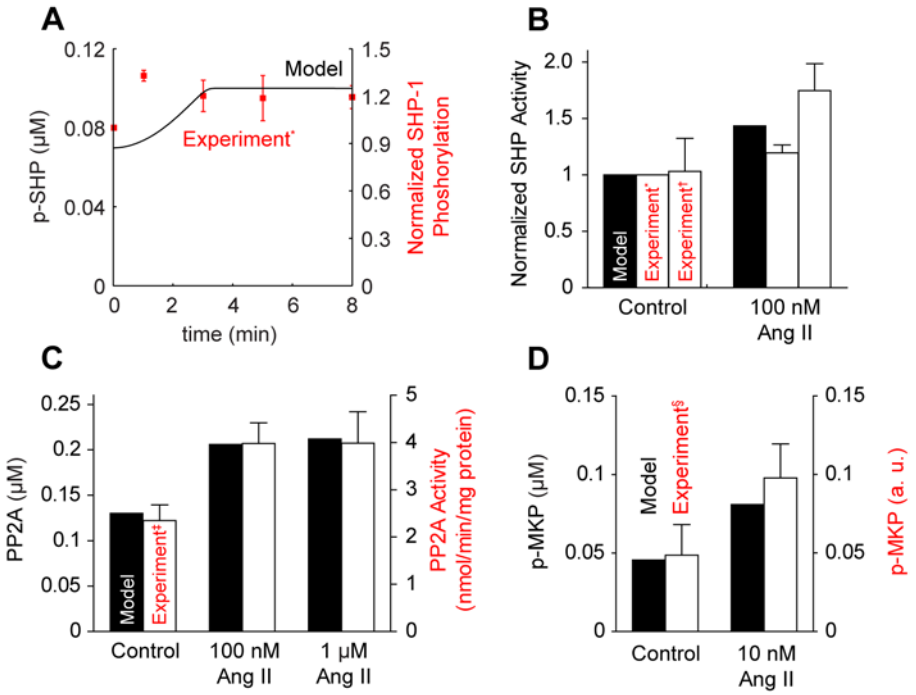

Figure 5.3 Phosphatase responses to Ang II. A, SHP activation saturates within 5 min in response to 100 nM Ang II[238]. B, Ang II increases SHP activation[234,238]. C, Ang II enhances PP2A activity[239]. D, Ang II also increases MKP activity[237].

Because MMP2 and MMP3 expression is regulated by a host of transcription factors (e.g., NF-κB, AP-1, SP1, PEA3), we estimated MMP expression as a linear combination of transcription factors which could be activated by ERK or JNK. Model predictions for MMP expression changes agreed well with observations in human heart diseases. For example, the model predicted a significantly larger increase in MMP2 expression rate than MMP3 expression rate in response to elevated Ang II (Figure 5.4A). This is consistent with independent observations in left ventricular hypertrophy and congestive heart failure[221]. Moreover, JNK activity increased faster than ERK activity under sustained Ang II stimulation, as evidenced by an increase in the ratio of JNK to ERK activity. These model predictions support the hypothesis that stress-induced MAPKs like JNK may have a more pro-apoptotic (and therefore pro-fibrotic remodeling) role than ERK MAPKs[240].

AT_2R Signaling is Anti-Fibrotic

Treatments targeted at reducing Ang II signaling are effective in curbing the effects of heart disease[231]. In 2008, there were 89 clinical trials targeted at Ang II signaling in the heart[241]. Most of these trials either targeted Ang II production or activation of the AT_1Rs. AT_2Rs have also been considered as a potential therapeutic target[242], but it is unclear if AT_2R signaling is anti-fibrotic under physiological conditions. Moreover, there is little quantitative evidence to compare AT_2R agonists with therapies in use or development.

To determine if AT_2Rs play a strongly antagonistic role in Ang II-induced remodeling, we compared Ang II responses under normal (wild-type) and AT_2R over-expression

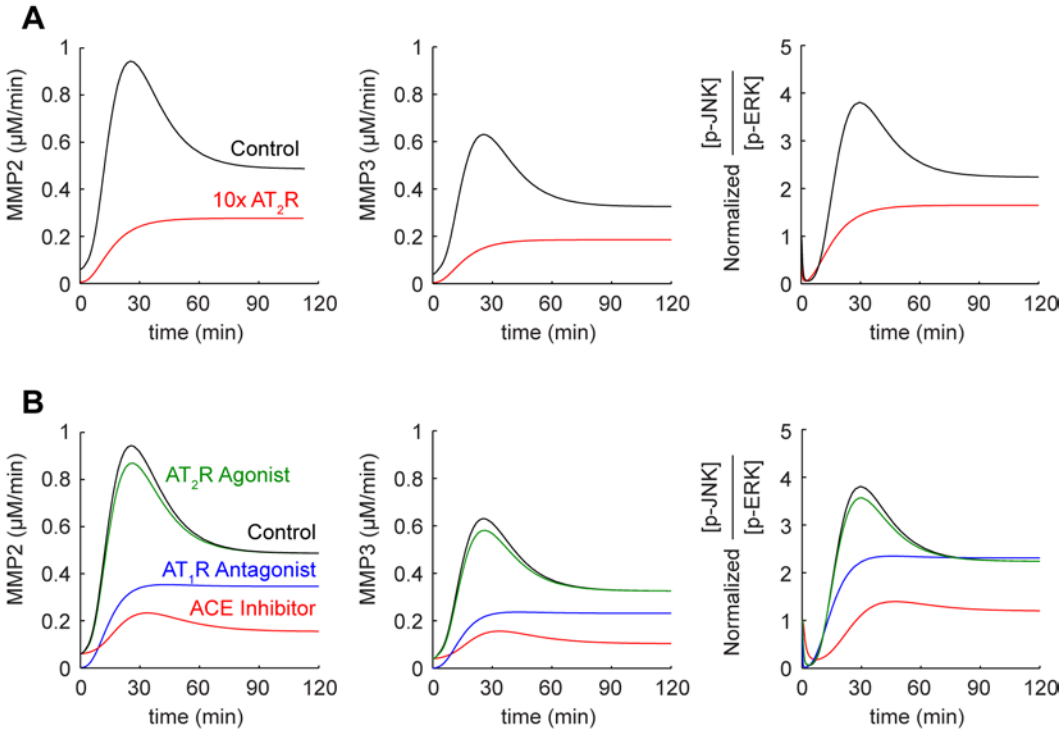

Figure 5.4 MMP expression rates in response to Ang II stimulation and pharamacologic intervention. A, 1 μM Ang II induces a rapid increase in MMP2 and MMP3 expression and preferentially activates JNK over ERK. 10-fold over-expression of AT_2Rs inhibits increase in MMP expression rates. B, ACE inhibitors have greater efficacy over AT_1R antagonists and AT_2R agonists in reducing MMP expression.

conditions. AT_2Rs over-expression was modeled by increasing the concentration of AT_2Rs one order of magnitude (10-fold). Under these conditions, the total expression rate of both MMP2 and MMP3 increased by similar magnitudes in contrast to the much larger increase in MMP2 expression than MMP3 expression seen under the wild-type conditions (Figure 5.4A). The relative increase in JNK activity over ERK activity was also smaller in these conditions, suggesting that AT_2Rs may specifically attenuate stress-activated MAPK responses. These results suggest that AT_2R stimulation may directly attenuate Ang II-induced remodeling responses.

AT_2R Agonists are Not Effective Anti-Fibrosis Agents

AT_2R agonists are an effective method for stimulating AT_2R activity, but there had not been any experiments or clinical studies evaluating the actions of these drugs on the heart. To determine if AT_2R agonists may be a meaningful treatment for fibrotic remodeling, we compared the responses of our model to simulated ACE inhibition (in clinical use), AT_1R antagonists (in clinical trials) and AT_2R agonists. ACE inhibitors in our model were represented by reducing the total effective concentration of Ang II by one order of magnitude (from 1 μM to 100 nM). AT_1R antagonists were represented by a two order of magnitude increase in the effective K_d of the AT_1R (due to competitive inhibition; from 0.95 nM to 95 nM). AT_2R agonists were represented by the addition of 10 μM ligand which can only bind the AT_2R and stimulate AT_2R signaling. These representations corresponded to ideal drugs from each of these three families.

Of the three simulated therapies, ACE inhibitors had the most robust anti-fibrotic result, reducing MMP2 and MMP3 expression to nearly basal rates (Figure 5.4B). The fold change in JNK to ERK activity was also nearly reduced to 1 in these conditions. These results support clinical observations that ACE inhibitors are effective treatments for patients with heart disease. AT_1R antagonists in our model also attenuated excess MMP expression, but were unable to fully block excess JNK activity. This result would indicate that while AT_1R antagonists may attenuate fibrotic remodeling, they may still result in pathologic consequences by over-stimulating stress-induced MAPKs[240].

In contrast, AT_2R agonists in our model had limited effect in blocking MMP expression or ERK and JNK activity. This counterintuitive result could be explained by the observation that the phosphatases induced by AT_2R are highly active at normal physiological Ang II concentrations (Figure 5.5). However, this saturation may be overcome by increasing the total number of available AT_2Rs (Figure 5.4A), suggesting AT_2Rs are already maximally engaged under physiological conditions. Together, these results suggest that while AT_2R signaling is anti-fibrotic, AT_2R agonists would have limited effect in treating fibrotic remodeling. Therapies designed to limit Ang II signaling should therefore focus on either inhibition of Ang II production or enhancement of AT_2R expression rather than inhibition of AT_1R activity or elevation of AT_2R activity.

MKPs are Key Endogenous Regulators of ERK and JNK Activity

A key challenge in designing therapeutic strategies is identification of the most efficacious intervention target. To identify key signaling proteins regulating ERK and

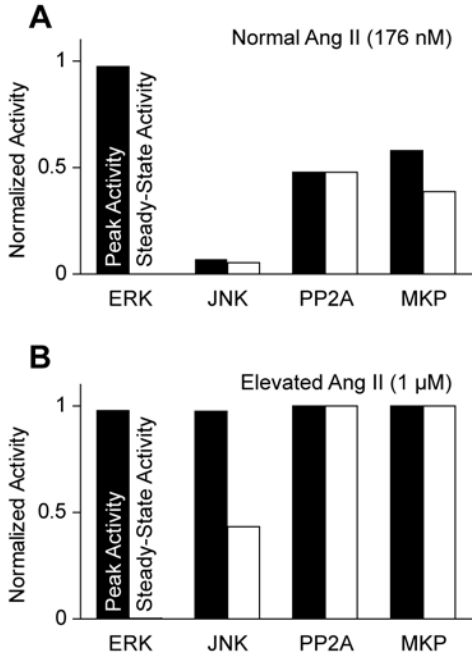

Figure 5.5 Peak and steady-state MAPK and phosphatase activities in response to normal and elevated Ang II stimulation. A, Model stimulation with normal physiologic Ang II concentrations[243] induces a transient increase in ERK and JNK activity, which is silenced at steady-state by increased phosphatase activity. B, Under conditions of sustained, elevated Ang II treatment, phosphatase activities are saturated and steady-state JNK activity increases.

JNK activation by Ang II, we performed a sensitivity analysis, varying each parameter over seven orders of magnitude and measuring ERK and JNK activities (Figure 5.6). We then quantitatively compared the dynamic range for the parameter sensitivities the fractional range of ERK (JNK) activation (0 – 100%) as the sensitivity metric. These were determined by taking the ratio of the difference between ERK (JNK) activities at 1000-fold increased and 1000-fold decreased parameter values over the total ERK (JNK) concentration. This analysis indicated that while ERK is sensitive to most reactions involving PP2A and MKP (Figure 5.7A), JNK is preferentially sensitive to reactions including MKP and displays much smaller dynamic range for these reactions (Figure 5.7B). These suggested that strongly pro-fibrotic JNK activity is more tightly regulated than ERK activity.

Though ERK and JNK are both members of the MAPK family, they appeared to play opposite roles in the development of heart disease. Normal JNK activity appears to be pathologic in cardiac remodeling[244], whereas normal ERK activity may be cardioprotective[245]. To identify proteins which uniquely regulate JNK activity, but not ERK activity, we calculated two other sensitivity metrics. First, we calculated the ratio of ERK and JNK activities over the range of parameter perturbations. This metric is small when the JNK activity is significantly greater than ERK activity and large when ERK activity is significantly greater than JNK activity. Using this metric, MKPs emerge as the single most sensitive signaling protein for minimizing JNK activity relative to ERK activity (Figure 5.8A). Second, we calculated the ratio of the JNK and ERK parameter sensitivities. The absolute value of this metric is large when JNK sensitivity is large and

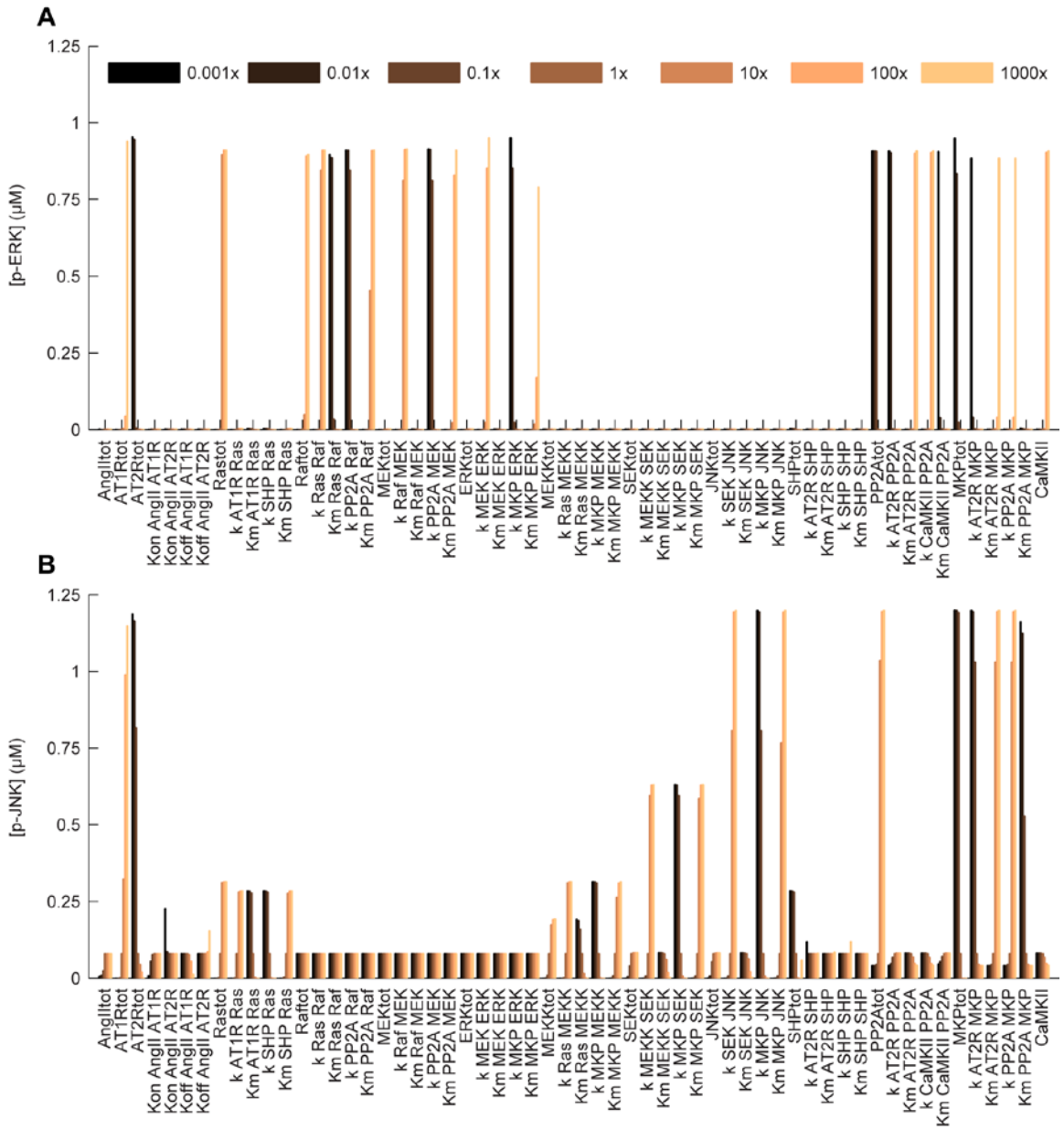

Figure 5.6 Parameter sensitivity over 7 orders of magnitude. A, ERK activity is uniformly sensitive to Ras, Raf, MEK, PP2A and MKP. B, JNK activity is more specifically sensitive to MKP.

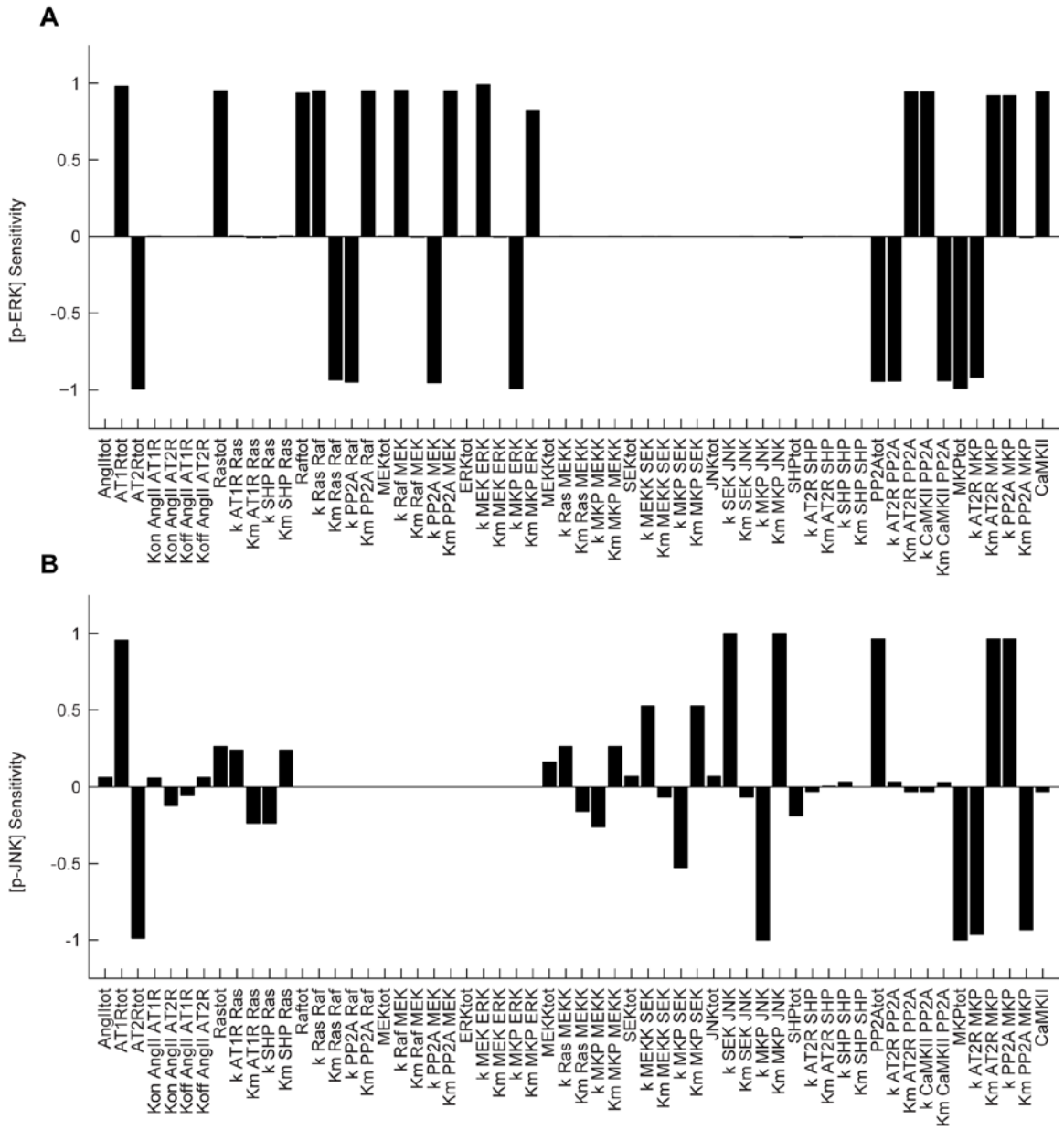

Figure 5.7 ERK and JNK sensitivity dynamic range. A, ERK sensitivity exhibits a large dynamic range for parameters related to Ras, Raf, MEK, PP2A and MKP. B, JNK sensitivity exhibits a large dynamic range only for MKP parameters.

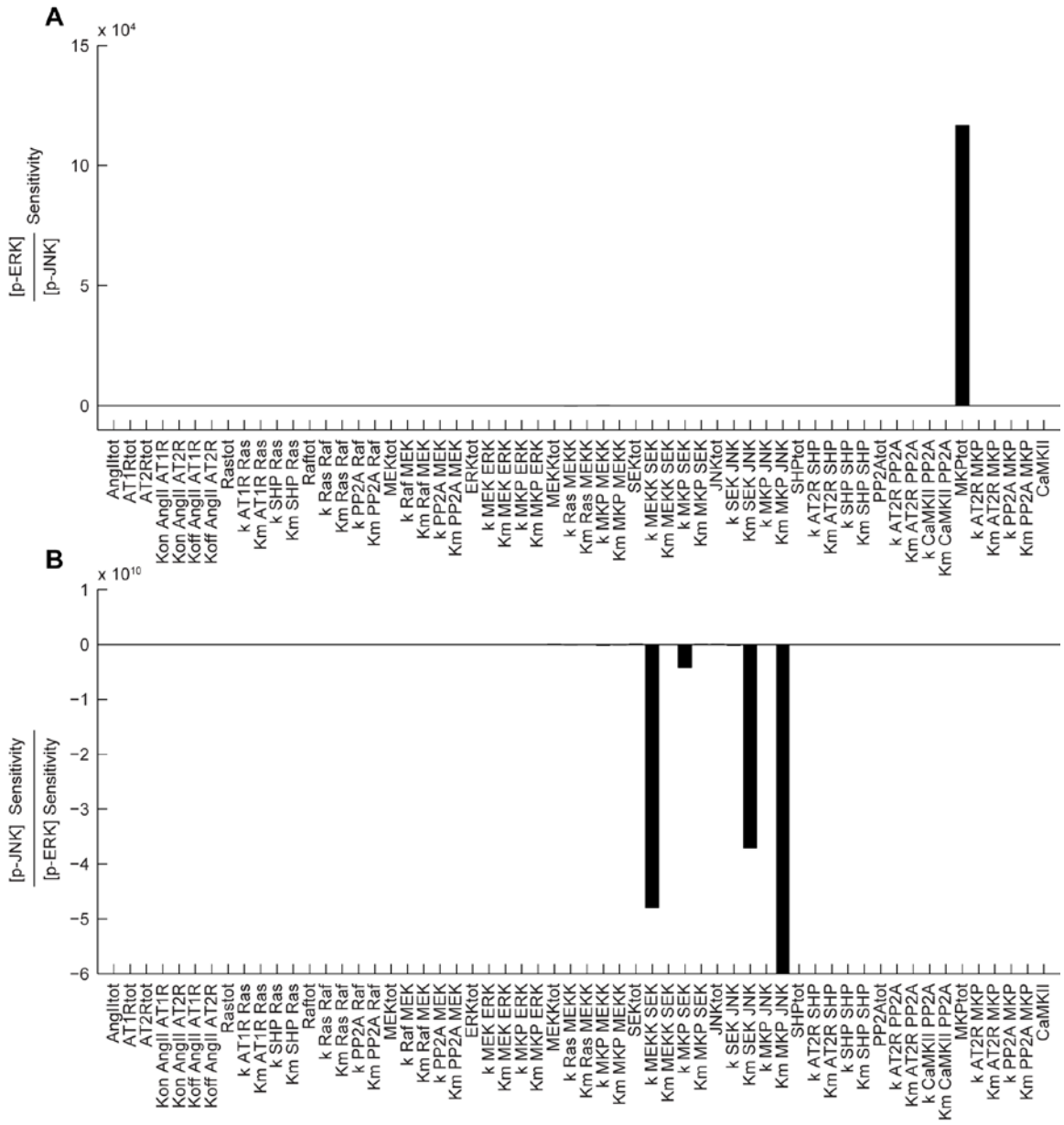

Figure 5.8 Normalized parameter sensitivities. A, MKP is the single most important protein for biasing MAPK activation toward ERK. B, Negative parameter sensitivity ratios indicate parameter manipulation changes JNK and ERK activities in opposite directions. MKP and SEK emerge as most powerful signaling proteins for inhibiting JNK activity.

ERK sensitivity is small. The sign of these values is positive when ERK and JNK are both up- or down-regulated and negative when the actions on ERK and JNK occur in opposing directions. Using this metric, we find that the reactions which most significantly reduce JNK activity relative to ERK activity involve MKPs and SEK, which directly activates JNK(Figure 5.8B). Together, these results identify MKPs as the key regulator of ERK and JNK activities. These results provide support for a hypothesis that MKPs may be a useful interventional target for inhibiting Ang II signaling.

MKP Inhibition as a Therapeutic Strategy

Quantitatively constrained mechanistic models are useful for hypothesis testing and generating new research directions[211]. Interestingly, ERK can trigger MKP expression in response to Ang II stimulation, creating a transcriptional negative feedback loop that may occur over larger time scales than the signaling dynamics modeled here[226,237]. To test if this endogenous negative feedback loop may antagonize JNK activity and MMP expression, we increased the total MKP concentration 4-fold, which is equivalent to the steady-state increase in MKP expression following long-term Ang II treatment[226]. This is an appropriate assumption because the time scale separation between this transcriptional feedback and the dynamics we modeled was large. Our model qualitatively suggests that a MKP-mediated transcriptional negative feedback loop was sufficient for inducing a significant long-term antagonistic effect on AT_1R-stimulated fibrosis (Figure 5.9).

Together, these results identify MKPs as key regulators of ERK and JNK in response to Ang II signaling and suggest endogenous feedback mechanisms have evolved to limit

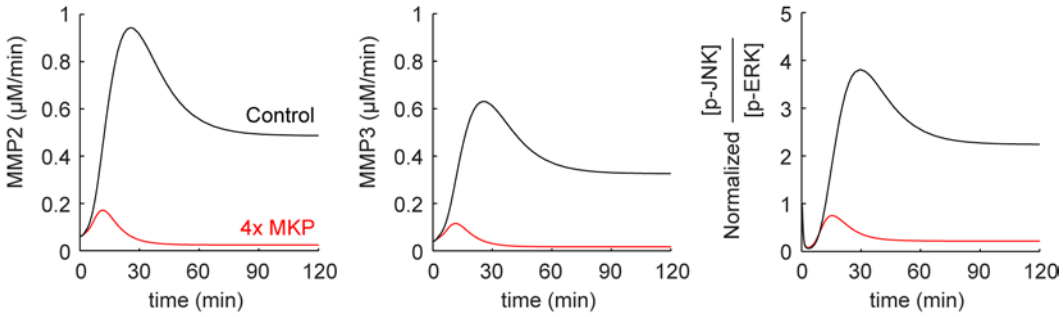

Figure 5.9 Enhanced MKP expression limits Ang II-stimulated fibrosis. Increasing total MKP concentration blocks enhancements to MMP expression rate and JNK activation in the presence of 1 μM Ang II.

long-term responses to sustained Ang II stimulation by increasing MKP expression. An important new experimental direction will be to characterize the relationship between this feedback and fibrotic remodeling. Therapies targeted at stimulating JNK-specific MKP production may be more effective for treating this remodeling than therapies targeted at either global Ang II concentrations or Ang II receptors.

Ang II Signaling Responses are Deactivated by Incoherent Feed-Forward Control

Ang II receptors are G-protein coupled receptors (GPCRs), a particularly important family of cardiac signaling receptors which include beta-adrenergic receptors[63]. In β_1-adrenergic receptors (β_1-ARs), receptor desensitization is an important mechanism for limiting responses to sustained stimulation. Beta arrestins play a particularly important role in this desensitization by targeting GPCRs for endocytic internalization and ubiquidination and by sterically inhibiting the G-protein activity. In contrast, beta arrestins play a stimulating role in Ang II receptors signaling by scaffolding the AT_1 and AT_2 receptors to other key signaling proteins[246]. While it is clear that Ang II elicits transient ERK and JNK activation (Figure 5.2), the mechanisms for adaptation in Ang II signaling are not well understood. Moreover, while AT_1Rs are known to undergo endocytic internalization, AT_2Rs do not internalize[247]. It is therefore unclear if normal GPCR desensitization mechanisms are necessary for conferring adaptation to Ang II signaling responses.

In constructing this model, we found that AT_2R signaling alone is sufficient to explain long-term adaptation of AT_1R signaling responses (Figure 5.2). To test the role of AT_2R

signaling in limiting ERK and JNK activities, we removed SHP, PP2A and MKP activation by AT_2Rs. In these conditions, ERK and JNK exceeded normal activities, reaching full activation near total ERK and JNK concentrations (Figure 5.10A). These suggested AT_2R signaling is necessary for maintaining the physiological ranges for ERK and JNK activities.

However, receptor internalization may also limit AT_1R responses. To test the hypothesis that AT_1R signaling deactivation may be explained by AT_1R internalization, we modeled the effects of AT_1R internalization in the absence of AT_2R signaling. To do this, we introduce an internalization term into the expression for AT_1R activation by Ang II with a time constant of 136 s [247] (Figure 10B). Under these conditions, only 30% of the Ang II-bound AT_1Rs remained non-internalized at steady-state (Figure 5.10C). However, our model predicted that even with 70% inhibition of the AT_1Rs, ERK and JNK activities fully saturated at steady state in the absence of AT_2R signaling (Figures 5.10A). These results indicated AT_1R internalization cannot account for the transient deactivation of ERK and JNK activities. Simulating both AT_2R engagement and AT_1R internalization resulted in lower ERK and JNK activity than including AT_2R signaling alone (Figure 5.11). Together, these results suggested that while AT_1R internalization may participate in the acute inactivation of Ang II signaling responses, AT_2R signaling alone is both sufficient and necessary to explain long-term deactivation.

An important observation is that Ang II activates both the (pro-fibrotic) AT_1Rs and (anti-fibrotic) AT_2Rs simultaneously (Figure 5.12A). However, the phosphatases stimulated by

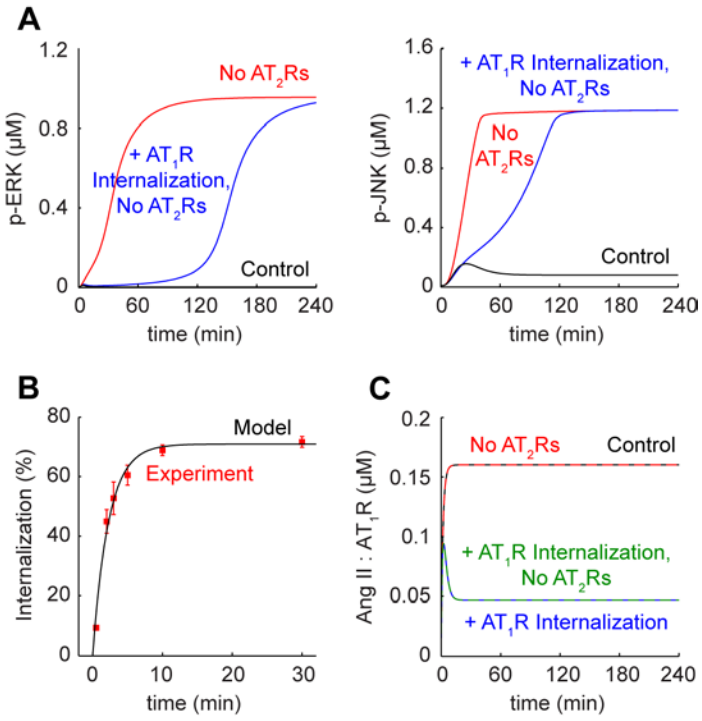

Figure 5.10 MAPK adaptation is not explained by receptor internalization. A, AT_2R signaling, but not AT_1R internalization, is sufficient and necessary for explaining ERK and JNK adaptation responses to 1 μM Ang II. B, Functional model implementation of AT_1R internalization[247]. C, AT_1R internalization reduces steady-state signaling AT_1Rs by 70%. AT_2R competition for Ang II ligand is insignificant.

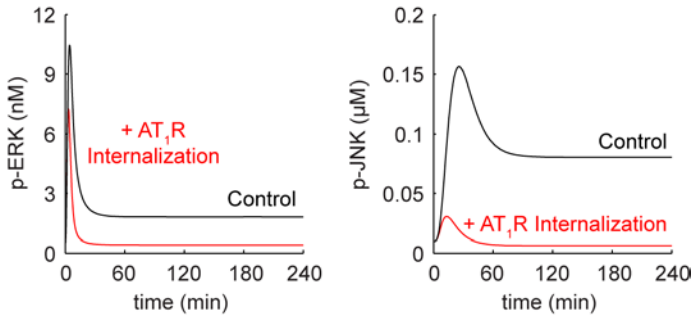

Figure 5.11 AT_1R internalization further limits MAPK activation. A,B, While AT_1R internalization alone is insufficient for explaining JNK and ERK adaptation responses to 1 μM Ang II, internalization may play an additional role in limiting MAPK induction.

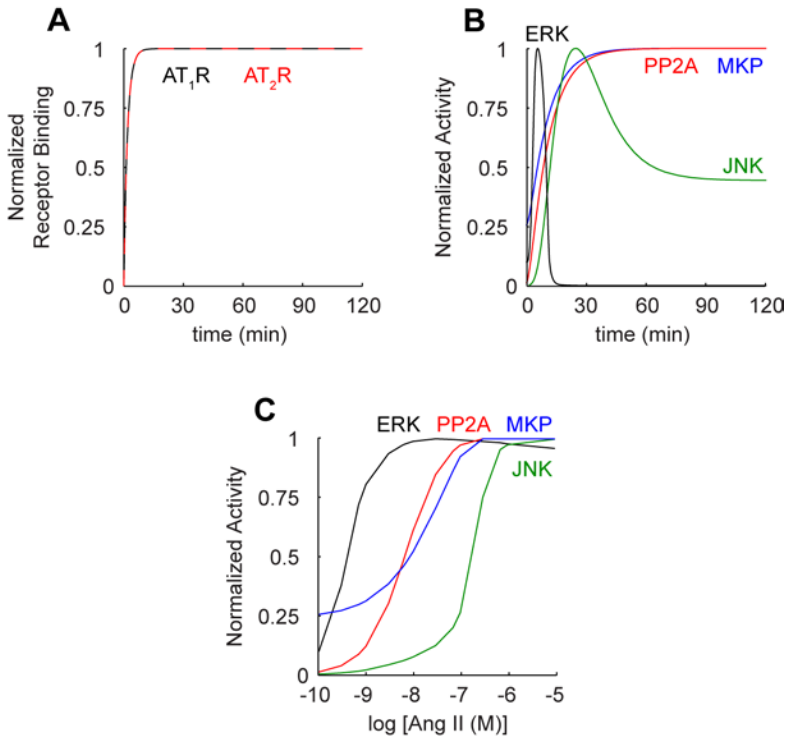

Figure 5.12 A unified hypothesis for Ang II-mediated fibrosis. A, AT_1Rs and AT_2Rs share similar activation kinetics. B, Kinase and phosphatase activated by Ang II differ considerably. C, Over normal physiological Ang II tissue concentrations (6-100 nM), JNK activation is small and kept in check by PP2A and MKP, which exhibit large dynamic range. At elevated Ang II concentrations, PP2A and MKP activities are saturated and JNK activity increases significantly.

AT_2Rs reach maximum activation significantly more slowly than the kinases stimulated by AT_1Rs (Figure 5.12B). This delay provides a small window for MMP expression to increase significantly (Figure 5.2A) before phosphatase activity is sufficient for causing adaptation in the MAPK activities. Moreover, steady-state activation of these two pathways is unbalanced, resulting in increased overall steady-state MMP expression under Ang II stimulation. Interestingly, the AT_2R pathway is insensitive to signaling events in the AT_1R pathway. How then does AT_2R signaling limit the long-term responses to sustained Ang II stimulation? Our results indicate that the AT_2Rs do this by robustly intervening at multiple stages of the AT_1R pathway. This signaling motif is a form of incoherent feed-forward control, where Ang II acts on the AT_2Rs as intermediates in exerting control over anticipated AT_1R responses.

Feed-forward control mechanisms are effective when the output of a system (in this case, pro-fibrotic ERK and JNK activities) must be maintained in a bounded range. In contrast to the significant and sustained activation of PP2A and MKP under both basal and Ang II-stimulated conditions, ERK and JNK activities are transient and significant steady-state JNK activation only occurs under Ang II-stimulated conditions (Figure 5.5).

Testing our model across different concentrations of Ang II, we found that the $EC_{50}s$ for PP2A and MKP (7 nM and 10 nM, respectively) were orders of magnitude different from the $EC_{50}s$ for ERK and JNK (200 nM and 0.5 nM, respectively) (Figure 5.12C). These suggest that under physiological Ang II concentrations (6 – 100 nM), ERK activity is saturated while JNK activity is inactive and under-stimulated. However, PP2A and MKP

activities are most sensitive at these concentrations allowing these phosphatases to exert strong control over ERK and JNK. As Ang II increases beyond normal physiological concentrations, PP2A and MKP activities may become saturated and JNK activity can increase rapidly and escape control of saturated PP2A and MKP activities. This loss of control over ERK and JNK activities exemplifies a limitation of incoherent feed-forward control: the system breaks down when stimulated output responses exceed the dynamic range for the intermediate controller[79].

In the context of cardiac health and disease, health is maintained when physiological responses are kept within specific ranges, but pathologies can form when a biological network is stimulated beyond what the system can handle. Our simulations suggest Ang II signaling responses are deactivated by an incoherent feed-forward control and that fibrotic MMP expression may occur when AT_1Rs are stimulated beyond the control of AT_2Rs, as occurs in global elevations to circulating Ang II. New experiments are needed to test this hypothesis and to characterize other possible Ang II control mechanisms.

Limitations

MAPK signaling pathways are well-studied canonical signaling pathways, regulated by many signaling proteins. Because MAPKs are regulated by transcriptional feedback loops with much longer time scales (hours, days) than the dynamics investigated here (min), we made a number of simplifying assumptions in constructing this model. First, we assume that signaling dynamics are insensitive to long-term changes in expression of individual signaling species. Second, the model also simplifies many intermediate steps between

Ang II receptor binding and Ras or phosphatase activation as lumped, rapidly equilibriating steps. Such assumptions are permissible in the absence of sufficient data to constrain steps in a model or when the simplified steps are not the focus of the main phenomena under investigation. This model could be improved with better biochemical measurements in cardiac fibroblasts. However, while increasing modeling detail may increase the scope of the model, we show here that simple, quantitatively constrained mechanistic models are sufficient and useful for generating new insight.

5.5 Conclusions

One implicit goal of this study was to use a computational model as an inference tool for accelerating biological insight and for proposing novel experimentally-testable therapeutic concepts. In this chapter, we have identified three important findings in the regulation of Ang II-stimulated fibrosis:

i.) AT_2R signaling is anti-fibrotic, but AT_2R-specific agonists are not effective for inhibiting fibrotic remodeling

ii.) MKPs are key endogenous regulators of ERK and JNK activity

iii.) Ang II signaling responses are deactivated by incoherent feed-forward control

These findings inspire a number of therapeutic concepts. First, our simulations comparing ACE inhibitors, AT_1R antagonists and AT_2R agonists suggest Ang II-based anti-fibrosis therapies should focus more on inhibiting Ang II production or increasing AT_2R expression rather than blocking AT_1R activity or stimulating AT_2R activity. We show

AT_2R agonists may be ineffective therapeutic agents due to saturation of phosphatase activities under physiological conditions. These model predictions can be directly tested *in vitro* by stimulating cardiac fibroblasts with these three classes of small molecules and quantifying MMP secretion. Moreover, phosphatase saturation may be tested by treating fibroblasts with phosphatase agonists to characterize the full dynamic range of phosphatase activity.

Second, our sensitivity analysis identified MKPs as key ERK and JNK regulators, suggesting pharmaceutical or gene therapies targeted at stimulating MKP expression or activity may be more effective than receptor/ligand-based therapies. These hypotheses may be tested *in vivo* by evaluating transgenic over-expression of MKPs in an established *in vivo* heart failure model. Further studies will also be necessary to explore the relationship between ERK activation and MKP negative feedback *in vitro* to determine if MKP expression is capable of perturbing MMP expression.

Finally, our model predicts the mechanism for fibrosis induction in elevated Ang II signaling is escape from the incoherent feed-forward control of saturated AT_2R signaling by elevated AT_1R activity. Therapeutically, AT_2R-mediated control may be enhanced by elevating AT_2R expression using gene therapy. However, a more comprehensive study including all MAPKs and relevant phosphatases cross-talking on MMP expression will be necessary to more precisely characterize the control systems regulating Ang II-mediated fibrosis.

Together, this chapter demonstrates how a simple, but carefully constrained model of a disease-relevant cardiac signaling pathway can elucidate signaling mechanisms and provide quantitative support for comparing therapeutic strategies. In the context of Ang II-mediated fibrosis, this work also highlights a third consequence of incoherent feed-forward signaling: in addition to providing adaptation and acceleration mechanisms, incoherent feed-forward motifs can produce sharp biological thresholds for limiting receptor-stimulated behaviors.

Chapter 6

Regulation of Nuclear PKA Activity Revealed by cAMP Manipulation and Model-Based Inference

Work from this chapter is published in *Regulation of nuclear PKA revealed by spatiotemporal manipulation of cAMP*. Sample, V.*, DiPilato, L.M.*, Yang, J.H.*, Ni, Q., Saucerman, J.J., Zhang, J. Nat. Chem. Biol. 2012; 8(4):375-82.

(*) denotes equal contribution

6.1 Foreword

In addition to its effects on acute contractility, β-adrenergic signaling is an important mediator of cardiac remodeling. In the heart, β-adrenergic signaling responses are primarily exerted via PKA activation by cAMP. Because cardiac remodeling is a long-term, transcriptionally regulated process, we hypothesized that nuclear PKA activity may be relevant to β-adrenergic signaling-stimulated remodeling. However, it remains unclear if nuclear PKA activity is distinct from cytosolic PKA activity and if so, how nuclear PKA activity may be regulated. Numerous studies have shown cAMP compartmentation may be an important regulator for PKA[248]. In this chapter, we take an integrated approach combining computational modeling with live-cell imaging to examine nuclear PKA regulation in a commonly used cell line.

6.2 Introduction

cAMP plays a ubiquitous signaling role across cells from many species. In the classic mammalian model, activation of G-protein coupled receptors (GPCRs) initates a cascade of signaling events involving the activation of stimulatory G_α subunit and transmembrane adenylyl cyclase (tmAC), which catalyzes the conversion of ATP to cAMP. cAMP then diffuses throughout the cell, binding to and activating its known effectors: cAMP dependent protein kinase (PKA), exchange protein directly activated by cAMP (Epac), and cyclic nucleotide-gated channels[249]. Remarkably, despite the large number of GPCRs that are coupled to cAMP generation, cAMP elicits highly specific cellular responses to external stimuli. This specificity is believed to be achieved by compartmentation[248],

wherein spatially heterogeneous cAMP gradients are formed despite cAMP's fast diffusion. Phosphodiesterases (PDEs), which degrade cAMP to 5'-AMP, have been identified as important regulators of these heterogeneous cAMP dynamics[250]. Subcellular cAMP signaling microdomains can be further defined by distinct environments within cellular organelles as well as the assembly of signaling complexes at intracellular sites via scaffolding proteins such as A-kinase anchoring proteins (AKAPs)[251].

The nucleus is a good example of one such cAMP-PKA microdomain is the nucleus, where PKA plays important functional roles in regulating transcription[252] and RNA splicing[253]. The contemporary hypothesis for cAMP-PKA signaling in the nucleus states that cAMP production by tmACs activates cytosolic PKA holoenzyme, in which cAMP-binding induces catalytic subunit dissociation from the regulatory subunit in an isoform-specific manner[254] and translocates into the nucleus via diffusion[255], serving as the only functional source of nuclear PKA[249,252,256]. In contrast to this hypothesis, resident pools of nuclear PKA holoenzyme have been proposed, evidenced by immunoblot and immunofluorescence observations of PKA regulatory and catalytic subunits in the nuclei of different cell types[257-258]. Moreover, a recent study identified a splicing factor (SRFS17A) as a nuclear AKAP requiring the presence of PKA regulatory subunit to regulate alternative splicing[259], suggesting expression of endogenous nuclear PKA holoenzyme. However, the existence of nuclear PKA holoenzyme has not been well characterized, in part due to lack of functional data on cell responses stimulated by nuclear PKA holoenzyme.

In this chapter, we developed a versatile system for precisely manipulating the location, kinetics and magnitude of intracellular cAMP signals via activation of targeted soluble ACs (sACs). Using these sACs as cAMP point sources, we coupled real-time cAMP and PKA imaging with mechanistic computational modeling to investigate mechanisms regulating nuclear cAMP-PKA signaling in HEK 293 cells. We observed PKA dynamics at the membrane, cytosol and nucleus were differentially sensitive to the location of cAMP generation, indicating distinct pools of PKA holoenzyme. Using a computational model, we inferred the involvement of a nuclear pool of PKA holoenzyme to be necessary for explaining the measured cAMP and PKA dynamics. We confirmed these model predictions by immunofluorescence and immunblot analysis. Using the model, we further predicted that nuclear PKA holoenzyme is insulated from membrane-generated cAMP signals by a nuclear AKAP-PDE complex, which we also validated experimentally. These results provide evidence supporting the existence of a distinct nuclear signaling complex sensitive to local cAMP generation.

6.3 Materials and Methods

Gene construction

sAC-NES fusion was formed by cloning the first 469 amino acids from truncated rat sAC via PCR amplification using NcoI and SalI restriction sites for N- and C- termini and ligating it into pRSETB vector bacterial vector (Invitrogen). An internal BamHI site was silently mutated using QuikChange mutagenesis. mCherry without a stop codon was subcloned into the sAC-containing vector between SalI and EcoRI sites and the entire sequence was subcloned into the mammalian expression vector, pcDNA3 (Invitrogen),

containing an NES sequence (5'-LPPLERLTL) at the C-terminus of the MCS using BamHI and EcoRI restriction sites. For -NLS and PM- targeting, sAC-mCherry was subcloned into pcDNA3 vectors containing the sequences coding for 5'-PKKKRKVEDA at the C-terminus between EcoRI and XbaI sites and 5'-GCIKSKRKDK at the N-terminus between HindIII and BamHI sites, respectively.

Cell culture

HEK 293 cells were maintained in Dulbecco's Modified Eagle Medium with 10% fetal bovine serum and 1% penicillin/streptomycin at 37°C with 5% CO_2. For imaging experiments, cells were first cultured on sterilized glass coverslips in 35-mm dishes coated with poly-D-lysine. Cells were then transfected with calcium phosphate at 50-60% confluency and allowed to grow for 18–24 hours before imaging.

Live-cell imaging

Cells were washed twice with and maintained in Hanks' balanced salt solution buffer and allowed to equilibrate for 10 minutes at room temperature in the dark. Cells with low sAC expression (less than 2-fold expression of RFP above background) were chosen for imaging experiments to minimize basal activity. After selection, cells were treated with $NaHCO_3$ (Sigma), KH7, Na_2HPO_4 (Sigma), forskolin (FSK; Calbiochem) and IBMX (3-isobytl-1-methylxanthine; Sigma) as indicated. Dual emission ratio imaging was performed on a Zeiss Axiovert 200M microscope with a MicroMAX BFT512 cooled CCD camera (Roper Scientific) controlled by METAFLUOR 6.2 software (Molecular Devices). Emission ratios were obtained using a 420DF20 excitation filter, a 450DRLP

dichroic mirror, and two emission filters (475DF40 for ECFP and Cerulean and 535DF25 for cpVenus) alternated by Lambda 10–2 filter-changer (Sutter Instruments). RFP images were taken with a 568DF55 excitation filter, a 600DRLP dichroic mirror and a 653DF95 emission filter. Images were taken every 20s with an exposure time of 100-500ms. Fluorescent images were background-corrected by subtracting autofluorescence intensities of untransfected cells (or background with no cells) from the emission intensities of fluorescent cells expressing reporters.

Computational model development

A computational model was developed to specifically describe cAMP and PKA dynamics in HEK 293 cells in MATLAB (Mathworks, Natick, MA) (*Appendix C*). The final model consists of three spatial compartments (plasma membrane, cytosol, and nucleus) and one functional compartment (AKAP). Equations describing PKA activation by cAMP were based on work by Rich, *et al.*[260-261]. Equations describing ICUE and AKAR activity were based on Saucerman, *et al.*[4]. cAMP generated by transmembrane and soluble adenylyl cyclases was permitted to freely diffuse across all compartments and activate PKA. Active PKA catalytic subunit was also permitted to diffuse across all compartments. PDE degradation of cAMP and AKAR regulation by PKA and phosphatases were described using Michaelis-Menten kinetics. Parameters for adenylyl cyclase activity, cAMP and PKA diffusion, PDE activity and phosphatase activity were estimated by nonlinear least squares fitting from randomized initial parameter sets, constrained by the magnitudes or t_{50} values from corresponding ICUE and AKAR experimental measurements. For each simulation, the model was run to steady state before stimulation by FSK, FSK+IBMX or

$NaHCO_3$. Simulations ran for 60 min, corresponding to the average length of the nuclear ICUE and AKAR experiments.

Model analysis

Comparisons between the suitability of different model structures were made using the Akaike Information Criterion (AIC), an empirical estimate of the information given by a particular model structure[262-263]. The AIC rewards model agreement with fitted experimental data and penalizes the addition of fit parameters. For the least squares case with a small sample size, the corrected AIC is given by

$$AIC = n\log(\frac{RSS}{n}) + 2K \cdot \frac{n}{n-K-1},$$

where n is the number of experimental measurements, RSS is the residual sum of squared errors and K is the number of model parameters. Within a set of fitted models, the 'best model' minimizes the AIC. The probability that a given model within a set of models is most representative of a set of experimental data is given by the Akaike weight[262]:

$$w_i = \frac{\exp\left(-\frac{1}{2}\Delta_i\right)}{\sum_{r=1}^{R}\exp\left(-\frac{1}{2}\Delta_r\right)},$$

where Δ_i is the difference between the AIC of the ith model with the minimum AIC from a set of R models. These Akaike weights are equivalent to the Bayesian posterior model probabilities and sum to 1 for any particular set of models.

Immunofluorescence

HEK 293 cells were grown to 70% confluency in 35 mm dishes and fixed with 4% paraformaldehyde at room temperature for 20 min. The cells were then washed thrice with DPBS and permeabilized with 0.2% Triton X-100 (Sigma) followed by three washes with DPBS. Following the wash, cells were incubated in 4% bovine serum albumin (BSA) for an hour and then incubated with mouse primary antibodies for pan PKA RI, PKA RIIβ and PKA catalytic α subunits (1:250 dilution, each) followed by a 30 min incubation with Alexa546 conjugated goat anti-mouse secondary antibodies (Invitrogen Molecular Probes). For nuclear colocalization studies, immunofluorescence images using Alexa546 conjugated goat anti-mouse antibody were obtained on a spinning disk confocal unit (CSU10: Yokogawa) while DAPI (Invitrogen), a cell permeable dye was used to label the nucleus. For Alexa546 images, excitation was conducted with an argon laser (CVI-Melles Griot) using a 514DF25 excitation filter and a 620DF60 emission filter (Chroma Technology). DAPI images were acquired with a 365WB50 excitation filter and a 482DF32 emission filter. Fluorescence images were procured with a CCD camera (Orca ER, Hamamatsu Photonics), controlled by Metamorph 7.5 imaging software (Molecular Devices) using a 40x objective (Zeiss) fitted on an Axiovert 200 microscope.

Nuclear fractionation

HEK 293 cells were grown in 10 cm dishes to 90% confluency, washed twice with 5 mL ice cold PBS, scraped and collected in a 15 mL falcon tube. The cells were then centrifuged at 1500 rpm for 10 min at 4^{o}C. After removing the supernatant, the pellet was loosened by gentle vortexing for 5 sec and resuspended in 4 mL ice cold sucrose buffer I.

Sucrose buffers I and II were made as per protocol from Current Protocols in Molecular Biology[264]. The cells were then transferred to an ice cold Dounce homogenizer and the cells were lysed by 5-10 strokes of a B pestle. The solution with the lysed cells were then removed to a 50 mL faclon tube and gently mixed with 4 mL of sucrose buffer II. This solution was carefully layered onto a 4.4 mL cushion of sucrose buffer II in a polyallomer SW40.1 and the tube was filled to the top with sucrose buffer I. The tubes were then spun in a Beckman centrifuge maintained at 4^{o}C in a SW41Ti rotor at 30,000x g for 45 minutes. A fraction of the supernatant was saved for Western analysis and the remaining supernatant was removed. The nuclear pellet was suspended in 200 μL 2x SDS sample buffer and sonicated three times at power 3 for 5 sec each. The two fractions were run on a 10% SDS gel and Western blot analysis was performed as per standard procedure. The membrane was then probed with antibodies for CREB, tubulin, GAPDH, pan PKA RI, PKA RIIβ and PKA catalytic α subunits.

6.4 Results

Establishing a System for Local cAMP Manipulation

To better quantify the effect of cAMP compartmentation on PKA dynamics, we developed a system for local cAMP manipulation using recombinant sACs. Endogenous sACs are sensitive to sodium bicarbonate ($NaHCO_3$), which activates sAC by inducing closure of the active site and metal recruitment, resulting in enhanced ATP turnover[265]. Here, we ligated the monomeric red fluorescent protein mCherry to a truncated, catalytically active form of sAC[266-267] at the carboxy terminus as an expression marker

for transfection. In addition, we ligated localization sequences targeting the mCherry-sAC to the plasma membrane, cytosol or nucleus at the N- or C- terminus to generate localized $NaHCO_3$-sensitive point sources for cAMP generation.

We first tested this system in HEK 293 cells by co-expressing a cytosolic targeted version of these constructs containing a nuclear export signal (NES) (sAC-NES, Figure 6.1A) with the cytosolic targeted FRET-based cAMP indicator ICUE-NES to monitor cAMP accumulation[268-269]. Treatment of HEK 293 cells co-expressing sAC-NES and ICUE-NES with 15 mM $NaHCO_3$ induced a rapid and robust FRET response (29.3 ± 3.8%; n =10 cells; mean ± SEM) which was readily reversed by washing out $NaHCO_3$ (Figure 6.1B). These reversal kinetics were similar to reversal kinetics observed by β-adrenergic receptor antagonists[269], suggesting reversal kinetics were due to cAMP depletion. These responses were specific to expression of our targeted sAC, as the addition of 100 μM KH7, a sAC-specific inhibitor, also reversed the ICUE response (Figure 6.1C).

To determine if these cAMP signals were functionally relevant, we probed PKA dynamics by using a cytosolic targeted FRET reporter for PKA activity (AKAR-NES), which indicates changes in PKA activity by phosphorylation-dependent changes in FRET[270]. Upon $NaHCO_3$ stimulation of HEK 293 cells co-expressing sAC-NES and AKAR-NES, we observed an immediate and robust FRET response (19.3 ± 2.8%; n = 5 cells) with a t_{50} of 0.9 ± 0.1 min (Figure 6.1D). PKA activity was sustained in the presence of 15 mM $NaHCO_3$ and reversed immediately upon washout, demonstrating that

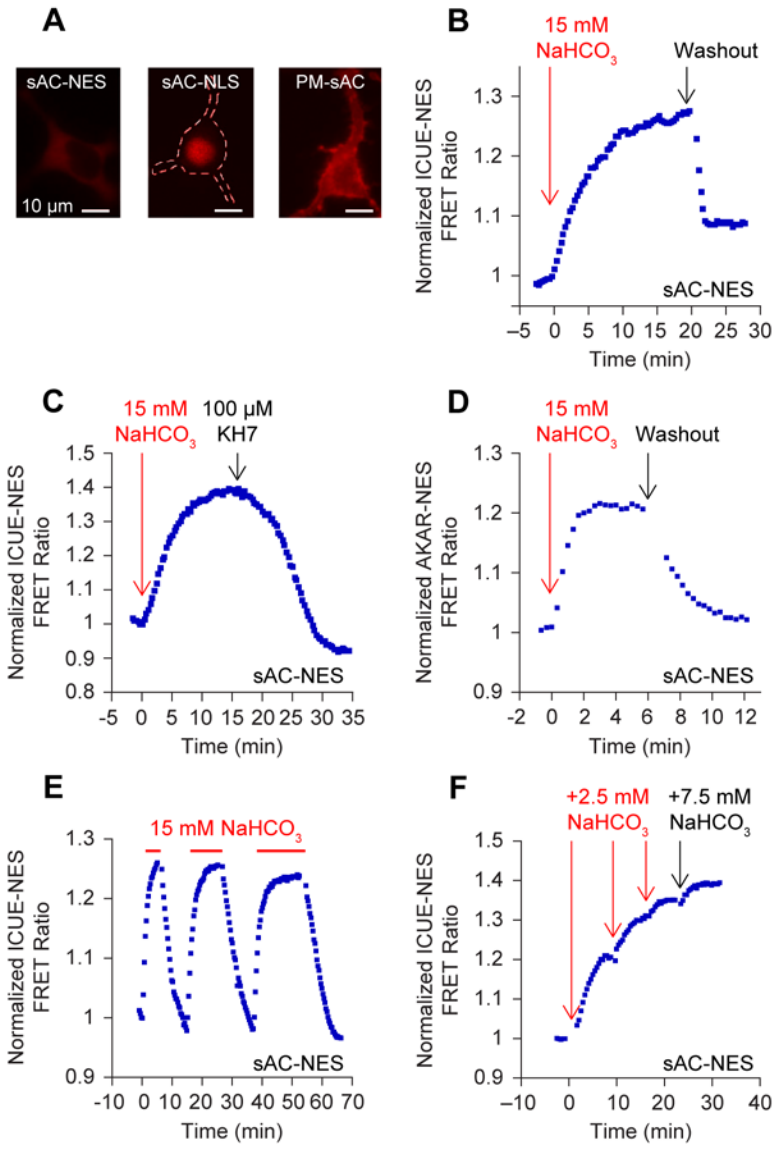

Figure 6.1 Local cAMP manipulation using soluble adenylyl cyclases (sAC). A, Representative images of targeted sAC expression. sAC-NES expression is cytosolic. sAC-NLS expression is nuclear. PM-sAC expression is at the plasma membrane. B, Local cAMP accumulation by sAC-NES is fast and reversible. C, $NaHCO_3$-stimulated cAMP responses are specifically stimulated by expressed sAC, evidenced by deactivation with 100 µM KH7, a sAC inhibitor. D, Local cytosolic PKA activity is similarly fast and reversible. E, sAC reversibility kinetics are fast and robust to multiple $NaHCO_3$ treatments. F, $NaHCO_3$-stimulated cAMP accumulation is dose dependent and tunable.

this targeted sAC system was effective for manipulating both compartmented cAMP accumulation and downstream PKA activity.

We next tested the fidelity and precision of this system by exposing cells to pulses of 15 mM $NaHCO_3$ at 5 min increments, followed by washout (Figure 6.1E). After each stimulus, an immediate and robust cAMP response was observed, sustained without significant photobleaching or signal decay. Thus we demonstrated that this system is highly reversible, sensitive and without memory, while permitting precise control of signal duration.

To further test this system's ability to manipulate cAMP concentrations, we co-expressed sAC-NES and ICUE-NES and stimulated cells with three concentrations of $NaHCO_3$. A small dose of 2.5 mM $NaHCO_3$ elicited a small ICUE response (19.3 ± 0.017%; n =3 cells) (Figure 6.1F), while subsequent increments of 2.5 mM and 7.5 mM $NaHCO_3$ resulted in step-wise increases in FRET responses and cAMP concentrations, demonstrating the targeted sACs were capable of prescribing specific cAMP concentrations.

Having characterized the robustness of the cytosolic sAC to different stimulus conditions, we decided to generalize this system for other compartments. To generate a nuclear cAMP source, we ligated a nuclear localization signal (-NLS) sequence[269] to sAC. Similarly, we targeted the sAC to the plasma membrane (PM-) by ligating a lipid modification domain derived from Lyn kinase, which can be myristoylated or

palmitoylated[268]. To test the local cAMP generation by these constructs, we co-expressed sAC-NLS and ICUE-NLS and stimulated with 2.5 mM $NaHCO_3$, which produced a rapid ICUE-NLS response (21.3 ± 2.5%; n = 5 cells) (Figure 6.2A). Interestingly, subsequent incremental doses of $NaHCO_3$ did not further enhance the magnitude of the ICUE-NLS response significantly.

However, distal cAMP responses exhibited different dynamics, as co-expression of sAC-NLS with PM-ICUE did not elicit a PM-ICUE response with 2.5 mM $NaHCO_3$ (Figure 6.2B). Only after stimulating with larger doses of $NaHCO_3$ were detectable responses elicited, suggesting the null response by 2.5 mM $NaHCO_3$ was due to diminished plasma membrane cAMP accumulation from nuclear cAMP generation by sAC-NLS. Similarly, when we performed the converse experiment, we observed saturating local ICUE responses and weak distal ICUE responses. Co-expression of PM-sAC with PM-ICUE elicited a maximal response (11.4 ± 0.9%; n = 2 cells) (Figure 6.2D) whereas co-expression of PM-sAC with ICUE-NLS elicited a small response (4.1 ± 0.4%; n = 3 cells) (Figure 6.2C). These results demonstrate our targeted sAC system was capable for eliciting spatially localized cAMP generation and that endogenous cAMP compartmentation mechanisms generated spatially heterogeneous cAMP gradients in these cells.

Nuclear PKA Dynamics are Sensitive to Locations of cAMP Generation

Armed with a system for generating highly localized cAMP accumulation, we were interested in how cAMP compartmentation may regulate nuclear PKA activity. We first

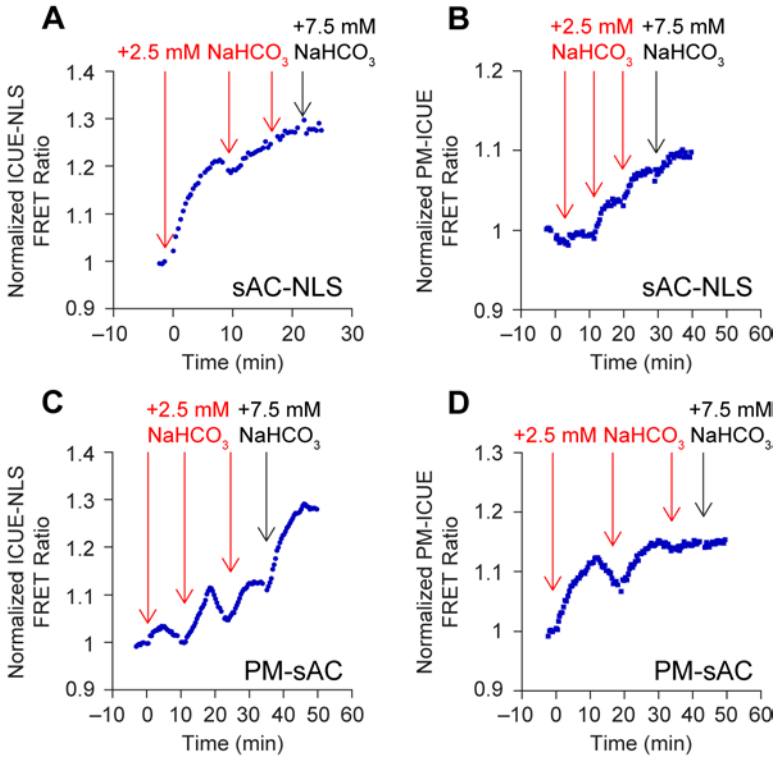

Figure 6.2 cAMP accumulation is sensitive to local and distal cAMP generation. A Local nuclear cAMP accumulation from cAMP generation by sAC-NLS induces a nearly saturating ICUE-NLS response. B, Distal plasma membrane cAMP accumulation from sAC-NLS is non-saturating. C, Similarly, distal nuclear cAMP accumulation from cAMP generation by PM-sAC is non-saturating, while, D, local plasma membrane cAMP accumulation from cAMP generation by PM-sAC is saturating.

examined nuclear PKA activation by PM-sAC to mimic the effects of stimulating endogenous tmACs. Treating cells co-expressing PM-sAC and AKAR-NLS with 15 mM $NaHCO_3$ evoked a slow nuclear AKAR response with a t_{50} of 20.2 ± 3.0 min (n = 4 cells) (Figure 6.3A), whereas a small stimulus of 2.5 mM $NaHCO_3$ did not induce consistent responses. These responses were similar to those elicited by direct activation of tmAC with forskolin (FSK) (t_{50} = 26.0 ± 1.6 min; n = 13 cells) (Figure 6.3B), with no statistically significant difference between the t_{50}s of the two experiments. These slow kinetics were also consistent with observations that nuclear PKA activity may be rate-limited by slow diffusion of cytosolic PKA catalytic subunit[255,271].

In contrast, $NaHCO_3$ stimulation of either sAC-NES or sAC-NLS resulted in faster AKAR-NLS responses with a t_{50} of 3.5 ± 0.3 min (n = 9 cells) and 4.2 ± 0.5 min (n = 7 cells), respectively (Figure 6.3B). While the kinetics of nuclear PKA responses stimulated by nuclear- and cytosolic-generated cAMP were not different, these rates were significantly faster than those evoked by membrane-generated cAMP via endogenous tmAC ($p < 0.001$ for both) or PM-sAC ($p = 0.01$ for both). To exclude the possibility that sAC over-expression had additional effects on PKA, we treated cells expressing sAC-NLS with FSK and observed similarly slow AKAR-NLS responses (t_{50} = 29.8 ± 2.3 min; n = 2 cells) to those in cells containing untargeted sAC (t_{50} = 26.0 ± 1.6 min; n = 13 cells) (Figure 6.3B). To further demonstrate that fast nuclear AKAR responses were induced by local cAMP generation, we stimulated HEK 293 cells expressing sAC-NLS with $NaHCO_3$ and examined the phosphorylation of CREB, an endogenous substrate of PKA in the nucleus. Similar to AKAR-NLS responses, we observed rapid CREB

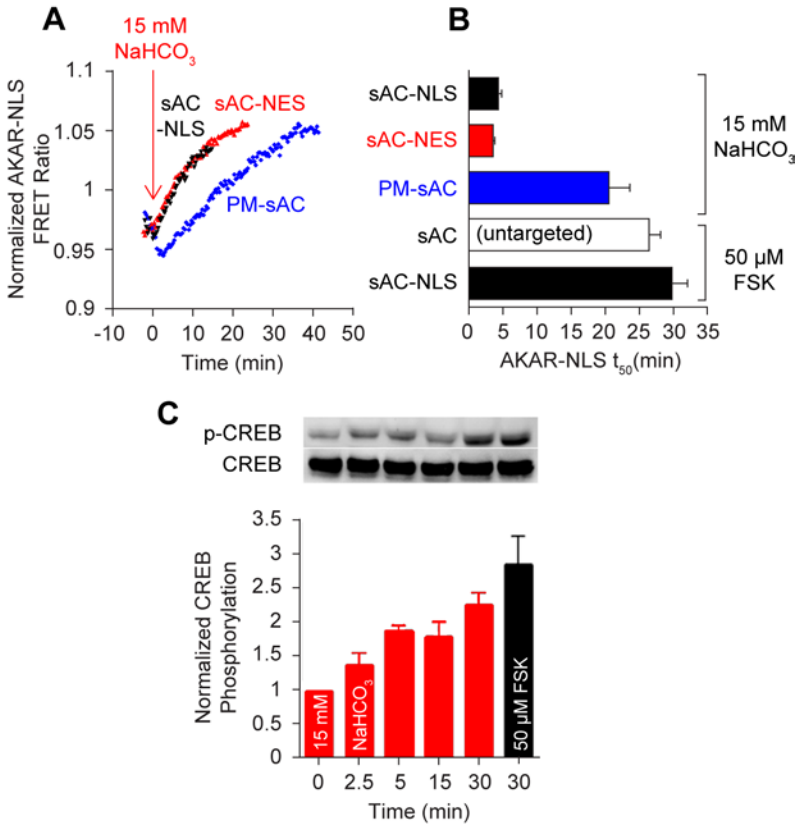

Figure 6.3 Nuclear PKA dynamics are sensitive to the location of cAMP generation. A, Nuclear PKA dynamics from cAMP generation at the plasma membrane are significantly slower than dynamics from cAMP generation at the cytosol or nucleus. B, NaHCO3-stimulated nuclear PKA dynamics from membrane cAMP generation are similar to membrane-stimulated responses on endogenous tmAC using FSK. C, Slow nuclear PKA dynamics are functionally validated by slow CREB phosphorylation.

phosphorylation kinetics in the presence of stimulated sAC-NLS (Figure 6.3C). The rapid AKAR-NLS response and CREB phosphorylation elicited by nuclear or cytosolic cAMP production were surprising. These contradicted the prevailing notion that nuclear PKA activity is rate-limited by slow diffusion of cytosolic PKA catalytic subunit in the nucleus[255,271]. With this classic hypothesis, we expected nuclear PKA dynamics to be insensitive to the location of cAMP generation.

Model-Based Inference for Nuclear PKA Holoenzyme

To quantitatively clarify if this prevailing notion is able to explain our data, we constructed a biochemically mechanistic computational model describing cAMP and PKA dynamics in the three spatial subcellular compartments (plasma membrane, cytosol, nucleus) represented in our experiments (Figure 6.4; *Appendix C*). This 'Classical Model' model consists of endogenous adenylyl cyclase at the plasma membrane, PKA holoenzyme exclusively at the membrane and cytosol, and PDEs and phosphatases in all the three compartments.

We first fit this model to our plasma membrane and nuclear ICUE measurements generated by $NaHCO_3$ stimulation of plasma membrane and nuclear targeted sAC to determine if this model adequately captured cAMP dynamics (Figure 6.5A). Similar to our experimental measurements, the model predicted that local ICUE responses saturate at lower $NaHCO_3$ doses than distal ICUE responses, irrespective of the location of sAC. Simulated ICUE responses have similar shape and qualitative trends, indicating the model is a good representation of both cAMP dynamics and ICUE activity.

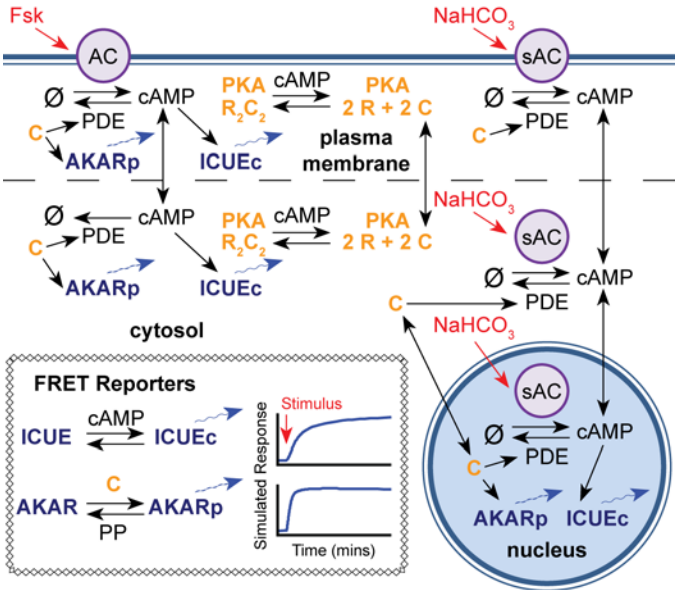

Figure 6.4 Model schematic for cAMP compartmentation manipulation using sACs. Endogenous tmACs (AC) are membrane-bound and sensitive to FSK. sACs can be targeted to the plasma membrane, cytosol or nucleus using localization sequences. sACs are sensitive to $NaHCO_3$.FRET reporters for cAMP (ICUE) and PKA (AKAR) can also be targeted to different subcellular compartments to give local quantification of cAMP and PKA dynamics.

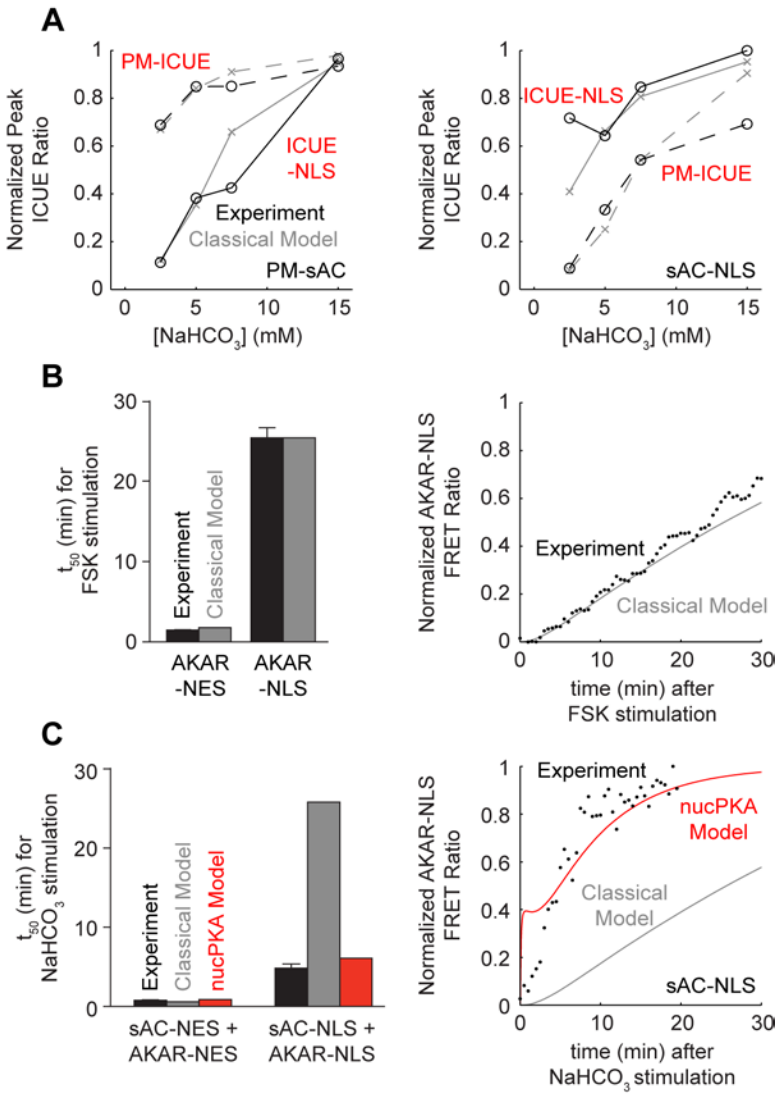

Figure 6.5 Model-based inference for nuclear PKA holoenzyme. A, The *Classical Model* for diffusion limited nuclear PKA activity can explain local and distal cAMP accumulation to dose-dependent $NaHCO_3$ treatment. B, The Classical Model also adequately explains slow nuclear PKA dynamics from FSK stimulation of endogenous tmACs. C, The Classical Model fails to predict fast local nuclear PKA dynamics from nuclear cAMP generation from sAC-NLS. Inclusion of nuclear PKA holoenzyme (*nucPKA Model*) is capable of capturing the faster nuclear PKA kinetics.

To determine if the model adequately captured nuclear PKA dynamics, we simultaneously fit this model to our FSK-stimulated AKAR-NES and AKAR-NLS measurements (Figure 6.5B). Simulated cytosolic AKAR-NES dynamics were fast (t_{50} = 1.79 min vs. experimental t_{50} = 1.5 ± 0.1 min; n = 8 cells), while simulated nuclear AKAR-NLS dynamics are slow (t_{50} = 25.4 min vs. experimental t_{50} = 25.4 ± 1.3 min; n = 28 cells). Confident that the Classical Model adequately described the cAMP and PKA dynamics under our experimental conditions, we simulated cytosolic PKA dynamics stimulated by $NaHCO_3$-activated sAC-NES as well as nuclear PKA dynamics stimulated by $NaHCO_3$-activated sAC-NLS (Figure 6.3C). This model predicted rapid cytosolic PKA activation by sAC-NES (t_{50} = 0.6 min), which was qualitatively similar to the experimentally measured AKAR-NES response (t_{50} = 0.9 ± 0.1 min; n = 5 cells). However, under nuclear sAC stimulation, the model predicted slow nuclear PKA responses with a t_{50} = 24.7 min, which was in sharp contrast to the experimentally measured AKAR-NLS kinetics (t_{50} = 4.8 ± 0.5 min; n = 7 cells). This identified a failure of the Classical Model to explain the fast nuclear PKA responses.

We hypothesized that the presence of an independent pool of PKA holoenzyme in the nucleus could account for the observed fast nuclear PKA kinetics, and incorporated a nuclear PKA holoenzyme as a free parameter into the model, now termed ‘nucPKA Model’ (*Appendix C*). The nucPKA Model was refitted to both our targeted ICUE and AKAR data and predicted similar ICUE responses as the Classical Model. While the predictions for the PKA response kinetics in the cytosol remained relatively unchanged (t_{50} = 0.9 min), the nucPKA Model gave a significant improvement in predicting nuclear

PKA responses (t_{50} = 6.1 min nucPKA Model vs. experimental t_{50} = 4.8 ± 0.5 min; n = 7 cells) (Figure 6.3C).

Increasing model complexity risks trivially improve model fits to experimental data, while risking increased model uncertainty. To quantitatively compare the appropriateness of selecting one model over the other, we took an information theoretic approach to determine which model structure is most likely. We first computed the Akaike Information Criterion (AIC) [262-263] for both the Classical Model (AIC = -59.12) and the nucPKA Model (AIC = -60.71), which rewards improvements in model fits and penalizes increases in the number of fitted parameters. The smaller AIC value for the nucPKA Model indicates that the nucPKA Model is a better description for the observed PKA dynamics than the Classical Model. Using these AICs, we also computed the Akaike weights, which quantify the probability that a model structure within a set of models is likely to best describe the respective experimental data. The nucPKA Model had a higher Akaike weight (w = 0.69) than the Classical Model (w = 0.31), giving a greater than 2-to-1 evidence ratio for the nucPKA Model. These findings suggested a nuclear pool of PKA holoenzyme is likely to be an important component of nuclear PKA dynamics.

Experimental Validation for Nuclear PKA Holoenzyme

To validate this model prediction, we performed immunofluorescence studies using anti-pan PKA RI, anti-PKA RIIβ and anti-PKA catalytic subunit antibodies and tested for the presence of nuclear PKA holoenzyme. All the three antibodies showed weak but distinct staining in the nuclei of HEK 293 cells (Figures 6.6A and 6.6B), whereas staining with

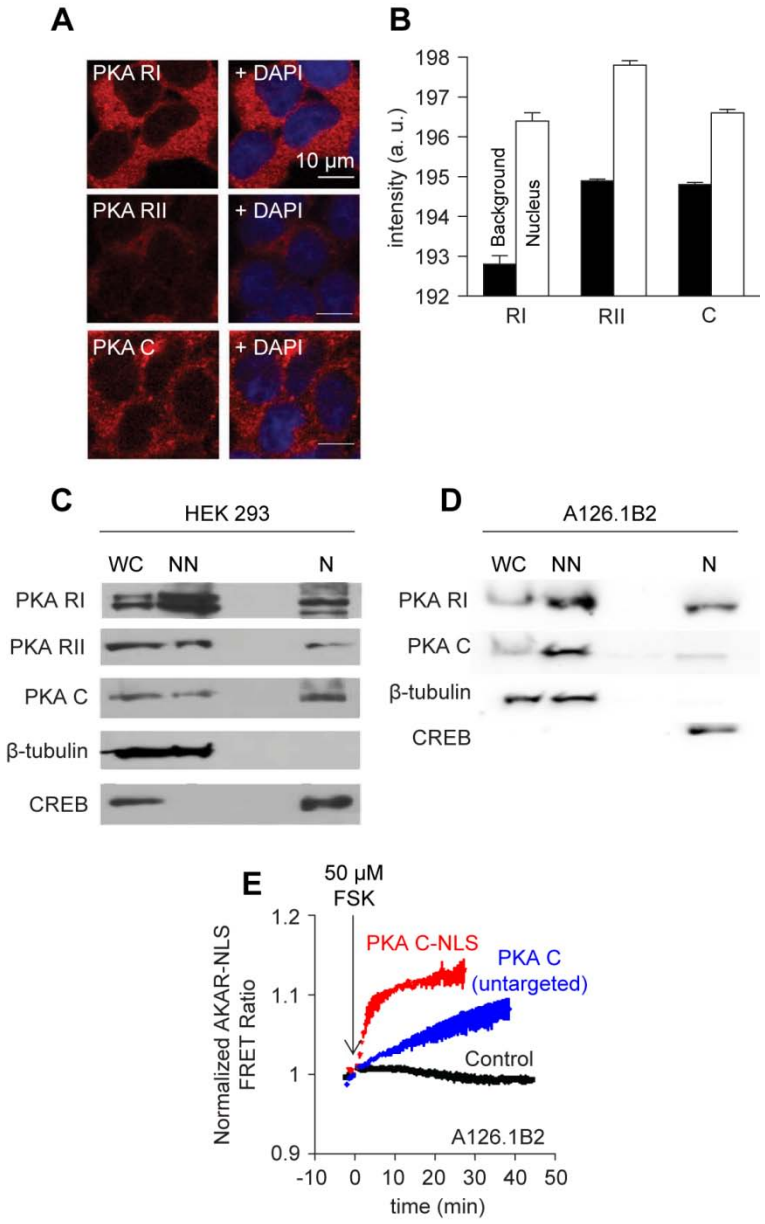

Figure 6.6 Experimental validation of nuclear PKA holoenzyme prediction. A, Representative immunofluorescence imaging of nuclear PKA regulatory and catalytic subunit expression. B, Nuclear PKA expression is small, but significant over background noise. C, Western blot confirmation of nuclear PKA holoenzyme from whole cell (WC), non-nuclear (NN) and nuclear (N) fractions. D, Mutant A126.1B2 cells contain reduced nuclear PKA catalytic subunit, but intact regulatory subunit. E, Reconstitution of nuclear PKA holoenzyme with nuclear catalytic subunit (C-NLS) expression confers fast nuclear PKA responses to FSK stimulation.

secondary antibodies alone did not give a signal in the nucleus. To ensure these results were not due to non-specific labeling, we isolated the nuclei of HEK 293 cells by density centrifugation through a sucrose gradient and performed Western blot analysis on the nuclear and non-nuclear fractions to further substantiate the existence of a PKA pool in the nucleus. These fractions were first probed with antibodies against cAMP response element-binding protein (CREB) as a nuclear fraction reporter, as well as antibodies against β-tubulin as cytosolic fraction reporters. The nuclear fraction gave positive indication by anti-CREB antibodies with undetectable levels of β-tubulin antibodies (Figure 6.6C), indicating that the nuclear fraction was free of cytosolic contaminants. Having confirmed the purity of the nuclear fraction, we probed the two fractions with anti-pan PKA RI, anti-PKA RIIβ and anti-PKA catalytic subunit antibodies. The nuclear fraction gave a positive signal for both PKA regulatory and catalytic subunits, providing direct evidence for the presence of PKA holoenzyme in the nucleus.

To further link nuclear PKA holoenzyme expression with the fast functional nuclear PKA responses, we performed rescue experiments using a mutant PC12 cell line (A126.1B2) deficient in nuclear PKA activity[272]. This mutant cell line exhibits significantly decreased PKA catalytic subunit in the nucleus (Figure 6.6D), and stimulation with FSK does not elicit an AKAR-NLS response (Figure 6.6E). However, because PKA RI subunit are still highly expressed in the nuclei of these cells (Figure 6.6D), we tested if increasing the expression of nuclear catalytic subunit could enrich nuclear PKA holoenzymes and enable fast nuclear PKA responses. Indeed, FSK-stimulation in A126.1B2 cells over-expressing nucleus targeted PKA catalytic subunit generated fast AKAR-NLS responses

(t_{50} = 2.9 ± 0.3 min; n = 2 cells; Figure 6.6E). These rapid response were consistent with the kinetics of activation of the nuclear PKA holoenzyme predicted by the nucPKA model (t_{50} = 6.1 min) as well as our sAC-NLS, AKAR-NLS co-expression experiments (t_{50} = 4.8 ± 0.5 min; n = 7 cells). In contrast, A126.1B2 cells stably transfected with untargeted catalytic subunit gave slow AKAR-NLS responses to FSK stimulation (Figure 6.6E). Collectively, this data suggests that fast nuclear PKA responses require locally activatable nuclear PKA holoenzyme.

PDE4 regulates PKA responses in the nucleus

Having confirmed the model-predicted nuclear PKA holoenzyme expression, we turned attention to identify mechanisms regulating nuclear PKA responses. It is well established that PDEs can shape cAMP gradients in sub cellular compartments by restricting cAMP diffusion[250]. To test the role of PDEs in regulating nuclear PKA responses, we treated HEK 293 cells with 3-isobytl-1-methylxanthine (IBMX), a non-selective PDE inhibitor, and monitored AKAR-NLS responses to tmAC activation by FSK. Inhibition of PDEs with IBMX significantly accelerated the kinetics of FSK-stimulated nuclear PKA activity as indicated by a decreased t_{50} of 12.5 ± 2.1 min (n = 18 cells). In 44% of these cells, a very fast response (t_{50} = 3.1 ± 1.2 min; n = 8 cells) was observed (Figure 6.7A), matching the kinetics of the nuclear PKA holoenzyme activation that were experimentally determined by nuclear cAMP generation (t_{50} = 4.8 ± 0.5 min; n = 7 cells) and those predicted by the nucPKA Model (t_{50} = 6.1 min). These results suggested a role for PDEs in limiting the activation of the endogenous nuclear PKA pool when cAMP is produced at the plasma membrane.

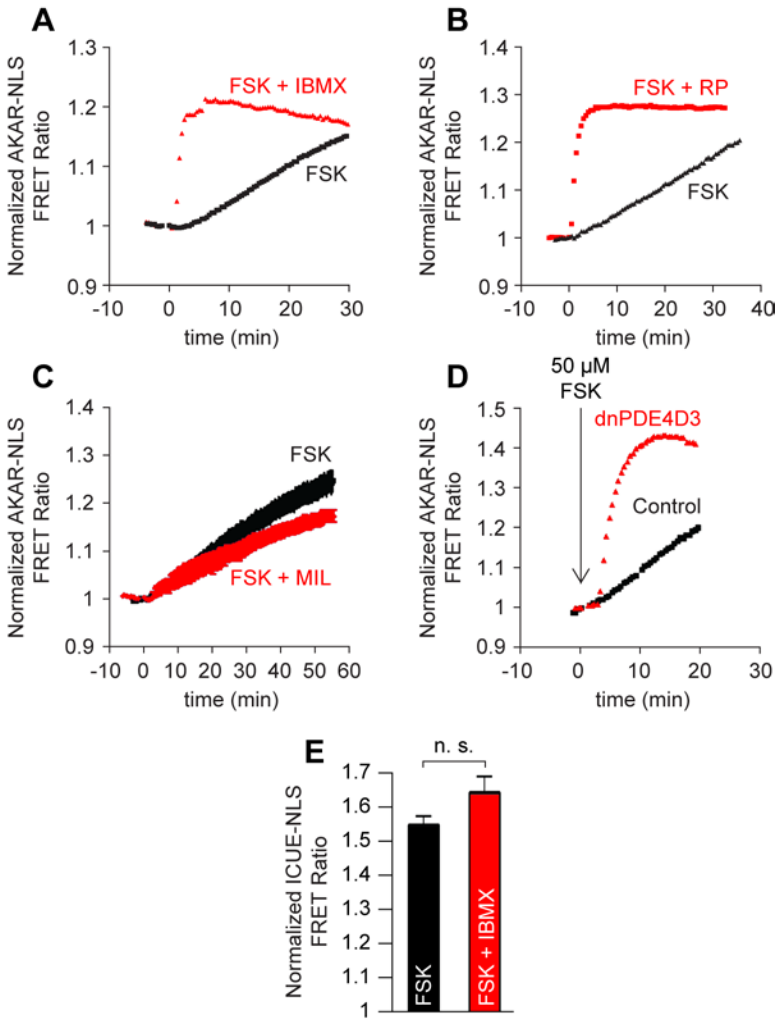

Figure 6.7 Nuclear PKA dynamics are regulated by PDE4D. A, PDE inhibition with 100 µM IBMX accelerates nuclear PKA responses to 50 µM FSK. B, PDE4-specific inhibition with 10 µM rolipram (RP) also accelerates nuclear PKA responses to FSK. C, PDE3-specific inhibition with milrinone (MIL) did not accelerate nuclear PKA-responses to FSK, suggesting PDE4 rate-limits nuclear PKA activation. D, Expression of dominant negative PDE4D3 (dnPDE4D3) accelerates nuclear PKA activity. E, Nuclear cAMP accumulation is saturated under stimulation of endogenous tmAC by FSK alone.

PDE3 and PDE4 have been identified as the two major subfamilies of PDEs expressed in HEK 293 cells[273]. To identify which PDE isoform regulates PKA responses in the nucleus, we treated cells with FSK in the presence of either milrinone, a PDE3-selective inhibitor, or rolipram, a PDE4-selective inhibitor. The rolipram/FSK cocktail induced a fast AKAR-NLS response (t_{50} = 5.4 ± 2.14 min; n = 8 cells; Figure 6.7B), while treatment with milrinone/FSK induced a slow AKAR-NLS response, similar to FSK stimulation alone (Figure 6.7C). These data suggested that PDE4 is the predominant isoform responsible for regulating nuclear PKA responses. To more carefully identify the specific PDE4 subfamilies involved in regulating nuclear PKA activity, we co-expressed dominant negative (dn-) mutants of PDE4B and PDE4D with AKAR-NLS[274-275]. These catalytically-inactive mutants exert an inhibitory effect by dislodging the endogenous PDE4 isoforms from their appropriate anchor sites[274-275]. FSK elicited a slow AKAR-NLS response in cells over-expressing either dnPDE4B1 or dnPDE4B2, but fast in cells over-expressing dnPDE4D3 (Figure 6.7D), suggesting that PDE4D3 is responsible for regulating nuclear PKA responses in HEK 293 cells.

In light of the IBMX experiments, we hypothesized that PDE4 may play an important role in limiting the cAMP diffusion from the plasma membrane to the nucleus. To test this hypothesis, we examined the effect of PDE inhibition on ICUE-NLS responses to cAMP generation at the plasma membrane. However, FSK stimulation led to fast, saturated ICUE-NLS responses both with and without PDE inhibition (Figure 6.7E), suggesting cAMP is capable of quickly diffusing to the nucleus. This data presented a paradox: if cAMP generated at the plasma membrane accumulates fast in the nucleus and

produces a maximal response from ICUE-NLS (which has a lower affinity for cAMP than PKA[276-277]), why are nuclear PKA holoenzymes not being activated by this pool of cAMP? Indeed, when the nucPKA model was refitted to all of the ICUE and AKAR responses, it predicted fast nuclear responses of PKA irrespective of where cAMP was synthesized (Figure 6.8A), in contrast to the experimental observations (Figure 6.3B).

Model-Based Inference for a Nuclear AKAP-PDE4 Complex

To reconcile how PDE4 may limit nuclear PKA activation despite adequate nuclear cAMP accumulation by FSK stimulation, we hypothesized that PDE4 may form a signaling complex with nuclear PKA holoenzyme. Such an arrangement may allow nuclear PDEs to degrade cAMP immediately local to the nuclear PKA holoenzyme, insulating nuclear PKA activity by raising the cAMP activation threshold. The existence of such signaling complexes has been documented in literature[278]. For example, a peri-nuclear AKAP (mAKAP) has been shown to tether PDE4 to the AKAP-PKA complex and modulate local cAMP levels[279]. We therefore inferred the existence of a subnuclear AKAP which may bring nuclear PKA holoenzyme in close proximity to PDEs.

To test the validity of this hypothesis, we revised the nucPKA Model by adding a phenomenological subnuclear AKAP compartment (‘nucAKAP Model’). We assumed all nuclear PKA holoenzyme resides in this subnuclear AKAP compartment and that the apparent PDE concentrations in this compartment are raised significantly by protein tethering. Refitting the nucPKA Model to each of the data sets, we observed significant improvement in the model predictions for nuclear PKA dynamics. Specifically, while

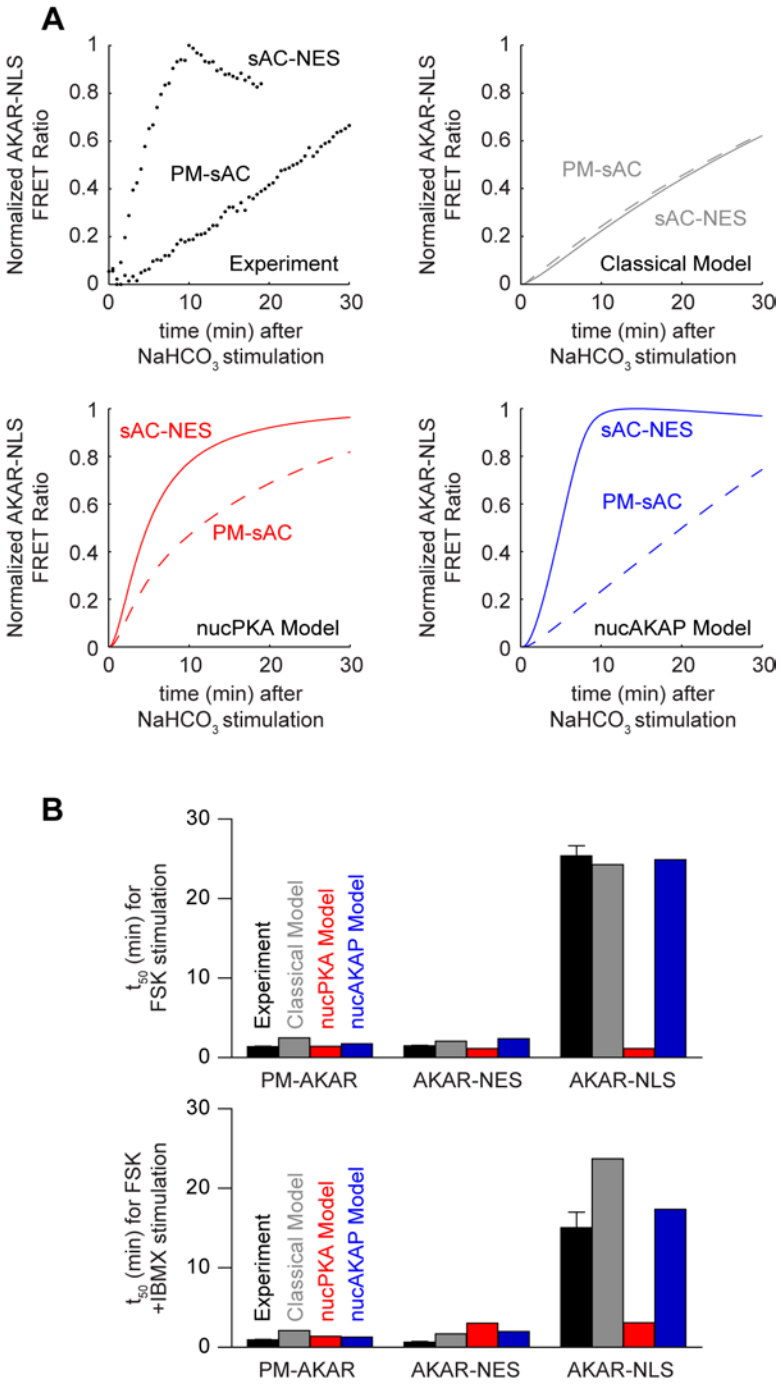

Figure 6.8 Model-based inference for nuclear AKAP complex. A, Both Classical and nucPKA Models fail to predict nuclear PKA activation by local and distal cAMP generation. Inclusion of a nuclear AKAP complex (*nucAKAP Model*) recovers the experimentally observed dynamics. B, nucAKAP Model best fits the dynamics observed from FSK-stimulated cAMP generation by endogenous tmAC with and without PDE inhibition by IBMX.

both the refitted Classical Model and the nucPKA Model failed to predict the differences in nuclear PKA dynamics in response to membrane and cytosolic cAMP generation (Figure 6.8A), nuclear PKA response kinetics computed by the nucAKAP model matched the experimental kinetics, for the membrane cAMP production (nucAKAP Model t_{50} = 20.1 min vs. experimental t_{50} = 20.4 ± 3.02 min; n =4 cells) as well as for cytosolic cAMP generation (nucAKAP Model t_{50} = 5.0 min vs. experimental t_{50} = 3.5 ± 0.3 min; n = 9 cells). These simulations suggest that differences in nuclear PKA kinetics may be explained by differences in apparent cAMP concentration which are specified by AKAP-bound PDE4. In this scenario, cytosolic sAC stimulation may generate a much larger cAMP signal than membrane sAC or tmAC stimulation, driving activation of a nuclear AKAP-bound PKA pool.

We also simulated PKA activity in the membrane, cytosol and nucleus in response to FSK in the absence or presence of IBMX for each of the three models (Figure 6.8B). The nucAKAP Model best captured the slow nuclear PKA response to FSK (t_{50} = 24.9 min vs. t_{50} = 26.0 ± 1.6 min; n = 13 cells) and accelerated nuclear PKA response to FSK in the presence of IBMX (t_{50} = 17.4 min vs. t_{50} = 12.5 ± 2.1; n = 18 cells). The computed AIC values for the Classical Model (AIC = 3.95), nucPKA Model (AIC = 5.81) and nucAKAP Model (AIC = -37.50) suggest that the nucAKAP Model best describes the responses of nuclear PKA in our experiments, significantly outweighing both the Classical and nucPKA Models in explaining the differences in nuclear PKA dynamics. The corresponding Akaike weights for these models were < 0.001 for both the Classical and nucPKA Models and > 0.999 for the nucAKAP Model indicating that both the Classical

and nucPKA Models are incapable of explaining how PDE4 limits nuclear PKA responses to tmAC stimulation.

Experimental Validation for AKAP Regulation of Nuclear PKA Activity

To test the prediction for a AKAP-PDE4-PKA complex, we pre-incubated HEK 293 cells expressing AKAR-NLS with Ht31, a peptide that blocks the interaction between PKA and AKAP[279]. This treatment is experimentally analogous to reducing the nucAKAP Model to the nucPKA Model, with the expectation that disruption of the AKAP-PKA interaction should accelerate nuclear PKA activation since PKA is no longer localized in the same signaling microdomain as the AKAP-tethered PDEs. Upon stimulation with FSK, we observed faster AKAR-NLS kinetics (t_{50} = 7.6 ± 1.2 min; n = 14 cells) (Figure 6.9A), which were similar to those evoked by PDE inhibition. In contrast, when cells were pre-incubated with a negative control scrambled peptide (Ht31P) and then treated with FSK, we observed slow AKAR-NLS responses (t_{50} = 25.3 ± 1.8 min; n = 9 cells), comparable to treatment with FSK alone (Figure 6.9B). Together, these results confirm an important role for AKAPs in regulating the nuclear PKA response and support our conceptual model of a subnuclear AKAP- PDE4-PKA signaling complex.

6.5 Discussion

The ability to both monitor and precisely manipulate cAMP concentrations at different subcellular loci is important for fully understanding the role of compartmented cAMP signaling in cells. Towards this end, we describe a new method using targeted sACs for prescribing the location, kinetics and magnitude of cAMP accumulation. This system is

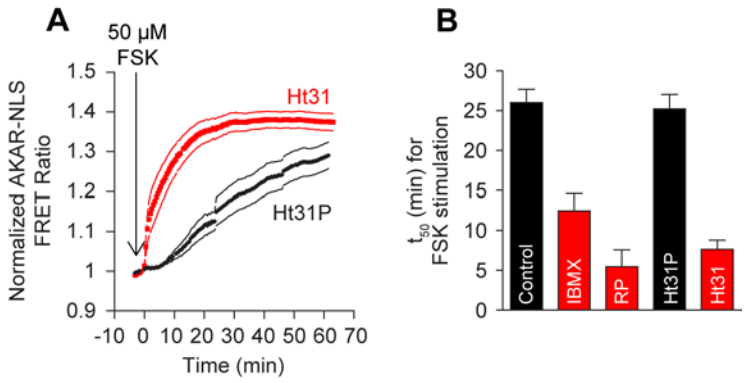

Figure 6.9 Experimental validation of nuclear AKAP complex prediction. A, AKAP disruption by pre-treatment with 50 μM Ht31 accelerates nuclear PKA responses to FSK. Pre-treatment with 50 μM Ht31P negative control gives slow nuclear PKA responses. B, Nuclear PKA dynamics with Ht31 pre-treatment are similar to dynamics with PDE4 inhibition by IBMX and RP, suggesting an AKAP complexes nuclear PKA holoenzyme with PDE4.

advantageous over photolytic uncaging of cAMP analogs[280], since these sACs can be genetically targeted to functional organelle microdomains (*e.g.*, mitochondria and vesicles) or cellular nanodomains (*e.g.*, membrane rafts) using localization sequences. Moreover, activation of sAC leads to more efficient cAMP generation than photolytic uncaging due to its catalytic nature, permitting temporal control of $NaHCO_3$ -mediated responses. In addition, targeted sAC can be scalable to *in vivo* transgenic models to examine multi-cellular or tissue relevance. Recently, light-sensitive adenylyl cyclases from *Euglena gracilis* and the soil bacteria *Beggiatoa* have also been exploited to generate cAMP upon stimulation with light[281-282], though cAMP generation in specific organelles has yet to be demonstrated by this method. The present method allows organelle-specific and efficient cAMP generation under strict temporal control, thereby enabling mechanistic dissection of the spatiotemporal regulation of cAMP signaling in specific subcellular compartments.

On the computational modeling front, we adopted a unique strategy of assaying model structures via parameter estimation to infer the regulatory structure of a cell signaling network. Mechanistic models are often presumed to contain an appropriate structure and are used as surrogates for an experimental system[59]. Here, we draw upon findings in information theory to directly infer and test different model structures when they are not fully known *a priori*[262]. While traditional approaches in systems biology seek to quantify known relationships or integrate large data sets[283], our approach here illustrates a relatively under-utilized, but important application for computational models in

complementing experimental studies: providing quantitative evidence for selecting from directly competing hypotheses.

In this chapter, we combined targeted sAC expression with live-cell imaging and mathematical modeling to investigate how cAMP signals are translated into nuclear PKA activity. We revise the existing dogma of cAMP-PKA signaling in the nucleus[249,252,256] and form a new conceptual model for the regulation of nuclear PKA responses: PKA signaling dynamics in the nucleus is governed by two distinct pools of PKA holoenzyme, a translocated cytosolic pool and a resident nuclear pool. In this conceptual model, the presence of an AKAP-mediated signaling complex that localizes PDE4 in close proximity to nuclear PKA holoenzyme largely controls nuclear PKA activity. When cAMP is generated at the plasma membrane and diffuses into the nucleus, cAMP concentrations immediately local to the nuclear PKA holoenzyme are kept low by AKAP-anchored PDE4s and are not capable of efficiently activating nuclear PKA holoenzyme. And as a result, nuclear PKA responses are characterized by slow kinetics, rate-limited by the translocation of the catalytic domain of cytosolic PKA. However, when the local cAMP concentration is elevated above a threshold, for example by activation of cytoplasmic- or nuclear-targeted sAC, activation of nuclear PKA holoenzyme can occur and generate fast kinetics of nuclear PKA responses. This nuclear PKA signaling domain assembled by a subnuclear AKAP therefore elevates the cAMP activation threshold and translates spatially distinct cAMP signals into temporally variant nuclear PKA kinetics. New studies will need to focus on identifying the responsible AKAP and more fully characterize the signaling complex. In addition, the functional

impact of this nuclear PKA holoenzyme on processes such as transcription and RNA splicing will need to be clarified. However, there is some evidence to suggest that endogenous sACs can be found in the nuclei of several cell types and engaged in response to metabolic stress[258].

6.6 Conclusions

In summary, we combine targeted biochemical cAMP manipulation, real-time cAMP and PKA measurement and quantitative mechanistic modeling to provide evidence for the existence and distinct regulation of nuclear PKA holoenzyme. We propose a new model that a subnuclear signaling complex establishes a local signaling threshold which translates spatial second messenger signals into temporal control of kinase activity. The quantitative native biochemistry approach[284-286] utilized here should facilitate further testing of this model in this and other cell systems, leading to a better understanding of the mechanistic intricacies that underlie compartmentalized cAMP signaling.

Chapter 7

Regulation of PKA Catalytic Subunit Compartmentation in Cardiac Myocytes

Work from this chapter is in preparation for publication.

7.1 Foreword

In the previous chapter, we inferred a subnuclear AKAP-PDE4-PKA signaling complex as a putative local cAMP compartmentation mechanism which can regulate nuclear PKA dynamics in the commonly used HEK 293 cell line. Moreover, we showed how an integrated modeling-experimental approach can be useful for hypothesis generation. However, the primary focus of this dissertation is to understand how β-adrenergic signaling regulates cardiac remodeling processes such as hypertrophy. In this chapter, we directly test the hypothesis that nuclear PKA activity directly and specifically regulates cardiac myocytehypertrophy, *in vitro*. Moreover, we show cardiac nuclear PKA activity is regulated by compartmentation of the PKA catalytic subunit, rather than cAMP compartmentation. These findings have important implications for the therapeutic management of cardiac disease.

7.2 Introduction

Congestive heart failure is a complex disease characterized by the failing heart's inability to adequately supply blood to meet the body's demand. In normal physiology, the body responds to acute deficiencies in blood flow by releasing catecholamines and stimulating sympathetic activity in the heart[1]. However, the contemporary view of heart failure states that in addition to acute enhancements in contractility, sympathetic overdrive initiates cardiac remodeling events such as hypetrophy and fibrosis, which further weaken cardiac tissue (the *neurohormonal hypothesis*)[8,18]. Over time, this further stimulates

catecholamine release, locking the heart in a vicious cycle until the heart suffers electromechanical disfunction and sudden cardiac death.

Consistent with this view, β-adrenergic receptor antagonists (β-blockers) have risen as highly efficacious first-line therapies for managing the progression of heart failure[21,85]. However, the β-adrenergic receptor/protein kinase A (PKA) signaling pathway is complex and it remains unclear how β-adrenergic signaling can sometimes elicit some signaling responses (*e.g.*, contractility enhancements) but not others (*e.g.*, cell hypertrophy)[3]. Moreover, while β-blockers have demonstrated success in attenuating cardiac remodeling, β-blocker treatment also risks leaving patients susceptible to bradycardia and low blood pressure due to their antagonistic actions on heart rate and contractility[21,85]. These concerns raise many questions on how β-adrenergic signaling contributes to the progression of heart failure[34-35].

Many groups, including our own, have observed spatiotemporal heterogeneity in β-adrenergic signaling in the cardiac myocyte, prompting the hypothesis that local 'compartmentation' of β-adrenergic signaling species may underlie selection of different receptor-stimulated behaviors[44-45]. Common to most of these studies is the hypothesis that spatially heterogeneous cAMP gradients or PKA holoenzyme expression restricts the activity of PKA catalytic subunit to small local signaling microdomains, coupled to β-adrenergic signaling responses. Here we test a complementary hypothesis that compartmentation of PKA catalytic subunit itself may also be an important regulator of β-adrenergic signaling specificity.

Taking a multi-disciplinary approach of combining live-cell imaging with high-throughput hypertrophy screening and computational modeling, we demonstrate β-adrenergic receptor-stimulated enhancements to Ca^{2+} and cell size have different sensitivities to receptor activation. These differences in sensitivity are also present in cytosolic and nuclear PKA activity, suggesting selection of these behaviors may be regulated by local PKA. Moreover, we show that differences in cytosolic and nuclear PKA activity are not explained by differences in cytosolic and nuclear cAMP accumulation, indicating these compartmented PKA dynamics are not regulated by compartmented cAMP accumulation. Rather, differences in cytosolic and nuclear PKA activity can be directly explained by rate-limiting PKA catalytic subunit diffusion. Using a computational model, we infer the existence of a PKI-mediated nuclear PKA signaling microdomain, which we confirm experimentally. Finally, over-expressing PKA catalytic subunit in both the cytosol and nucleus, we demonstrate PKA catalytic subunit compartmentation is sufficient for regulating differential activation of β-adrenergic signaling responses.

7.3 Materials and Methods

Cardiomyocyte Isolation and Culture

Neonatal rat ventricular myocytes were isolated from 2-3 day old Sprague-Dawley rats using the Neomyt Cardiomyocyte Isolation Kit (Cellutron Life Technologies, Baltimore, MD). All procedures were performed in accordance with the Guide for the Care and Use of Laboratory Animals published by the National Institutes of Health and approved by the University of Virginia Institutional Animal Care and Use Committee. Myocytes were

cultured in media containing 65% Dulbecco's Modified Eagle Medium, 17% Medium 199, 10% horse serum, 5% fetal bovine serum, 2% penicillin / streptomycin and 1% L-glutamine on either 35 mm glass-bottom dishes (MatTek, Ashland, MA) or CellBIND coated 96-well plates (Corning, Corning, NY).

Ca^{2+} Imaging

Two days after isolation, myocytes cultured in 35 mm glass-bottom dishes were transferred to serum-free media (76.8% Dulbecco's Modified Eagle Medium, 19.2% Medium 199, 2% penicillin / streptomycin and 1% insulin-transferrin-sodium selenite) for 24 hours. Three days after isolation, cultured myocytes were loaded by incubating in Fluo-4 AM (Invitrogen, Carlsbad, CA) dissolved in Tyrode's Solution for 30 minutes. Loaded myocytes were then de-esterified by washing out the Fluo-4/Tyrode's mixture and incubating myocytes for an additional 30 minutes in Tyrode's Solution. De-esterified myocytes were then field stimulated at 1 Hz pacing using the C-Pace EP Culture Pacer (IonOptix, Milton, MA) and stimulated using isoproterenol (ISO; Tocris, Minneapolis, MN) dissolved in Tyrode's Solution. Paced myocytes were imaged on an IX-81 inverted microscope (Olympus, Center Valley, PA) with a Digital CCD C9300-221 camera (Hamamatsu, Bridgewater, NJ) at 10 Hz using MetaMorph (Molecular Devices, Sunnyvale, CA). Cells were segmented in ImageJ (National Institutes of Health, Bethesda, MA) and analyzed in MATLAB (Mathworks, Natick, MA).

Hypertrophy Measurements

Two days after isolation, myocytes cultured in 96-well plates were transfected with cTnT-EGFP plasmid[287] using Lipofectamine 2000 (Invitrogen, Carlsbad, CA). Two days following transfection, myocytes were cultured in serum-free media containing various concentrations of ISO for 24 hours. Following incubation, myocytes were imaged on an Olympus IX-81 inverted microscope with an automated stage (Prior Scientific, Rockland, MA) and an Orca-AG CCD camera (Hamamatsu, Bridgewater, NJ) using IPLab (Scanalytics, Fairfax, VA). Images were segmented and analyzed in MATLAB using custom image processing algorithms. For mCherry and PKA over-expression experiments, myocytes were co-transfected with cTnT-mCherry-C1(Clontech, Mountain View, CA), CMV-PKA-NES or CMV-PKA-NLS plasmid and imaged 24 hours following culture in serum-free media.

FRET Imaging

Two days after isolation, myocytes cultured in 35 mm glass-bottom dishes were transfected with CMV-AKAR-NES[270], CMV-AKAR-NLS[270], CMV-ICUE-NES[268] or CMV-ICUE-NLS[268] plasmid using Lipofectamine 2000. Following transfection, myocytes were cultured in serum-free media for 24 hours. Following incubation, myocytes were washed and incubated in Tyrode's Solution. Imaging was performed on an Olympus IX-81 inverted microscope with an Orca-AG CCD camera using IPLab. Cells were segmented in ImageJ and analyzed in MATLAB. One minute after the beginning of each experiment, Tyrode's Solution was added to each dish as a negative control. Cells were then treated with ISO dissolved in Tyrode's Solution at different

concentrations. Finally, cells were treated with 50 μM forskolin (Tocris, Minneapolis, MN) and 100 μM 3-isobytl-1-methylxanthine (Sigma-Aldrich, St. Louis, MO) as a positive control. FRET computations were performed in MATLAB using the PFRET algorithm[288]. Cells were then segmented in ImageJ and FRET responses were normalized to positive and negative controls in MATLAB. For wheat germ agglutinin (WGA, Sigma-Aldrich, St. Louis, MO) experiments, myocytes were pre-incubated in Tyrode's Solution with 20 μg/mL WGA before each experiment.

Computational Modeling

Nuclear PKA activity was modeled by modifying our previously published ordinary differential equation implementation of cardiac β-adrenergic signaling[5-6,289] to include nuclear PKA transport, PKI transport and AKAR expression/phosphorylation (*Appendix D*). The expanded model was implemented in MATLAB and constrained to parameters estimated from published literature. The final model contained 34 state variables and 104 parameters. Before each simulation, fresh initial conditions were generated by running the model to steady-state with no ISO stimulation.

Immunofluorescence

Two days after isolation, myocytes cultured in 35 mm glass-bottom dishes were fixed in 4% paraformaldehyde (Fisher Scientific, Pittsburgh, PA) for 20 minutes. Myocytes were then permeabilized with 0.2% Triton X-100 (MP Biomedicals, Solon, OH) for 2 minutes. Myocytes were then blocked with 1% bovine serum albumin (Sigma-Aldrich, St. Louis, MO) for 45 minutes. After blocking, myocytes were incubated with 1:200 rabbit

polyclonal anti-PKIA primary antibodies (Lifespan Biosciences, Seattle WA) for 1 hour. Myocytes were then blocked with 2% normal goat serum (Sigma-Aldrich, St. Louis, MO) for 30 minutes. After blocking, myocytes were incubated with 1:200 goat anti-rabbit secondary antibodies conjugated with Alexa fluorophors (Invitrogen, Carlsbad, CA). Following washout, cells were imaged on an Olympus IX-81 inverted microscope with an Orca-AG CCD camera using IPLab. Cells were analyzed using ImageJ.

Western Blot Measurements

Two days after isolation, myocytes cultured in 6-well plates were treated with ISO for 30 minutes and then rinsed with ice cold phosphate buffered solution. Cellular lysates were prepared in Pierce RIPA Buffer (Thermo Scientific, Rockford, IL) supplemented with Complete Protease Inhibitor Cocktail Tablets (Roche, Indianapolis, IN) and Halt Phosphatase Inhibitor Cocktail (Thermo Scientific, Rockford, IL). Protein concentrations from cell lysates were quantified using the Micro BCA Protein Assay Kit (Thermo Scientific, Rockford, IL) and all samples were normalized for protein concentration. Lysed cells were then mixed with 4x SDS-sample buffer. Samples for pCREB detection were boiled for 5 min at 95°C. Equal amounts of total protein from each sample were resolved on 15% SDS-polyacrylamide gels by electrophoresis and then transferred to Immobilon-FL PVDF membranes (Millipore, Billerica, MA). These membranes were rinsed with phosphate buffer solution and then incubated with Odyssey Blocking Buffer (LI-COR Biosciences, Lincoln, NE). Blots were labeled using primary rabbit anti-phospho-PLB (Ser16/Thr17) antibodies (Cell Signaling Technology, Danvers, MA) or rabbit anti-phospho-CREB (Ser133) (Cell Signaling Technology, Danvers, MA). Mouse

anti-α-tubulin (LI-COR Biosciences, Lincoln, NE) were used as protein loading controls. PLB and CREB were detected using goat anti-rabbit IRDye800 CW (LI-COR Biosciences, Lincoln, NE) secondary antibodies. α-tubulin was detected using goat anti-mouse IRDye680 CW (LI-COR Biosciences, Lincoln, NE) secondary antibodies. All membranes were scanned using an Odyssey scanner (LI-COR Biosciences, Lincoln, NE).

Statistical Analysis

All statistical analyses were performed using Prism (GraphPad, La Jolla, CA). EC_{50}s for ISO-stimulated Ca^{2+} enhancements, hypertrophy, FRET responses and PLB and CREB phosphorylation were fitted to a variable slope dose-response curve. Unpaired *t*-tests were performed on ICUE and AKAR t_{50}s for statistical significance. Non-parametric Mann-Whitney tests were performed on hypertrophy measurements. Hypertrophy measurements are reported as median ± mean absolute deviation. All other statistics are reported as mean ± standard error of mean.

7.4 Results

β-Adrenergic Signaling Responses are Differentially Sensitive to ISO

β-adrenergic signaling stimulates many cardiac behaviors via PKA, eliciting coordinated control of both contractile and hypertrophic responses[3]. To characterize contractile and hypertrophic responses to β-adrenergic stimulation, we treated neonatal rat ventricular myocytes with isoproterenol (ISO) and measured enhancements to Ca^{2+} transients and cell size. At 1 μM ISO, steady-state Ca^{2+} transient amplitudes exhibited a 63.5 ± 15.1%

(mean ± SEM; n = 8 experiments) enhancement in Fluo-4 loaded myocytes (Figure 7.1A). Similarly, 1 μM ISO induced a 24.2 ± 3.5% (median ± standard error of median, n > 100 cells) increase in cell size after a 24 hour culture in serum-free media (Figure 7.1B). Interestingly, enhancements to Ca^{2+} handling exhibited marked increases in ISO sensitivity over hypertrophic responses (Figure 7.1C). Increases in Ca^{2+} amplitudes exhibited significantly higher sensitivity for ISO (EC_{50} = 1.84 nM; n ≥ 3 experiments each) than increases in cell size (EC_{50} = 85.88 nM; n > 250 cells each) (Figure 7.1D). These suggest PKA-mediated β-AR responses may be differentially regulated by the magnitude of receptor stimulation.

PKA Activity is Compartmented and Differentially Sensitive to ISO

We reasoned that because PKA substrates regulating Ca^{2+} handling are mostly cytosolic (*e.g.*, ion channel regulators) and PKA substrates regulating hypertrophy may be mostly nuclear (*e.g.*, transcription factors), differential regulation of these behaviors may be explained by compartmented PKA activity. We therefore hypothesized that PKA activity in the cytosol and nucleus may also be differentially sensitive to β-adrenergic stimulation. To test this hypothesis, we expressed PKA-specific FRET reporters targeted to either the cytosol (AKAR-NES) or nucleus (AKAR-NLS) (Figure 7.2A). Stimulating these myocytes with 1 μM ISO, PKA activity was saturated faster in the cytosol (t_{50} = 3.71 ± 0.25 min; mean ± SEM, n = 8 cells) than in the nucleus (t_{50} = 10.60 ± 0.68 min; n = 6 cells) (Figure 7.2B). Treatment with 10 μM propranolol (PRO), a non-selective beta blocker, deactivated PKA activity – also faster in the cytosol than in the nucleus. Moreover, cytosolic PKA activity (EC_{50} = 1.22 nM; n ≥ 9 cells each) was indeed

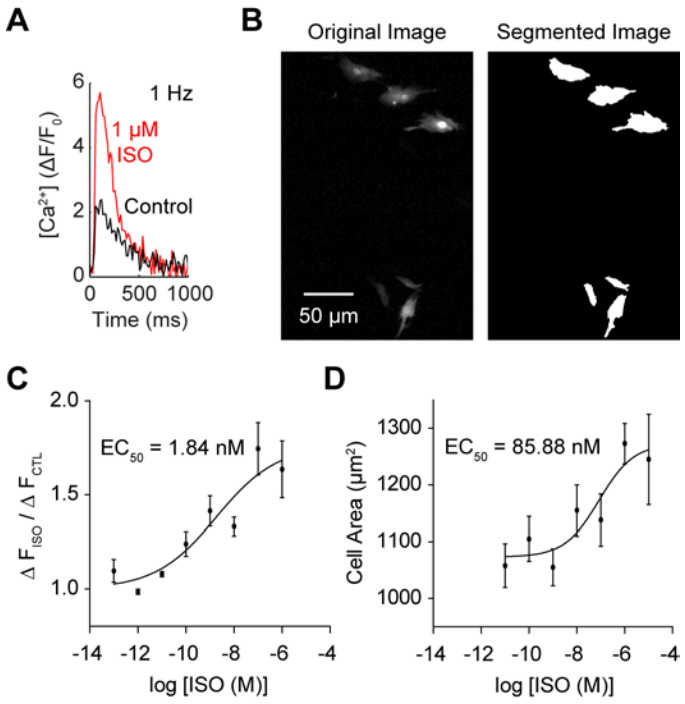

Figure 7.1 β-adrenergic signaling responses exhibit different ISO sensitivities. A, Representative Fluo-4 measurements from control and 1 μM ISO-stimulated myocytes paced at 1 Hz. B, Representative automated cell segmentations from myocytes cultured in 1 μM ISO for 24 hours. C, ISO-stimulated Ca^{2+} enhancmements exhibit high ISO sensitivity (mean ± SEM, n ≥ 3 experiments per ISO concentration). D, 24 hour myocyte hypertrophy responses are less sensitive to ISO (median ± standard error of median, n > 250 cells per ISO concentration).

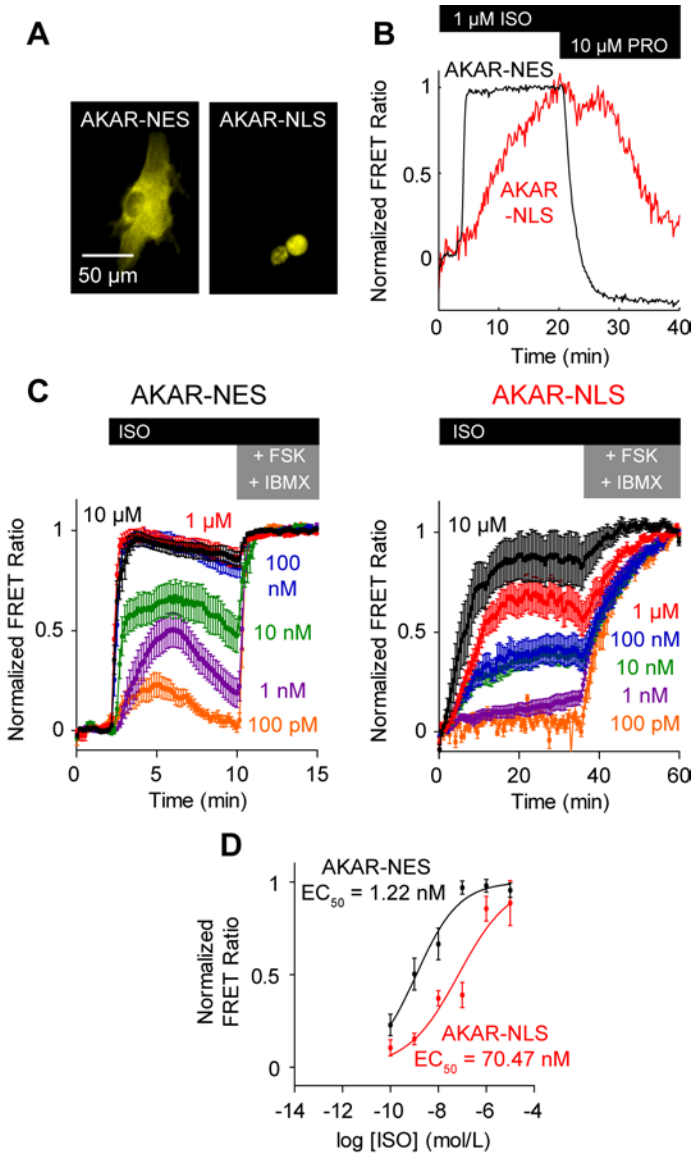

Figure 7.2 Cytosolic PKA and nuclear PKA differ in dynamics and ISO sensitivity. A, Representative expression of cytosolic AKAR-NES and nuclear AKAR-NLS FRET reporters. B, Representative responses to 1 µM ISO and 10 µM PRO. Nuclear PKA activity is slower than cytosolic PKA activity. C, Averaged AKAR-NES and AKAR-NLS responses to ISO stimulation, normalized to 50 µM FSK / 100 µM IBMX (mean ± SEM, n ≥ 9 cells each). D, Cytosolic PKA activity exhibits a higher ISO sensitivity than nuclear PKA activity.

sensitized to ISO over nuclear PKA activity (EC_{50} = 70.47 nM) (Figures 7.2C and 7.2D). The cytosolic AKAR-NES EC_{50} was similar to untargeted AKAR EC_{50} reported by others[290], providing support that published reports of PKA dynamics using these FRET reporters are specifically representative of cytosolic PKA activity. These differences in cytosolic and nuclear PKA sensitivity were surprising since differential regulation of PKA substrate phosphorylation is thought to be, in part, by A-kinase anchoring proteins (AKAPs), which may directly localize PKA substrates to PKA holoenzyme[51]. However, no endogenous AKAPs are expected to have affinity for recombinant AKAR-NES or AKAR-NLS.

Nuclear PKA Compartmentation is Not Explained by cAMP Compartmentation

cAMP compartmentation (*e.g.*, by phosphodiesterases) is also thought to regulate spatially heterogeneous PKA activity. We tested if cAMP compartmentation may explain the observed differences in cytosolic and nuclear PKA dynamics by treating myocytes with 50 μM forskolin (FSK), an adenylyl cyclase activator, and 100 μM 3-isobutyl-1-methylxanthine (IBMX), a non-selective phosphodiesterase inhibitor. In myocytes expressing cAMP-specific FRET reporters targeted to both the cytosol (ICUE-NES) and nucleus (ICUE-NLS), FSK/IBMX induced a rapid and robust cAMP response (cytosol: t_{50} = 1.62 ± 0.13 min; nucleus: t_{50} = 0.77 ± 0.05 min; mean ± SEM, n = 12 cells each) (Figures 7.3A and 7.3C). In contrast, FSK/IBMX induced a rapid PKA response in the cytosol (t_{50} = 0.59 ± 0.02 min; n = 9 cells), but not in the nucleus (t_{50} = 7.15 ± 0.70 min; n = 11 cells) (Figures 7.3B, 7.3C). These suggest the differences in cytosolic and nuclear PKA dynamics are not explained by rate-limiting cAMP compartmentation.

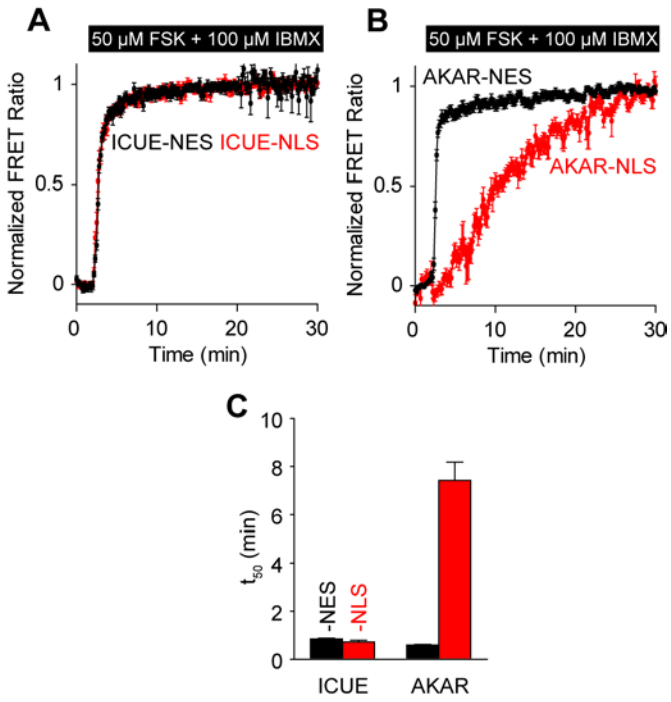

Figure 7.3 Nuclear PKA dynamics are not explained by cAMP compartmentation. A, Mean cytosolic ICUE-NES (mean ± SEM, n = 12 cells) and nuclear ICUE-NLS (n = 12 cells) responses to 50 μM FSK / 100 μM IBMX. B, Mean cytosolic AKAR-NES (n = 9 cells) and nuclear AKAR-NLS (n = 11 cells) responses to 50 μM FSK / 100 μM IBMX. C, cAMP accumulation occurs rapidly in both the cytosol and nucleus, while PKA activation occurs rapidly in the cytosol only. These suggest nuclear PKA activity is not rate-limited by nuclear cAMP accumulation.

A Computational Model for Nuclear PKA Activity

Computational models have contributed significantly to the investigation of cardiac signaling networks[211]. We have previously modeled the β_1-adrenergic signaling pathway[5] and its actions on cytosolic rat[6] and mouse myocyte physiology. Here, we extended these models with a nuclear compartment to generate hypotheses for explaining the observed PKA activity compartmentation (Figure 7.4A; *Appendix D*). In this new model, activated PKA catalytic subunit passively diffuses across the nuclear envelope via nuclear pore complexes[255], where it may phosphorylate and activate cAMP response element binding protein (CREB)[291]. In turn, phospho-CREB is dephosphorylated by protein phosphatase 2A (PP2A)[292]. Protein kinase inhibitor (PKI) inhibits this process by binding and inactivating free PKA catalytic subunit (C)[293]. PKI may also diffuse across the nuclear envelope and inactivate nuclear PKA catalytic subunits, upon which a nuclear export signal (NES) is exposed and PKA catalytic subunit is shuttled from the nucleus to the cytosol in an ATP-dependent manner. In addition, we modeled the expression of AKAR-NES and AKAR-NLS as in previous studies[4]. When fitted to the experimental data, simulated AKAR responses to ISO were similar to measured AKAR in both dynamics responses (Figure 7.4B) and ISO sensitivity (Figure 7.4C).

Nuclear PKA Activity Dynamics are Rate-Limited by PKA Catalytic Subunit Diffusion

PKA catalytic subunit is a 38 kDa protein, while cAMP is a small molecule with a molar mass of 329.2. Empirically, nuclear pore complexes have been shown to have a cargo threshold of ~40 kDa[294]. We therefore hypothesized that nuclear PKA activation may be rate-limited by PKA catalytic subunit diffusion rather than cAMP diffusion, consistent

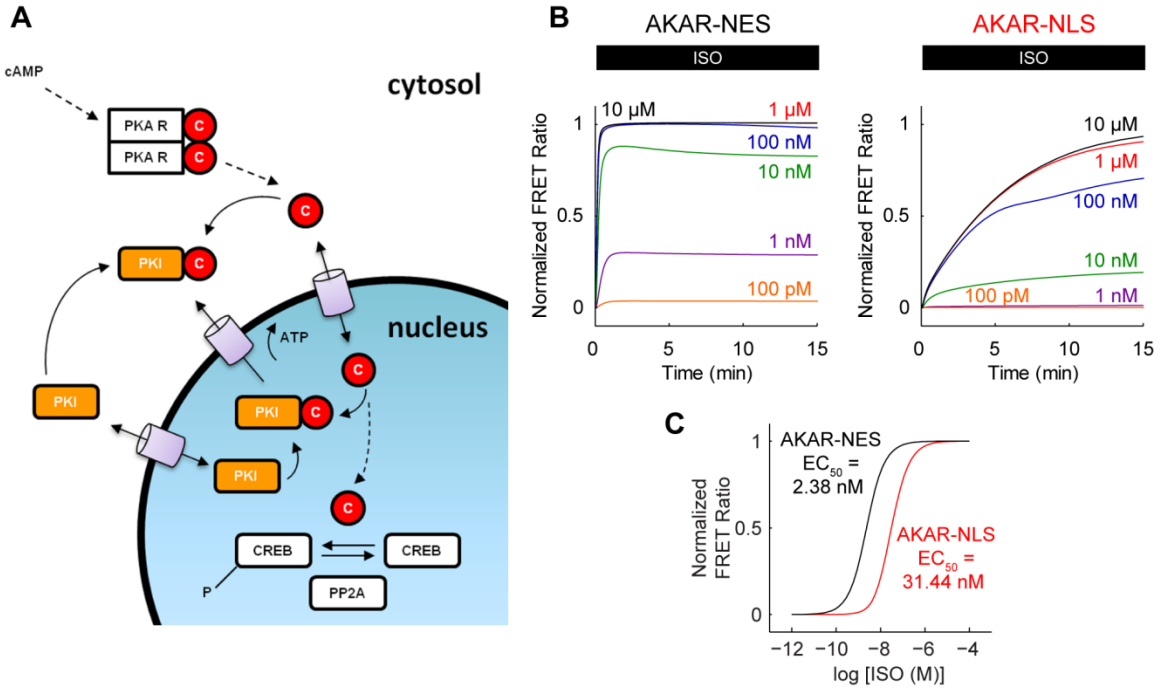

Figure 7.4 A computational model for PKA compartmention in cardiac myocytes. A, Schematic for nuclear PKA compartment extension to our previously published β-adrenergic signaling models. B, Model-predicted AKAR-NES and AKAR-NLS responses to ISO stimulation. C, Model-predicted AKAR-NES and AKAR-NLS ISO sensitivities. Model responses are qualitatively similar to experimentally measured differences in dynamics and ISO sensitivity.

with observations that nuclear PKA accumulation is slow following cytosolic catalytic subunit microinjection[255]. Using the model, we simulated the role of changes to passive nuclear transport in shaping ISO-stimulated nuclear PKA dynamics. Model simulations predicted a step-wise decrease in the rate and steady-state magnitude of nuclear PKA activity, suggesting PKA catalytic subunit diffusion plays a key role in rate-limiting nuclear PKA dynamics (Figure 7.6A). Reducing nuclear transport in the model to 5% nearly ablated the simulated AKAR-NLS response to 1 μM ISO. We tested this model prediction experimentally by pre-incubating myocytes expressing AKAR-NLS with 20 μg/mL wheat germ agglutinin (WGA), which directly inhibits nuclear transport by binding nuclear pores[295], for 30 min. We then applied 1 μM ISO and measured the AKAR-NLS response. Consistent with model predictions, myocytes pre-incubated with WGA displayed a significantly attenuated AKAR-NLS response (Figure 7.6B; n = 22 cells). These support a hypothesis that nuclear PKA activity in cardiac myocytes is regulated, not by cAMP compartmentation, but direct compartmentation of the PKA catalytic subunit.

Biased PKIα Expression Underlies Differential ISO Sensitivity

Our finding that nuclear PKA sensitivity to ISO was significantly smaller than cytosolic PKA sensitivity (Figure 7.2D) suggests the nucleus may comprise a PKA signaling microdomain independent of the cytosol. In forming the computational model, we reasoned this shift in sensitivity was due either to the presence of a novel nuclear competitive inhibitor or expression of a PKA inhibitor biased towards the nucleus. Protein kinase inhibitor (PKI) is one such endogenous competitive inhibitor of PKA[293],

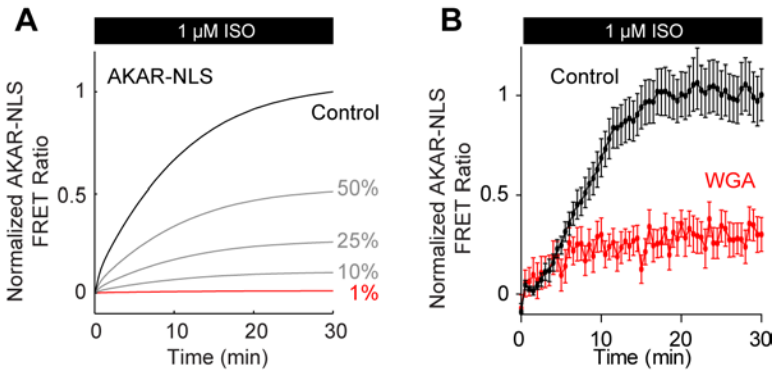

Figure 7.5 Nuclear PKA activity is rate-limited by slow diffusion. A, Model-predicted AKAR-NLS responses to 1 μM ISO stimulation. Increasing the nuclear pore complex diffusion barrier by restricting the diffusion rate shrinks the rate and magnitude of AKAR-NLS phosphorylation. B, Experimental validation for model prediction. Mean AKAR-NLS responses to 1 μM ISO stimulation following 30 min pre-incubation with 20 μg/mL WGA (mean ± SEM, n = 22 cells).

which we have previously predicted to be capable of conferring ultra-sensitive cytosolic PKA activation by cAMP[5]. Indeed, when nuclear PKI concentrations were constrained to be equal to cytosolic PKI concentrations, the model predicted a loss of differential ISO sensitivity between cytosolic and nuclear PKA (Figure 7.6A). We tested this model prediction by immunolabeling fixed myocytes with anti-PKIα antibodies and surprisingly found nearly exclusive nuclear PKIα expression (Figure 7.6B). These results suggest the nuclear bias in PKIα expression may be an important component of limiting nuclear PKA sensitivity to β-adrenergic stimulation.

PKA Compartmentation Differentially Phosphorylates Endogenous PKA Substrates

Because cytosolic and nuclear PKA activity exhibited similar differences in ISO sensitivity in both our FRET experiments and computational model, we hypothesized the functional differences in ISO sensitivity of β-AR-stimulated Ca^{2+} enhancements and hypertrophy may be explained by nuclear PKA compartmentation. We first modeled the phosphorylation of endogenous PKA substrates relevant to Ca^{2+} enhancement (PLB, phospholamban) and hypertrophy (CREB, cAMP response element binding protein). The model predicted a rightward shift in CREB ISO sensitivity over PLB (Figure 7.7A). Consistent with our expectations, the ISO sensitivity for PLB (EC_{50} = 4.95 nM) and CREB (EC_{50} = 31.46 nM) phosphorylation paralleled the ISO sensitivities for cytosolic and nuclear PKA measured by AKAR-NES and AKAR-NLS. We validated this model prediction by Western blotting steady-state PLB and CREB phosphorylation over a large range of ISO concentrations (Figures 7B and 7C; PLBp EC_{50} = 0.58 nM; CREBp EC_{50} = 52.68 nM; n = 3 experiments each). These results suggest PKA catalytic subunit

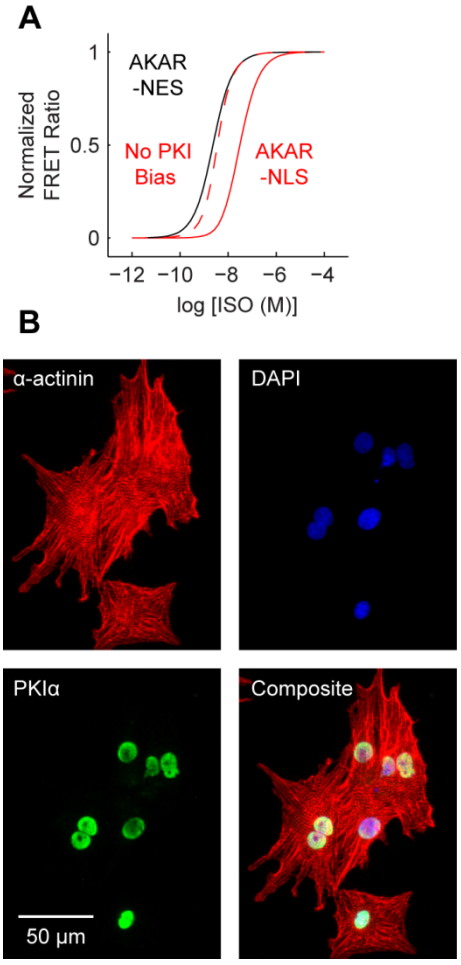

Figure 7.6 Nuclear PKA sensitivity to ISO is regulated by biased PKIα expression. A, Model prediction for nuclear PKA ISO sensitivity with PKI bias eliminated (dashed red). B, Immunofluorescence labeling with anti-PKIα antibodies identify nearly exclusive PKIα expression, consistent with model prediction for PKI expression biased to the nucleus.

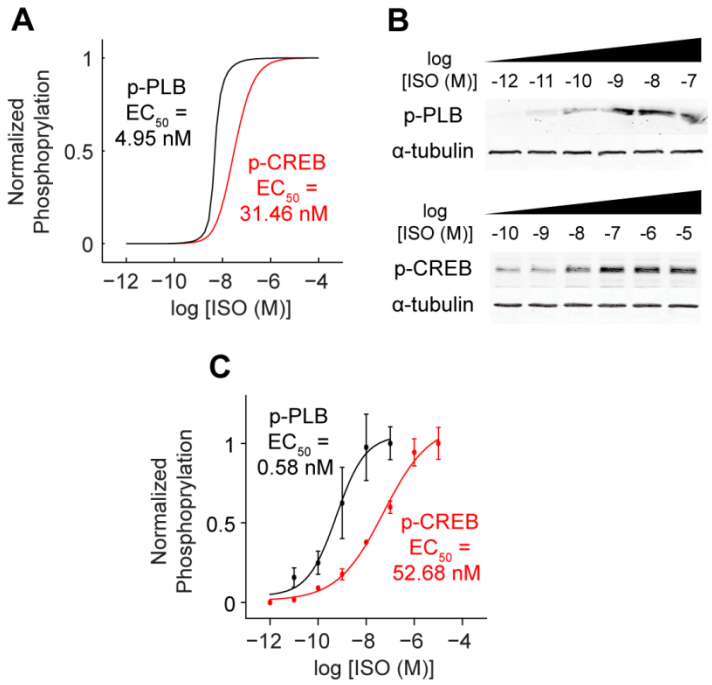

Figure 7.7 PKA compartmentation underlies PKA substrate phosphorylation. A, Model prediction for phosphorylated PLB and CREB sensitivity to ISO. PLBp and CREBp EC_{50}s parallel cytosolic and nuclear PKA EC_{50}s, respectively. B, Representative Western blot validations for model predictions. C, PLB phosphorylation is significantly more sensitive to ISO than CREB phosphorylation (mean ± SEM, n = 3 experiments each).

compartmentation may be functionally relevant for specifically selecting different β-adrenergic signaling responses to ISO.

PKA Compartmentation Differentially Elicits Contractile and Hypertrophic Responses

We further tested the specific consequences of cytosolic and nuclear PKA catalytic subunit compartmentation by over-expressing mCherry-labeled PKA catalytic subunit targeted to either the cytosol (PKA-NES) or nucleus (PKA-NLS) (Figure 7.8A). Western blot anaylsis demonstrated that PKA-NES expressing myocytes specifically had increased cytosolic PLB phosphorylation over mCherry over-expression alone, while PKA-NLS expressing myocytes did not (Figure 7.8B). Conversely, both PKA-NLS and PKA-NES exhibited increased CREB phosphorylation. These indicated both targeted PKA constructs were localized correctly and catalytically active.

We functionally assessed the effect of targeted PKA over-expression by quantifying Ca^{2+} responses to 1 μM ISO and enhancements to cell size following targeted PKA over-expression. Pacing these myocytes at 1 Hz, we observer larger baseline Ca^{2+} transients in PKA-NES myocytes over either mCherry or PKA-NLS myocytes (Figures 7.8C and 7.8D). These were complemented by ablated sensitivity to 1 μM ISO addition (Figure 7.8E), suggesting PKA-NES over-expression was saturating the phosphorylation of contractility-relevant PKA substrates, while PKA-NLS over-expression had no effect on these targets. In contrast, PKA-NLS myocytes were hypertrophied (1401 ± 38 μm^2; median ± standard error of median, n = 1324 cells) over both mCherry (1213 ± 37 μm^2; n = 944 cells) and mCherry-PKA-NES myocytes (1291 ± 44 μm^2; n = 945 cells) (Figure

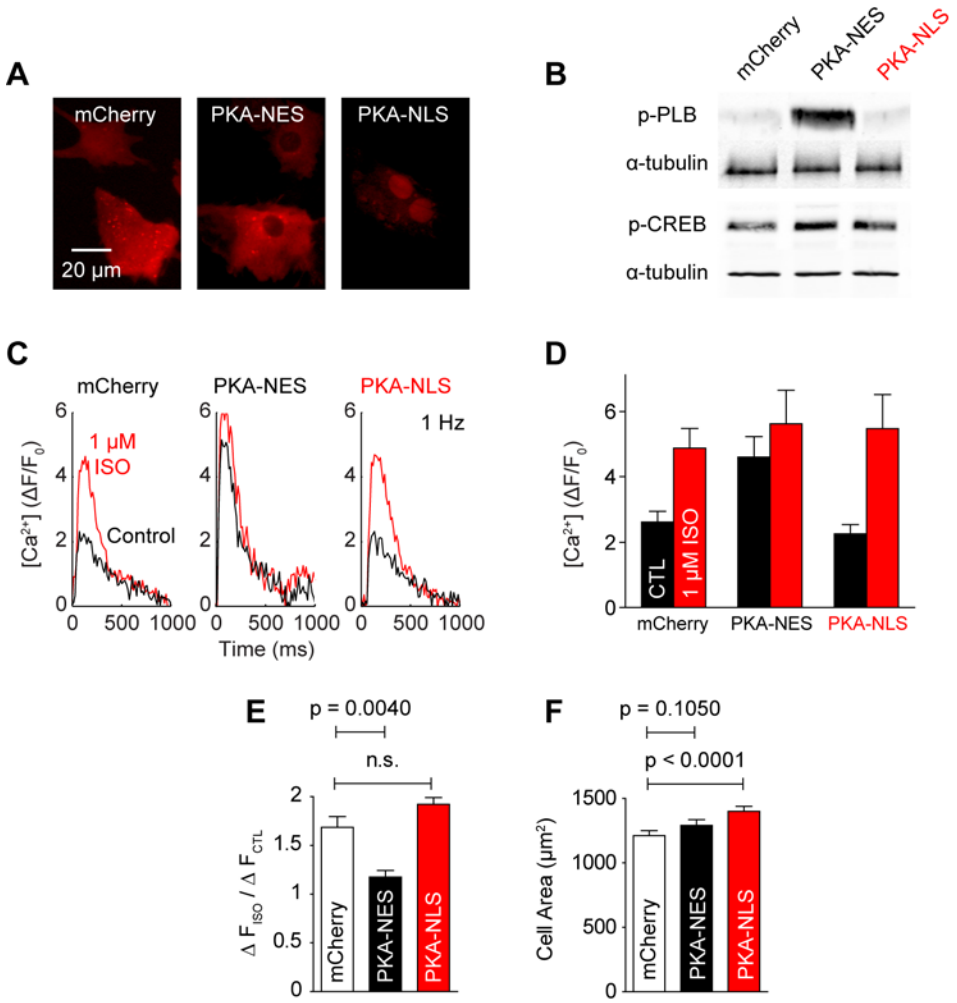

Figure 7.8 PKA compartmentation underlies selection of contractile and cell hypertrophic β-adrenergic signaling responses. A, Expression of mCherry, PKA-NES and PKA-NLS plasmids. B, Western blots for PLB and CREB phosphorylation by PKA-NES and PKA-NLS. Both plasmids are catalytically active and capable of phosphorylating PKA substrates over mCherry control. C, Representative Fluo-4 Ca^{2+} responses to 1 µM ISO for expressing cells under 1 Hz pacing. D, Mean Fluo-4 Ca^{2+} transients before and after stimulation by 1 µM ISO (mean ± SEM, n ≥ 3 experiments each). Baseline (Control: CTL) Fluo-4 Ca^{2+} transients are nearly saturated in PKA-NES myocytes. E, Mean enhancements to Fluo-4 Ca^{2+} transients by 1 µM ISO stimulation. 1 µM ISO elicits robust enhancements to mCherry and PKA-NLS myocytes, but not PKA-NES myocytes (mean ± SEM, n > 3 experiments each). F, Median cell size measurements in expressing cells. PKA-NLS induces hypertrophic growth to cell area, while PKA-NES does not (median ± standard error of median, n > 900 cells each).

7.8F). Together, these indicate a specific role for cytosolic PKA in enhancing contractile behaviors under β-adrenergic signaling and a specific role for nuclear PKA in enhancing hypertrophic behaviors, supporting the hypothesis that compartmented signaling in these two microdomains were functionally relevant to regulating the overall β-adrenergic signaling response.

7.5 Discussion

Compartmentation in β-Adrenergic Signaling

Over the last two decades, numerous studies have investigated mechanisms regulating spatiotemporal heterogeneity in cardiac β-adrenergic signaling[45]. While some have focused on receptor organization[47,52-53], receptor subtype[296-297] or PKA regulatory subunit subtype[298], PDEs[48-49,299] and AKAPs[50-51,54,300] have prominently risen as key regulatory mechanisms of compartmented β-adrenergic signaling. The underlying hypothesis of these studies is that β-adrenergic signaling responses are managed by phosphorylation of PKA substrates local to PKA holoenzyme (for instance, localized by AKAPs), which become activated by spatially heterogeneous cAMP gradients (restricted by spatially heterogeneous adenylyl cyclase and PDE activity).

We have previously shown that nuclear PKA dynamics may be explained by nuclear PDE4D-PKA-AKAP complexes, as inferred in HEK 293 cells[301]. However, the most convincing evidence that nuclear PKA activity was rate-limited by cAMP diffusion in those studies were observations that nuclear PKA dynamics were accelerated under PDE inhibition by IBMX and AKAP disruption by Ht31. Here, we observe slow nuclear PKA

activity despite rapid nuclear cAMP accumulation in the presence of IBMX (Figure 7.3). Together, these results support a simpler model for cardiac myocytes where nuclear PKA activity is rate-limited by slow diffusion of PKA catalytic subunit[255]. Interestingly, we show that distal (nuclear) PKA phosphorylation events are not only slower in dynamics than local (cytosolic) PKA phosphorylation events, but also significantly less sensitive to β-adrenergic receptor stimulation (Figure 7.2). Our modeling and immunofluorescence studies suggest these differences in sensitivity are explained by spatially heterogeneous PKI expression, which limits PKA activity similar to how PDEs limit cAMP activity. As there are few published reports on the significance of PKI in the heart, further study will be necessary to evaluate how PKA catalytic subunit compartmentation may be regulated.

Relevance to Cardiac Physiology and Disease

In this chapter we demonstrate that PKA catalytic subunit compartmentation is functionally significant, as indicated by the targeted over-expression data. These results are important in two ways. First, the differences in cytosolic and nuclear PKA sensitivity to ISO suggest PKI-mediated compartmentation may serve to insulate myocytes from inducing hypertrophic growth whenever β-adrenergic receptors are engaged to enhance contractility. This itself has therapeutic implications since treatment with β-blockers are effective for attenuating cardiac remodeling during heart failure, but also put patients at risk for bradycardia and low blood pressure[21,85]. If chronotropic and inotropic responses can be separated from hypertrophic responses by cytosolic-nuclear compartmentation, these results suggest nuclear PKA activity inhibition may be a more attractive gene

therapy target than enhancements to excitation-contraction coupling or antagonism to β-adrenergic signaling alone[302].

Second, we show nuclear PKA activity is an order of magnitude slower than cytosolic PKA activity. These results add a second layer of insulation to PKA-stimulated transcriptional activity: the requirement for sustained β-adrenergic receptor stimulation. These suggest that while contractile responses may be activated by small and acute sympathetic activity, hypertrophic responses associated with pathologic cardiac remodeling may require large and chronic sympathetic activity. These could in part explain how daily engagement of the *fight-or-flight* response does not drive the heart toward a failing phenotype, while chronically elevated sympathetic activity may lock the heart in a vicious deteriorating cycle[35]. Indeed, while further *in vivo* studies will be necessary to confirm these preliminary *in vitro* findings, the current work proposes PKA catalytic subunit compartmentation may contribute to the bifurcation between physiologic β-adrenergic signaling engagement and pathologic β-adrenergic signaling-driven remodeling.

β-Adrenergic Signaling-Stimulated Hypertrophy

While it is well-recognized that β-adrenergic stimulation by ISO is sufficient for stimulating cardiac hypertrophy[303], the exact mechanisms for these observations remain unclear. Transgenic over-expression studies indicate that activity by β_1-AR[30], $G_{s\alpha}$[31] or PKA[32] are all sufficient for inducing hypertrophy and heart failure *in vivo*. However, the complexities of cardiac hypertrophy signaling networks[64,304] convolute understanding. For instance, a number of studies have now shown that β-adrenergic signaling may

stimulate hypertrophy in a PKA-independent manner via cAMP activation of Epac[305-307]. Moreover, because β-adrenergic stimulation enhances Ca^{2+} signaling, PKA-mediated hypertrophy may be managed by enhanced CaMKII[308-309] or calcineurin/NFAT[310-311] signaling. Additionally, some evidence suggests PKA activation may inhibit hypertrophy via histone deacetylase 5 (HDAC5) phosphorylation[312] or HDAC4 proteolysis[313]. Indeed, future work will need to clarify the direct role of PKA in cardiac hypertrophy.

In this chapter, we specifically over-expressed PKA catalytic subunit in the cytosol and nucleus, indicating a sufficient role for nuclear, but not cytosolic, PKA to stimulate myocyte hypertrophy (Figure 7.8). These results are not mutually exclusive with findings from others, but support a hypothesis that catecholamine-stimulated hypertrophy is driven by a direct action of PKA on nuclear transcription factors, rather than network cross-talk via Ca^{2+} or Epac. These data imply a model where chronic β-adrenergic stimulation can stimulate PKA catalytic subunit to escape local control by PDE or AKAP compartmentation mechanisms and distally initiate cardiac remodeling events.

Limitations and Considerations

In this chapter, we have taken a multi-disciplinary approach to investigating PKA catalytic subunit compartmentation, integrating live-cell imaging experiments from neonatal rat ventricular myocytes with computational modeling. While seminal studies in cardiac β-adrenergic compartmentation were performed using neonatal rat myocytes[4,298,314-318], care must be taken in inferring the role of this PKA catalytic subunit compartmentation in human heart failure. Moreover, we have chosen myocyte cell

hypertrophy as an approximation for ventricular hypertrophy in the intact heart. While these *in vitro* findings alone do not prove that nuclear PKA activity critically drives pathologic cardiac hypertrophy in heart failure, these results do support the hypothesis that PKA activity in the cytosol and nucleus exerts different cardiac behaviors. Indeed, these findings will be strengthened by future *in vivo* studies investigating the consequences of nuclear PKA compartmentation on the heart as an organ.

Moreover, while we chose CREB as a representative endogenous PKA-sensitive transcription factor, these results do not clearly implicate CREB as the mechanistic link between nuclear PKA activity and myocyte hypertrophy. The role of CREB in regulating cardiac hypertrophy is controversial. While there is some evidence that PKA-dependent hypertrophy may be managed by CREB phosphorylation[319-321], other studies suggest CREB is not critical for cardiac function[322] and have shown that transgenic inhibition of CREB phosphorylation is also sufficient for driving hypertrophy and heart failure[320]. Moreover, the observation that cytosolic PKA over-expression is capable of evoking significant CREB phosphorylation was a surprising result. We reason that this may be due to volume differences between the nucleus and cytosol, where total cytosolic PKA over-expression may be larger than total nuclear PKA over-expression. However, the appropriate subcellular localization of our targeted PKA over-expression, coupled with the enhancement in PLB phosphorylation by cytosolic PKA over-expression and enhancement in CREB phosphorylation by nuclear PKA over-expression, together indicated that both targeted PKA constructs were enzymatically functional. We therefore reasoned that the phenotypic differences between cytosolic and nuclear PKA over-

expression were direct consequences of targeted nuclear over-expression, and not some other mechanism. New studies will be necessary to clarify the mechanistic link between nuclear PKA activity and myocyte hypertrophy.

In addition, while quantifying cell area under ISO-stimulated and PKA over-expression conditions, we observed significant cell-cell variability (Figures 7.9A and 7.9B). In the present work, the automated image acquisition and image segmentation cell hypertrophy assay permitted high-throughput quantification with greater than 100 cells measured per condition. We found that cell-cell variability was greater with experimental repeats than across experimental repeats, prompting us to pool single cell measurements rather than average across repeats. Because cell area measurements were distributed non-Gaussian, we reported median ± standard error and performed non-parametric Mann-Whitney tests for statistical significance.

Finally, carefully constrained computational models can provide significant insight into the mechanics of cell signaling and provide inspiration for new experimental studies[211]. However, interpretation of modeling results requires careful attention. Here, we carefully assembled and validated our model from published biochemical data and used the model as a hypothesis-generating inference tool to investigate mechanisms underlying PKA catalytic subunit compartmentation. We minimized bias in these simulations by first making prospective modeling predictions and then following with subsequent experimental validations. By performing our study under these standards, we built confidence that the computational model was an adequate description of the biology in

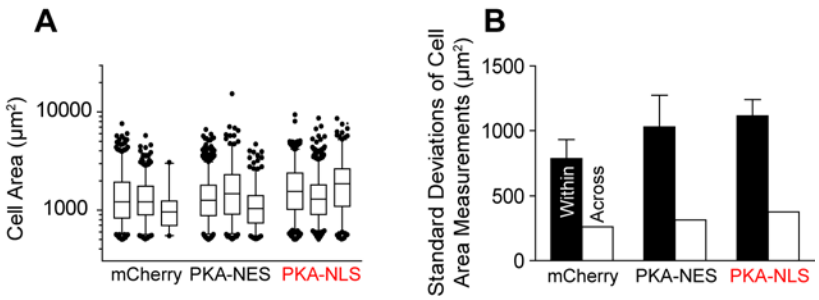

Figure 7.9 Cell area measurement variability. A, Cell area measurements for cardiac myocytes over-expressing mCherry, PKA-NES or PKA-NLS (3 experiments each). Expressing cells contained greater variability within individual experiments than across multiple experiments. B, Quantification of cell area variability within and across experimental repeats (taken as standard deviation of mean measurements).

our experiments and that the model predictions were reasonable hypotheses for compartmentation signaling mechanisms.

7.6 Conclusion

In this chapter, we have provided direct evidence that PKA catalytic subunit can itself form functionally relevant, diffusion-limited signaling compartments. We show PKA activity in the nucleus is slower and less sensitivity to extracellular β-adrenergic receptor agonists than cytosolic PKA activity. These differences in signaling sensitivity are prescribed by biased nuclear PKI expression. Moreover, cytosolic PKA activity directly enhances Ca^{2+} transients, but has no effect on myocyte hypertrophy. Conversely, nuclear PKA activity directly induces myocyte hypertrophy, but has no effect on Ca^{2+} transients. Together, these findings suggest PKA catalytic subunit compartmentation may help explain how chronic, but not acute, β-adrenergic stimulation may initiate cardiac remodeling events and drive the progression of heart failure.

Chapter 8

Dissertation Conclusions

8.1 Contributions and Conclusions

The overall goal of this dissertation was to investigate how the β-adrenergic signaling network differentially regulates contractile and hypertrophic responses to β-AR stimulation. We hypothesized that two key network properties were important for managing these responses: *incoherent feed-forward signaling* and *PKA catalytic subunit compartmentation*. In testing this hypothesis and achieving this goal, we have

i.) developed novel biochemically mechanistic computational models of β-adrenergic and Angiotensin II signaling in cardiac myocytes

ii.) identified an incoherent feed-forward loop which accelerates and generates adaptation in β-AR-stimulated contractility

iii.) characterized PKA catalytic subunit compartmentation as a novel form of β-adrenergic signaling compartmentation

iv.) demonstrated nuclear PKA activity may directly regulate hypertrophy of the cardiac myocyte

In Chapters 4 and 5 (**Aim 1**), we described the development of computational models for β-adrenergic receptor-stimulated contractility and Angiotensin II receptor-stimulated fibrosis. Using these models, we provide strong evidence that incoherent feed-forward signaling regulates the dynamics of short-term cardiac contractility and long-term cardiac fibrosis. Collectively, we identify important roles played by network topology in managing cardiac cell signaling responses.

In Chapters 6 and 7 (**Aim 2**), we described the application of β-adrenergic signaling models to live cell imaging experiments for investigating the regulation and function of nuclear PKA compartmentation. Using these models as inference tools, we generated many model-driven hypotheses, which we validated experimentally, identifying a nuclear PKA-PDE-AKAP signaling complex in HEK 293 cells and discovering PKA catalytic subunit compartmentation is sufficient for selectively regulating cytosolic vs. hypertrophic β-adrenergic signaling responses. Together, these results identify a novel form of β-adrenergic signaling compartmentation which may be functionally relevant for the development of cardiac hypertrophy.

In conclusion, our data shows that both incoherent feed-forward signaling and PKA compartmentation are important regulators of β-adrenergic signaling responses. These mechanisms not only control the kinetics of cardiac contractility and hypertrophy, but also aid in creating specificity for eliciting different signaling responses under varying environmental conditions.

8.2 Translational Relevance

Current therapeutic options for treating cardiovascular disease largely rely on small molecule pharmaceutics, whose effectiveness can be limited by hereditary factors. Over the past decade, gene therapy strategies have emerged as promising alternatives to small molecule pharmaceutics for addressing these pharmacogenomic challenges in cardiovascular disease[302,323-325]. Effective cardiovascular gene therapy requires cardiovascular-specific gene transduction and long-term transgene expression[326]. In

particular, AAV vectors have risen as a front-runner in cardiac gene delivery[324,327]. The major advantages of AAVs are their reduced immunogenicity, long-term transgene expression and organ specificities. Of the over 75 clinical trials involving AAVs, only three are targeted at cardiovascular diseases[328-330].

These three studies have focused on rescuing contractility in the failing heart by delivering the sarcoplasmic reticulum calcium ATPase (SERCA2a) gene[329,331-332]. Preliminary reports from Phase I demonstrated a 52% risk-reduction in cardiovascular related clinical events, supporting Phase II trials[332-333]. These too have indicated a resounding success, demonstrating safety and efficacious benefit over 12 months[334], providing support for larger, confirmatory trials[302,330]. The success from these preliminary studies gives promise to the clinical viability of AAV-mediated therapeutics for treating human cardiac diseases.

Our work here suggests targeting PKA catalytic subunit compartmentation may be one novel strategy for blocking β-adrenergic signaling-stimulated remodeling, while retaining contractile responsiveness. In this chapter, we have shown that this compartmentation is endogenously regulated by PKI, indicating cardiac-specific PKIα over-expression may be an ideal gene therapy strategy. While many more studies are necessary to investigate the specific *in vivo* role of PKIα in regulating nuclear PKA-stimulated behaviors, our results suggest signaling compartmentation may itself be an innovative therapeutic target for specifically eliciting some behaviors (but not all) of β-adrenergic signaling for intervening in the progression of cardiac disease.

8.3 Future Directions

Collectively, our results motivate three exciting research directions for follow-up studies:

i.) *in vivo* characterization of nuclear PKA compartmentation in cardiac physiology and pathophysiology

ii.) *in vitro* characterization of PKI-mediated PKA compartmentation

iii.) *in vivo* characterization of PKI-based gene therapy interventions in cardiac disease models

Here, we provide direct evidence supporting the hypothesis that β-adrenergic signaling may stimulate cardiac hypertrophy via nuclear PKA-mediate phosphorylation of transcriptional regulators, *in vitro*. Our observations that cytosolic PKA over-expression is insufficient to stimulate a hypertrophic response suggest remodeling events observed in the PKA over-expression mouse[32] may be specifically explained by elevated nuclear PKA activity. This hypothesis may be directly tested in a follow-up study by over-expressing cytosolic PKA and nuclear PKA in parallel mouse cohorts using an established method for robust cardiomyocyte-specific gene delivery with the AAV9 vector and under the cardiac troponin T promoter[287]. Quantifying hemodynamic and histological parameters of these transgenic mice will elucidate whether or not nuclear PKA activity may in fact specifically contribute to *in vivo* remodeling. These studies may be complemented by quantifying histological sections of healthy and failing hearts labeled with PKA catalytic subunit-specific antibodies to determine if nuclear PKA activity is elevated during cardiac disease.

Second, preliminary data from these studies indicate the three PKI isoforms (α, β and γ) have very different expression patterns in the cardiac myocyte (Figure 8.1). Though observations of PKI-mediated inhibition of PKA were first published in the 1960s[335-336], to date there are relatively few published studies of PKI's regulation of PKA. Here, we have used a computational model to explain how PKI may have an important role in functionally restricting PKA catalytic subunit activity in an analogous way to how PDEs restrict cAMP activity. Because these three PKI isoforms also have different affinities for PKA catalytic subunit[293], the spatially heterogeneous expression of these PKI isoforms raises interesting questions on how they may compartment PKA activity. Future *in vitro* studies will be necessary to more fully characterize the role of PKI in prescribing PKA catalytic subunit compartmentation and the physiological consequences of such compartmentation. This is a completely unexplored dimension to β-adrenergic signaling compartmentation and is ripe for investigation.

Finally, PKI-mediated interventions may be tested by over-expressing PKIα in various heart failure models (*e.g.*, transverse aortic constriction, coronary artery ligation) using similar gene delivery vehicles. Quantifying hemodynamic and histological parameters of these mice will indicate if nuclear PKA inhibition can attenuate or rescue the heart failure phenotype. Conversely, because our immunofluorescence data indicates endogenous PKIα is almost exclusively nuclear (Figure 8.1), over-expressing cardiomyocyte-specific PKIα siRNA in healthy mice will show if enhancement of nuclear PKA activity (by release of nuclear PKA inhibition) is sufficient for inducing cardiac hypertrophy and remodeling *in vivo*.

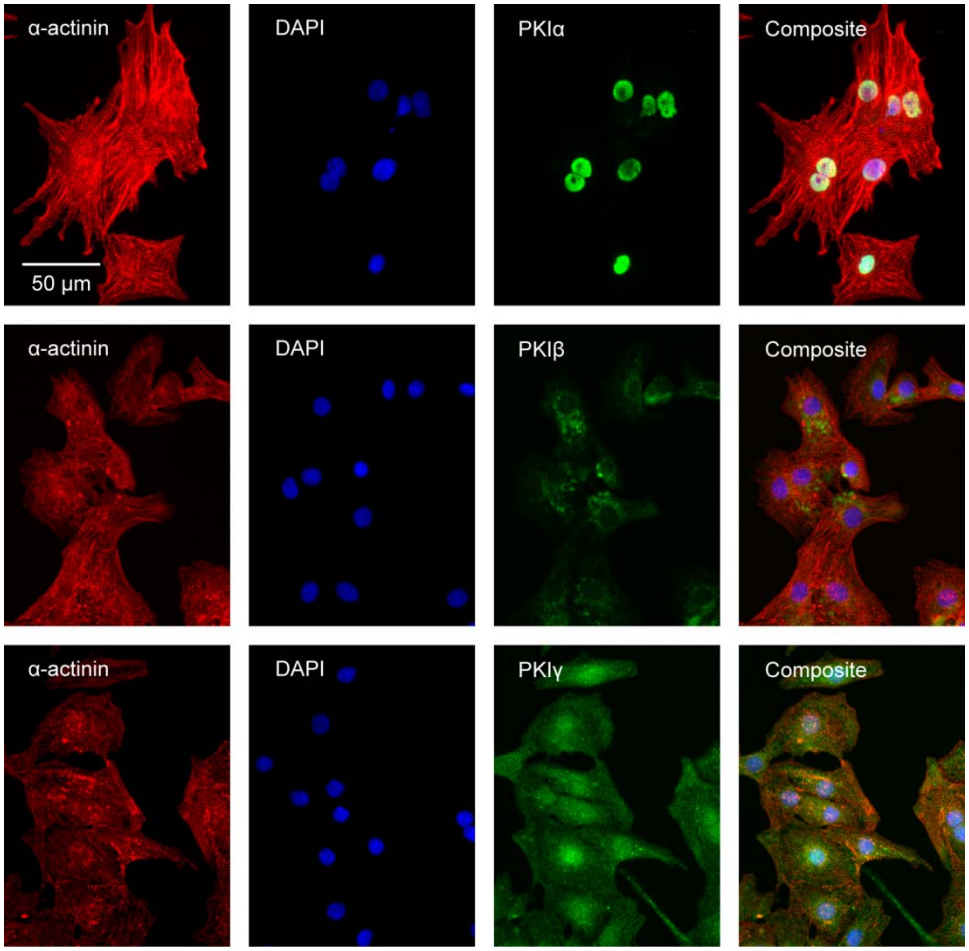

Figure 8.1 PKI isoforms express differentially in the neonatal rat ventricular myocyte. PKIα has a preferentially nuclear expression, while PKIβ has a preferentially peri-nuclear expression. PKIγ has a ubiquitous cytosolic and nuclear expression. These differences in PKI expression patterns may help PKI establish PKA catalytic subunit compartmentation.

Appendix A

Integrated Mouse β-Adrenergic Signaling / Excitation-Contraction Coupling Model

β_1-Adrenergic Signaling

β-Adrenergic Receptor / Gsα

Parameter	Description	Value	Units	Source
ISO	isoproterenol concentration (when used)	1	µM	-
b1ARtot	total β1-adrenergic receptors	0.00528	µM	adapted
Gstot	total Gs protein	3.83	µM	[5]
kf_LR	β1-AR binding to ligand	1	1/[µM ms]	[5-6]
kr_LR	β1-AR binding to ligand	0.285	1/ms	[5-6]
kf_LRG	ligand bound β1-AR associating with G-protein	1	1/[µM ms]	[5-6]
kr_LRG	ligand bound β1-AR associating with G-protein	0.062	1/ms	[5-6]
kf_RG	unbound β1-AR associating with G-protein	1	1/[µM ms]	[5-6]
kr_RG	unbound β1-AR associating with G-protein	33.0	1/ms	[5-6]
k_G_act	Gs-alpha activation	16.0e-3	1/ms	[5-6]
k_G_hyd	Gs-alpha hydrolysis	0.8e-6	1/ms	[5-6]
k_G_reassoc	Gs-alpha reassociation	1.21	1/[µM ms]	[5-6]
kf_bark	β1-AR desensitization by β-arrestin	1.1e-6	1/ms	[5-6]
kr_bark	β1-AR resensitization	2.2e-6	1/ms	[5-6]
kf_pka	β1-AR desensitization by PKA	3.6e-6	1/[µM ms]	[5-6]
kr_pka	β1-AR resensitization	2.2e-6	1/ms	[6]

$$b1ARact = b1ARtot - b1AR\_S464 - b1AR\_S301$$

$$b1AR = b1ARact - LR - LRG - RG$$

$$Gs = Gstot - LRG - RG - Gsby$$

$$\frac{dLR}{dt} = kf\_LR \cdot ISO \cdot b1AR - kr\_LR \cdot LR$$

$$\frac{dLRG}{dt} = kf\_LRG \cdot LR \cdot Gs - kr\_LRG \cdot LRG - k\_G\_act \cdot LRG$$

$$\frac{dRG}{dt} = kf\_RG \cdot b1AR \cdot Gs - kr\_RG \cdot Gs - k\_G\_act \cdot RG$$

$$\frac{db1AR\_S464}{dt} = kf\_bARK \cdot (LR + LRG) - kr\_bARK \cdot b1AR\_S464$$

$$\frac{db1AR\_S301}{dt} = kf\_PKA \cdot PKACI \cdot b1ARact - kr\_PKA \cdot b1AR\_S301$$

$$\frac{dGsaGTPtot}{dt} = k\_G\_act \cdot (RG + LRG) - k\_G\_hyd \cdot GsaGTPtot$$

$$\frac{dGsaGDP}{dt} = k\_G\_hyd \cdot GsaGTPtot - k\_G\_reassoc \cdot GsaGDP \cdot Gsby$$

$$\frac{dGsby}{dt} = k\_G\_act \cdot (RG + LRG) - k\_G\_reassoc \cdot GsaGDP \cdot Gsby$$

cAMP

Parameter	Description	Value	Units	Source
ACtot	total adenylyl cyclase	70.57e-3	µM	adapted
ATP	total ATP	5.0e3	µM	[5-6]
PDEtot	total phosphodiesterases	22.85e-3	µM	[5]
IBMX	isobutylmethylxanthine concentration	0.0	µM	[6]
FSK	forskolin concentration	0.0	µM	[6]
k_AC_basal	basal AC activity	0.2e-3	1/ms	[5-6]
Km_AC_basal	basal AC affinity for ATP	1.03e3	µM	[5-6]
k_AC_Gsa	AC activity with Gs-alpha activation	8.5e-3	1/ms	[6]
Km_AC_Gsa	AC:Gs-alpha affinity for ATP	315.0	µM	[5-6]
kf_AC_Gsa	AC activation by Gs-alpha	1	1/[µM ms]	[6]
kr_AC_Gsa	AC activation by Gs-alpha	0.4	1/ms	[6]
k_AC_FSK	AC activation by forskolin	7.3e-3	1/ms	[6]
Km_AC_FSK	AC:FSK affinity for ATP	860.0	µM	[6]
kf_AC_FSK	AC activation by forskolin	1	1/[µM ms]	[6]
kr_AC_FSK	AC activation by forskolin	44	1/ms	[6]
k_cAMP_PDE	cAMP degradation by PDEs	5.0e-3	1/ms	[6]
k_cAMP_PDEp	cAMP degradation by phosphorylated PDEs	10.0e-3	1/ms	[260]
Km_PDE_cAMP	PDE affinity for cAMP	1.3	µM	[5-6]
Kd_PDE_IBMX	PDE inhibition by IBMX	30.0	µM	[5-6]
k_PKA_PDE	PDE phosphorylation by PKA	7.5e-3	1/ms	[260]
k_PP_PDE	PDE inhibition by IBMX	1.5e-3	1/ms	[260]

$$cAMP = cAMPtot - (RCcAMP\_I + 2 \cdot RCcAMPcAMP\_I + 2 \cdot RcAMPcAMP\_I) - (RCcAMP\_II + 2 \cdot RCcAMPcAMP\_II + 2 \cdot RcAMPcAMP\_II)$$

$$AC = ACtot - AC\_GsaGTP$$

$$GsaGTP = GsaGTPtot - AC\_GsaGTP$$

$$\frac{dAC\_GsaGTP}{dt} = kf\_AC\_Gsa \cdot GsaGTP \cdot AC - kr\_AC\_Gsa \cdot AC\_GsaGTP$$

$$AC\_FSK = \frac{FSK \cdot AC}{Kd\_AC\_FSK}$$

$$PDE\_IBMX = \frac{PDEtot \cdot IBMX}{Kd\_PDE\_IBMX}$$

$$PDE = PDEtot - PDE\_IBMX - PDEp$$

$$\frac{dPDEp}{dt} = k_{PKA_{PDE}} \cdot PKACII \cdot PDE - k\_PP\_PDE \cdot PDEp$$

$$\frac{dcAMPtot}{dt} = \frac{k\_AC\_basal \cdot AC \cdot ATP}{Km\_AC\_basal + ATP} + \frac{k\_AC\_Gsa \cdot AC\_GsaGTP \cdot ATP}{Km\_AC\_Gsa + ATP} + \frac{k\_AC\_FSK \cdot AC\_FSK \cdot ATP}{Km\_AC\_FSK + ATP} - \frac{k\_cAMP\_PDE \cdot PDE \cdot cAMP}{Km\_PDE\_cAMP + cAMP} - \frac{k\_cAMP\_PDEp \cdot PDEp \cdot cAMP}{Km\_PDE\_cAMP + cAMP}$$

PKA

Parameter	Description	Value	Units	Source
PKAItot	total type 1 protein kinase A	0.59	µM	[5]
PKAIItot	total type 2 protein kinase A	0.059	µM	adapted
PKItot	total protein kinase inhibitor	0.18	µM	[5-6]
kf_RC_cAMP	cAMP association with PKA	1	1/[µM ms]	[5-6]
kr_RC_cAMP	cAMP association with PKA	1.64	1/ms	[5-6]
kf_RCcAMP_cAMP	cAMP association with PKA	1	1/[µM ms]	[5-6]
kr_RCcAMP_cAMP	cAMP association with PKA	9.14	1/ms	[5-6]
kf_RcAMPcAMP_C	catalytic subunit dissociation	4.375	1/[µM ms]	[5-6]
kr_RcAMPcAMP_C	catalytic subunit dissociation	1	1/ms	[5-6]
kf_PKA_PKI	PKA inhibition by PKI	1	1/[µM ms]	[5-6]
kr_PKA_PKI	PKA inhibition by PKI	0.2e-3	1/ms	[5-6]

$$PKI = PKItot - PKACI\_PKI - PKACII\_PKI$$

$$\frac{dRC\_I}{dt} = -kf\_RC\_cAMP \cdot RC\_I \cdot cAMP + kr\_RC\_cAMP \cdot RCcAMP\_I$$

$$\frac{dRCcAMP\_I}{dt} = -kr\_RC\_cAMP \cdot RCcAMP\_I + kf\_RC\_cAMP \cdot RC\_I \cdot cAMP - kf\_RCcAMP\_cAMP \cdot RCcAMP\_I \cdot cAMP + kr\_RCcAMP\_cAMP \cdot RCcAMPcAMP\_I$$

$$\frac{dRCcAMPcAMP\_I}{dt} = -kr\_RCcAMP\_cAMP \cdot RCcAMPcAMP\_I + kf\_RCcAMP\_cAMP \cdot RCcAMP\_I \cdot cAMP - kf\_RcAMPcAMP\_C \cdot RCcAMPcAMP\_I + kr\_RcAMPcAMP\_C \cdot RcAMPcAMP\_I \cdot PKACI$$

$$\frac{dRcAMPcAMP\_I}{dt} = -kr\_RcAMPcAMP\_C \cdot RcAMPcAMP\_I \cdot PKACI + kf\_RcAMPcAMP\_C \cdot RCcAMPcAMP\_I$$

$$\frac{dPKACI}{dt} = -kr\_RcAMPcAMP\_C \cdot RcAMPcAMP\_I \cdot PKACI + kf\_RcAMPcAMP\_C \cdot RCcAMPcAMP\_I - kf\_PKA\_PKI \cdot PKACI \cdot PKI + kr\_PKA\_PKI \cdot PKACI\_PKI$$

$$\frac{dPKA\_CI\_PKI}{dt} = -kr\_PKA\_PKI \cdot PKACI\_PKI + kf\_PKA\_PKI \cdot PKACI \cdot PKI$$

$$\frac{dRC\_II}{dt} = -kf\_RC\_cAMP \cdot RC\_II \cdot cAMP + kr\_RC\_cAMP \cdot RCcAMP\_II$$

$$\frac{dRCcAMP\_II}{dt} = -kr\_RC\_cAMP \cdot RCcAMP\_II + kf\_RC\_cAMP \cdot RC\_II \cdot cAMP - kf\_RCcAMP\_cAMP \cdot RCcAMP\_II \cdot cAMP + kr\_RCcAMP\_cAMP \cdot RCcAMPcAMP\_II$$

$$\frac{dRCcAMPcAMP\_II}{dt} = -kr\_RCcAMP\_cAMP \cdot RCcAMPcAMP\_II + kf\_RCcAMP\_cAMP \cdot RCcAMP\_II \cdot cAMP - kf\_RcAMPcAMP\_C \cdot RCcAMPcAMP\_II + kr\_RcAMPcAMP\_C \cdot RcAMPcAMP\_II \cdot PKACII$$

$$\frac{dRcAMPcAMP\_II}{dt} = -kr\_RcAMPcAMP\_C \cdot RcAMPcAMP\_II \cdot PKACII + kf\_RcAMPcAMP\_C \cdot RCcAMPcAMP\_II$$

$$\frac{dPKACII}{dt} = -kr\_RcAMPcAMP\_C \cdot RcAMPcAMP\_II \cdot PKACII + kf\_RcAMPcAMP\_C \cdot RCcAMPcAMP\_II - kf\_PKA\_PKI \cdot PKACII \cdot PKI + kr\_PKA\_PKI \cdot PKACII\_PKI$$

$$\frac{dPKA\_CII\_PKI}{dt} = -kr\_PKA\_PKI \cdot PKACII\_PKI + kf\_PKA\_PKI \cdot PKACII \cdot PKI$$

I-1/PP1

Parameter	Description	Value	Units	Source
PP1tot	total phosphatase 1	0.89	µM	[5-6]
I1tot	total inhibitor 1	0.3	µM	[5-6]
k_PKA_I1	PKA phosphorylation of inhibitor 1	60e-3	1/ms	[5-6]
Km_PKA_I1	PKA phosphorylation of inhibitor 1	1.0	µM	[5-6]
Vmax_PP2A_I1	PP2A dephosphorylation of phospholamban	14.0e-3	µM/ms	[5-6]
Km_PP2A_I1	PP2A dephosphorylation of phospholamban	1.0	µM	[5-6]
kf_PP1_I1	PP1 inhibition by inhibitor 1	1.0	1/[µM ms]	[5-6]
kr_PP1_I1	PP1 inhibition by inhibitor 1	1.0e-3	1/ms	[5-6]

$$I1 = I1tot - I1ptot$$

$$PP1 = PP1tot - I1p\_PP1$$

$$I1p = I1ptot - I1p\_PP1$$

$$\frac{dI1p\_PP1}{dt} = kf\_PP1\_I1 \cdot PP1 \cdot I1p - kr\_PP1\_I1 \cdot I1p\_PP1$$

$$\frac{dI1ptot}{dt} = \frac{k\_PKA\_I1 \cdot PKACI \cdot I1}{Km\_PKA\_I1 + I1} - \frac{Vmax\_PP2A\_I1 \cdot I1ptot}{Km\_PP2A\_I1 + I1ptot}$$

LCC

Parameter	Description	Value	Units	Source
LCCtot	total L-type Ca channel	0.025	µM	[5-6]
PKACII_LCCtot	total PKA local to L-type Ca channel	0.025	µM	[5-6]
PP1_LCC	total PP1 local to L-type Ca channel	0.025	µM	[5-6]
PP2A_LCC	total PP2A local to L-type Ca channel	0.025	µM	[5-6]
epsilon	AKAP-mediated scaling factor	10	-	[5-6]
k_PKA_LCC	PKA phosphorylation of LCC	54e-3	1/ms	[5-6]
Km_PKA_LCC	PKA phosphorylation of LCC	21	µM	[5-6]
k_PP1_LCC	PP1 dephosphorylation of LCC	8.52e-3	1/ms	[5-6]
Km_PP1_LCC	PP1 dephosphorylation of LCC	3	µM	[5-6]
k_PP2A_LCC	PP2A dephosphorylation of LCC	10.1e-3	1/ms	[5-6]
Km_PP2A_LCC	PP2A dephosphorylation of LCC	3	µM	[5-6]

$$PKACII\_LCC = \frac{PKACII\_LCCtot}{PKAIItot} \cdot PKACII$$

$$LCCa = LCCtot - LCCap$$

$$\frac{dLCCap}{dt} = \frac{epsilon \cdot k\_PKA\_LCC \cdot PKACII\_LCC \cdot LCCa}{Km\_PKA\_LCC + epsilon \cdot LCCa} - \frac{epsilon \cdot k\_PP2A\_LCC \cdot PP2A\_LCC \cdot LCCap}{Km\_PP2A\_LCC + epsilon \cdot LCCap}$$

$$LCCb = LCCtot - LCCbp$$

$$\frac{dLCCbp}{dt} = \frac{epsilon \cdot k\_PKA\_LCC \cdot PKACII\_LCC \cdot LCCb}{Km\_PKA\_LCC + epsilon \cdot LCCb} - \frac{epsilon \cdot k\_PP1\_LCC \cdot PP1\_LCC \cdot LCCbp}{Km\_PP1\_LCC + epsilon \cdot LCCbp}$$

PLB

Parameter	Description	Value	Units	Source
PLBtot	total phospholamban	106	µM	[6]
k_PKA_PLB	PKA phosphorylation of phospholamban	54e-3	1/ms	[5-6]
Km_PKA_PLB	PKA phosphorylation of phospholamban	21	µM	[5-6]
k_PP1_PLB	PP1 dephosphorylation of phospholamban	8.5e-3	1/ms	[5-6]
Km_PP1_PLB	PP1 dephosphorylation of phospholamban	7.0	µM	[5-6]

$$PLB = PLBtot - PLBp$$

$$\frac{dPLBp}{dt} = \frac{k\_PKA\_PLB \cdot PKACI \cdot PLB}{Km\_PKA\_PLB + PLB} - \frac{k\_PP1\_PLB \cdot PP1 \cdot PLBp}{Km\_PP1\_PLB + PLBp}$$

PLM

Parameter	Description	Value	Units	Source
PLMtot	total phospholemman	48	µM	adapted
k_PKA_PLM	PKA phosphorylation of phospholemman	54e-3	1/ms	adapted
Km_PKA_PLM	PKA phosphorylation of phospholemman	21	µM	adapted
k_PP1_PLM	PP1 dephosphorylation of phospholemman	8.5e-3	1/ms	adapted
Km_PP1_PLM	PP1 dephosphorylation of phospholemman	7.0	µM	adapted

$$PLM = PLMtot - PLMp$$

$$\frac{dPLMp}{dt} = \frac{k\_PKA\_PLM \cdot PKACI \cdot PLM}{Km\_PKA\_PLM + PLM} - \frac{k\_PP1\_PLM \cdot PP1 \cdot PLMp}{Km\_PP1\_PLM + PLMp}$$

TnI

Parameter	Description	Value	Units	Source
TnItot	total troponin I	70	µM	[6]
PP2A_TnI	total PP2A local to troponin I	0.67	µM	[6]
k_PKA_TnI	PKA phosphorylation of troponin I	54e-3	1/ms	[6]
Km_PKA_TnI	PKA phosphorylation of troponin I	21	µM	[6]
k_PP2A_TnI	PP2A dephosphorylation of troponin I	10.1e-3	1/ms	[6]
Km_PP2A_TnI	PP2A dephosphorylation of troponin I	4.1	µM	[6]

$$TnI = TnItot - TnIp$$

$$\frac{dTnIp}{dt} = \frac{k\_PKA\_TnI \cdot PKACI \cdot TnI}{Km\_PKA\_TnI + TnI} - \frac{k\_PP2A\_TnI \cdot PP2a\_TnI \cdot TnIp}{Km\_PP2A\_TnI + TnIp}$$

Mouse Ventricular Myocyte Excitation-Contraction Coupling

General Paramters

Parameter	Description	Value	Units	Source
F	Faraday's constant	96.5	C/mmol	[184]
T	temperature	298	K	-
R	universal gas constant	8.314	J/[mol K]	[184]
Cm	membrane capacitance	1	μF/cm^2	[184]
Acap	capacitive membrane area	1.387e-4	cm^2	adapted
Csa	cell surface area capacitance	1.387e-4	μF	adapted
Vmyo	cytoplasmic volume	25.84e-6	μL	[184]
VSR	sarcoplasmic reticulum volume	1.3902e-6	μL	adapted
VSS	dyadic subspace volume	5.168e-13	μL	adapted
Istimmax	paced stimulus amplitude	-20	pA/pF	[184]
Ko	extracellular potassium	5.4e3	μM	[184]
Mgi	intracellular magnesium	1e3	μM	[189]
Cao	extracellular calcium	1.8e3	μM	[184]
Nao	extracellular sodium	140e3	μM	[184]

Nernst Potentials

$$ECa = \frac{RT}{2F} \cdot \log\left(\frac{Cao}{Cai}\right)$$

$$EK = \frac{RT}{F} \cdot \log\left(\frac{Ko}{Ki}\right)$$

$$ENa = \frac{RT}{F} \cdot \log\left(\frac{Nao}{Nai}\right)$$

Ca^{2+} Buffering

Parameter	Description	Value	Units	Source
CaMtot	total cytosolic calmodulin	24	μM	[189]
TnCLtot	total low-affinity troponin sites	70	μM	[189]
TnCHtot	total high-affinity troponin sites	140	μM	[189]
Myosintot	total myosin	140	μM	[189]
CSQNtot	total SR calsequestrin	2.6e3	μM	[189]
CaSRbtot	total SR membrane buffer	47	μM	[175]
CaSLtot	total inner sarcolemmal buffer	42	μM	[175]
CaSLhtot	total high affinity sarcolemmal buffer	15	μM	[175]
CaATPtot	total ATP buffer	5000	μM	[175]
CaPCrtot	total phosphocreatine buffer	12000	μM	[175]
kon_CaM	kon for Ca^{2+} binding to cytosolic calmodulin	45e-3	1/[μM ms]	[189]

Parameter	Description	Value	Units	Source
koff_CaM	koff for Ca^{2+} binding to cytosolic calmodulin	238e-3	1/ms	[189]
kon_TnCL	kon for Ca^{2+} binding to low-affinity troponin	32.7e-3	1/[μM ms]	[189]
koff_TnCL	koff for Ca^{2+} binding to low-affinity troponin	19.6e-3	1/ms	[189]
kon_TnCHCa	kon for Ca^{2+} binding to high-affinity troponin	2.37e-3	1/[μM ms]	[189]
koff_TnCHCa	koff for Ca^{2+} binding to high-affinity troponin	0.032e-3	1/ms	[189]
kon_TnCHMg	kon for Mg^{2+} binding to high-affinity troponin	0.003e-3	1/[μM ms]	[189]
koff_TnCHMg	koff for Mg^{2+} binding to high-affinity troponin	3.33e-3	1/ms	[189]
kon_MyosinCa	kon for Ca^{2+} binding to myosin	13.8e-3	1/[μM ms]	[189]
koff_MyosinCa	koff for Ca^{2+} binding to myosin	0.46e-3	1/ms	[189]
kon_MyosinMg	kon for Mg^{2+} binding to myosin	0.0157e-3	1/[μM ms]	[189]
koff_MyosinMg	koff for Mg^{2+} binding to myosin	0.057e-3	1/ms	[189]
kon_CaSRb	kon for Ca^{2+} binding to SR membrane	60e-3	1/[μM ms]	[175]
koff_CaSRb	koff for Ca^{2+} binding to SR membrane	100e-3	1/ms	[175]
kon_CaSL	kon for Ca^{2+} binding to sarcolemmal membrane	100e-3	1/[μM ms]	[175]
koff_CaSL	koff for Ca^{2+} binding to sarcolemmal membrane	1300e-3	1/ms	[175]
kon_CaSLh	kon for Ca^{2+} binding to high affinity	100e-3	1/[μM ms]	[175]
koff_CaSLh	koff for Ca^{2+} binding to high affinity	30e-3	1/ms	[175]
kon_CaATP	kon for Ca^{2+} binding to ATP	100e-3	1/[μM ms]	[175]
koff_CaATP	koff for Ca^{2+} binding to ATP	20	1/ms	[175]
Ki_MgATP	Mg^{2+} competition for ATP	83.3	μM	[175]
kon_CaPCr	kon for Ca^{2+} binding to phosphocreatine	100e-3	1/[μM ms]	[175]
koff_CaPCr	koff for Ca^{2+} binding to phosphocreatine	7107.3	1/ms	[175]
Km_CSQN	Km for Ca^{2+} binding to calsequestrin	650	μM	[189]

$$\frac{dTnCLCa}{dt} = kon\_TnCL \cdot Cai \cdot (TnCLtot - TnClCa) - koff\_TnCL \cdot TnClCa$$

$$\frac{dTnCHCa}{dt} = kon\_TnCHCa \cdot Cai \cdot (TnCHtot - TnCHCa - TnCHMg) - koff\_TnCHCa \cdot TnCHCa$$

$$\frac{dTnCHMg}{dt} = kon\_TnCHMg \cdot Mgi \cdot (TnCHtot - TnCHCa - TnCHMg) - koff\_TnCHMg \cdot TnCHMg$$

$$\frac{dMyosinCa}{dt} = kon\_MyosinCa \cdot Cai \cdot (Myosintot - MyosinCa - MyosinMg) - koff\_MyosinCa \cdot MyosinCa$$

$$\frac{dMyosinMg}{dt} = kon\_MyosinMg \cdot Mgi \cdot (Myosintot - MyosinCa - MyosinMg) - koff\_MyosinMg \cdot MyosinMg$$

$$\frac{dCaMCa}{dt} = kon\_CaM \cdot Cai \cdot (CaMtot - CaMCa) - koff\_CaM \cdot CaMCa$$

$$\frac{dCaSRb}{dt} = kon\_CaSRb \cdot Cai \cdot (CaSRbtot - CaSRb) - koff\_CaSRb \cdot CaSRb$$

$$\frac{dCaSL}{dt} = kon\_CaSL \cdot Cai \cdot (CaSLtot - CaSL) - koff\_CaSL \cdot CaSL$$

$$\frac{dCaSLh}{dt} = kon\_CaSLh \cdot Cai \cdot (CaSLhtot - CaSLh) - koff\_CaSLh \cdot CaSLh$$

$$\frac{dCaATP}{dt} = kon\_CaATP \cdot Cai \cdot (CaATPtot - CaATP) - koff\_CaATP \cdot \left(1 + \frac{Mgi}{Ki\_MgATP}\right) \cdot CaATP$$

$$\frac{dCaPCr}{dt} = kon\_CaPCR \cdot Cai \cdot (CaPCRtot - CaPCR) - koff\_CaPCR \cdot CaPCr$$

$$CaBSR = \frac{1}{1 + \frac{CSQNtot \cdot Km\_CSQN}{(Km\_CSQN + CaSR)^2}}$$

Ca^{2+}-Induced Ca^{2+}-Release

Parameter	Description	Value	Units	Source
NCaRU	number of Ca^{2+} release units	50000	-	[185]
r_xfer	Ca^{2+} flux rate from SS to cytosol	220	1/ms	[185]
PCaL	unitary LCC permeability	27.39e-13	cm^3/s	adapted
JRyRmax	unitary Ca^{2+} flux rate through RyR	31.36	1/ms	adapted
fL	L-type Ca^{2+} channel rate constant	0.85	1/ms	[185]
aL	L-type Ca^{2+} channel rate constant	12.88782	-	[185]
bL	L-type Ca^{2+} channel rate constant	32.1948	-	[185]
gammaL	L-type Ca^{2+} channel rate constant	4.170162e-3	1/[µM ms]	adapted
omegaL	L-type Ca^{2+} channel rate constant	0.0269659	1/ms	[185]
k12	ryanodine receptor rate constant	125.3571e-6	$1/[\mu M^2$ ms]	adapted
k21	ryanodine receptor rate constant	1250	1/ms	[185]
k23	ryanodine receptor rate constant	235.8	$1/[\mu M^2$ ms]	[185]
k32	ryanodine receptor rate constant	9.6	1/ms	[185]
k34	ryanodine receptor rate constant	1.415	$1/[\mu M^2$ ms]	[185]
k43	ryanodine receptor rate constant	13.65	1/ms	[185]
k45	ryanodine receptor rate constant	0.07	1/ms	[185]
k54	ryanodine receptor rate constant	93.385e-6	$1/[\mu M^2$ ms]	[185]
k56	ryanodine receptor rate constant	18.87	$1/[\mu M^2$ ms]	[185]

Parameter	Description	Value	Units	Source
k65	ryanodine receptor rate constant	30	1/ms	[185]
Parameter	**Description**	**Value**	**Units**	**Source**
k25	ryanodine receptor rate constant	2.358	1/[μM^2 ms]	[185]
k52	ryanodine receptor rate constant	0.001235	1/ms	[185]
SRmax	RyR luminal sensitivity	0.3	-	[183,337]
SRmin	RyR luminal sensitivity	2	-	[183,337]
SREC50	RyR luminal sensitivity	0.5	-	[183,337]
SRH	RyR luminal sensitivity	1	-	[183,337]
r_leak	passive SR leak rate through RyRs	0.0053	1/ms	adapted

Local dyadic Ca^{2+} concentrations

$$CaSS_1 = \frac{r\_leak \cdot CaSR + r\_xfer \cdot Cai}{r\_leak + r\_xfer}$$

$$CaSS_2 = \frac{\frac{PCaL}{Vss} \cdot \frac{2VF}{RT} \cdot \frac{0.341 \cdot Cao}{e^{\frac{2VF}{RT}} - 1} + r\_leak \cdot CaSR + r\_xfer \cdot Cai}{\frac{PCaL}{Vss} \cdot \frac{2VF}{RT} \cdot \frac{1}{1 - e^{\frac{-2VF}{RT}}} + r\_leak + r\_xfer}$$

$$CaSS_3 = \frac{(JRyRmax + r\_leak) \cdot CaSR + r\_xfer \cdot Cai}{JRyRmax + r\_leak + r\_xfer}$$

$$CaSS_4 = \frac{\frac{PCaL}{Vss} \cdot \frac{2VF}{RT} \cdot \frac{0.341 \cdot Cao}{e^{\frac{2VF}{RT}} - 1} + (JRyRmax + r\_leak) \cdot CaSR + r\_xfer \cdot Cai}{\frac{PCaL}{Vss} \cdot \frac{2VF}{RT} \cdot \frac{1}{1 - e^{\frac{-2VF}{RT}}} + JRyRmax + r\_leak + r\_xfer}$$

LCC and RyR rate constants

$$alphaL = 0.835399 \cdot e^{0.0269241 \cdot (V-35)}$$

$$betaL = 0.0331584 \cdot e^{-0.0934594 \cdot (V-35)}$$

$$yCainf = \frac{0.95}{1 + e^{\frac{V+25}{5}}} + 0.05$$

$$tauyCa = \frac{340}{1 + e^{\frac{V+30}{12}}} + 60$$

$$kby = \frac{yCainf}{tauyCa}$$

$$kfy = \frac{1 - yCainf}{tauyCa}$$

$$\lambda_{1,2} = alphaL$$

$$\lambda_{2,1} = betaL$$

$$\lambda_{2,3} = fL$$

$$\lambda_{3,2} = gL$$

$$\lambda_{1,4,CaSS1} = gammaL \cdot CaSS_1$$

$$\lambda_{1,4,CaSS3} = gammaL \cdot CaSS_3$$

$$\lambda_{4,1} = omegaL$$

$$\lambda_{4,5} = aL \cdot alphaL$$

$$\lambda_{5,4} = \frac{betaL}{bL}$$

$$\lambda_{2,5,CaSS1} = aL \cdot gammaL \cdot CaSS_1$$

$$\lambda_{2,5,CaSS3} = aL \cdot gammaL \cdot CaSS_3$$

$$\lambda_{5,2} = \frac{omegaL}{b_L}$$

$$\lambda_{6,7} = alphaL$$

$$\lambda_{7,6} = betaL$$

$$\lambda_{7,8} = fL$$

$$\lambda_{8,7} = gL$$

$$\lambda_{6,9,CaSS1} = gammaL \cdot CaSS_1$$

$$\lambda_{6,9,CaSS3} = gammaL \cdot CaSS_3$$

$$\lambda_{9,6} = omegaL$$

$$\lambda_{9,10} = aL \cdot alphaL$$

$$\lambda_{10,9} = \frac{betaL}{bL}$$

$$\lambda_{7,10,CaSS1} = aL \cdot gammaL \cdot CaSS_1$$

$$\lambda_{7,10,CaSS3} = aL \cdot gammaL \cdot CaSS_3$$

$$\lambda_{10,7} = \frac{omegaL}{bL}$$

$$\lambda_{1,6} = kfy$$

$$\lambda_{2,7} = kfy$$

$$\lambda_{3,8} = kfy$$

$$\lambda_{4,9} = kfy$$

$$\lambda_{5,10} = kfy$$

$$\lambda_{6,1} = kby$$

$$\lambda_{7,2} = kby$$

$$\lambda_{8,3} = kby$$

$$\lambda_{9,4} = kby$$

$$\lambda_{10,5} = kby$$

$$klumen = SRmax - \frac{SRmax - SRmin}{1 + \left(\frac{SREC50}{CaSR}\right)^{SRH}}$$

$$k12 = k12 \cdot klumen$$

$$k23 = k23 \cdot klumen$$

$$k54 = k54 \cdot klumen$$

$$k25 = \frac{k25}{klumen}$$

$$k45 = \frac{k45}{klumen}$$

$$\rho_{1,2,CaSS1} = k12 \cdot {CaSS_1}^2$$

$$\rho_{1,2,CaSS2} = k12 \cdot {CaSS_2}^2$$

$$\rho_{2,1} = k21$$

$$\rho_{2,3,CaSS1} = k23 \cdot {CaSS_1}^2$$

$$\rho_{2,3,CaSS2} = k23 \cdot {CaSS_2}^2$$

$$\rho_{3,4,CaSS3} = \frac{k32 \cdot k43}{k34 \cdot {CaSS_3}^2 + k43}$$

$$\rho_{3,4,CaSS4} = \frac{k32 \cdot k43}{k34 \cdot {CaSS_4}^2 + k43}$$

$$\rho_{2,4,CaSS1} = k24 \cdot {CaSS_1}^2$$

$$\rho_{2,4,CaSS2} = k24 \cdot {CaSS_2}^2$$

$$\rho_{4,2,CaSS1} = \frac{k52 \cdot k65}{k56 \cdot {CaSS_1}^2 + k65}$$

$$\rho_{4,2,CaSS2} = \frac{k52 \cdot k65}{k56 \cdot {CaSS_2}^2 + k65}$$

$$\rho_{3,4,CaSS3} = \frac{k45 \cdot k34 \cdot {CaSS_3}^2}{k34 \cdot {CaSS_3}^2 + k43}$$

$$\rho_{3,4,CaSS4} = \frac{k45 \cdot k34 \cdot {CaSS_4}^2}{k34 \cdot {CaSS_4}^2 + k43}$$

$$\rho_{4,3,CaSS1} = \frac{k65 \cdot k54 \cdot {CaSS_1}^2}{k56 \cdot {CaSS_1}^2 + k65}$$

$$\rho_{4,3,CaSS2} = \frac{k65 \cdot k54 \cdot {CaSS_2}^2}{k56 \cdot {CaSS_2}^2 + k65}$$

LCC and RyR state transitions

$$\frac{dLR1}{dt} = -\left(\lambda_{1,2} + \lambda_{1,4,CaSS1} + \lambda_{1,6} + \rho_{1,2,CaSS1}\right) \cdot LR1 + \lambda_{2,1} \cdot LR2 + \lambda_{4,1} \cdot LR4 + \lambda_{6,1} \cdot LR6 + \rho_{2,1} \cdot LR11$$

$$\frac{dLR2}{dt} = -\left(\lambda_{2,1} + \lambda_{2,3} + \lambda_{2,5,CaSS1} + \lambda_{2,7} + \rho_{1,2,CaSS1}\right) \cdot LR2 + \lambda_{1,2} \cdot LR1 + \lambda_{3,2} \cdot LR3 + \lambda_{5,2} \cdot LR5 + \lambda_{7,2} \cdot LR7 + \rho_{2,1} \cdot LR12$$

$$\frac{dLR3}{dt} = -\left(\lambda_{3,2} + \lambda_{3,8} + \rho_{1,2,CaSS2}\right) \cdot LR3 + \lambda_{2,3} \cdot LR2 + \lambda_{8,3} \cdot LR8 + \rho_{2,1} \cdot LR13$$

$$\frac{dLR4}{dt} = -\left(\lambda_{4,1} + \lambda_{4,5} + \lambda_{4,9} + \rho_{1,2,CaSS1}\right) \cdot LR4 + \lambda_{1,4,CaSS1} \cdot LR1 + \lambda_{5,4} \cdot LR5 + \lambda_{9,4} \cdot LR9 + \rho_{2,1} \cdot LR14$$

$$\frac{dLR5}{dt} = -\left(\lambda_{5,2} + \lambda_{5,4} + \lambda_{5,10} + \rho_{1,2,CaSS1}\right) \cdot LR5 + \lambda_{2,5,CaSS1} \cdot LR2 + \lambda_{4,5} \cdot LR4 + \lambda_{10,5} \cdot LR10 + \rho_{2,1} \cdot LR15$$

$$\frac{dLR6}{dt} = -\left(\lambda_{6,1} + \lambda_{6,7} + \lambda_{6,9,CaSS1} + \rho_{1,2,CaSS1}\right) \cdot LR6 + \lambda_{1,6} \cdot LR1 + \lambda_{7,6} \cdot LR7 + \lambda_{9,6} \cdot LR9 + \rho_{2,1} \cdot LR16$$

$$\frac{dLR7}{dt} = -\left(\lambda_{7,2} + \lambda_{7,6} + \lambda_{7,8} + \lambda_{7,10,CaSS1} + \rho_{1,2,CaSS1}\right) \cdot LR7 + \lambda_{2,7} \cdot LR2 + \lambda_{6,7} \cdot LR6 + \lambda_{8,7} \cdot LR8 + \lambda_{10,7} \cdot LR10 + \rho_{2,1} \cdot LR17$$

$$\frac{dLR8}{dt} = -\left(\lambda_{8,3} + \lambda_{8,7} + \rho_{1,2,CaSS1}\right) \cdot LR8 + \lambda_{3,8} \cdot LR3 + \lambda_{7,8} \cdot LR7 + \rho_{2,1} \cdot LR18$$

$$\frac{dLR9}{dt} = -\left(\lambda_{9,4} + \lambda_{9,6} + \lambda_{9,10} + \rho_{1,2,CaSS1}\right) \cdot LR9 + \lambda_{4,9} \cdot LR4 + \lambda_{6,9,CaSS1} \cdot LR6 + \lambda_{10,9} \cdot LR10 + \rho_{2,1} \cdot LR19$$

$$\frac{dLR10}{dt} = -\left(\lambda_{10,5} + \lambda_{10,7} + \lambda_{10,9} + \rho_{1,2,CaSS1}\right) \cdot LR10 + \lambda_{5,10} \cdot LR5 + \lambda_{7,10,CaSS1} \cdot LR7 + \lambda_{9,10} \cdot LR9 + \rho_{2,1} \cdot LR20$$

$$\frac{dLR11}{dt} = -\left(\rho_{2,1} + \lambda_{1,2} + \lambda_{1,4,CaSS1} + \lambda_{1,6} + \rho_{2,3,CaSS1} + \rho_{2,4,CaSS1}\right) \cdot LR11 + \rho_{1,2,CaSS1} \cdot LR1 + \lambda_{2,1} \cdot LR12 + \lambda_{4,1} \cdot LR14 + \lambda_{6,1} \cdot LR16 + \rho_{3,2,CaSS3} \cdot LR21 + \rho_{4,2,CaSS1} \cdot LR31$$

$$\frac{dLR12}{dt} = -\left(\rho_{2,1} + \lambda_{2,1} + \lambda_{2,3} + \lambda_{2,5,CaSS1} + \lambda_{2,7} + \rho_{2,3,CaSS1} + \rho_{2,4,CaSS1}\right) \cdot LR12 + \rho_{1,2,CaSS1} \cdot LR2 + \lambda_{1,2} \cdot LR11 + \lambda_{3,2} \cdot LR13 + \lambda_{5,2} \cdot LR15 + \lambda_{7,2} \cdot LR17 + \rho_{3,2,CaSS3} \cdot LR22 + \rho_{4,2,CaSS1} \cdot LR32$$

$$\frac{dLR13}{dt} = -\left(\rho_{2,1} + \lambda_{3,2} + \lambda_{3,8} + \rho_{2,3,CaSS2} + \rho_{2,4,CaSS2}\right) \cdot LR13 + \rho_{1,2,CaSS2} \cdot LR3 + \lambda_{2,3} \cdot LR12 + \lambda_{8,3} \cdot LR18 + \rho_{3,2,CaSS4} \cdot LR23 + \rho_{4,2,CaSS2} \cdot LR33$$

$$\frac{dLR14}{dt} = -\left(\rho_{2,1} + \lambda_{4,1} + \lambda_{4,5} + \lambda_{4,9} + \rho_{2,3,CaSS1} + \rho_{2,4,CaSS1}\right) \cdot LR14 + \rho_{1,2,CaSS1} \cdot LR4 + \lambda_{1,4,CaSS1} \cdot LR11 + \lambda_{5,4} \cdot LR15 + \lambda_{9,4} \cdot LR19 + \rho_{3,2,CaSS3} \cdot LR24 + \rho_{4,2,CaSS1} \cdot LR34$$

$$\frac{dLR15}{dt} = -\left(\rho_{2,1} + \lambda_{5,2} + \lambda_{5,4} + \lambda_{5,10} + \rho_{2,3,CaSS1} + \rho_{2,4,CaSS1}\right) \cdot LR15 + \rho_{1,2,CaSS1} \cdot LR5 + \lambda_{2,5,CaSS1} \cdot LR12 + \lambda_{4,5} \cdot LR14 + \lambda_{10,5} \cdot LR20 + \rho_{3,2,CaSS3} \cdot LR25 + \rho_{4,2,CaSS1} \cdot LR35$$

$$\frac{dLR16}{dt} = -\left(\rho_{2,1} + \lambda_{6,1} + \lambda_{6,7} + \lambda_{6,9,CaSS1} + \rho_{2,3,CaSS1} + \rho_{2,4,CaSS1}\right) \cdot LR16 + \rho_{1,2,CaSS1} \cdot LR6 + \lambda_{1,6} \cdot LR11 + \lambda_{7,6} \cdot LR17 + \lambda_{9,6} \cdot LR19 + \rho_{3,2,CaSS3} \cdot LR26 + \rho_{4,2,CaSS1} \cdot LR36$$

$$\frac{dLR17}{dt} = -\left(\rho_{2,1} + \lambda_{7,2} + \lambda_{7,6} + \lambda_{7,8} + \lambda_{7,10,CaSS1} + \rho_{2,3,CaSS1} + \rho_{2,4,CaSS1}\right) \cdot LR17 + \rho_{1,2,CaSS1} \cdot LR7 + \lambda_{2,7} \cdot LR12 + \lambda_{6,7} \cdot LR16 + \lambda_{8,7} \cdot LR18 + \lambda_{10,7} \cdot LR20 + \rho_{3,2,CaSS3} \cdot LR27 + \rho_{4,2,CaSS1} \cdot LR37$$

$$\frac{dLR18}{dt} = -\left(\rho_{2,1} + \lambda_{8,3} + \lambda_{8,7} + \rho_{2,3,CaSS1} + \rho_{2,4,CaSS1}\right) \cdot LR18 + \rho_{1,2,CaSS1} \cdot LR8 + \lambda_{3,8} \cdot LR13 + \lambda_{7,8} \cdot LR17 + \rho_{3,2,CaSS3} \cdot LR28 + \rho_{4,2,CaSS1} \cdot LR38$$

$$\frac{dLR19}{dt} = -\left(\rho_{2,1} + \lambda_{9,4} + \lambda_{9,6} + \lambda_{9,10} + \rho_{2,3,CaSS1} + \rho_{2,4,CaSS1}\right) \cdot LR19 + \rho_{1,2,CaSS1} \cdot LR9 + \lambda_{4,9} \cdot LR14 + \lambda_{6,9,CaSS1} \cdot LR16 + \lambda_{10,9} \cdot LR20 + \rho_{3,2,CaSS3} \cdot LR29 + \rho_{4,2,CaSS1} \cdot LR39$$

$$\frac{dLR20}{dt} = -\left(\rho_{2,1} + \lambda_{10,5} + \lambda_{10,7} + \lambda_{10,9} + \rho_{2,3,CaSS1} + \rho_{2,4,CaSS1}\right) \cdot LR20 + \rho_{1,2,CaSS1} \cdot LR10 + \lambda_{5,10} \cdot LR15 + \lambda_{7,10,CaSS1} \cdot LR17 + \lambda_{9,10} \cdot LR19 + \rho_{3,2,CaSS3} \cdot LR30 + \rho_{4,2,CaSS1} \cdot LR40$$

$$\frac{dLR21}{dt} = -\left(\rho_{3,2,CaSS3} + \lambda_{1,2} + \lambda_{1,4,Cass3} + \lambda_{1,6} + \rho_{3,4,CaSS3}\right) \cdot LR21 + \rho_{2,3,CaSS1} \cdot LR11 + \lambda_{2,1} \cdot LR22 + \lambda_{4,1} \cdot LR24 + \lambda_{6,1} \cdot LR26 + \rho_{4,3,CaSS1} \cdot LR31$$

$$\frac{dLR22}{dt} = -\left(\rho_{3,2,CaSS3} + \lambda_{2,1} + \lambda_{2,3} + \lambda_{2,5,CaSS3} + \lambda_{2,7} + \rho_{3,4,CaSS3}\right) \cdot LR22 + \rho_{2,3,CaSS1} \cdot LR12 + \lambda_{1,2} \cdot LR21 + \lambda_{3,2} \cdot LR23 + \lambda_{5,2} \cdot LR25 + \lambda_{7,2} \cdot LR27 + \rho_{4,3,CaSS1} \cdot LR32$$

$$\frac{dLR23}{dt} = -\left(\rho_{3,2,CaSS4} + \lambda_{3,2} + \lambda_{3,8} + \rho_{3,4,CaSS4}\right) \cdot LR23 + \rho_{3,2,CaSS4} \cdot LR23 + \lambda_{2,3} \cdot LR22 + \lambda_{8,3} \cdot LR28 + \rho_{4,3,CaSS2} \cdot LR33$$

$$\frac{dLR24}{dt} = -\left(\rho_{3,2,CaSS3} + \lambda_{4,1} + \lambda_{4,5} + \lambda_{4,9} + \rho_{3,4,CaSS3}\right) \cdot LR24 + \rho_{2,3,CaSS1} \cdot LR14 + \lambda_{1,4,CaSS3} \cdot LR21 + \lambda_{5,4} \cdot LR25 + \lambda_{9,4} \cdot LR29 + \rho_{4,3,CaSS1} \cdot LR34$$

$$\frac{dLR25}{dt} = -\left(\rho_{3,2,CaSS3} + \lambda_{5,2} + \lambda_{5,4} + \lambda_{5,10} + \rho_{3,4,CaSS3}\right) \cdot LR25 + \rho_{2,3,CaSS1} \cdot LR15 + \lambda_{2,5,CaSS3} \cdot LR22 + \lambda_{4,5} \cdot LR24 + \lambda_{10,5} \cdot LR30 + \rho_{4,3,CaSS1} \cdot LR35$$

$$\frac{dLR26}{dt} = -\left(\rho_{3,2,CaSS3} + \lambda_{6,1} + \lambda_{6,7} + \lambda_{6,9,CaSS3} + \rho_{3,4,CaSS3}\right) \cdot LR26 + \rho_{2,3,CaSS1} \cdot LR16 + \lambda_{1,6} \cdot LR21 + \lambda_{4,5} \cdot LR24 + \lambda_{10,5} \cdot LR30 + \rho_{4,3,CaSS1} \cdot LR35$$

$$\frac{dLR27}{dt} = -\left(\rho_{3,2,CaSS3} + \lambda_{7,2} + \lambda_{7,6} + \lambda_{7,8} + \lambda_{7.10.CaSS3} + \rho_{3,4,CaSS3}\right) \cdot LR27 + \rho_{2,3,CaSS1} \cdot LR17 + \lambda_{2,7} \cdot LR22 + \lambda_{6,7} \cdot LR26 + \lambda_{8,7} \cdot LR28 + \lambda_{10,7} \cdot LR30 + \rho_{4,3,CaSS1} \cdot LR37$$

$$\frac{dLR28}{dt} = -\left(\rho_{3,2,CaSS3} + \lambda_{8,3} + \lambda_{8,7} + \rho_{3,4,CaSS3}\right) \cdot LR28 + \rho_{2,3,CaSS1} \cdot LR18 + \lambda_{3,8} \cdot LR23 + \lambda_{7,8} \cdot LR27 + \rho_{4,3,CaSS1} \cdot LR38$$

$$\frac{dLR29}{dt} = -\left(\rho_{3,2,CaSS3} + \lambda_{9,4} + \lambda_{9,6} + \lambda_{9,10} + \rho_{3,4,CaSS3}\right) \cdot LR29 + \rho_{2,3,CaSS1} \cdot LR19 + \lambda_{4,9} \cdot LR24 + \lambda_{6,9,CaSS3} \cdot LR26 + \lambda_{10,9} \cdot LR30 + \rho_{4,3,CaSS1} \cdot LR39$$

$$\frac{dLR30}{dt} = -\left(\rho_{3,2,CaSS3} + \lambda_{10,5} + \lambda_{10,7} + \lambda_{10,9} + \rho_{3,4,CaSS3}\right) \cdot LR30 + \rho_{2,3,CaSS1} \cdot LR20 + \lambda_{5,10} \cdot LR25 + \lambda_{7,10,CaSS3} \cdot LR27 + \lambda_{9,10} \cdot LR29 + \rho_{4,3,CaSS1} \cdot LR40$$

$$\frac{dLR31}{dt} = -\left(\rho_{4,2,CaSS1} + \rho_{4,3,CaSS1} + \lambda_{1,2} + \lambda_{1,4,CaSS1} + \lambda_{1,6}\right) \cdot LR31 + \rho_{2,4,CaSS1} \cdot LR11 + \rho_{3,4,CaSS3} \cdot LR21 + \lambda_{2,1} \cdot LR32 + \lambda_{4,1} \cdot LR34 + \lambda_{6,1} \cdot LR36$$

$$\frac{dLR32}{dt} = -\left(\rho_{4,2,CaSS1} + \rho_{4,3,CaSS1} + \lambda_{2,1} + \lambda_{2,3} + \lambda_{2,5,CaSS1} + \lambda_{2,7}\right) \cdot LR32 + \rho_{2,4,CaSS1} \cdot LR12 + \rho_{3,4,CaSS3} \cdot LR22 + \lambda_{1,2} \cdot LR31 + \lambda_{3,2} \cdot LR33 + \lambda_{5,2} \cdot LR35 + \lambda_{7,2} \cdot LR37$$

$$\frac{dLR33}{dt} = -\left(\rho_{4,2,CaSS2} + \rho_{4,3,CaSS2} + \lambda_{3,2} + \lambda_{3,8}\right) \cdot LR33 + \rho_{2,4,CaSS2} \cdot LR13 + \rho_{3,4,CaSS4} \cdot LR23 + \lambda_{2,3} \cdot LR32 + \lambda_{8,3} \cdot LR38$$

$$\frac{dLR34}{dt} = -\left(\rho_{4,2,CaSS1} + \rho_{4,3,CaSS1} + \lambda_{4,1} + \lambda_{4,5} + \lambda_{4,9}\right) \cdot LR34 + \rho_{2,4,CaSS1} \cdot LR14 + \rho_{3,4,CaSS3} \cdot LR24 + \lambda_{1,4,CaSS1} \cdot LR31 + \lambda_{5,4} \cdot LR35 + \lambda_{9,4} \cdot LR39$$

$$\frac{dLR35}{dt} = -\left(\rho_{4,2,CaSS1} + \rho_{4,3,CaSS1} + \lambda_{5,2} + \lambda_{5,4} + \lambda_{5,10}\right) \cdot LR35 + \rho_{2,4,CaSS1} \cdot LR15 + \rho_{3,4,CaSS3} \cdot LR25 + \lambda_{2,5,CaSS1} \cdot LR32 + \lambda_{4,5} \cdot LR34 + \lambda_{10,5} \cdot LR40$$

$$\frac{dLR36}{dt} = -\left(\rho_{4,2,CaSS1} + \rho_{4,3,CaSS1} + \lambda_{6,1} + \lambda_{6,7} + \lambda_{6,9,CaSS1}\right) \cdot LR36 + \rho_{2,4,CaSS1} \cdot LR16 + \rho_{3,4,CaSS3} \cdot LR26 + \lambda_{1,6} \cdot LR31 + \lambda_{7,6} \cdot LR39 + \lambda_{9,6} \cdot LR39$$

$$\frac{dLR37}{dt} = -\left(\rho_{4,2,CaSS1} + \rho_{4,3,CaSS1} + \lambda_{7,2} + \lambda_{7,6} + \lambda_{7,8} + \lambda_{7,10,CaSS1}\right) \cdot LR37 + \rho_{2,4,CaSS1} \cdot LR17 + \rho_{3,4,CaSS3} \cdot LR27 + \lambda_{2,7} \cdot LR32 + \lambda_{6,7} \cdot LR36 + \lambda_{8,7} \cdot LR38 + \lambda_{10,7} \cdot LR40$$

$$\frac{dLR38}{dt} = -\left(\rho_{4,2,CaSS1} + \rho_{4,3,CaSS1} + \lambda_{8,3} + \lambda_{8,7}\right) \cdot LR38 + \rho_{2,4,CaSS1} \cdot LR18 + \rho_{3,4,CaSS3} \cdot LR28 + \lambda_{3,8} \cdot LR33 + \lambda_{7,8} \cdot LR37$$

$$\frac{dLR39}{dt} = -\left(\rho_{4,2,CaSS1} + \rho_{4,3,CaSS1} + \lambda_{9,4} + \lambda_{9,6} + \lambda_{9,10}\right) \cdot LR39 + \rho_{2,4,CaSS1} \cdot LR19 + \rho_{3,4,CaSS3} \cdot LR29 + \lambda_{4,9} \cdot LR34 + \lambda_{6,9,CaSS1} \cdot LR36 + \lambda_{10,9} \cdot LR40$$

$$\frac{dLR40}{dt} = -\left(\rho_{4,2,CaSS1} + \rho_{4,3,CaSS1} + \lambda_{10,5} + \lambda_{10,7} + \lambda_{10,9}\right) \cdot LR40 + \rho_{2,4,CaSS1} \cdot LR20 + \rho_{3,4,CaSS3} \cdot LR30 + \lambda_{5,10} \cdot LR35 + \lambda_{7,10,CaSS1} \cdot LR37 + \lambda_{9,10} \cdot LR39$$

$$PCaSS_2 = LR3 + LR13 + LR33$$

$$PCaSS_3 = LR21 + LR22 + LR24 + LR25 + LR26 + LR27 + LR28 + LR29 + LR30$$

$$PCaSS_4 = LR23$$

$$PCaSS_1 = 1 - PCaSS_2 - PCaSS_3 - PCaSS_4$$

LCC current and RyR fluxes

$$I_{Ca,L} = \frac{NCaRU}{Csa} \cdot PCaL \cdot \frac{4VF^2}{RT} \cdot \frac{PCaSS_2 \cdot \left(CaSS_2 \cdot e^{\frac{2VF}{RT}} - 0.341 \cdot Cao\right) + PCaSS_4 \cdot \left(CaSS_4 \cdot e^{\frac{2VF}{RT}} - 0.341 \cdot Cao\right)}{e^{\frac{2VF}{RT}} - 1}$$

$$J_{RyR} = NCaRU \cdot JRyRmax \cdot (PCaSS_4 \cdot (CaSR - CaSS_4) + PCaSS_3 \cdot (CaSR - CaSS_3))$$

Subspace Ca^{2+} handling

$$J_{xfer} = NCaRU \cdot r_{xfer} \cdot \left(PCaSS_1 \cdot (CaSS_1 - Cai) + PCaSS_2 \cdot (CaSS_2 - Cai) + PCaSS_3 \cdot (CaSS_3 - Cai) + PCaSS_4 \cdot (CaSS_4 - Cai)\right)$$

$$J_{SRleak} = NCaRU \cdot r_{xfer} \cdot \left(PCaSS_1 \cdot (CaSR - CaSS_1) + PCaSS_2 \cdot (CaSR - CaSS_2) + PCaSS_3 \cdot (CaSR - CaSS_3) + PCaSS_4 \cdot (CaSR - CaSS_4)\right)$$

$$CaSS = PCaSS_1 \cdot CaSS_1 - PCaSS_2 \cdot CaSS_2 - PCaSS_3 \cdot CaSS_3 - PCaSS_4 \cdot CaSS_4$$

Ca^{2+} Channels

Parameter	Description	Value	Units	Source
g_ICab	Ca background current	0.000035	mS/µF	adapted
Vmax	Na/Ca exchange rate	0.65	pA/pF	adapted
KmNai	Na/Ca exchanger Na affinity	12e3	µM	[189]
KmCai	Na/Ca exchanger Ca affinity	3.6	µM	[189]
KmCao	Na/Ca exchanger Ca affinity	1.4e3	µM	[189]
ksat	Na/Ca exchanger	0.27	-	[189]
eta	Na/Ca exchanger	0.35	-	[189]
IpCamax	sarcolemmal Ca pump	0.006	pA/pF	adapted
Km_IpCa	sarcolemmal Ca pump Ca affinity	0.289	µM	adapted
Kfb	SERCA forward Ca affinity	0.3	µM	[189]
Krb	SERCA reverse Ca affinity	2.1e3	µM	[189]
N	sarcoplasmic reticulum Ca pump	1.787	-	[189]
vmax	SERCA max forward rate	328.9e-3	µM/ms	adapted

Ca^{2+} Background Current

$$ICab = g\_ICab \cdot (V - ECa)$$

Na^+/Ca^{2+} Exchanger

$$KmNao\_NaCa = \left(KmNai\_NaCa^3 \cdot \frac{KmCao\_NaCa}{KmCai\_NaCa}\right)^{1/3}$$

$$ssCai = Cai + 3 \cdot (Cai - 0.1)$$

$$INaCa = \frac{Vmax}{1 + ksat \cdot e^{(eta-1)\frac{VF}{RT}}} \cdot \frac{Nai^3 \cdot Cao \cdot e^{eta\frac{VF}{RT}} - Nao^3 \cdot ssCai \cdot e^{(eta-1)\frac{VF}{RT}}}{KmCao \cdot Nai^3 + KmNao \cdot ssCai + KmNai \cdot Cao \cdot (1 + \frac{ssCai}{KmCai}) + KmCai \cdot Nao^3 \cdot (1 + \frac{Nai^3}{KmNai^3}) + Nai^3 \cdot Cao + Nao^3 \cdot ssCai}$$

Sarcolemmal Ca^{2+} ATP-ase

$$IpCa = IpCamax \cdot \frac{Cai^2}{Km\_IpCa^2 + Cai^2}$$

Sarcoplasmic/Endoplasmic Reticulum Ca^{2+}-ATPase

$$Jup = vmax \cdot \frac{\left(\frac{Cai}{Kfb}\right)^N - \left(\frac{CaSR}{Krb}\right)^N}{1 + \left(\frac{Cai}{Kfb}\right)^N + \left(\frac{CaSR}{Krb}\right)^N}$$

Na^+ Channels

Parameter	Description	Value	Units	Source
g_INa	fast Na channel	13	mS/µF	[184]
g_INab	Na background current	0.002	mS/µF	adapted
INaKmax	Na/K pump max exchanger current	2	pA/pF	adapted
Km_Nai	Na/K pump Na affinity	18.8e3	µM	[177]
Km_Nao	Na/K pump K affinity	1.5e3	µM	[184]

Fast Na^+ Current

$$INa = g\_INa \cdot ONa \cdot (V - ENa)$$

$$aNa11 = \frac{3.802}{0.1027 \cdot e^{\frac{-(V+2.5)}{17}} + 0.2 \cdot e^{\frac{-(V+2.5)}{150}}}$$

$$bNa11 = 0.1917 \cdot e^{\frac{-(V+2.5)}{20.3}}$$

$$aNa12 = \frac{3.802}{0.1027 \cdot e^{\frac{-(V+2.5)}{17}} + 0.23 \cdot e^{\frac{-(V+2.5)}{150}}}$$

$$bNa12 = 0.2 \cdot e^{\frac{-(V+2.5)}{20.3}}$$

$$aNa13 = \frac{3.802}{0.1027 \cdot e^{\frac{-(V+2.5)}{17}} + 0.25 \cdot e^{\frac{-(V-2.5)}{150}}}$$

$$bNa13 = 0.22 \cdot e^{\frac{-(V-7.5)}{20.3}}$$

$$aNa3 = 7e - 7 \cdot e^{\frac{-(V+7)}{7.7}}$$

$$bNa3 = 0.0084 + 0.00002 \cdot (V + 7)$$

$$aNa2 = \frac{1}{0.188495 \cdot e^{\frac{-(V+7)}{16.6}} + 0.393956}$$

$$bNa2 = \frac{aNa13 \cdot aNa2 \cdot aNa3}{bNa13 \cdot bNa3}$$

$$aNa4 = \frac{aNa2}{1000}$$

$$bNa4 = aNa3$$

$$aNa5 = \frac{aNa2}{95000}$$

$$bNa5 = \frac{aNa3}{50}$$

$$\frac{dCNa1}{dt} = -(bNa12 + aNa13 + bNa3) \cdot CNa1 + aNa12 \cdot CNa2 + bNa13 \cdot ONa + aNa3 \cdot IFNa$$

$$\frac{dCNa2}{dt} = -(bNa11 + aNa12 + bNa3) \cdot CNa2 + aNa11 \cdot CNa3 + bNa12 \cdot CNa1 + aNa3 \cdot ICNa2$$

$$\frac{dIFNa}{dt} = -(bNa2 + aNa3 + aNa4 + bNa12) \cdot IFNa + aNa2 \cdot ONa + bNa3 \cdot CNa1 + bNa4 \cdot INa1 + aNa12 \cdot ICNa2$$

$$\frac{dINa1}{dt} = -(bNa4 + aNa5) \cdot INa1 + aNa4 \cdot IFNa + bNa5 \cdot INa2$$

$$\frac{dINa2}{dt} = -bNa5 \cdot INa2 + aNa5 \cdot INa1$$

$$\frac{dICNa2}{dt} = -(bNa11 + aNa12 + aNa3) \cdot ICNa2 + aNa11 \cdot ICNa3 + bNa12 \cdot IFNa + bNa3 \cdot ICNa$$

$$\frac{dICNa3}{dt} = -(aNa11 + aNa3) \cdot ICNa3 + bNa11 \cdot ICNa2 + bNa3 \cdot CNa3$$

$$\frac{dONa}{dt} = -(bNa13 + aNa2) \cdot ONa + aNa13 \cdot CNa + bNa2 \cdot IFNa$$

$$CNa3 = 1 - (ONa + CNa1 + CNa2 + IFNa + INa1 + INa2 + ICNa2 + ICNa3)$$

Na^+ Background Current

$$INab = g\_INab \cdot (V - ENa)$$

Na^+/K^+ ATPase

$$INaK = INaKmax \cdot f_{NaK} \cdot \frac{Nai^{3.2}}{Km\_Nai^{3.2} + Nai^{3.2}} \cdot \frac{Ko}{Km\_Ko + Ko}$$

$$\sigma = \frac{1}{7} \cdot \left(e^{\frac{Nao}{67300}} - 1\right)$$

$$f_{NaK} = \frac{1}{1 + 0.1245 \cdot e^{\frac{-0.1VF}{RT}} + 0.0365 \cdot \sigma \cdot e^{\frac{-VF}{RT}}}$$

K^+ Channels

Parameter	Description	Value	Units	Source
g_IKtof	fast transient outward K current	0.26	mS/µF	adapted
g_IKss	non-inactivating steady-state K current	0.047	mS/µF	adapted
g_IKs	slow delayed rectifier K current	0.00575	mS/µF	[184]
IKr_kb	rapid delayed rectifier K current	0.036778	1/ms	[184]
IKr_kf	rapid delayed rectifier K current	0.023761	1/ms	[184]
g_IKr	rapid delayed rectifier K current	0.078	mS/µF	[184]
g_IKur	ultra-rapid delayed rectifier K current	0.2	mS/µF	adapted

Fast Transient Outward K^+ Current

$$IKtof = g\_IKtof \cdot atof^3 \cdot itof \cdot (V - EK)$$

$$\alpha_a = 0.18064 \cdot e^{0.03577 \cdot (V+30)}$$

$$\beta_a = 0.3956 \cdot e^{-0.06237 \cdot (V+30)}$$

$$\alpha_i = \frac{0.000152 \cdot e^{\frac{-(V+13.5)}{7}}}{0.0067083 \cdot e^{\frac{-(V+33.5)}{7}} + 1}$$

$$\beta_i = \frac{0.00095 \cdot e^{\frac{V+33.5}{7}}}{0.051335 \cdot e^{\frac{V+33.5}{7}} + 1}$$

$$\frac{datof}{dt} = \alpha_a \cdot (1 - atof) - \beta_a \cdot atof$$

$$\frac{ditof}{dt} = \alpha_i \cdot (1 - itof) - \beta_i \cdot itof$$

Non-Inactivating Steady-State K^+ Current

$$IKss = g\_IKss \cdot aKss \cdot (V - EK)$$

$$ass = \frac{1}{1 + e^{-(V+22.5)/7.7}}$$

$$\tau_{IKss} = 39.3 \cdot e^{-0.0862 \cdot V} + 13.17$$

$$\frac{daKss}{dt} = \frac{ass - aKss}{\tau_{IKss}}$$

Rapid Delayed Inward Rectifier K^+ Current

$$IKr = g\_IKr \cdot OK \cdot \left[V - \frac{RT}{F} \cdot \ln\left(\frac{0.98 \cdot Ko + 0.02 \cdot Nao}{0.98 \cdot Ki + 0.02 \cdot Nai}\right)\right]$$

$$\alpha_{a0} = 0.022348 \cdot e^{0.1176 \cdot V}$$

$$\beta_{a0} = 0.047002 \cdot e^{-0.0631 \cdot V}$$

$$\alpha_{a1} = 0.013733 \cdot e^{0.038198 \cdot V}$$

$$\beta_{a1} = 0.0000689 \cdot e^{-0.04178 \cdot V}$$

$$\alpha_i = 0.090821 \cdot e^{0.023391 \cdot (V+5)}$$

$$\beta_i = 0.006497 \cdot e^{-0.03268 \cdot (V+5)}$$

$$\frac{dCK1}{dt} = -(\beta_{a0} + IKr\_kf) \cdot CK1 + \alpha_{a0} \cdot CK0 + IKr_{kb} \cdot CK2$$

$$\frac{dCK2}{dt} = -(IKr\_kb + \alpha_{a1}) \cdot CK2 + IKr_{kf} \cdot CK1 + \beta_{a1} \cdot OK$$

$$\frac{dIK}{dt} = -\beta_i \cdot IK + \alpha_i \cdot OK$$

$$\frac{dOK}{dt} = -(\beta_{a1} + \alpha_i) \cdot OK + \alpha_{a1} \cdot CK2 + \beta_i \cdot CKI$$

$$CK0 = 1 - CK1 - CK2 - OK - IK$$

Slow Delayed Inward Rectifier K^+ Current

$$IKs = g\_IKS \cdot {n_{Ks}}^2 \cdot (V - EK)$$

$$a_n = \frac{0.00000481333 \cdot (V + 26.5)}{1 - e^{-0.128 \cdot (V+26.5)}}$$

$$\beta_n = 0.0000953333 \cdot e^{-0.038 \cdot (V+26.5)}$$

$$\frac{dn_{Ks}}{dt} = \alpha_n \cdot (1 - n_{Ks}) - \beta_n \cdot n_{Ks}$$

Ultra-Rapid Delayed Inward Rectifier K^+ Current

$$IKur = g\_IKur \cdot aur \cdot iur \cdot (V - EK)$$

$$ass = \frac{1}{1 + e^{-(V+22.5)/7.7}}$$

$$\tau_{aur} = 0.493 \cdot e^{-0.0629 \cdot V} + 2.058$$

$$iss = \frac{1}{1 + e^{(V+45.2)/5.7}}$$

$$\tau_{iur} = 1200 - \frac{170}{1 + e^{\frac{V+45.2}{5.7}}}$$

$$\frac{daur}{dt} = \frac{ass - aur}{\tau_{aur}}$$

$$\frac{diur}{dt} = \frac{iss - iur}{\tau_{iur}}$$

Time-Independent Inward Rectifier K^+ Current

$$IK1 = \frac{0.25 \cdot Ko}{Ko + 210} \cdot \frac{V - EK}{1 + e^{0.0896 \cdot (V - EK)}}$$

Membrane Potential

$$\frac{dV}{dt} = \frac{-1}{Cm} \cdot (ICaL + IpCa + INaCa + ICab + INa + INab + INaK + IKtof + IK1 + IKs + IKur + IKss + IKr + Istim)$$

Ion Concentrations

$$\frac{dCai}{dt} = Jxfer \cdot \frac{Vss}{Vmyo} - \left[Jup + \frac{Csa}{2 \cdot Vmyo \cdot F} \cdot (ICab + IpCa - 2 \cdot INaCa)\right] - (dTnCLCa + dTnCHCa + dMyosinCa + dCaMCa + dCaSRb + dCaSL + dCaSLh + dCaATP + dCaPCR)$$

$$\frac{dCaSR}{dt} = CaBSR \cdot \left(Jup \cdot \frac{Vmyo}{VSR} + JRyR \cdot \frac{VSS}{VSR} - JSRleak \cdot \frac{VSS}{VSR}\right)$$

$$\frac{dNai}{dt} = \frac{-Csa}{2 \cdot Vmyo \cdot F} \cdot (INa + INab + 3 \cdot INaK + 3 \cdot INaCa)$$

$$\frac{dKi}{dt} = \frac{-Csa}{2 \cdot Vmyo \cdot F} \cdot (IKtof + IK1 + IKs + IKss + IKur + IKr - 2 \cdot INaK + Istim)$$

β_1-Adrenergic Signaling Effects

Ca^{2+} Buffering

$$koff\_TnCL = \left(0.5524 \cdot \frac{TnIp}{TnItot} + 0.9923\right) \cdot koff\_TnCL$$

L-Type Ca^{2+} Channel

$$f_{mode1} = -0.4212 \cdot \frac{LCCap}{LCCtot} + 1.0413$$

$$g_L = \frac{0.161214 \cdot f_{mode1} + 0.545455}{-0.189663 \cdot f_{mode1} + 0.545455}$$

$$PCaL = \left(1.3047 \cdot \frac{LCCbp}{LCCtot} + 0.8509\right) \cdot PCaL$$

Na^{+}/K^{+} ATPase

$$Km\_Nai = \left(1.0099 \cdot \frac{PLMp}{PLMtot} - 0.3551\right) \cdot Km\_Nai$$

Sarcoplasmic/Endoplasmic Reticulum Ca^{2+}-ATPase

$$Kfb = \left(1.0071 - 0.545 \cdot \frac{PLBp}{PLBtot}\right) \cdot Kfb$$

Transgenic Mouse Myocytes

PLM-KO

Parameter	Description	Value	Units	Source
JRyRmax	unitary Ca^{2+} flux rate through RyR	23.52	1/mS	adapted

PLB-KO

Parameter	Description	Value	Units	Source
g_INab	Na background current	0.0048	mS/μF	adapted
INaKmax	Na/K pump max exchanger current	1.6	pA/pF	adapted

Appendix 2

Angiotensin II Receptor-Stimulated Fibrosis Model

AT_1 and AT_2 Receptor Binding

Parameter	Description	Value	Units	Source
AngIItot	total Angiotensin II	0.0060535	µM	[338-339]
AT1Rtot	total Type 1 Ang II receptor	0.160308	µM	[243]
AT2Rtot	total Type 2 Ang II receptor	0.011972	µM	[243]
kon_AngII_AT1R	kon for AT_1R activation	1e-5	1/[µM ms]	[243]
koff_AngII_AT1R	koff for AT_1R activation	9.5e-9	1/ms	[243]
kon_AngII_AT2R	kon for AT_2R activation	1e-6	1/[µM ms]	[243]
koff_AngII_AT2R	koff for AT_2R activation	9.5e-9	1/ms	[243]

$$AngII = AngIItot - AT1R\_AngII - AT2R\_AngII$$

$$AT1R = AT1Rtot - AT1R\_AngII$$

$$AT2R = AT2Rtot - AT2R\_AngII$$

$$\frac{dAT1R\_AngII}{dt} = kon\_AngII\_AT1R \cdot AngII \cdot AT1R - koff\_AngII\_AT1R \cdot AT1R\_AngII$$

$$\frac{dAT2R\_AngII}{dt} = kon\_AngII\_AT2R \cdot AngII \cdot AT2R - koff\_AngII\_AT2R \cdot AT2R\_AngII$$

Ras Activation

Parameter	Description	Value	Units	Source
Rastot	total Ras	0.4	µM	[340]
k_AT1R_Ras	Ras activation by AT_1R	0.0039	1/ms	[341-342]
Km_AT1R_Ras	AT_1R affinity for AT_1R	0.386	µM	[341-342]
k_SHP_Ras	SHP-mediated Ras deactivation	0.0054	1/ms	[232-233]
Km_SHP_Ras	SHP-mediated Ras deactivation	0.23	µM	[232-233]

$$Ras = Rastot - Rasact$$

$$\frac{dRasact}{dt} = \frac{k\_AT1R\_Ras \cdot AT1R\_AngII \cdot Ras}{Km\_AT1R\_Ras + Ras} - \frac{k\_SHP\_Ras \cdot SHPp \cdot Rasact}{Km\_SHP\_Ras + Rasact}$$

Raf / MEK / ERK Activation

Parameter	Description	Value	Units	Source
Raftot	total Raf	0.013	µM	[340]
k_Ras_Raf	Raf phosphorylation by Ras	1.53e-6	1/ms	[343]
Km_Ras_Raf	Ras affinity for Raf	0.117	µM	[343]
k_PP2A_Raf	Raf dephosphorylation by PP2A	3.365e-6	1/ms	[239]
Km_PP2A_Raf	PP2A affinity for Raf	8.07e-3	µM	[343]

$$Raf = Raftot - Rafp$$

$$\frac{dRafp}{dt} = \frac{k\_Ras\_Raf \cdot Rasact \cdot Raf}{Km\_Ras\_Raf + Raf} - \frac{k\_PP2A\_Raf \cdot PP2A \cdot Rafp}{Km\_PP2A\_Raf + Rafp}$$

Parameter	Description	Value	Units	Source
MEKtot	total MEK	1.4	µM	[340]
k_Raf_MEK	MEK phosphorylation by Raf	9e-4	1/ms	[340]
Km_Raf_MEK	Raf affinity for MEK	0.3769	µM	[340]
k_PP2A_MEK	MEK dephosphorylation by PP2A	1e-5	1/ms	[340]
Km_PP2A_MEK	PP2A affinity for MEK	0.06	µM	[343]

$$MEK = MEKtot - MEKp$$

$$\frac{dRafp}{dt} = \frac{k\_Ras\_MEK \cdot Rafp \cdot MEK}{Km\_Raf\_MEK + MEK} - \frac{k\_PP2A\_MEK \cdot PP2A \cdot MEKp}{Km\_PP2A\_MEK + MEKp}$$

Parameter	Description	Value	Units	Source
ERKtot	total ERK	0.96	µM	[340]
k_MEK _ERK	ERK phosphorylation by MEK	2.2e-4	1/ms	[340]
Km_MEK_ERK	MEK affinity for ERK	0.35	µM	[340]
k_MKP_ERK	ERK dephosphorylation by PP2A	2.1e-4	1/ms	[340]
Km_MKP_ERK	PP2A affinity for ERK	0.06	µM	[343]

$$ERK = ERKtot - ERKp$$

$$\frac{dERKp}{dt} = \frac{k\_MEK\_ERK \cdot MEKp \cdot ERK}{Km\_MEK\_ERK + ERK} - \frac{k\_MKP\_ERK \cdot MKPp \cdot ERKp}{Km\_MKP\_ERK + ERKp}$$

MEKK / SEK / JNK Activation

Parameter	Description	Value	Units	Source
MEKKtot	total MEKK	0.1	µM	[233]
k_Ras_MEKK	Raf phosphorylation by MEKK	3.12e-6	1/ms	[233]
Km_Ras_MEKK	Ras affinity for MEKK	0.117	µM	[233]
k_MKP_MEKK	MEKK dephosphorylation by MKP	3.365e-6	1/ms	[233]
Km_MKP_MEKK	MKP affinity for MEKK	8.07e-3	µM	[233]

$$MEKK = MEKKtot - MEKKp$$

$$\frac{dMEKKp}{dt} = \frac{k\_Ras\_MEKK \cdot Rasact \cdot MEKK}{Km\_Ras\_MEKK + MEKK} - \frac{k\_MKP\_MEKKp \cdot MKPp \cdot MEKKp}{Km\_MKP\_MEKK + MEKKp}$$

Parameter	Description	Value	Units	Source
SEKtot	total SEK	1.2	µM	[344]
k_MEKK_SEK	SEK phosphorylation by MEKK	9e-6	1/ms	[233]
Km_MEKK_SEK	MEKK affinity for SEK	0.03769	µM	[233]
k_MKP_SEK	SEK dephosphorylation by MKP	1e-4	1/ms	[233]
Km_ MKP _SEK	MKP affinity for SEK	12	µM	[233]

$$SEK = SEKtot - SEKp$$

$$\frac{dSEKp}{dt} = \frac{k\_MEKK\_SEK \cdot MEKKp \cdot SEK}{Km\_MEKK\_SEK + SEK} - \frac{k\_MKP\_SEK \cdot MKPp \cdot SEKp}{Km\_MKP\_SEK + SEKp}$$

Parameter	Description	Value	Units	Source
ERKtot	total ERK	1.2	µM	[344]
k_MEK _ERK	ERK phosphorylation by MEK	2.2e-6	1/ms	[233]
Km_MEK_ERK	MEK affinity for ERK	0.035	µM	[233]
k_MKP_ERK	ERK dephosphorylation by PP2A	2.8e-4	1/ms	[233]
Km_MKP_ERK	PP2A affinity for ERK	12	µM	[233]

$$JNK = JNKtot - JNKp$$

$$\frac{dJNKp}{dt} = \frac{k\_SEK\_JNK \cdot SEKp \cdot JNK}{Km\_SEK\_JNK + JNK} - \frac{k\_MKP\_JNK \cdot MKPp \cdot JNKp}{Km\_MKP\_JNK + JNKp}$$

Phosphatase Activation

Parameter	Description	Value	Units	Source
SHPtot	total SHP	0.1	µM	[345-346]
k_AT2R_SHP	SHP activation by AT_2Rs	1.7e-4	1/ms	[234-235]
Km_AT2R_SHP	AT_2R affinity for SHP	1.4e-3	µM	[347]
k_SHP_SHP	SHP auto-dephosphorylation by SHP	2.5e-7	1/ms	[234-235]
Km_SHP_SHP	SHP affinity for SHP	0.9	µM	[234-235]

$$SHP = SHPtot - SHPp$$

$$\frac{dSHPp}{dt} = \frac{k\_AT2R\_SHP \cdot AT2R\_AngII \cdot SHP}{Km\_AT2R\_SHP + SHP} - \frac{k\_SHP\_SHP \cdot SHPp \cdot SHPp}{Km\_SHP\_SHP + SHPp}$$

Parameter	Description	Value	Units	Source
PP2Atot	total PP2A	0.22	μM	[348]
CaMKII	total CaMKII	0.2	μM	[111]
k_AT2R_PP2A	PP2A activation by AT_2R	2.5e-4	1/ms	[239]
Km_ AT2R_PP2A	PP2A affinity for AT_2R	1.7	μM	[239]
k_CaMKII_PP2A	CaMKII phosphorylation of PP2A	1.75e-6	1/ms	[239]
Km_ CaMKII_PP2A	CaMKII affinity for PP2A	5.1	μM	[349-350]

$$PP2Ap = PP2Atot - PP2A$$

$$\frac{dPP2A}{dt} = \frac{k\_AT2R\_PP2A \cdot AT2R\_AngII \cdot PP2Ap}{Km\_AT2R\_PP2A + PP2Ap} - \frac{k\_CaMKII\_PP2A \cdot CaMKII \cdot PP2A}{Km\_CaMKII\_PP2A + PP2A}$$

Parameter	Description	Value	Units	Source
MKPtot	total ERK	0.2	μM	[343]
k_AT2R_MKP	MKP activation by AT_2R	2.25e-4	1/ms	[237]
Km_AT2R_MKP	MKP affinity for AT_2R	1.9	μM	[237]
k_PP2A_MKP	MKP dephosphorylation by PP2A	1e-6	1/ms	[237]
Km_PP2A_MKP	PP2A affinity for MKP	1	μM	[237]

$$MKP = MKPtot - MKPp$$

$$\frac{dMKPp}{dt} = \frac{k\_AT2R\_MKP \cdot AT2R\_AngII \cdot MKP}{Km\_AT2R\_MKP + MKP} - \frac{k\_PP2A\_MKP \cdot PP2A \cdot MKPp}{Km\_PP2A\_MKP + MKPp}$$

Appendix C

cAMP Compartmentation Model

Classical vs. Nuclear PKA (nucPKA) Model

Endogenous Adenylyl Cyclases

Parameter	Description	Classical	nucPKA	Units	Source
ACtot	total adenylyl cyclase	10	10	µM	[5]
kf_AC_FSK	adenylyl cyclase activation by FSK	1.286e-4	6.181e-4	1/[µM s]	fitted
kr_AC_FSK	adenylyl cyclase activation by FSK	5.659e-3	2.720e-2	1/s	fitted
k_AC_basal	basal AC activity	5.334e-3	5.801e-3	1/s	fitted
k_AC_FSK	FSK-stimulated AC activity	0.2077	0.2195	1/s	fitted

cAMP / PKA Transport

Parameter	Description	Classical	nucPKA	Units	Source
V_pm	volume of plasma membrane	0.04	0.04	pL	[351]
V_cyt	volume of cytosol	2	2	pL	[351]
V_nuc	volume of nucleus	0.5	0.5	pL	[352]
D_cAMP_pm_cyt	cAMP diffusion rate	2.453e-3	2.507e-3	pL/s	fitted
D_cAMP_cyt_nuc	cAMP diffusion rate	5.339e-3	2.832e-3	pL/s	fitted
D_PKA_pm_cyt	PKA diffusion rate	1.209e-3	2.80e-2	pL/s	fitted
D_PKA_cyt_nuc	PKA diffusion rate	1.060e-4	9.509e-4	pL/s	fitted

Soluble Adenylyl Cyclases

Parameter	Description	Classical	nucPKA	Units	Source
E_sAC_pm_basal	plasma membrane sAC	0.40501	0.5639	mM/s	fitted
E_sAC_pm_step	plasma membrane sAC	3.342e-3	1.403e-3	mM/s	fitted
E_sAC_cyt_basal	cytosolic sAC	6.544e-2	5.828e-2	mM/s	fitted
E_sAC_cyt_step	cytosolic sAC	0.4953	0.2825	mM/s	fitted
E_sAC_nuc_basal	nuclear sAC	7.107e-3	5.326e-3	mM/s	fitted
E_sAC_nuc_step	nuclear sAC	2.850e-2	4.141e-2	mM/s	fitted

Phosphodiesterases

Parameter	Description	Classical	nucPKA	Units	Source
PDEtot_pm	total PDE at membrane	0.9443	0.8539	mM	fitted
PDEtot_cyt	total PDE at cytosol	1.492e-3	2.415e-2	mM	fitted
PDEtot_nuc	total PDE at nucleus	0.2313	0.4260	mM	fitted
k_PDE	cAMP hydrolysis rate	0.15	0.15	1/s	[261]
k_PDEp	cAMP hydrolysis rate	0.375	0.375	1/s	[261]
Km_PDE	PDE affinity for cAMP	1	1	mM	[261]
k_PKA_PDE	PDE phosphorylation	0.015	0.015	1/[mM s]	[260]
k_PP_PDE	PDE dephosphorylation	0.005	0.005	1/s	[260]
KI_IBMX	PDE inhibition by IBMX	11	11	mM	[260]

PKA

Parameter	Description	Classical	nucPKA	Units	Source
k_f_a	PKA activation by cAMP	5	5	1/[mM s]	[260]
k_r_a	PKA activation by cAMP	1	1	1/s	[260]
k_f_b	PKA activation by cAMP	0.4	0.4	1/[mM s]	[260]
k_r_b	PKA activation by cAMP	0.2	0.2	1/s	[260]
k_act	PKA activation by cAMP	70	70	1/s	[260]
k_deact	PKA activation by cAMP	0.75	0.75	$1/[mM^2\ s]$	[260]

Phosphatases

Parameter	Description	Classical	nucPKA	Units	Source
PP_pm	total membrane phosphatase	2.497	2.599	mM	fitted
PP_cyt	total cytosolic phosphatase	2.512	2.144	mM	fitted
PP_nuc	total nuclear phosphatase	2.501	2.430	mM	fitted

ICUE / AKAR FRET Reporters

Parameter	Description	Classical	nucPKA	Units	Source
ICUEtot_pm	total membrane ICUE	0.065	0.065	mM	estimated
ICUEtot_cyt	total cytosolic ICUE	0.15	0.15	mM	estimated
ICUEtot_nuc	total nuclear ICUE	0.25	0.25	mM	estimated
k_f_ICUE	ICUE activation by cAMP	5	5	1/[mM s]	[260]
k_r_ICUE	ICUE activation by cAMP	10	10	1/s	[276]
AKARtot_pm	total membrane AKAR	0.69	0.69	mM	estimated
AKARtot_cyt	total cytosolic AKAR	1.25	1.25	mM	estimated
AKARtot_nuc	total nuclear AKAR	3.48	3.48	mM	estimated
k_PKA_AKAR	AKAR phosphorylation	21	21	1/s	[4]
Km_PKA_AKAR	AKAR phosphorylation	54	54	mM	[4]
k_PP_AKAR	AKAR dephosphorylation	8.5	8.5	1/[mM s]	[4]

Plasma Membrane Equations

$$cAMP\_pm = cAMPtot\_pm - RaC\_pm - RbC\_pm - 2 \cdot RabC\_pm - Ra\_pm - Rb\_pm - 2 \cdot Rab\_pm - ICUEc\_pm$$

$$PDE\_pm = PDEtot\_pm - PDEp\_pm$$

$$ICUE\_pm = ICUEtot\_pm - ICUEc\_pm$$

$$AKAR\_pm = AKARtot\_pm - AKARp\_pm$$

$$AC = ACtot - AC\_FSK$$

$$\frac{dAC\_FSK}{dt} = kf\_AC\_FSK \cdot AC \cdot FSK - kr\_AC\_FSK \cdot AC\_FSK$$

$$E\_AC = k\_AC\_basal \cdot AC + k\_AC\_FSK \cdot AC\_FSK$$

$$E\_AC\_pm = E\_AC + E\_sAC\_pm$$

$$\frac{dcAMPtot\_pm}{dt} = E\_AC\_pm - \frac{PDE\_pm \cdot cAMP\_pm \cdot k\_PDE}{cAMP\_pm + Km\_PDE \cdot \left(1 + \frac{IBMX}{KI\_IBMX}\right)} - \frac{PDEp\_pm \cdot cAMP\_pm \cdot k\_PDEp}{cAMP\_pm + Km\_PDE \cdot \left(1 + \frac{IBMX}{KI\_IBMX}\right)} - \frac{D\_cAMP\_pm\_cyt}{V\_pm} \cdot (cAMPtot\_pm - cAMPtot\_cyt)$$

$$\frac{dPDEp\_pm}{dt} = k\_PKA\_PDE \cdot C\_pm \cdot PDE\_pm - k\_PP\_PDE \cdot PP\_pm \cdot PDEp\_pm$$

$$\frac{dR\_pm}{dt} = -(k\_f\_a + k\_f\_b) \cdot cAMP\_pm \cdot R\_pm + k\_r\_a \cdot Ra\_pm + k\_r\_b \cdot Rb\_pm - k\_deact \cdot R\_pm \cdot C\_pm \cdot C\_pm$$

$$\frac{dRa\_pm}{dt} = -k\_f\_b \cdot cAMP\_pm \cdot Ra\_pm - k\_r\_a \cdot Ra\_pm + k\_f\_a \cdot cAMP\_pm \cdot R\_pm + k\_r\_b \cdot Rab\_pm - k\_deact \cdot Ra\_pm \cdot C\_pm \cdot C\_pm$$

$$\frac{dRb\_pm}{dt} = -k\_f\_a \cdot cAMP\_pm \cdot Rb\_pm - k\_r\_b \cdot Rb\_pm + k\_f\_b \cdot cAMP\_pm \cdot R\_pm + k\_r\_a \cdot Rab\_pm - k\_deact \cdot Rb\_pm \cdot C\_pm \cdot C\_pm$$

$$\frac{dRab\_pm}{dt} = -(k\_r\_a + k\_r\_b) \cdot Rab\_pm + k\_f\_b \cdot cAMP\_pm \cdot Ra\_pm + k\_f\_a \cdot cAMP\_pm \cdot Rb\_pm + k\_act \cdot RabC\_pm$$

$$\frac{dRC\_pm}{dt} = -(k\_f\_a + k\_f\_b) \cdot cAMP\_pm \cdot RC\_pm + k\_r\_a \cdot RaC\_pm + k\_r\_b \cdot RbC\_pm + k\_deact \cdot R\_pm \cdot C\_pm \cdot C\_pm$$

$$\frac{dRaC\_pm}{dt} = -k\_f\_b \cdot cAMP\_pm \cdot RaC\_pm - k\_r\_a \cdot RaC\_pm + k\_f\_a \cdot cAMP\_pm \cdot RC\_pm + k\_r\_b \cdot RabC\_pm - k\_deact \cdot Ra\_pm \cdot C\_pm \cdot C\_pm$$

$$\frac{dRbC\_pm}{dt} = -k\_f\_a \cdot cAMP\_pm \cdot RbC\_pm - k\_r\_b \cdot RbC\_pm + k\_f\_b \cdot cAMP\_pm \cdot RC\_pm + k\_r\_a \cdot RabC\_pm - k\_deact \cdot Rb\_pm \cdot C\_pm \cdot C\_pm$$

$$\frac{dRabC\_pm}{dt} = -(k\_r\_a + k\_r\_b + k\_act) \cdot RabC\_pm + k\_f\_b \cdot cAMP\_pm \cdot RaC\_pm + k\_f\_a \cdot cAMP\_pm \cdot RbC\_pm$$

$$\frac{dC\_pm}{dt} = -k\_deact \cdot C\_pm \cdot C\_pm \cdot (R\_pm + Ra\_pm + Rb\_pm) + k\_act \cdot RabC\_pm - \frac{D\_PKA\_pm\_cyt}{V\_pm} \cdot (C\_pm - C\_cyt)$$

$$\frac{dICUEc\_pm}{dt} = kon\_ICUE \cdot cAMP\_pm \cdot ICUE\_pm - koff\_ICUE \cdot ICUEc\_pm$$

$$\frac{dAKARp\_pm}{dt} = \frac{k\_PKA\_AKAR \cdot C\_pm \cdot AKAR\_pm}{Km\_PKA\_AKAR + AKAR\_pm} \cdot AKARp\_pm - k\_PP\_AKAR \cdot PP\_pm$$

Cytosol Equations

$$cAMP\_cyt = cAMPtot\_cyt - RaC\_cyt - RbC\_cyt - 2 \cdot RabC\_cyt - Ra\_cyt - Rb\_cyt - 2 \cdot Rab\_cyt - ICUEc\_cyt$$

$$PDE\_cyt = PDEtot\_cyt - PDEp\_cyt$$

$$ICUE\_cyt = ICUEtot\_cyt - ICUEc\_cyt$$

$$AKAR\_cyt = AKARtot\_cyt - AKARp\_cyt$$

$$\frac{dcAMPtot\_cyt}{dt} = E\_AC\_cyt - \frac{PDE\_cyt \cdot cAMP\_cyt \cdot k\_PDE}{cAMP\_cyt + Km\_PDE \cdot \left(1 + \frac{IBMX}{KI\_IBMX}\right)} - \frac{PDEp\_cyt \cdot cAMP\_cyt \cdot k\_PDEp}{cAMP\_cyt + Km\_PDE \cdot \left(1 + \frac{IBMX}{KI\_IBMX}\right)} - \frac{D\_cAMP\_pm\_cyt}{V\_cyt} \cdot (cAMPtot\_cyt - cAMPtot\_pm) - \frac{D\_cAMP\_cyt\_nuc}{V\_cyt} \cdot (cAMPtot\_cyt - cAMPtot\_nuc)$$

$$\frac{dPDEp\_cyt}{dt} = k\_PKA\_PDE \cdot C\_cyt \cdot PDE\_cyt - k\_PP\_PDE \cdot PP\_cyt \cdot PDEp\_cyt$$

$$\frac{dR\_cyt}{dt} = -(k\_f\_a + k\_f\_b) \cdot cAMP\_cyt \cdot R\_cyt + k\_r\_a \cdot Ra\_cyt + k\_r\_b \cdot Rb\_cyt - k\_deact \cdot R\_cyt \cdot C\_cyt \cdot C\_cyt$$

$$\frac{dRa\_cyt}{dt} = -k\_f\_b \cdot cAMP\_cyt \cdot Ra\_cyt - k\_r\_a \cdot Ra\_cyt + k\_f\_a \cdot cAMP\_cyt \cdot R\_cyt + k\_r\_b \cdot Rab\_cyt - k\_deact \cdot Ra\_cyt \cdot C\_cyt \cdot C\_cyt$$

$$\frac{dRb\_cyt}{dt} = -k\_f\_a \cdot cAMP\_cyt \cdot Rb\_cyt - k\_r\_b \cdot Rb\_cyt + k\_f\_b \cdot cAMP\_cyt \cdot R\_cyt + k\_r\_a \cdot Rab\_cyt - k\_deact \cdot Rb\_cyt \cdot C\_cyt \cdot C\_cyt$$

$$\frac{dRab\_cyt}{dt} = -(k\_r\_a + k\_r\_b) \cdot Rab\_cyt + k\_f\_b \cdot cAMP\_cyt \cdot Ra\_cyt + k\_f\_a \cdot cAMP\_cyt \cdot Rb\_cyt + k\_act \cdot RabC\_cyt$$

$$\frac{dRC\_cyt}{dt} = -(k\_f\_a + k\_f\_b) \cdot cAMP\_cyt \cdot RC\_cyt + k\_r\_a \cdot RaC\_cyt + k\_r\_b \cdot RbC\_cyt + k\_deact \cdot R\_cyt \cdot C\_cyt \cdot C\_cyt$$

$$\frac{dRaC\_cyt}{dt} = -k\_f\_b \cdot cAMP\_cyt \cdot RaC\_cyt - k\_r\_a \cdot RaC\_cyt + k\_f\_a \cdot cAMP\_cyt \cdot RC\_cyt + k\_r\_b \cdot RabC\_cyt - k\_deact \cdot Ra\_cyt \cdot C\_cyt \cdot C\_cyt$$

$$\frac{dRbC\_cyt}{dt} = -k\_f\_a \cdot cAMP\_cyt \cdot RbC\_cyt - k\_r\_b \cdot RbC\_cyt + k\_f\_b \cdot cAMP\_cyt \cdot RC\_cyt + k\_r\_a \cdot RabC\_cyt - k\_deact \cdot Rb\_cyt \cdot C\_cyt \cdot C\_cyt$$

$$\frac{dRabC\_cyt}{dt} = -(k\_r\_a + k\_r\_b + k\_act) \cdot RabC\_cyt + k\_f\_b \cdot cAMP\_cyt \cdot RaC\_cyt + k\_f\_a \cdot cAMP\_cyt \cdot RbC\_cyt$$

$$\frac{dC\_cyt}{dt} = -k\_deact \cdot C\_cyt \cdot C\_cyt \cdot (R\_cyt + Ra\_cyt + Rb\_cyt) + k\_act \cdot RabC\_cyt - \frac{D\_PKA\_pm\_cyt}{V\_cyt} \cdot (C\_cyt - C\_pm) - \frac{D\_PKA\_cyt\_nuc}{V\_cyt} \cdot (C\_cyt - C\_nuc)$$

$$\frac{dICUEc\_cyt}{dt} = kon\_ICUE \cdot cAMP\_cyt \cdot ICUE\_cyt - koff\_ICUE \cdot ICUEc\_cyt$$

$$\frac{dAKARp\_cyt}{dt} = \frac{k\_PKA\_AKAR \cdot C\_cyt \cdot AKAR\_cyt}{Km\_PKA\_AKAR + AKAR\_cyt} \cdot AKARp\_cyt - k\_PP\_AKAR \cdot PP\_cyt$$

Nucleus Equations

$$cAMP\_nuc = cAMPtot\_nuc - RaC\_nuc - RbC\_nuc - 2 \cdot RabC\_nuc - Ra\_nuc - Rb\_nuc - 2 \cdot Rab\_nuc - ICUEc\_nuc$$

$$PDE\_nuc = PDEtot\_nuc - PDEp\_nuc$$

$$ICUE\_nuc = ICUEtot\_nuc - ICUEc\_nuc$$

$$AKAR\_nuc = AKARtot\_nuc - AKARp\_nuc$$

$$\frac{dcAMPtot\_nuc}{dt} = E\_AC\_nuc - \frac{PDE\_nuc \cdot cAMP\_nuc \cdot k\_PDE}{cAMP\_nuc + Km\_PDE \cdot \left(1 + \frac{IBMX}{KI\_IBMX}\right)} - \frac{PDEp\_nuc \cdot cAMP\_nuc \cdot k\_PDEp}{cAMP\_nuc + Km\_PDE \cdot \left(1 + \frac{IBMX}{KI\_IBMX}\right)} - \frac{D\_cAMP\_cyt\_nuc}{V\_nuc} \cdot (cAMPtot\_nuc - cAMPtot\_cyt)$$

$$\frac{dPDEp\_nuc}{dt} = k\_PKA\_PDE \cdot C\_nuc \cdot PDE\_nuc - k\_PP\_PDE \cdot PP\_nuc \cdot PDEp\_nuc$$

$$\frac{dR\_nuc}{dt} = -(k\_f\_a + k\_f\_b) \cdot cAMP\_nuc \cdot R\_nuc + k\_r\_a \cdot Ra\_nuc + k\_r\_b \cdot Rb\_nuc - k\_deact \cdot R\_nuc \cdot C\_nuc \cdot C\_nuc$$

$$\frac{dRa\_nuc}{dt} = -k\_f\_b \cdot cAMP\_nuc \cdot Ra\_nuc - k\_r\_a \cdot Ra\_nuc + k\_f\_a \cdot cAMP\_nuc \cdot R\_nuc + k\_r\_b \cdot Rab\_nuc - k\_deact \cdot Ra\_nuc \cdot C\_nuc \cdot C\_nuc$$

$$\frac{dRb\_nuc}{dt} = -k\_f\_a \cdot cAMP\_nuc \cdot Rb\_nuc - k\_r\_b \cdot Rb\_nuc + k\_f\_b \cdot cAMP\_nuc \cdot R\_nuc + k\_r\_a \cdot Rab\_nuc - k\_deact \cdot Rb\_nuc \cdot C\_nuc \cdot C\_nuc$$

$$\frac{dRab\_nuc}{dt} = -(k\_r\_a + k\_r\_b) \cdot Rab\_nuc + k\_f\_b \cdot cAMP\_nuc \cdot Ra\_nuc + k\_f\_a \cdot cAMP\_nuc \cdot Rb\_nuc + k\_act \cdot RabC\_nuc$$

$$\frac{dRC\_nuc}{dt} = -(k\_f\_a + k\_f\_b) \cdot cAMP\_nuc \cdot RC\_nuc + k\_r\_a \cdot RaC\_nuc + k\_r\_b \cdot RbC\_nuc + k\_deact \cdot R\_nuc \cdot C\_nuc \cdot C\_nuc$$

$$\frac{dRaC\_nuc}{dt} = -k\_f\_b \cdot cAMP\_nuc \cdot RaC\_nuc - k\_r\_a \cdot RaC\_nuc + k\_f\_a \cdot cAMP\_nuc \cdot RC\_nuc + k\_r\_b \cdot RabC\_nuc - k\_deact \cdot Ra\_nuc \cdot C\_nuc \cdot C\_nuc$$

$$\frac{dRbC\_nuc}{dt} = -k\_f\_a \cdot cAMP\_nuc \cdot RbC\_nuc - k\_r\_b \cdot RbC\_nuc + k\_f\_b \cdot cAMP\_nuc \cdot RC\_nuc + k\_r\_a \cdot RabC\_nuc - k\_deact \cdot Rb\_nuc \cdot C\_nuc \cdot C\_nuc$$

$$\frac{dRabC\_nuc}{dt} = -(k\_r\_a + k\_r\_b + k\_act) \cdot RabC\_nuc + k\_f\_b \cdot cAMP\_nuc \cdot RaC\_nuc + k\_f\_a \cdot cAMP\_nuc \cdot RbC\_nuc$$

$$\frac{dC\_nuc}{dt} = -k\_deact \cdot C\_nuc \cdot C\_nuc \cdot (R\_nuc + Ra\_nuc + Rb\_nuc) + k\_act \cdot RabC\_nuc - \frac{D\_PKA\_cyt\_nuc}{V\_nuc} \cdot (C\_nuc - C\_cyt)$$

$$\frac{dICUEc\_nuc}{dt} = kon\_ICUE \cdot cAMP\_nuc \cdot ICUE\_nuc - koff\_ICUE \cdot ICUEc\_nuc$$

$$\frac{dAKARp\_nuc}{dt} = \frac{k\_PKA\_AKAR \cdot C\_nuc \cdot AKAR\_nuc}{Km\_PKA\_AKAR + AKAR\_nuc} \cdot AKARp\_nuc - k\_PP\_AKAR \cdot PP\_nuc$$

Classical vs. Nuclear PKA (nucPKA) vs. Nuclear AKAP (nucAKAP) Model

cAMP / PKA Transport

Parameter	Description	Classical	nucPKA	nucAKAP	Units
V_pm	volume of plasma membrane	0.04	0.04	0.04	pL
V_cyt	volume of cytosol	2	2	2	pL
V_nuc	volume of nucleus	0.5	0.5	0.5	pL
V_AKAP	volume of nuclear AKAP	-	-		pL
D_cAMP_pm_cyt	cAMP diffusion rate	2.536e-3	2.268e-3	1.697e-2	pL/s
D_cAMP_cyt_nuc	cAMP diffusion rate	5.280e-3	5.888e-4	1.783e-2	pL/s
D_cAMP_nuc_AKAP	cAMP diffusion rate	-	-	5.850e-3	pL/s
D_PKA_pm_cyt	PKA diffusion rate	1.249e-2	2.729e-2	4.613e-3	pL/s
D_PKA_cyt_nuc	PKA diffusion rate	1.337e-4	4.026e-3	3.410e-5	pL/s
D_PKA_nuc_AKAP	PKA diffusion rate	-	-	3.910e-3	pL/s

Soluble Adenylyl Cyclases

Parameter	Description	Classical	nucPKA	nucAKAP	Units
E_sAC_pm_basal	plasma membrane sAC	0.4048	0.5317	0.1663	mM/s
E_sAC_pm_step	plasma membrane sAC	2.973e-3	1.643e-3	8.556e-3	mM/s
E_sAC_cyt_basal	cytosolic sAC	6.482e-2	6.212e-2	2.121e-2	mM/s
E_sAC_cyt_step	cytosolic sAC	0.4943	5.915e-3	0.1726	mM/s
E_sAC_nuc_basal	nuclear sAC	7.637e-3	1.685e-3	1.059e-2	mM/s
E_sAC_nuc_step	nuclear sAC	3.640e-2	5.630e-2	3.941e-2	mM/s

Phosphodiesterases

Parameter	Description	Classical	nucPKA	nucAKAP	Units
PDEtot_pm	total PDE at membrane	0.9427	0.9942	0.8963	mM
PDEtot_cyt	total PDE at cytosol	0.01430	0.02121	0.01124	mM
PDEtot_nuc	total PDE at nucleus	0.2309	0.2874	8.215e-3	mM
PDEtot_AKAP	total PDE at AKAP	-	-	0.1695	mM
k_PDE	cAMP hydrolysis rate	0.15	0.15	0.15	1/s
k_PDEp	cAMP hydrolysis rate	0.375	0.375	0.375	1/s
Km_PDE	PDE affinity for cAMP	1	1	1	mM
k_PKA_PDE	PDE phosphorylation	0.015	0.015	0.015	1/[mM s]
k_PP_PDE	PDE dephosphorylation	0.005	0.005	0.005	1/s
KI_IBMX	PDE inhibition by IBMX	11	11	11	mM

PKA

Parameter	Description	Classical	nucPKA	nucAKAP	Units
k_f_a	PKA activation by cAMP	5	5	5	1/[mM s]
k_r_a	PKA activation by cAMP	1	1	1	1/s
k_f_b	PKA activation by cAMP	0.4	0.4	0.4	1/[mM s]
k_r_b	PKA activation by cAMP	0.2	0.2	0.2	1/s
k_act	PKA activation by cAMP	70	70	70	1/s
k_deact	PKA activation by cAMP	0.75	0.75	0.75	1/[mM^2 s]

Phosphatases

Parameter	Description	Classical	nucPKA	nucAKAP	Units
PP_pm	total membrane phosphatase	2.494	2.518	2.519	mM
PP_cyt	total cytosolic phosphatase	2.511	2.579	2.397	mM
PP_nuc	total nuclear phosphatase	2.500	2.519	2.578	mM
PP_AKAP	total AKAP phosphatase	-	-	10.15	mM

ICUE / AKAR FRET Reporters

Parameter	Description	Classical	nucPKA	nucAKAP	Units
ICUEtot_pm	total membrane ICUE	0.065	0.065	0.065	mM
ICUEtot_cyt	total cytosolic ICUE	0.15	0.15	0.15	mM
ICUEtot_nuc	total nuclear ICUE	0.25	0.25	0.25	mM
k_f_ICUE	ICUE activation by cAMP	5	5	5	1/[mM s]
k_r_ICUE	ICUE activation by cAMP	10	10	10	1/s
AKARtot_pm	total membrane AKAR	0.69	0.69	0.69	mM
AKARtot_cyt	total cytosolic AKAR	1.25	1.25	1.25	mM
AKARtot_nuc	total nuclear AKAR	3.48	3.48	3.48	mM
k_PKA_AKAR	AKAR phosphorylation	21	21	21	1/s
Km_PKA_AKAR	AKAR phosphorylation	54	54	54	mM
k_PP_AKAR	AKAR dephosphorylation	8.5	8.5	8.5	1/[mM s]

Plasma Membrane Equations

$$cAMP\_pm = cAMPtot\_pm - RaC\_pm - RbC\_pm - 2 \cdot RabC\_pm - Ra\_pm - Rb\_pm - 2 \cdot Rab\_pm - ICUEc\_pm$$

$$PDE\_pm = PDEtot\_pm - PDEp\_pm$$

$$ICUE\_pm = ICUEtot\_pm - ICUEc\_pm$$

$$AKAR\_pm = AKARtot\_pm - AKARp\_pm$$

$$AC = ACtot - AC\_FSK$$

$$\frac{dAC\_FSK}{dt} = kf\_AC\_FSK \cdot AC \cdot FSK - kr\_AC\_FSK \cdot AC\_FSK$$

$$E\_AC = k\_AC\_basal \cdot AC + k\_AC\_FSK \cdot AC\_FSK$$

$$E\_AC\_pm = E\_AC + E\_sAC\_pm$$

$$\frac{dcAMPtot\_pm}{dt} = E\_AC\_pm - \frac{PDE\_pm \cdot cAMP\_pm \cdot k\_PDE}{cAMP\_pm + Km\_PDE \cdot \left(1 + \frac{IBMX}{KI\_IBMX}\right)} - \frac{PDEp\_pm \cdot cAMP\_pm \cdot k\_PDEp}{cAMP\_pm + Km\_PDE \cdot \left(1 + \frac{IBMX}{KI\_IBMX}\right)} - \frac{D\_cAMP\_pm\_cyt}{V\_pm} \cdot (cAMPtot\_pm - cAMPtot\_cyt)$$

$$\frac{dPDEp\_pm}{dt} = k\_PKA\_PDE \cdot C\_pm \cdot PDE\_pm - k\_PP\_PDE \cdot PP\_pm \cdot PDEp\_pm$$

$$\frac{dR\_pm}{dt} = -(k\_f\_a + k\_f\_b) \cdot cAMP\_pm \cdot R\_pm + k\_r\_a \cdot Ra\_pm + k\_r\_b \cdot Rb\_pm - k\_deact \cdot R\_pm \cdot C\_pm \cdot C\_pm$$

$$\frac{dRa\_pm}{dt} = -k\_f\_b \cdot cAMP\_pm \cdot Ra\_pm - k\_r\_a \cdot Ra\_pm + k\_f\_a \cdot cAMP\_pm \cdot R\_pm + k\_r\_b \cdot Rab\_pm - k\_deact \cdot Ra\_pm \cdot C\_pm \cdot C\_pm$$

$$\frac{dRb\_pm}{dt} = -k\_f\_a \cdot cAMP\_pm \cdot Rb\_pm - k\_r\_b \cdot Rb\_pm + k\_f\_b \cdot cAMP\_pm \cdot R\_pm + k\_r\_a \cdot Rab\_pm - k\_deact \cdot Rb\_pm \cdot C\_pm \cdot C\_pm$$

$$\frac{dRab\_pm}{dt} = -(k\_r\_a + k\_r\_b) \cdot Rab\_pm + k\_f\_b \cdot cAMP\_pm \cdot Ra\_pm + k\_f\_a \cdot cAMP\_pm \cdot Rb\_pm + k\_act \cdot RabC\_pm$$

$$\frac{dRC\_pm}{dt} = -(k\_f\_a + k\_f\_b) \cdot cAMP\_pm \cdot RC\_pm + k\_r\_a \cdot RaC\_pm + k\_r\_b \cdot RbC\_pm + k\_deact \cdot R\_pm \cdot C\_pm \cdot C\_pm$$

$$\frac{dRaC\_pm}{dt} = -k\_f\_b \cdot cAMP\_pm \cdot RaC\_pm - k\_r\_a \cdot RaC\_pm + k\_f\_a \cdot cAMP\_pm \cdot RC\_pm + k\_r\_b \cdot RabC\_pm - k\_deact \cdot Ra\_pm \cdot C\_pm \cdot C\_pm$$

$$\frac{dRbC\_pm}{dt} = -k\_f\_a \cdot cAMP\_pm \cdot RbC\_pm - k\_r\_b \cdot RbC\_pm + k\_f\_b \cdot cAMP\_pm \cdot RC\_pm + k\_r\_a \cdot RabC\_pm - k\_deact \cdot Rb\_pm \cdot C\_pm \cdot C\_pm$$

$$\frac{dRabC\_pm}{dt} = -(k\_r\_a + k\_r\_b + k\_act) \cdot RabC\_pm + k\_f\_b \cdot cAMP\_pm \cdot RaC\_pm + k\_f\_a \cdot cAMP\_pm \cdot RbC\_pm$$

$$\frac{dC\_pm}{dt} = -k\_deact \cdot C\_pm \cdot C\_pm \cdot (R\_pm + Ra\_pm + Rb\_pm) + k\_act \cdot RabC\_pm - \frac{D\_PKA\_pm\_cyt}{V\_pm} \cdot (C\_pm - C\_cyt)$$

$$\frac{dICUEc\_pm}{dt} = kon\_ICUE \cdot cAMP\_pm \cdot ICUE\_pm - koff\_ICUE \cdot ICUEc\_pm$$

$$\frac{dAKARp\_pm}{dt} = \frac{k\_PKA\_AKAR \cdot C\_pm \cdot AKAR\_pm}{Km\_PKA\_AKAR + AKAR\_pm} \cdot AKARp\_pm - k\_PP\_AKAR \cdot PP\_pm$$

Cytosol Equations

$$cAMP\_cyt = cAMPtot\_cyt - RaC\_cyt - RbC\_cyt - 2 \cdot RabC\_cyt - Ra\_cyt - Rb\_cyt - 2 \cdot Rab\_cyt - ICUEc\_cyt$$

$$PDE\_cyt = PDEtot\_cyt - PDEp\_cyt$$

$$ICUE\_cyt = ICUEtot\_cyt - ICUEc\_cyt$$

$$AKAR\_cyt = AKARtot\_cyt - AKARp\_cyt$$

$$\frac{dcAMPtot\_cyt}{dt} = E\_AC\_cyt - \frac{PDE\_cyt \cdot cAMP\_cyt \cdot k\_PDE}{cAMP\_cyt + Km\_PDE \cdot \left(1 + \frac{IBMX}{KI\_IBMX}\right)} - \frac{PDEp\_cyt \cdot cAMP\_cyt \cdot k\_PDEp}{cAMP\_cyt + Km\_PDE \cdot \left(1 + \frac{IBMX}{KI\_IBMX}\right)} - \frac{D\_cAMP\_pm\_cyt}{V\_cyt} \cdot (cAMPtot\_cyt - cAMPtot\_pm) - \frac{D\_cAMP\_cyt\_nuc}{V\_cyt} \cdot (cAMPtot\_cyt - cAMPtot\_nuc)$$

$$\frac{dPDEp\_cyt}{dt} = k\_PKA\_PDE \cdot C\_cyt \cdot PDE\_cyt - k\_PP\_PDE \cdot PP\_cyt \cdot PDEp\_cyt$$

$$\frac{dR\_cyt}{dt} = -(k\_f\_a + k\_f\_b) \cdot cAMP\_cyt \cdot R\_cyt + k\_r\_a \cdot Ra\_cyt + k\_r\_b \cdot Rb\_cyt - k\_deact \cdot R\_cyt \cdot C\_cyt \cdot C\_cyt$$

$$\frac{dRa\_cyt}{dt} = -k\_f\_b \cdot cAMP\_cyt \cdot Ra\_cyt - k\_r\_a \cdot Ra\_cyt + k\_f\_a \cdot cAMP\_cyt \cdot R\_cyt + k\_r\_b \cdot Rab\_cyt - k\_deact \cdot Ra\_cyt \cdot C\_cyt \cdot C\_cyt$$

$$\frac{dRb\_cyt}{dt} = -k\_f\_a \cdot cAMP\_cyt \cdot Rb\_cyt - k\_r\_b \cdot Rb\_cyt + k\_f\_b \cdot cAMP\_cyt \cdot R\_cyt + k\_r\_a \cdot Rab\_cyt - k\_deact \cdot Rb\_cyt \cdot C\_cyt \cdot C\_cyt$$

$$\frac{dRab\_cyt}{dt} = -(k\_r\_a + k\_r\_b) \cdot Rab\_cyt + k\_f\_b \cdot cAMP\_cyt \cdot Ra\_cyt + k\_f\_a \cdot cAMP\_cyt \cdot Rb\_cyt + k\_act \cdot RabC\_cyt$$

$$\frac{dRC\_cyt}{dt} = -(k\_f\_a + k\_f\_b) \cdot cAMP\_cyt \cdot RC\_cyt + k\_r\_a \cdot RaC\_cyt + k\_r\_b \cdot RbC\_cyt + k\_deact \cdot R\_cyt \cdot C\_cyt \cdot C\_cyt$$

$$\frac{dRaC\_cyt}{dt} = -k\_f\_b \cdot cAMP\_cyt \cdot RaC\_cyt - k\_r\_a \cdot RaC\_cyt + k\_f\_a \cdot cAMP\_cyt \cdot RC\_cyt + k\_r\_b \cdot RabC\_cyt - k\_deact \cdot Ra\_cyt \cdot C\_cyt \cdot C\_cyt$$

$$\frac{dRbC\_cyt}{dt} = -k\_f\_a \cdot cAMP\_cyt \cdot RbC\_cyt - k\_r\_b \cdot RbC\_cyt + k\_f\_b \cdot cAMP\_cyt \cdot RC\_cyt + k\_r\_a \cdot RabC\_cyt - k\_deact \cdot Rb\_cyt \cdot C\_cyt \cdot C\_cyt$$

$$\frac{dRabC\_cyt}{dt} = -(k\_r\_a + k\_r\_b + k\_act) \cdot RabC\_cyt + k\_f\_b \cdot cAMP\_cyt \cdot RaC\_cyt + k\_f\_a \cdot cAMP\_cyt \cdot RbC\_cyt$$

$$\frac{dC\_cyt}{dt} = -k\_deact \cdot C\_cyt \cdot C\_cyt \cdot (R\_cyt + Ra\_cyt + Rb\_cyt) + k\_act \cdot RabC\_cyt - \frac{D\_PKA\_pm\_cyt}{V\_cyt} \cdot (C\_cyt - C\_pm) - \frac{D\_PKA\_cyt\_nuc}{V\_cyt} \cdot (C\_cyt - C\_nuc)$$

$$\frac{dICUEc\_cyt}{dt} = kon\_ICUE \cdot cAMP\_cyt \cdot ICUE\_cyt - koff\_ICUE \cdot ICUEc\_cyt$$

$$\frac{dAKARp\_cyt}{dt} = \frac{k\_PKA\_AKAR \cdot C\_cyt \cdot AKAR\_cyt}{Km\_PKA\_AKAR + AKAR\_cyt} \cdot AKARp\_cyt - k\_PP\_AKAR \cdot PP\_cyt$$

Nucleus Equations

$$cAMP\_nuc = cAMPtot\_nuc - RaC\_nuc - RbC\_nuc - 2 \cdot RabC\_nuc - Ra\_nuc - Rb\_nuc - 2 \cdot Rab\_nuc - ICUEc\_nuc$$

$$PDE\_nuc = PDEtot\_nuc - PDEp\_nuc$$

$$ICUE\_nuc = ICUEtot\_nuc - ICUEc\_nuc$$

$$AKAR\_nuc = AKARtot\_nuc - AKARp\_nuc$$

$$\frac{dcAMPtot\_nuc}{dt} = E\_AC\_nuc - \frac{PDE\_nuc \cdot cAMP\_nuc \cdot k\_PDE}{cAMP\_nuc + Km\_PDE \cdot \left(1 + \frac{IBMX}{KI\_IBMX}\right)} - \frac{PDEp\_nuc \cdot cAMP\_nuc \cdot k\_PDEp}{cAMP\_nuc + Km\_PDE \cdot \left(1 + \frac{IBMX}{KI\_IBMX}\right)} - \frac{D\_cAMP\_cyt\_nuc}{V\_nuc} \cdot (cAMPtot\_nuc - cAMPtot\_cyt) - \frac{D\_cAMP\_nuc\_AKAP}{V\_nuc} \cdot (cAMPtot\_nuc - cAMPtot\_AKAP)$$

$$\frac{dPDEp\_nuc}{dt} = k\_PKA\_PDE \cdot C\_nuc \cdot PDE\_nuc - k\_PP\_PDE \cdot PP\_nuc \cdot PDEp\_nuc$$

$$\frac{dR\_nuc}{dt} = -(k\_f\_a + k\_f\_b) \cdot cAMP\_nuc \cdot R\_nuc + k\_r\_a \cdot Ra\_nuc + k\_r\_b \cdot Rb\_nuc - k\_deact \cdot R\_nuc \cdot C\_nuc \cdot C\_nuc$$

$$\frac{dRa\_nuc}{dt} = -k\_f\_b \cdot cAMP\_nuc \cdot Ra\_nuc - k\_r\_a \cdot Ra\_nuc + k\_f\_a \cdot cAMP\_nuc \cdot R\_nuc + k\_r\_b \cdot Rab\_nuc - k\_deact \cdot Ra\_nuc \cdot C\_nuc \cdot C\_nuc$$

$$\frac{dRb\_nuc}{dt} = -k\_f\_a \cdot cAMP\_nuc \cdot Rb\_nuc - k\_r\_b \cdot Rb\_nuc + k\_f\_b \cdot cAMP\_nuc \cdot R\_nuc + k\_r\_a \cdot Rab\_nuc - k\_deact \cdot Rb\_nuc \cdot C\_nuc \cdot C\_nuc$$

$$\frac{dRab\_nuc}{dt} = -(k\_r\_a + k\_r\_b) \cdot Rab\_nuc + k\_f\_b \cdot cAMP\_nuc \cdot Ra\_nuc + k\_f\_a \cdot cAMP\_nuc \cdot Rb\_nuc + k\_act \cdot RabC\_nuc$$

$$\frac{dRC\_nuc}{dt} = -(k\_f\_a + k\_f\_b) \cdot cAMP\_nuc \cdot RC\_nuc + k\_r\_a \cdot RaC\_nuc + k\_r\_b \cdot RbC\_nuc + k\_deact \cdot R\_nuc \cdot C\_nuc \cdot C\_nuc$$

$$\frac{dRaC\_nuc}{dt} = -k\_f\_b \cdot cAMP\_nuc \cdot RaC\_nuc - k\_r\_a \cdot RaC\_nuc + k\_f\_a \cdot cAMP\_nuc \cdot RC\_nuc + k\_r\_b \cdot RabC\_nuc - k\_deact \cdot Ra\_nuc \cdot C\_nuc \cdot C\_nuc$$

$$\frac{dRbC\_nuc}{dt} = -k\_f\_a \cdot cAMP\_nuc \cdot RbC\_nuc - k\_r\_b \cdot RbC\_nuc + k\_f\_b \cdot cAMP\_nuc \cdot RC\_nuc + k\_r\_a \cdot RabC\_nuc - k\_deact \cdot Rb\_nuc \cdot C\_nuc \cdot C\_nuc$$

$$\frac{dRabC\_nuc}{dt} = -(k\_r\_a + k\_r\_b + k\_act) \cdot RabC\_nuc + k\_f\_b \cdot cAMP\_nuc \cdot RaC\_nuc + k\_f\_a \cdot cAMP\_nuc \cdot RbC\_nuc$$

$$\frac{dC\_nuc}{dt} = -k\_deact \cdot C\_nuc \cdot C\_nuc \cdot (R\_nuc + Ra\_nuc + Rb\_nuc) + k\_act \cdot RabC\_nuc - \frac{D\_PKA\_cyt\_nuc}{V\_nuc} \cdot (C\_nuc - C\_cyt) - \frac{D\_PKA\_nuc\_AKAP}{V\_nuc} \cdot (C\_nuc - C\_AKAP)$$

$$\frac{dICUEc\_nuc}{dt} = kon\_ICUE \cdot cAMP\_nuc \cdot ICUE\_nuc - koff\_ICUE \cdot ICUEc\_nuc$$

$$\frac{dAKARp\_nuc}{dt} = \frac{k\_PKA\_AKAR \cdot C\_nuc \cdot AKAR\_nuc}{Km\_PKA\_AKAR + AKAR\_nuc} \cdot AKARp\_nuc - k\_PP\_AKAR \cdot PP\_nuc$$

Nuclear AKAP Equations

$$cAMP\_AKAP = cAMPtot\_AKAP - RaC\_AKAP - RbC\_AKAP - 2 \cdot RabC\_AKAP - Ra\_AKAP - Rb\_AKAP - 2 \cdot Rab\_AKAP - ICUEc\_AKAP$$

$$PDE\_AKAP = PDEtot\_AKAP - PDEp\_AKAP$$

$$\frac{dcAMPtot\_AKAP}{dt} = -\frac{PDE\_AKAP \cdot cAMP\_AKAP \cdot k\_PDE}{cAMP\_AKAP + Km\_PDE \cdot \left(1 + \frac{IBMX}{KI\_IBMX}\right)} - \frac{PDEp\_AKAP \cdot cAMP\_AKAP \cdot k\_PDEp}{cAMP\_AKAP + Km\_PDE \cdot \left(1 + \frac{IBMX}{KI\_IBMX}\right)} - \frac{D\_cAMP\_nuc\_AKAP}{V\_AKAP} \cdot (cAMPtot\_AKAP - cAMPtot\_nuc)$$

$$\frac{dPDEp\_AKAP}{dt} = k\_PKA\_PDE \cdot C\_AKAP \cdot PDE\_AKAP - k\_PP\_PDE \cdot PP\_AKAP \cdot PDEp\_AKAP$$

$$\frac{dR\_AKAP}{dt} = -(k\_f\_a + k\_f\_b) \cdot cAMP\_AKAP \cdot R\_AKAP + k\_r\_a \cdot Ra\_AKAP + k\_r\_b \cdot Rb\_AKAP - k\_deact \cdot R\_AKAP \cdot C\_AKAP \cdot C\_AKAP$$

$$\frac{dRa\_AKAP}{dt} = -k\_f\_b \cdot cAMP\_AKAP \cdot Ra\_AKAP - k\_r\_a \cdot Ra\_AKAP + k\_f\_a \cdot cAMP\_AKAP \cdot R\_AKAP + k\_r\_b \cdot Rab\_AKAP - k\_deact \cdot Ra\_AKAP \cdot C\_AKAP \cdot C\_AKAP$$

$$\frac{dRb\_AKAP}{dt} = -k\_f\_a \cdot cAMP\_AKAP \cdot Rb\_AKAP - k\_r\_b \cdot Rb\_AKAP + k\_f\_b \cdot cAMPAKAP \cdot R\_AKAP + k\_r\_a \cdot Rab\_AKAP - k\_deact \cdot Rb\_AKAP \cdot C\_AKAP \cdot C\_AKAP$$

$$\frac{dRab\_AKAP}{dt} = -(k\_r\_a + k\_r\_b) \cdot Rab\_AKAP + k\_f\_b \cdot cAMP\_AKAP \cdot Ra\_AKAP + k\_f\_a \cdot cAMP\_AKAP \cdot Rb\_AKAP + k\_act \cdot RabC\_AKAP$$

$$\frac{dRC\_AKAP}{dt} = -(k\_f\_a + k\_f\_b) \cdot cAMP\_AKAP \cdot RC\_AKAP + k\_r\_a \cdot RaC\_AKAP + k\_r\_b \cdot RbC\_AKAP + k\_deact \cdot R\_AKAP \cdot C\_AKAP \cdot C\_AKAP$$

$$\frac{dRaC\_AKAP}{dt} = -k\_f\_b \cdot cAMP\_AKAP \cdot RaC\_AKAP - k\_r\_a \cdot RaC\_AKAP + k\_f\_a \cdot cAMP\_AKAP \cdot RC\_AKAP + k\_r\_b \cdot RabC\_AKAP - k\_deact \cdot Ra\_AKAP \cdot C\_AKAP \cdot C\_AKAP$$

$$\frac{dRbC\_AKAP}{dt} = -k\_f\_a \cdot cAMP\_AKAP \cdot RbC\_AKAP - k\_r\_b \cdot RbC\_AKAP + k\_f\_b \cdot cAMP\_AKAP \cdot RC\_AKAP + k\_r\_a \cdot RabC\_AKAP - k\_deact \cdot Rb\_AKAP \cdot C\_AKAP \cdot C\_AKAP$$

$$\frac{dRabC\_AKAP}{dt} = -(k\_r\_a + k\_r\_b + k\_act) \cdot RabC\_AKAP + k\_f\_b \cdot cAMP\_AKAP \cdot RaC\_AKAP + k\_f\_a \cdot cAMP\_AKAP \cdot RbC\_AKAP$$

$$\frac{dC\_AKAP}{dt} = -k\_deact \cdot C\_AKAP \cdot C\_AKAP \cdot (R\_AKAP + Ra\_AKAP + Rb\_AKAP) + k\_act \cdot RabC\_AKAP - \frac{D\_PKA\_nuc\_AKAP}{V\_AKAP} \cdot (C\_AKAP - C\_nuc)$$

Appendix D

Cardiac PKA Compartmentation Model

β-Adrenergic Receptor / Gsα

Parameter	Description	Value	Units	Source
ISO	isoproterenol concentration (when used)	1	μM	-
b1ARtot	total β1-adrenergic receptors	0.0132	μM	5-6
Gstot	total Gs protein	3.83	μM	5
kf_LR	β1-AR binding to ligand	1	1/[μM ms]	5-6
kr_LR	β1-AR binding to ligand	0.285	1/ms	5-6
kf_LRG	ligand bound β1-AR associating with G-protein	1	1/[μM ms]	5-6
kr_LRG	ligand bound β1-AR associating with G-protein	0.062	1/ms	5-6
kf_RG	unbound β1-AR associating with G-protein	1	1/[μM ms]	5-6
kr_RG	unbound β1-AR associating with G-protein	33.0	1/ms	5-6
k_G_act	Gs-alpha activation	16.0e-3	1/ms	5-6
k_G_hyd	Gs-alpha hydrolysis	0.8e-6	1/ms	5-6
k_G_reassoc	Gs-alpha reassociation	1.21	1/[μM ms]	5-6
kf_bark	β1-AR desensitization by β-arrestin	1.1e-6	1/ms	5-6
kr_bark	β1-AR resensitization	2.2e-6	1/ms	5-6
kf_pka	β1-AR desensitization by PKA	3.6e-6	1/[μM ms]	5-6
kr_pka	β1-AR resensitization	2.2e-6	1/ms	6

$$b1ARact = b1ARtot - b1AR\_S464 - b1AR\_S301$$

$$b1AR = b1ARact - LR - LRG - RG$$

$$Gs = Gstot - LRG - RG - Gsby$$

$$\frac{dLR}{dt} = kf\_LR \cdot ISO \cdot b1AR - kr\_LR \cdot LR$$

$$\frac{dLRG}{dt} = kf\_LRG \cdot LR \cdot Gs - kr\_LRG \cdot LRG - k\_G\_act \cdot LRG$$

$$\frac{dRG}{dt} = kf\_RG \cdot b1AR \cdot Gs - kr\_RG \cdot Gs - k\_G\_act \cdot RG$$

$$\frac{db1AR\_S464}{dt} = kf\_bARK \cdot (LR + LRG) - kr\_bARK \cdot b1AR\_S464$$

$$\frac{db1AR\_S301}{dt} = kf\_PKA \cdot PKACI \cdot b1ARact - kr\_PKA \cdot b1AR\_S301$$

$$\frac{dGsaGTPtot}{dt} = k\_G\_act \cdot (RG + LRG) - k\_G\_hyd \cdot GsaGTPtot$$

$$\frac{dGsaGDP}{dt} = k\_G\_hyd \cdot GsaGTPtot - k\_G\_reassoc \cdot GsaGDP \cdot Gsby$$

$$\frac{dGsby}{dt} = k\_G\_act \cdot (RG + LRG) - k\_G\_reassoc \cdot GsaGDP \cdot Gsby$$

cAMP

Parameter	Description	Value	Units	Source
ACtot	total adenylyl cyclase	49.7e-3	µM	5-6
ATP	total ATP	5.0e3	µM	5-6
PDEtot	total phosphodiesterases	22.85e-3	µM	5
IBMX	isobutylmethylxanthine concentration	0.0	µM	6
FSK	forskolin concentration	0.0	µM	6
k_AC_basal	basal AC activity	0.2e-3	1/ms	5-6
Km_AC_basal	basal AC affinity for ATP	1.03e3	µM	5-6
k_AC_Gsa	AC activity with Gs-alpha activation	8.5e-3	1/ms	6
Km_AC_Gsa	AC:Gs-alpha affinity for ATP	315.0	µM	5-6
kf_AC_Gsa	AC activation by Gs-alpha	1	1/[µM ms]	6
kr_AC_Gsa	AC activation by Gs-alpha	0.4	1/ms	6
k_AC_FSK	AC activation by forskolin	7.3e-3	1/ms	6
Km_AC_FSK	AC:FSK affinity for ATP	860.0	µM	6
kf_AC_FSK	AC activation by forskolin	1	1/[µM ms]	6
kr_AC_FSK	AC activation by forskolin	44	1/ms	6
k_cAMP_PDE	cAMP degradation by PDEs	5.0e-3	1/ms	6
k_cAMP_PDEp	cAMP degradation by phosphorylated PDEs	10.0e-3	1/ms	260
Km_PDE_cAMP	PDE affinity for cAMP	1.3	µM	5-6
Kd_PDE_IBMX	PDE inhibition by IBMX	30.0	µM	5-6
k_PKA_PDE	PDE phosphorylation by PKA	7.5e-3	1/ms	260
k_PP_PDE	PDE inhibition by IBMX	1.5e-3	1/ms	260

$$cAMP = cAMPtot - (RCcAMP\_I + 2 \cdot RCcAMPcAMP\_I + 2 \cdot RcAMPcAMP\_I) - (RCcAMP\_II + 2 \cdot RCcAMPcAMP\_II + 2 \cdot RcAMPcAMP\_II)$$

$$AC = ACtot - AC\_GsaGTP$$

$$GsaGTP = GsaGTPtot - AC\_GsaGTP$$

$$\frac{dAC\_GsaGTP}{dt} = kf\_AC\_Gsa \cdot GsaGTP \cdot AC - kr\_AC\_Gsa \cdot AC\_GsaGTP$$

$$AC\_FSK = \frac{FSK \cdot AC}{Kd\_AC\_FSK}$$

$$PDE\_IBMX = \frac{PDEtot \cdot IBMX}{Kd\_PDE\_IBMX}$$

$$PDE = PDEtot - PDE\_IBMX - PDEp$$

$$\frac{dPDEp}{dt} = k\_PKA\_PDE \cdot PKACII \cdot PDE - k\_PP\_PDE \cdot PDEp$$

$$PDE_{ACT} = \frac{k\_cAMP\_PDE \cdot PDE \cdot cAMP}{Km\_PDE\_cAMP + cAMP} + \frac{k\_cAMP\_PDEp \cdot PDEp \cdot cAMP}{Km\_PDE\_cAMP + cAMP}$$

$$\frac{dcAMPtot}{dt} = \frac{k\_AC\_basal \cdot AC \cdot ATP}{Km\_AC\_basal + ATP} + \frac{k\_AC\_Gsa \cdot AC\_GsaGTP \cdot ATP}{Km\_AC\_Gsa + ATP} + \frac{k\_AC\_FSK \cdot AC\_FSK \cdot ATP}{Km\_AC\_FSK + ATP} - \frac{k\_cAMP\_PDE \cdot PDE \cdot cAMP}{Km\_PDE\_cAMP + cAMP} - \frac{k\_cAMP\_PDEp \cdot PDEp \cdot cAMP}{Km\_PDE\_cAMP + cAMP}$$

PKA / PKI Transport

Parameter	Description	Value	Units	Source
VnucF	nuclear fractional volume	0.02	-	[175]
DPKIcn	PKI cytosol to nucleus diffusion rate	19.8e-6	1/ms	-
DPKACIIcn	PKA cytosol to nucleus diffusion rate	1.190476e-7	1/ms	-
DPKACII_PKInc	PKA-PKI active transport rate	3.2e-6	1/ms	-
PKIbias	PKI nuclear expression bias	50	-	-

$$PKI = PKItot - PKACI\_PKI - PKACII\_PKI - nPKI \cdot VnucF - nPKACII\_PKI \cdot VnucF$$

$$JPKACIIcn = DPKACIIcn \cdot (PKACII - nPKACII)$$

$$JPKIcn = DPKIcn \cdot \left(PKI - \frac{nPKI}{PKIbias}\right)$$

$$JPKACII\_PKIcn = -DPKACII\_PKInc \cdot nPKACII\_PKI \cdot VnucF$$

PKA

Parameter	Description	Value	Units	Source
PKAItot	total type 1 protein kinase A	0.59	µM	[5]
PKAIItot	total type 2 protein kinase A	0.059	µM	adapted
PKItot	total protein kinase inhibitor	0.18	µM	[5-6]
kf_RC_cAMP	cAMP association with PKA	1	1/[µM ms]	[5-6]
kr_RC_cAMP	cAMP association with PKA	1.64	1/ms	[5-6]
kf_RCcAMP_cAMP	cAMP association with PKA	1	1/[µM ms]	[5-6]
kr_RCcAMP_cAMP	cAMP association with PKA	9.14	1/ms	[5-6]
kf_RcAMPcAMP_C	catalytic subunit dissociation	4.375	1/[µM ms]	[5-6]
kr_RcAMPcAMP_C	catalytic subunit dissociation	1	1/ms	[5-6]
kf_PKA_PKI	PKA inhibition by PKI	1	1/[µM ms]	[5-6]
kr_PKA_PKI	PKA inhibition by PKI	0.2e-3	1/ms	[5-6]

$$\frac{dRC\_I}{dt} = -kf\_RC\_cAMP \cdot RC\_I \cdot cAMP + kr\_RC\_cAMP \cdot RCcAMP\_I$$

$$\frac{dRCcAMP\_I}{dt} = -kr\_RC\_cAMP \cdot RCcAMP\_I + kf\_RC\_cAMP \cdot RC\_I \cdot cAMP - kf\_RCcAMP\_cAMP \cdot RCcAMP\_I \cdot cAMP + kr\_RCcAMP\_cAMP \cdot RCcAMPcAMP\_I$$

$$\frac{dRCcAMPcAMP\_I}{dt} = -kr\_RCcAMP\_cAMP \cdot RCcAMPcAMP\_I + kf\_RCcAMP\_cAMP \cdot RCcAMP\_I \cdot cAMP - kf\_RcAMPcAMP\_C \cdot RCcAMPcAMP\_I + kr\_RcAMPcAMP\_C \cdot RcAMPcAMP\_I \cdot PKACI$$

$$\frac{dRcAMPcAMP\_I}{dt} = -kr\_RcAMPcAMP\_C \cdot RcAMPcAMP\_I \cdot PKACI + kf\_RcAMPcAMP\_C \cdot RCcAMPcAMP\_I$$

$$\frac{dPKACI}{dt} = -kr\_RcAMPcAMP\_C \cdot RcAMPcAMP\_I \cdot PKACI + kf\_RcAMPcAMP\_C \cdot RCcAMPcAMP\_I - kf\_PKA\_PKI \cdot PKACI \cdot PKI + kr\_PKA\_PKI \cdot PKACI\_PKI$$

$$\frac{dPKA\_CI\_PKI}{dt} = -kr\_PKA\_PKI \cdot PKACI\_PKI + kf\_PKA\_PKI \cdot PKACI \cdot PKI$$

$$\frac{dRC\_II}{dt} = -kf\_RC\_cAMP \cdot RC\_II \cdot cAMP + kr\_RC\_cAMP \cdot RCcAMP\_II$$

$$\frac{dRCcAMP\_II}{dt} = -kr\_RC\_cAMP \cdot RCcAMP\_II + kf\_RC\_cAMP \cdot RC\_II \cdot cAMP - kf\_RCcAMP\_cAMP \cdot RCcAMP\_II \cdot cAMP + kr\_RCcAMP\_cAMP \cdot RCcAMPcAMP\_II$$

$$\frac{dRCcAMPcAMP\_II}{dt} = -kr\_RCcAMP\_cAMP \cdot RCcAMPcAMP\_II + kf\_RCcAMP\_cAMP \cdot RCcAMP\_II \cdot cAMP - kf\_RcAMPcAMP\_C \cdot RCcAMPcAMP\_II + kr\_RcAMPcAMP\_C \cdot RcAMPcAMP\_II \cdot PKACII$$

$$\frac{dRcAMPcAMP\_II}{dt} = -kr\_RcAMPcAMP\_C \cdot RcAMPcAMP\_II \cdot PKACII + kf\_RcAMPcAMP\_C \cdot RCcAMPcAMP\_II$$

$$\frac{dPKACII}{dt} = -kr\_RcAMPcAMP\_C \cdot RcAMPcAMP\_II \cdot PKACII + kf\_RcAMPcAMP\_C \cdot RCcAMPcAMP\_II - kf\_PKA\_PKI \cdot PKACII \cdot PKI + kr\_PKA\_PKI \cdot PKACII\_PKI - JPKACIIcn$$

$$\frac{dPKA\_CII\_PKI}{dt} = -kr\_PKA\_PKI \cdot PKACII\_PKI + kf\_PKA\_PKI \cdot PKACII \cdot PKI - JPKACII\_PKIcn$$

$$\frac{dnPKI}{dt} = kr\_PKA\_PKI \cdot nPKACII\_PKI - kf\_PKA\_PKI \cdot nPKACII \cdot nPKI + \frac{JPKIcn}{VnucF}$$

$$\frac{dnPKACII}{dt} = kr\_PKA\_PKI \cdot nPKACII\_PKI - kf\_PKA\_PKI \cdot nPKACII \cdot nPKI + \frac{JPKACIIcn}{VnucF}$$

$$\frac{dnPKACII\_PKI}{dt} = -kr\_PKA\_PKI \cdot nPKACII\_PKI + kf\_PKA\_PKI \cdot nPKACII \cdot nPKI + \frac{JPKACII\_PKIcn}{VnucF}$$

I-1/PP1

Parameter	Description	Value	Units	Source
PP1tot	total phosphatase 1	0.89	µM	[5-6]
I1tot	total inhibitor 1	0.3	µM	[5-6]
k_PKA_I1	PKA phosphorylation of inhibitor 1	60e-3	1/ms	[5-6]
Km_PKA_I1	PKA phosphorylation of inhibitor 1	1.0	µM	[5-6]
Vmax_PP2A_I1	PP2A dephosphorylation of phospholamban	14.0e-3	µM/ms	[5-6]
Km_PP2A_I1	PP2A dephosphorylation of phospholamban	1.0	µM	[5-6]
kf_PP1_I1	PP1 inhibition by inhibitor 1	1.0	1/[µM ms]	[5-6]
kr_PP1_I1	PP1 inhibition by inhibitor 1	1.0e-3	1/ms	[5-6]

$$I1 = I1tot - I1ptot$$

$$PP1 = PP1tot - I1p\_PP1$$

$$I1p = I1ptot - I1p\_PP1$$

$$\frac{dI1p\_PP1}{dt} = kf\_PP1\_I1 \cdot PP1 \cdot I1p - kr\_PP1\_I1 \cdot I1p\_PP1$$

$$\frac{dI1ptot}{dt} = \frac{k\_PKA\_I1 \cdot PKACI \cdot I1}{Km\_PKA\_I1 + I1} - \frac{Vmax\_PP2A\_I1 \cdot I1ptot}{Km\_PP2A\_I1 + I1ptot}$$

LCC

Parameter	Description	Value	Units	Source
LCCtot	total L-type Ca channel	0.025	µM	[5-6]
PKACII_LCCtot	total PKA local to L-type Ca channel	0.025	µM	[5-6]
PP1_LCC	total PP1 local to L-type Ca channel	0.025	µM	[5-6]
PP2A_LCC	total PP2A local to L-type Ca channel	0.025	µM	[5-6]
epsilon	AKAP-mediated scaling factor	10	-	[5-6]
k_PKA_LCC	PKA phosphorylation of LCC	54e-3	1/ms	[5-6]
Km_PKA_LCC	PKA phosphorylation of LCC	21	µM	[5-6]
k_PP1_LCC	PP1 dephosphorylation of LCC	8.52e-3	1/ms	[5-6]
Km_PP1_LCC	PP1 dephosphorylation of LCC	3	µM	[5-6]
k_PP2A_LCC	PP2A dephosphorylation of LCC	10.1e-3	1/ms	[5-6]
Km_PP2A_LCC	PP2A dephosphorylation of LCC	3	µM	[5-6]

$$PKACII\_LCC = \frac{PKACII\_LCCtot}{PKAIItot} \cdot PKACII$$

$$LCCa = LCCtot - LCCap$$

$$\frac{dLCCap}{dt} = \frac{epsilon \cdot k\_PKA\_LCC \cdot PKACII\_LCC \cdot LCCa}{Km\_PKA\_LCC + epsilon \cdot LCCa} - \frac{epsilon \cdot k\_PP2A\_LCC \cdot PP2A\_LCC \cdot LCCap}{Km\_PP2A\_LCC + epsilon \cdot LCCap}$$

$$LCCb = LCCtot - LCCbp$$

$$\frac{dLCCbp}{dt} = \frac{epsilon \cdot k\_PKA\_LCC \cdot PKACII\_LCC \cdot LCCb}{Km\_PKA\_LCC + epsilon \cdot LCCb} - \frac{epsilon \cdot k\_PP1\_LCC \cdot PP1\_LCC \cdot LCCbp}{Km\_PP1\_LCC + epsilon \cdot LCCbp}$$

PLB

Parameter	Description	Value	Units	Source
PLBtot	total phospholamban	106	μM	[6]
k_PKA_PLB	PKA phosphorylation of phospholamban	54e-3	1/ms	[5-6]
Km_PKA_PLB	PKA phosphorylation of phospholamban	21	μM	[5-6]
k_PP1_PLB	PP1 dephosphorylation of phospholamban	8.5e-3	1/ms	[5-6]
Km_PP1_PLB	PP1 dephosphorylation of phospholamban	7.0	μM	[5-6]

$$PLB = PLBtot - PLBp$$

$$\frac{dPLBp}{dt} = \frac{k\_PKA\_PLB \cdot PKACI \cdot PLB}{Km\_PKA\_PLB + PLB} - \frac{k\_PP1\_PLB \cdot PP1 \cdot PLBp}{Km\_PP1\_PLB + PLBp}$$

PLM

Parameter	Description	Value	Units	Source
PLMtot	total phospholemman	48	μM	[289]
k_PKA_PLM	PKA phosphorylation of phospholemman	54e-3	1/ms	[289]
Km_PKA_PLM	PKA phosphorylation of phospholemman	21	μM	[289]
k_PP1_PLM	PP1 dephosphorylation of phospholemman	8.5e-3	1/ms	[289]
Km_PP1_PLM	PP1 dephosphorylation of phospholemman	7.0	μM	[289]

$$PLM = PLMtot - PLMp$$

$$\frac{dPLMp}{dt} = \frac{k\_PKA\_PLM \cdot PKACI \cdot PLM}{Km\_PKA\_PLM + PLM} - \frac{k\_PP1\_PLM \cdot PP1 \cdot PLMp}{Km\_PP1\_PLM + PLMp}$$

TnI

Parameter	Description	Value	Units	Source
TnItot	total troponin I	70	μM	[6]
PP2A_TnI	total PP2A local to troponin I	0.67	μM	[6]
k_PKA_TnI	PKA phosphorylation of troponin I	54e-3	1/ms	[6]
Km_PKA_TnI	PKA phosphorylation of troponin I	21	μM	[6]
k_PP2A_TnI	PP2A dephosphorylation of troponin I	10.1e-3	1/ms	[6]
Km_PP2A_TnI	PP2A dephosphorylation of troponin I	4.1	μM	[6]

$$TnI = TnItot - TnIp$$

$$\frac{dTnIp}{dt} = \frac{k\_PKA\_TnI \cdot PKACI \cdot TnI}{Km\_PKA\_TnI + TnI} - \frac{k\_PP2A\_TnI \cdot PP2A\_TnI \cdot TnIp}{Km\_PP2A\_TnI + TnIp}$$

CREB

Parameter	Description	Value	Units	Source
CREBtot	total CREB	0.9	μM	adapted
PP2A_CREB	total PP2A local to CREB	0.12	μM	adapted
k_PKA_CREB	PKA phosphorylation of CREB	54e-3	1/ms	[5-6]
Km_PKA_CREB	PKA phosphorylation of CREB	10	μM	adapted
k_PP2A_CREB	PP2A dephosphorylation of CREB	8.5e-3	1/ms	[5-6]
Km_PP2A_CREB	PP2A dephosphorylation of CREB	2.46	μM	adapted

$$CREB = CREBtot - CREBp$$

$$\frac{dCREBp}{dt} = \frac{k\_PKA\_CREB \cdot nPKACII \cdot CREB}{Km\_PKA\_CREB + CREB} - \frac{k\_PP2A\_CREB \cdot PP2A \cdot CREBp}{Km\_PP2A\_CREB + CREBp}$$

AKAR FRET Reporters

Parameter	Description	Value	Units	Source
AKARnestot	total AKAR-NES	1.25	μM	[301]
PP2A_AKARnes	total PP2A local to AKAR-NES	0.5	μM	[284]
k_PKA_AKARnes	PKA phosphorylation of AKAR-NES	152e-3	1/ms	[284]
Km_PKA_AKARnes	PKA phosphorylation of AKAR-NES	16	μM	[284]
k_PP2A_AKARnes	PP2A dephosphorylation of AKAR-NES	8.5e-3	1/ms	[5-6]
Km_PP2A_AKARnes	PP2A dephosphorylation of AKAR-NES	7	μM	[5-6]
AKARnlstot	total AKAR-NLS	3.48	μM	[301]
PP2A_AKARnls	total PP2A local to AKAR-NLS	0.5	μM	[284]
k_PKA_AKARnls	PKA phosphorylation of AKAR-NLS	152e-3	1/ms	[284]
Km_PKA_AKARnls	PKA phosphorylation of AKAR-NLS	16	μM	[284]
k_PP2A_AKARnls	PP2A dephosphorylation of AKAR-NLS	8.5e-3	1/ms	[5-6]
Km_PP2A_AKARnls	PP2A dephosphorylation of AKAR-NLS	7	μM	[5-6]

$$AKARnes = AKARnestot - AKARnesp$$

$$\frac{dAKARnesp}{dt} = \frac{k\_PKA\_AKARnes \cdot PKACII \cdot AKARnes}{Km\_PKA\_AKARnes + AKARnes} - \frac{k\_PP2A\_AKARnes \cdot PP2A \cdot AKARnesp}{Km\_PP2A\_AKARnes + AKARnesp}$$

$$AKARnls = AKARnlstot - AKARnlsp$$

$$\frac{dAKARnlsp}{dt} = \frac{k\_PKA\_AKARnls \cdot nPKACII \cdot AKARnls}{Km\_PKA\_AKARnls + AKARnls} - \frac{k\_PP2A\_AKARnls \cdot PP2A \cdot AKARnlsp}{Km\_PP2A\_AKARnls + AKARnlsp}$$

References

1. Katz, A.M. *Physiology of the heart*, xv, 576 p. (Wolters Kluwer Health/Lippincott Williams & Wilkins Health, Philadelphia, PA, 2011).
2. El-Armouche, A. & Eschenhagen, T. Beta-adrenergic stimulation and myocardial function in the failing heart. *Heart Fail Rev* **14**, 225-41 (2009).
3. Saucerman, J.J. & McCulloch, A.D. Cardiac beta-adrenergic signaling: from subcellular microdomains to heart failure. *Ann N Y Acad Sci* **1080**, 348-61 (2006).
4. Saucerman, J.J. et al. Systems analysis of PKA-mediated phosphorylation gradients in live cardiac myocytes. *Proc Natl Acad Sci U S A* **103**, 12923-8 (2006).
5. Saucerman, J.J., Brunton, L.L., Michailova, A.P. & McCulloch, A.D. Modeling beta-adrenergic control of cardiac myocyte contractility in silico. *J Biol Chem* **278**, 47997-8003 (2003).
6. Saucerman, J.J. & McCulloch, A.D. Mechanistic systems models of cell signaling networks: a case study of myocyte adrenergic regulation. *Prog Biophys Mol Biol* **85**, 261-78 (2004).
7. Association, A.H. Heart Disease and Stroke Statistics - 2010 Update. (American Heart Association, Dallas, TX, 2010).
8. Katz, A.M. The "modern" view of heart failure: how did we get here? *Circ Heart Fail* **1**, 63-71 (2008).
9. Tanaka, K. et al. Spatial distribution of fibrosis governs fibrillation wave dynamics in the posterior left atrium during heart failure. *Circ Res* **101**, 839-47 (2007).
10. Packer, M. How should physicians view heart failure? The philosophical and physiological evolution of three conceptual models of the disease. *Am J Cardiol* **71**, 3C-11C (1993).
11. Mann, D.L. & Bristow, M.R. Mechanisms and models in heart failure: the biomechanical model and beyond. *Circulation* **111**, 2837-49 (2005).
12. LeJemtel, T.H. et al. Sustained beneficial effects of oral amrinone on cardiac and renal function in patients with severe congestive heart failure. *Am J Cardiol* **45**, 123-9 (1980).
13. Simonton, C.A. et al. Milrinone in congestive heart failure: acute and chronic hemodynamic and clinical evaluation. *J Am Coll Cardiol* **6**, 453-9 (1985).
14. Chatterjee, K. et al. Oral hydralazine therapy for chronic refractory heart failure. *Circulation* **54**, 879-83 (1976).

15. Miller, R.R., Awan, N.A., Maxwell, K.S. & Mason, D.T. Sustained reduction of cardiac impedance and preload in congestive heart failure with the antihypertensive vasodilator prazosin. *N Engl J Med* **297**, 303-7 (1977).
16. Packer, M. & Leier, C.V. Survival in congestive heart failure during treatment with drugs with positive inotropic actions. *Circulation* **75**, IV55-63 (1987).
17. Goldstein, R.E., Boccuzzi, S.J., Cruess, D. & Nattel, S. Diltiazem increases late-onset congestive heart failure in postinfarction patients with early reduction in ejection fraction. The Adverse Experience Committee; and the Multicenter Diltiazem Postinfarction Research Group. *Circulation* **83**, 52-60 (1991).
18. Packer, M. The neurohormonal hypothesis: a theory to explain the mechanism of disease progression in heart failure. *J Am Coll Cardiol* **20**, 248-54 (1992).
19. Heart Disease Death Rates, Total Population. Vol. 2012 (Centers for Disease Control, 2010).
20. Packer, M. et al. Effect of carvedilol on survival in severe chronic heart failure. *N Engl J Med* **344**, 1651-8 (2001).
21. Javed, U. & Deedwania, P.C. Beta-adrenergic blockers for chronic heart failure. *Cardiol Rev* **17**, 287-92 (2009).
22. Pfeffer, M.A. et al. Effect of captopril on mortality and morbidity in patients with left ventricular dysfunction after myocardial infarction. Results of the survival and ventricular enlargement trial. The SAVE Investigators. *N Engl J Med* **327**, 669-77 (1992).
23. Javed, U. & Deedwania, P.C. Angiotensin receptor blockers: novel role in high-risk patients. *Cardiol Clin* **26**, 507-26 (2008).
24. McMurray, J.J. Clinical practice. Systolic heart failure. *N Engl J Med* **362**, 228-38 (2010).
25. Hunt, S.A. et al. 2009 focused update incorporated into the ACC/AHA 2005 Guidelines for the Diagnosis and Management of Heart Failure in Adults: a report of the American College of Cardiology Foundation/American Heart Association Task Force on Practice Guidelines: developed in collaboration with the International Society for Heart and Lung Transplantation. *Circulation* **119**, e391-479 (2009).
26. Dickstein, K. et al. ESC guidelines for the diagnosis and treatment of acute and chronic heart failure 2008: the Task Force for the diagnosis and treatment of acute and chronic heart failure 2008 of the European Society of Cardiology. Developed in collaboration with the Heart Failure Association of the ESC (HFA) and endorsed by the European Society of Intensive Care Medicine (ESICM). *Eur J Heart Fail* **10**, 933-89 (2008).
27. Pepper, G.S. & Lee, R.W. Sympathetic activation in heart failure and its treatment with beta-blockade. *Arch Intern Med* **159**, 225-34 (1999).
28. Rona, G. Catecholamine cardiotoxicity. *J Mol Cell Cardiol* **17**, 291-306 (1985).
29. Triposkiadis, F. et al. The sympathetic nervous system in heart failure physiology, pathophysiology, and clinical implications. *J Am Coll Cardiol* **54**, 1747-62 (2009).
30. Engelhardt, S., Hein, L., Wiesmann, F. & Lohse, M.J. Progressive hypertrophy and heart failure in beta1-adrenergic receptor transgenic mice. *Proc Natl Acad Sci U S A* **96**, 7059-64 (1999).

31. Gaudin, C. et al. Overexpression of Gs alpha protein in the hearts of transgenic mice. *J Clin Invest* **95**, 1676-83 (1995).
32. Antos, C.L. et al. Dilated cardiomyopathy and sudden death resulting from constitutive activation of protein kinase a. *Circ Res* **89**, 997-1004 (2001).
33. Port, J.D. & Bristow, M.R. Altered beta-adrenergic receptor gene regulation and signaling in chronic heart failure. *J Mol Cell Cardiol* **33**, 887-905 (2001).
34. Lohse, M.J., Engelhardt, S. & Eschenhagen, T. What is the role of beta-adrenergic signaling in heart failure? *Circ Res* **93**, 896-906 (2003).
35. Eschenhagen, T. Beta-adrenergic signaling in heart failure-adapt or die. *Nat Med* **14**, 485-7 (2008).
36. Kiuchi, K. et al. Myocardial beta-adrenergic receptor function during the development of pacing-induced heart failure. *J Clin Invest* **91**, 907-14 (1993).
37. Engelhardt, S., Bohm, M., Erdmann, E. & Lohse, M.J. Analysis of beta-adrenergic receptor mRNA levels in human ventricular biopsy specimens by quantitative polymerase chain reactions: progressive reduction of beta 1-adrenergic receptor mRNA in heart failure. *J Am Coll Cardiol* **27**, 146-54 (1996).
38. Ungerer, M., Bohm, M., Elce, J.S., Erdmann, E. & Lohse, M.J. Altered expression of beta-adrenergic receptor kinase and beta 1-adrenergic receptors in the failing human heart. *Circulation* **87**, 454-63 (1993).
39. Vinge, L.E. et al. Myocardial distribution and regulation of GRK and beta-arrestin isoforms in congestive heart failure in rats. *Am J Physiol Heart Circ Physiol* **281**, H2490-9 (2001).
40. Longabaugh, J.P., Vatner, D.E., Vatner, S.F. & Homcy, C.J. Decreased stimulatory guanosine triphosphate binding protein in dogs with pressure-overload left ventricular failure. *J Clin Invest* **81**, 420-4 (1988).
41. Ishikawa, Y. et al. Downregulation of adenylylcyclase types V and VI mRNA levels in pacing-induced heart failure in dogs. *J Clin Invest* **93**, 2224-9 (1994).
42. Danielsen, W. et al. Basal and isoprenaline-stimulated cAMP content in failing versus nonfailing human cardiac preparations. *J Cardiovasc Pharmacol* **14**, 171-3 (1989).
43. Feldman, R.D. Physiological and molecular correlates of age-related changes in the human beta-adrenergic receptor system. *Fed Proc* **45**, 48-50 (1986).
44. Steinberg, S.F. & Brunton, L.L. Compartmentation of G protein-coupled signaling pathways in cardiac myocytes. *Annu Rev Pharmacol Toxicol* **41**, 751-73 (2001).
45. Xiang, Y.K. Compartmentalization of beta-adrenergic signals in cardiomyocytes. *Circ Res* **109**, 231-44 (2011).
46. Rybin, V.O., Xu, X., Lisanti, M.P. & Steinberg, S.F. Differential targeting of beta -adrenergic receptor subtypes and adenylyl cyclase to cardiomyocyte caveolae. A mechanism to functionally regulate the cAMP signaling pathway. *J Biol Chem* **275**, 41447-57 (2000).
47. Xiang, Y., Rybin, V.O., Steinberg, S.F. & Kobilka, B. Caveolar localization dictates physiologic signaling of beta 2-adrenoceptors in neonatal cardiac myocytes. *J Biol Chem* **277**, 34280-6 (2002).

48. Fischmeister, R. et al. Compartmentation of cyclic nucleotide signaling in the heart: the role of cyclic nucleotide phosphodiesterases. *Circ Res* **99**, 816-28 (2006).
49. Zaccolo, M. & Movsesian, M.A. cAMP and cGMP signaling cross-talk: role of phosphodiesterases and implications for cardiac pathophysiology. *Circ Res* **100**, 1569-78 (2007).
50. Diviani, D., Dodge-Kafka, K.L., Li, J. & Kapiloff, M.S. A-kinase anchoring proteins: scaffolding proteins in the heart. *Am J Physiol Heart Circ Physiol* **301**, H1742-53 (2011).
51. Greenwald, E.C. & Saucerman, J.J. Bigger, better, faster: principles and models of AKAP anchoring protein signaling. *J Cardiovasc Pharmacol* **58**, 462-9 (2011).
52. Nikolaev, V.O., Bunemann, M., Schmitteckert, E., Lohse, M.J. & Engelhardt, S. Cyclic AMP imaging in adult cardiac myocytes reveals far-reaching beta1-adrenergic but locally confined beta2-adrenergic receptor-mediated signaling. *Circ Res* **99**, 1084-91 (2006).
53. Nikolaev, V.O. et al. Beta2-adrenergic receptor redistribution in heart failure changes cAMP compartmentation. *Science* **327**, 1653-7 (2010).
54. McConnachie, G., Langeberg, L.K. & Scott, J.D. AKAP signaling complexes: getting to the heart of the matter. *Trends Mol Med* **12**, 317-23 (2006).
55. Prasad, R. & Pugh, P.J. Drug and device therapy for patients with chronic heart failure. *Expert Rev Cardiovasc Ther* **10**, 313-5 (2012).
56. Hung, M.C. & Link, W. Protein localization in disease and therapy. *J Cell Sci* **124**, 3381-92 (2011).
57. Miller, C.L. & Yan, C. Targeting cyclic nucleotide phosphodiesterase in the heart: therapeutic implications. *J Cardiovasc Transl Res* **3**, 507-15 (2010).
58. Van Tassell, B.W., Radwanski, P., Movsesian, M. & Munger, M.A. Combination therapy with beta-adrenergic receptor antagonists and phosphodiesterase inhibitors for chronic heart failure. *Pharmacotherapy* **28**, 1523-30 (2008).
59. Kholodenko, B.N., Hancock, J.F. & Kolch, W. Signalling ballet in space and time. *Nat Rev Mol Cell Biol* **11**, 414-26 (2010).
60. Overington, J.P., Al-Lazikani, B. & Hopkins, A.L. How many drug targets are there? *Nat Rev Drug Discov* **5**, 993-6 (2006).
61. Olson, E.N. Gene regulatory networks in the evolution and development of the heart. *Science* **313**, 1922-7 (2006).
62. Wang, Y. Mitogen-activated protein kinases in heart development and diseases. *Circulation* **116**, 1413-23 (2007).
63. Rockman, H.A., Koch, W.J. & Lefkowitz, R.J. Seven-transmembrane-spanning receptors and heart function. *Nature* **415**, 206-12 (2002).
64. Heineke, J. & Molkentin, J.D. Regulation of cardiac hypertrophy by intracellular signalling pathways. *Nat Rev Mol Cell Biol* **7**, 589-600 (2006).
65. Yan, C., Miller, C.L. & Abe, J. Regulation of phosphodiesterase 3 and inducible cAMP early repressor in the heart. *Circ Res* **100**, 489-501 (2007).
66. Greenstein, J.L. & Winslow, R.L. Integrative systems models of cardiac excitation-contraction coupling. *Circ Res* **108**, 70-84 (2011).
67. Weiss, J.N., Nivala, M., Garfinkel, A. & Qu, Z. Alternans and arrhythmias: from cell to heart. *Circ Res* **108**, 98-112 (2011).

68. Trayanova, N.A. Whole-heart modeling: applications to cardiac electrophysiology and electromechanics. *Circ Res* **108**, 113-28 (2011).
69. Brown, H.F., Kimura, J., Noble, D., Noble, S.J. & Taupignon, A. The ionic currents underlying pacemaker activity in rabbit sino-atrial node: experimental results and computer simulations. *Proc R Soc Lond B Biol Sci* **222**, 329-47 (1984).
70. DiFrancesco, D. & Noble, D. A model of cardiac electrical activity incorporating ionic pumps and concentration changes. *Philos Trans R Soc Lond B Biol Sci* **307**, 353-98 (1985).
71. Luo, C.H. & Rudy, Y. A model of the ventricular cardiac action potential. Depolarization, repolarization, and their interaction. *Circ Res* **68**, 1501-26 (1991).
72. Feit, T.S. & Bass, B.G. Numerical study of the behavior of an activation parameter in a sliding filament cat papillary muscle model. *J Mechanochem Cell Motil* **4**, 275-302 (1977).
73. Smith, J.M. & Cohen, R.J. Simple finite-element model accounts for wide range of cardiac dysrhythmias. *Proc Natl Acad Sci U S A* **81**, 233-7 (1984).
74. Noble, D. Modeling the heart--from genes to cells to the whole organ. *Science* **295**, 1678-82 (2002).
75. Hunter, P., Robbins, P. & Noble, D. The IUPS human Physiome Project. *Pflugers Arch* **445**, 1-9 (2002).
76. Hunter, P.J., Nielsen, P.M. & Bullivant, D. The IUPS Physiome Project. International Union of Physiological Sciences. *Novartis Found Symp* **247**, 207-17; discussion 217-21, 244-52 (2002).
77. Aldridge, B.B., Burke, J.M., Lauffenburger, D.A. & Sorger, P.K. Physicochemical modelling of cell signalling pathways. *Nat Cell Biol* **8**, 1195-203 (2006).
78. Bhalla, U.S. & Iyengar, R. Emergent properties of networks of biological signaling pathways. *Science* **283**, 381-7 (1999).
79. Alon, U. Network motifs: theory and experimental approaches. *Nat Rev Genet* **8**, 450-61 (2007).
80. Milo, R. et al. Network motifs: simple building blocks of complex networks. *Science* **298**, 824-7 (2002).
81. Bers, D.M. Cardiac excitation-contraction coupling. *Nature* **415**, 198-205 (2002).
82. Bisognano, J.D. et al. Myocardial-directed overexpression of the human beta(1)-adrenergic receptor in transgenic mice. *J Mol Cell Cardiol* **32**, 817-30 (2000).
83. Wang, X. & Dhalla, N.S. Modification of beta-adrenoceptor signal transduction pathway by genetic manipulation and heart failure. *Mol Cell Biochem* **214**, 131-55 (2000).
84. DiPaola, N.R., Sweet, W.E., Stull, L.B., Francis, G.S. & Schomisch Moravec, C. Beta-adrenergic receptors and calcium cycling proteins in non-failing, hypertrophied and failing human hearts: transition from hypertrophy to failure. *J Mol Cell Cardiol* **33**, 1283-95 (2001).
85. Klapholz, M. Beta-blocker use for the stages of heart failure. *Mayo Clin Proc* **84**, 718-29 (2009).
86. Marx, S.O. et al. PKA phosphorylation dissociates FKBP12.6 from the calcium release channel (ryanodine receptor): defective regulation in failing hearts. *Cell* **101**, 365-76 (2000).

87. Eisner, D.A., Choi, H.S., Diaz, M.E., O'Neill, S.C. & Trafford, A.W. Integrative analysis of calcium cycling in cardiac muscle. *Circ Res* **87**, 1087-94 (2000).
88. Greenstein, J.L., Tanskanen, A.J. & Winslow, R.L. Modeling the actions of beta-adrenergic signaling on excitation--contraction coupling processes. *Ann N Y Acad Sci* **1015**, 16-27 (2004).
89. Kuzumoto, M. et al. Simulation analysis of intracellular Na+ and Cl- homeostasis during beta 1-adrenergic stimulation of cardiac myocyte. *Prog Biophys Mol Biol* **96**, 171-86 (2008).
90. Despa, S., Tucker, A.L. & Bers, D.M. Phospholemman-mediated activation of Na/K-ATPase limits [Na]i and inotropic state during beta-adrenergic stimulation in mouse ventricular myocytes. *Circulation* **117**, 1849-55 (2008).
91. Himeno, Y., Sarai, N., Matsuoka, S. & Noma, A. Ionic mechanisms underlying the positive chronotropy induced by beta1-adrenergic stimulation in guinea pig sinoatrial node cells: a simulation study. *J Physiol Sci* **58**, 53-65 (2008).
92. Kholodenko, B.N. Cell-signalling dynamics in time and space. *Nat Rev Mol Cell Biol* **7**, 165-76 (2006).
93. Iancu, R.V., Jones, S.W. & Harvey, R.D. Compartmentation of cAMP signaling in cardiac myocytes: a computational study. *Biophys J* **92**, 3317-31 (2007).
94. Iancu, R.V. et al. Cytoplasmic cAMP concentrations in intact cardiac myocytes. *Am J Physiol Cell Physiol* **295**, C414-22 (2008).
95. Couchonnal, L.F. & Anderson, M.E. The role of calmodulin kinase II in myocardial physiology and disease. *Physiology (Bethesda)* **23**, 151-9 (2008).
96. Bers, D.M. & Grandi, E. Calcium/calmodulin-dependent kinase II regulation of cardiac ion channels. *J Cardiovasc Pharmacol* **54**, 180-7 (2009).
97. Maier, L.S. & Bers, D.M. Role of Ca2+/calmodulin-dependent protein kinase (CaMK) in excitation-contraction coupling in the heart. *Cardiovasc Res* **73**, 631-40 (2007).
98. Zhang, T. & Brown, J.H. Role of Ca2+/calmodulin-dependent protein kinase II in cardiac hypertrophy and heart failure. *Cardiovasc Res* **63**, 476-86 (2004).
99. Mishra, S. et al. Cardiac Hypertrophy and Heart Failure Development Through Gq and CaM Kinase II Signaling. *J Cardiovasc Pharmacol* (2010).
100. Grimm, M. & Brown, J.H. Beta-adrenergic receptor signaling in the heart: role of CaMKII. *J Mol Cell Cardiol* **48**, 322-30 (2010).
101. Zhang, R. et al. Calmodulin kinase II inhibition protects against structural heart disease. *Nat Med* **11**, 409-17 (2005).
102. Anderson, M.E. Calmodulin kinase signaling in heart: an intriguing candidate target for therapy of myocardial dysfunction and arrhythmias. *Pharmacol Ther* **106**, 39-55 (2005).
103. Hund, T.J. & Rudy, Y. Rate dependence and regulation of action potential and calcium transient in a canine cardiac ventricular cell model. *Circulation* **110**, 3168-74 (2004).
104. Grandi, E. et al. Simulation of Ca-calmodulin-dependent protein kinase II on rabbit ventricular myocyte ion currents and action potentials. *Biophys J* **93**, 3835-47 (2007).

105. Hashambhoy, Y.L., Winslow, R.L. & Greenstein, J.L. CaMKII-induced shift in modal gating explains L-type Ca(2+) current facilitation: a modeling study. *Biophys J* **96**, 1770-85 (2009).
106. Hashambhoy, Y.L., Greenstein, J.L. & Winslow, R.L. Role of CaMKII in RyR leak, EC coupling and action potential duration: A computational model. *J Mol Cell Cardiol* (2010).
107. Soltis, A.R. & Saucerman, J.J. Synergy between CaMKII Substrates and beta-Adrenergic Signaling in Regulation of Cardiac Myocyte Ca(2+) Handling. *Biophys J* **99**, 2038-47 (2010).
108. Hund, T.J. et al. Role of activated CaMKII in abnormal calcium homeostasis and I(Na) remodeling after myocardial infarction: insights from mathematical modeling. *J Mol Cell Cardiol* **45**, 420-8 (2008).
109. Christensen, M.D. et al. Oxidized calmodulin kinase II regulates conduction following myocardial infarction: a computational analysis. *PLoS Comput Biol* **5**, e1000583 (2009).
110. Song, Q., Saucerman, J.J., Bossuyt, J. & Bers, D.M. Differential integration of Ca2+-calmodulin signal in intact ventricular myocytes at low and high affinity Ca2+-calmodulin targets. *J Biol Chem* **283**, 31531-40 (2008).
111. Saucerman, J.J. & Bers, D.M. Calmodulin mediates differential sensitivity of CaMKII and calcineurin to local Ca2+ in cardiac myocytes. *Biophys J* **95**, 4597-612 (2008).
112. Chiba, H., Schneider, N.S., Matsuoka, S. & Noma, A. A simulation study on the activation of cardiac CaMKII delta-isoform and its regulation by phosphatases. *Biophys J* **95**, 2139-49 (2008).
113. Peterson, B.Z., DeMaria, C.D., Adelman, J.P. & Yue, D.T. Calmodulin is the Ca2+ sensor for Ca2+ -dependent inactivation of L-type calcium channels. *Neuron* **22**, 549-58 (1999).
114. Peterson, B.Z. et al. Critical determinants of Ca(2+)-dependent inactivation within an EF-hand motif of L-type Ca(2+) channels. *Biophys J* **78**, 1906-20 (2000).
115. Tanskanen, A.J., Greenstein, J.L., Chen, A., Sun, S.X. & Winslow, R.L. Protein geometry and placement in the cardiac dyad influence macroscopic properties of calcium-induced calcium release. *Biophys J* **92**, 3379-96 (2007).
116. Tadross, M.R., Dick, I.E. & Yue, D.T. Mechanism of local and global Ca2+ sensing by calmodulin in complex with a Ca2+ channel. *Cell* **133**, 1228-40 (2008).
117. Cooling, M., Hunter, P. & Crampin, E.J. Modeling hypertrophic IP3 transients in the cardiac myocyte. *Biophys J* **93**, 3421-33 (2007).
118. Shin, S.Y. et al. Switching feedback mechanisms realize the dual role of MCIP in the regulation of calcineurin activity. *FEBS Lett* **580**, 5965-73 (2006).
119. Cooling, M.T., Hunter, P. & Crampin, E.J. Sensitivity of NFAT cycling to cytosolic calcium concentration: implications for hypertrophic signals in cardiac myocytes. *Biophys J* **96**, 2095-104 (2009).
120. Niederer, S.A. & Smith, N.P. A mathematical model of the slow force response to stretch in rat ventricular myocytes. *Biophys J* **92**, 4030-44 (2007).

121. Cortassa, S. et al. A computational model integrating electrophysiology, contraction, and mitochondrial bioenergetics in the ventricular myocyte. *Biophys J* **91**, 1564-89 (2006).
122. Southern, J. et al. Multi-scale computational modelling in biology and physiology. *Prog Biophys Mol Biol* **96**, 60-89 (2008).
123. Ten Tusscher, K.H., Hren, R. & Panfilov, A.V. Organization of ventricular fibrillation in the human heart. *Circ Res* **100**, e87-101 (2007).
124. Shim, E.B., Leem, C.H., Abe, Y. & Noma, A. A new multi-scale simulation model of the circulation: from cells to system. *Philos Transact A Math Phys Eng Sci* **364**, 1483-500 (2006).
125. Kerckhoffs, R.C. et al. Coupling of a 3D finite element model of cardiac ventricular mechanics to lumped systems models of the systemic and pulmonic circulation. *Ann Biomed Eng* **35**, 1-18 (2007).
126. Saucerman, J.J., Healy, S.N., Belik, M.E., Puglisi, J.L. & McCulloch, A.D. Proarrhythmic consequences of a KCNQ1 AKAP-binding domain mutation: computational models of whole cells and heterogeneous tissue. *Circ Res* **95**, 1216-24 (2004).
127. Nakamura, H. et al. Progesterone regulates cardiac repolarization through a nongenomic pathway: an in vitro patch-clamp and computational modeling study. *Circulation* **116**, 2913-22 (2007).
128. Hall, J.L. et al. Genomic profiling of the human heart before and after mechanical support with a ventricular assist device reveals alterations in vascular signaling networks. *Physiol Genomics* **17**, 283-91 (2004).
129. Hall, J.L. et al. Molecular signature of recovery following combination left ventricular assist device (LVAD) support and pharmacologic therapy. *Eur Heart J* **28**, 613-27 (2007).
130. Hong, S.E. et al. Identification of mouse heart transcriptomic network sensitive to various heart diseases. *Biotechnol J* **3**, 648-58 (2008).
131. Gao, Z. et al. Transcriptomic profiling of the canine tachycardia-induced heart failure model: global comparison to human and murine heart failure. *J Mol Cell Cardiol* **40**, 76-86 (2006).
132. Gao, Z. et al. Key pathways associated with heart failure development revealed by gene networks correlated with cardiac remodeling. *Physiol Genomics* **35**, 222-30 (2008).
133. Van Eyk, J.E. Proteomics: unraveling the complexity of heart disease and striving to change cardiology. *Curr Opin Mol Ther* **3**, 546-53 (2001).
134. Edwards, A.V., White, M.Y. & Cordwell, S.J. The role of proteomics in clinical cardiovascular biomarker discovery. *Mol Cell Proteomics* **7**, 1824-37 (2008).
135. Kislinger, T. et al. Global survey of organ and organelle protein expression in mouse: combined proteomic and transcriptomic profiling. *Cell* **125**, 173-86 (2006).
136. Bousette, N. et al. Large-scale characterization and analysis of the murine cardiac proteome. *J Proteome Res* **8**, 1887-901 (2009).
137. Arab, S. et al. Cardiovascular proteomics: tools to develop novel biomarkers and potential applications. *J Am Coll Cardiol* **48**, 1733-41 (2006).

138. Gramolini, A.O. et al. Comparative proteomics profiling of a phospholamban mutant mouse model of dilated cardiomyopathy reveals progressive intracellular stress responses. *Mol Cell Proteomics* **7**, 519-33 (2008).
139. Berger, S.I., Ma'ayan, A. & Iyengar, R. Systems pharmacology of arrhythmias. *Sci Signal* **3**, ra30 (2010).
140. Lage, K. et al. Dissecting spatio-temporal protein networks driving human heart development and related disorders. *Mol Syst Biol* **6**, 381 (2010).
141. Matkovich, S.J., Zhang, Y., Van Booven, D.J. & Dorn, G.W., 2nd. Deep mRNA sequencing for in vivo functional analysis of cardiac transcriptional regulators: application to Galphaq. *Circ Res* **106**, 1459-67 (2010).
142. Janes, K.A. & Yaffe, M.B. Data-driven modelling of signal-transduction networks. *Nat Rev Mol Cell Biol* **7**, 820-8 (2006).
143. Li, L. Dimension reduction for high-dimensional data. *Methods Mol Biol* **620**, 417-34 (2010).
144. Janes, K.A., Reinhardt, H.C. & Yaffe, M.B. Cytokine-induced signaling networks prioritize dynamic range over signal strength. *Cell* **135**, 343-54 (2008).
145. Morris, M.K., Saez-Rodriguez, J., Sorger, P.K. & Lauffenburger, D.A. Logic-based models for the analysis of cell signaling networks. *Biochemistry* **49**, 3216-24 (2010).
146. Albert, I., Thakar, J., Li, S., Zhang, R. & Albert, R. Boolean network simulations for life scientists. *Source Code Biol Med* **3**, 16 (2008).
147. Albert, R. & Wang, R.S. Discrete dynamic modeling of cellular signaling networks. *Methods Enzymol* **467**, 281-306 (2009).
148. Wittmann, D.M. et al. Transforming Boolean models to continuous models: methodology and application to T-cell receptor signaling. *BMC Syst Biol* **3**, 98 (2009).
149. Hansson, E.M., Lindsay, M.E. & Chien, K.R. Regeneration next: toward heart stem cell therapeutics. *Cell Stem Cell* **5**, 364-77 (2009).
150. Chavakis, E., Koyanagi, M. & Dimmeler, S. Enhancing the outcome of cell therapy for cardiac repair: progress from bench to bedside and back. *Circulation* **121**, 325-35 (2010).
151. Viswanathan, S. & Zandstra, P.W. Towards predictive models of stem cell fate. *Cytotechnology* **41**, 75-92 (2003).
152. Kirouac, D.C. et al. Cell-cell interaction networks regulate blood stem and progenitor cell fate. *Mol Syst Biol* **5**, 293 (2009).
153. Warner, J.K. et al. Direct evidence for cooperating genetic events in the leukemic transformation of normal human hematopoietic cells. *Leukemia* **19**, 1794-805 (2005).
154. Jacot, J.G. et al. Cardiac myocyte force development during differentiation and maturation. *Ann N Y Acad Sci* **1188**, 121-7 (2010).
155. Mann, D.L. Left ventricular size and shape: determinants of mechanical signal transduction pathways. *Heart Fail Rev* **10**, 95-100 (2005).
156. Hannigan, G.E., Coles, J.G. & Dedhar, S. Integrin-linked kinase at the heart of cardiac contractility, repair, and disease. *Circ Res* **100**, 1408-14 (2007).
157. Samarel, A.M. Costameres, focal adhesions, and cardiomyocyte mechanotransduction. *Am J Physiol Heart Circ Physiol* **289**, H2291-301 (2005).

158. Marin, T.M. et al. Shp2 negatively regulates growth in cardiomyocytes by controlling focal adhesion kinase/Src and mTOR pathways. *Circ Res* **103**, 813-24 (2008).
159. Sussman, M.A., McCulloch, A. & Borg, T.K. Dance band on the Titanic: biomechanical signaling in cardiac hypertrophy. *Circ Res* **91**, 888-98 (2002).
160. Blaauw, E. et al. Stretch-induced hypertrophy of isolated adult rabbit cardiomyocytes. *Am J Physiol Heart Circ Physiol* (2010).
161. Zobel, C. et al. Mechanisms of Ca2+-dependent calcineurin activation in mechanical stretch-induced hypertrophy. *Cardiology* **107**, 281-90 (2007).
162. Yamazaki, M. et al. Mechanisms of stretch-induced atrial fibrillation in the presence and the absence of adrenocholinergic stimulation: interplay between rotors and focal discharges. *Heart Rhythm* **6**, 1009-17 (2009).
163. Chorro, F.J. et al. Pharmacological modifications of the stretch-induced effects on ventricular fibrillation in perfused rabbit hearts. *Am J Physiol Heart Circ Physiol* **297**, H1860-9 (2009).
164. Seo, K. et al. Structural heterogeneity in the ventricular wall plays a significant role in the initiation of stretch-induced arrhythmias in perfused rabbit right ventricular tissues and whole heart preparations. *Circ Res* **106**, 176-84 (2010).
165. Rakesh, K. et al. beta-Arrestin-biased agonism of the angiotensin receptor induced by mechanical stress. *Sci Signal* **3**, ra46 (2010).
166. Malhotra, R. et al. G alpha(q)-mediated activation of GRK2 by mechanical stretch in cardiac myocytes: the role of protein kinase C. *J Biol Chem* **285**, 13748-60 (2010).
167. Burkhoff, D., Klotz, S. & Mancini, D.M. LVAD-induced reverse remodeling: basic and clinical implications for myocardial recovery. *J Card Fail* **12**, 227-39 (2006).
168. Klotz, S., Jan Danser, A.H. & Burkhoff, D. Impact of left ventricular assist device (LVAD) support on the cardiac reverse remodeling process. *Prog Biophys Mol Biol* **97**, 479-96 (2008).
169. Healy, S.N. & McCulloch, A.D. An ionic model of stretch-activated and stretch-modulated currents in rabbit ventricular myocytes. *Europace* **7 Suppl 2**, 128-34 (2005).
170. Youm, J.B. et al. Role of stretch-activated channels on the stretch-induced changes of rat atrial myocytes. *Prog Biophys Mol Biol* **90**, 186-206 (2006).
171. Wang, Y. et al. Stretch-activated channel activation promotes early afterdepolarizations in rat ventricular myocytes under oxidative stress. *Am J Physiol Heart Circ Physiol* **296**, H1227-35 (2009).
172. Kuijpers, N.H. et al. Mechanoelectric feedback leads to conduction slowing and block in acutely dilated atria: a modeling study of cardiac electromechanics. *Am J Physiol Heart Circ Physiol* **292**, H2832-53 (2007).
173. Trayanova, N.A., Constantino, J. & Gurev, V. Models of stretch-activated ventricular arrhythmias. *J Electrocardiol* (2010).
174. Keldermann, R.H., Nash, M.P., Gelderblom, H., Wang, V.Y. & Panfilov, A.V. Electromechanical wavebreak in a model of the human left ventricle. *Am J Physiol Heart Circ Physiol* **299**, H134-43 (2010).

175. Bers, D.M. *Excitation-contraction coupling and cardiac contractile force*, xxiv, 427 p. (Kluwer Academic Publishers, Dordrecht ; Boston, 2001).
176. Cheung, J.Y. et al. Phospholemman: a novel cardiac stress protein. *Clin Transl Sci* **3**, 189-96 (2010).
177. Despa, S. et al. Phospholemman-phosphorylation mediates the beta-adrenergic effects on Na/K pump function in cardiac myocytes. *Circ Res* **97**, 252-9 (2005).
178. Despa, S., Islam, M.A., Weber, C.R., Pogwizd, S.M. & Bers, D.M. Intracellular Na(+) concentration is elevated in heart failure but Na/K pump function is unchanged. *Circulation* **105**, 2543-8 (2002).
179. Fuller, W., Eaton, P., Bell, J.R. & Shattock, M.J. Ischemia-induced phosphorylation of phospholemman directly activates rat cardiac Na/K-ATPase. *FASEB J* **18**, 197-9 (2004).
180. Shattock, M.J. Phospholemman: its role in normal cardiac physiology and potential as a druggable target in disease. *Curr Opin Pharmacol* **9**, 160-6 (2009).
181. Bers, D.M., Despa, S. & Bossuyt, J. Regulation of Ca2+ and Na+ in normal and failing cardiac myocytes. *Ann N Y Acad Sci* **1080**, 165-77 (2006).
182. Cannell, M.B. & Kong, C.H. Local control in cardiac E-C coupling. *J Mol Cell Cardiol* (2011).
183. Gyorke, S. & Terentyev, D. Modulation of ryanodine receptor by luminal calcium and accessory proteins in health and cardiac disease. *Cardiovasc Res* **77**, 245-55 (2008).
184. Bondarenko, V.E., Szigeti, G.P., Bett, G.C., Kim, S.J. & Rasmusson, R.L. Computer model of action potential of mouse ventricular myocytes. *Am J Physiol Heart Circ Physiol* **287**, H1378-403 (2004).
185. Greenstein, J.L., Hinch, R. & Winslow, R.L. Mechanisms of excitation-contraction coupling in an integrative model of the cardiac ventricular myocyte. *Biophys J* **90**, 77-91 (2006).
186. Hinch, R., Greenstein, J.L., Tanskanen, A.J., Xu, L. & Winslow, R.L. A simplified local control model of calcium-induced calcium release in cardiac ventricular myocytes. *Biophys J* **87**, 3723-36 (2004).
187. Hinch, R., Greenstein, J.L. & Winslow, R.L. Multi-scale models of local control of calcium induced calcium release. *Prog Biophys Mol Biol* **90**, 136-50 (2006).
188. Shannon, T.R., Wang, F. & Bers, D.M. Regulation of cardiac sarcoplasmic reticulum Ca release by luminal [Ca] and altered gating assessed with a mathematical model. *Biophys J* **89**, 4096-110 (2005).
189. Shannon, T.R., Wang, F., Puglisi, J., Weber, C. & Bers, D.M. A mathematical treatment of integrated Ca dynamics within the ventricular myocyte. *Biophys J* **87**, 3351-71 (2004).
190. Shannon, T.R., Ginsburg, K.S. & Bers, D.M. Reverse mode of the sarcoplasmic reticulum calcium pump and load-dependent cytosolic calcium decline in voltage-clamped cardiac ventricular myocytes. *Biophys J* **78**, 322-33 (2000).
191. Shannon, T.R. & Bers, D.M. Integrated Ca2+ management in cardiac myocytes. *Ann N Y Acad Sci* **1015**, 28-38 (2004).
192. Hund, T.J., Kucera, J.P., Otani, N.F. & Rudy, Y. Ionic charge conservation and long-term steady state in the Luo-Rudy dynamic cell model. *Biophys J* **81**, 3324-31 (2001).

193. Chu, G. et al. Compensatory mechanisms associated with the hyperdynamic function of phospholamban-deficient mouse hearts. *Circ Res* **79**, 1064-76 (1996).
194. Bers, D.M., Barry, W.H. & Despa, S. Intracellular Na+ regulation in cardiac myocytes. *Cardiovasc Res* **57**, 897-912 (2003).
195. Li, L., Chu, G., Kranias, E.G. & Bers, D.M. Cardiac myocyte calcium transport in phospholamban knockout mouse: relaxation and endogenous CaMKII effects. *Am J Physiol* **274**, H1335-47 (1998).
196. Santana, L.F., Kranias, E.G. & Lederer, W.J. Calcium sparks and excitation-contraction coupling in phospholamban-deficient mouse ventricular myocytes. *J Physiol* **503 (Pt 1)**, 21-9 (1997).
197. Ma, W., Trusina, A., El-Samad, H., Lim, W.A. & Tang, C. Defining network topologies that can achieve biochemical adaptation. *Cell* **138**, 760-73 (2009).
198. Behar, M., Hao, N., Dohlman, H.G. & Elston, T.C. Mathematical and computational analysis of adaptation via feedback inhibition in signal transduction pathways. *Biophys J* **93**, 806-21 (2007).
199. Pierce, K.L., Premont, R.T. & Lefkowitz, R.J. Seven-transmembrane receptors. *Nat Rev Mol Cell Biol* **3**, 639-50 (2002).
200. Lefkowitz, R.J., Rockman, H.A. & Koch, W.J. Catecholamines, cardiac beta-adrenergic receptors, and heart failure. *Circulation* **101**, 1634-7 (2000).
201. Wang, J. et al. Phospholemman and beta-adrenergic stimulation in the heart. *Am J Physiol Heart Circ Physiol* **298**, H807-15 (2010).
202. Mangan, S., Itzkovitz, S., Zaslaver, A. & Alon, U. The incoherent feed-forward loop accelerates the response-time of the gal system of Escherichia coli. *J Mol Biol* **356**, 1073-81 (2006).
203. Tanskanen, A.J., Greenstein, J.L., O'Rourke, B. & Winslow, R.L. The role of stochastic and modal gating of cardiac L-type Ca2+ channels on early after-depolarizations. *Biophys J* **88**, 85-95 (2005).
204. Xiao, B. et al. Functional consequence of protein kinase A-dependent phosphorylation of the cardiac ryanodine receptor: sensitization of store overload-induced Ca2+ release. *J Biol Chem* **282**, 30256-64 (2007).
205. Benitah, J.P., Alvarez, J.L. & Gomez, A.M. L-type Ca(2+) current in ventricular cardiomyocytes. *J Mol Cell Cardiol* **48**, 26-36 (2010).
206. Song, L.S. et al. beta-Adrenergic stimulation synchronizes intracellular Ca(2+) release during excitation-contraction coupling in cardiac myocytes. *Circ Res* **88**, 794-801 (2001).
207. Frace, A.M., Mery, P.F., Fischmeister, R. & Hartzell, H.C. Rate-limiting steps in the beta-adrenergic stimulation of cardiac calcium current. *J Gen Physiol* **101**, 337-53 (1993).
208. Kentish, J.C. et al. Phosphorylation of troponin I by protein kinase A accelerates relaxation and crossbridge cycle kinetics in mouse ventricular muscle. *Circ Res* **88**, 1059-65 (2001).
209. Stelzer, J.E., Patel, J.R. & Moss, R.L. Protein kinase A-mediated acceleration of the stretch activation response in murine skinned myocardium is eliminated by ablation of cMyBP-C. *Circ Res* **99**, 884-90 (2006).
210. Bers, D.M. & Despa, S. Na/K-ATPase--an integral player in the adrenergic fight-or-flight response. *Trends Cardiovasc Med* **19**, 111-8 (2009).

211. Yang, J.H. & Saucerman, J.J. Computational models reduce complexity and accelerate insight into cardiac signaling networks. *Circ Res* **108**, 85-97 (2011).
212. Wang, L.J. & Sobie, E.A. Mathematical model of the neonatal mouse ventricular action potential. *Am J Physiol Heart Circ Physiol* **294**, H2565-75 (2008).
213. Shin, S.Y., Choo, S.M., Woo, S.H. & Cho, K.H. Cardiac systems biology and parameter sensitivity analysis: intracellular Ca2+ regulatory mechanisms in mouse ventricular myocytes. *Adv Biochem Eng Biotechnol* **110**, 25-45 (2008).
214. Koivumaki, J.T., Korhonen, T., Takalo, J., Weckstrom, M. & Tavi, P. Regulation of excitation-contraction coupling in mouse cardiac myocytes: integrative analysis with mathematical modelling. *BMC Physiol* **9**, 16 (2009).
215. Li, L. et al. A mathematical model of the murine ventricular myocyte: a data-driven biophysically based approach applied to mice overexpressing the canine NCX isoform. *Am J Physiol Heart Circ Physiol* **299**, H1045-63 (2010).
216. Li, L. et al. Calcium dynamics in the ventricular myocytes of SERCA2 knockout mice: A modeling study. *Biophys J* **100**, 322-31 (2011).
217. Huke, S. & Bers, D.M. Temporal dissociation of frequency-dependent acceleration of relaxation and protein phosphorylation by CaMKII. *J Mol Cell Cardiol* **42**, 590-9 (2007).
218. Ho, C.Y. et al. Myocardial fibrosis as an early manifestation of hypertrophic cardiomyopathy. *N Engl J Med* **363**, 552-63 (2010).
219. Swynghedauw, B. Molecular mechanisms of myocardial remodeling. *Physiol Rev* **79**, 215-62 (1999).
220. Spinale, F.G. Myocardial matrix remodeling and the matrix metalloproteinases: influence on cardiac form and function. *Physiol Rev* **87**, 1285-342 (2007).
221. Graham, H.K., Horn, M. & Trafford, A.W. Extracellular matrix profiles in the progression to heart failure. European Young Physiologists Symposium Keynote Lecture-Bratislava 2007. *Acta Physiol (Oxf)* **194**, 3-21 (2008).
222. Li, D. et al. Effects of angiotensin-converting enzyme inhibition on the development of the atrial fibrillation substrate in dogs with ventricular tachypacing-induced congestive heart failure. *Circulation* **104**, 2608-14 (2001).
223. Li, Y. et al. Effects of Cilazapril on atrial electrical, structural and functional remodeling in atrial fibrillation dogs. *J Electrocardiol* **40**, 100 e1-6 (2007).
224. Mehta, P.K. & Griendling, K.K. Angiotensin II cell signaling: physiological and pathological effects in the cardiovascular system. *Am J Physiol Cell Physiol* **292**, C82-97 (2007).
225. Lin, C.S. & Pan, C.H. Regulatory mechanisms of atrial fibrotic remodeling in atrial fibrillation. *Cell Mol Life Sci* **65**, 1489-508 (2008).
226. Fischer, T.A., Singh, K., O'Hara, D.S., Kaye, D.M. & Kelly, R.A. Role of AT1 and AT2 receptors in regulation of MAPKs and MKP-1 by ANG II in adult cardiac myocytes. *Am J Physiol* **275**, H906-16 (1998).
227. Berk, B.C. Angiotensin type 2 receptor (AT2R): a challenging twin. *Sci STKE* **2003**, PE16 (2003).
228. Wharton, J. et al. Differential distribution of angiotensin AT2 receptors in the normal and failing human heart. *J Pharmacol Exp Ther* **284**, 323-36 (1998).

229. Tsutsumi, Y. et al. Angiotensin II type 2 receptor is upregulated in human heart with interstitial fibrosis, and cardiac fibroblasts are the major cell type for its expression. *Circ Res* **83**, 1035-46 (1998).
230. Opie, L.H. & Sack, M.N. Enhanced angiotensin II activity in heart failure: reevaluation of the counterregulatory hypothesis of receptor subtypes. *Circ Res* **88**, 654-8 (2001).
231. Urata, H., Healy, B., Stewart, R.W., Bumpus, F.M. & Husain, A. Angiotensin II-forming pathways in normal and failing human hearts. *Circ Res* **66**, 883-90 (1990).
232. Zou, Y. et al. Cell type-specific angiotensin II-evoked signal transduction pathways: critical roles of Gbetagamma subunit, Src family, and Ras in cardiac fibroblasts. *Circ Res* **82**, 337-45 (1998).
233. Murasawa, S. et al. Angiotensin II initiates tyrosine kinase Pyk2-dependent signalings leading to activation of Rac1-mediated c-Jun NH2-terminal kinase. *J Biol Chem* **275**, 26856-63 (2000).
234. Li, J.M. et al. Angiotensin II-induced neural differentiation via angiotensin II type 2 (AT2) receptor-MMS2 cascade involving interaction between AT2 receptor-interacting protein and Src homology 2 domain-containing protein-tyrosine phosphatase 1. *Mol Endocrinol* **21**, 499-511 (2007).
235. Alvarez, S.E., Seguin, L.R., Villarreal, R.S., Nahmias, C. & Ciuffo, G.M. Involvement of c-Src tyrosine kinase in SHP-1 phosphatase activation by Ang II AT2 receptors in rat fetal tissues. *J Cell Biochem* **105**, 703-11 (2008).
236. Huang, X.C., Richards, E.M. & Sumners, C. Mitogen-activated protein kinases in rat brain neuronal cultures are activated by angiotensin II type 1 receptors and inhibited by angiotensin II type 2 receptors. *J Biol Chem* **271**, 15635-41 (1996).
237. Casal, A.J., Ryser, S., Capponi, A.M. & Wang-Buholzer, C.F. Angiotensin II-induced mitogen-activated protein kinase phosphatase-1 expression in bovine adrenal glomerulosa cells: implications in mineralocorticoid biosynthesis. *Endocrinology* **148**, 5573-81 (2007).
238. Alvarez, S.E., Fuentes, L.B. & Ciuffo, G.M. Angiotensin II mediates Tyr-dephosphorylation in rat fetal kidney membranes. *Mol Cell Biochem* **254**, 137-43 (2003).
239. Huang, X.C., Richards, E.M. & Sumners, C. Angiotensin II type 2 receptor-mediated stimulation of protein phosphatase 2A in rat hypothalamic/brainstem neuronal cocultures. *J Neurochem* **65**, 2131-7 (1995).
240. Baines, C.P. & Molkentin, J.D. STRESS signaling pathways that modulate cardiac myocyte apoptosis. *J Mol Cell Cardiol* **38**, 47-62 (2005).
241. www.ClinicalTrials.gov. U.S. National Institutes of Health, ClinicalTrials.gov. (2009).
242. Jones, E.S., Vinh, A., McCarthy, C.A., Gaspari, T.A. & Widdop, R.E. AT2 receptors: functional relevance in cardiovascular disease. *Pharmacol Ther* **120**, 292-316 (2008).
243. Matsubara, H. et al. Differential gene expression and regulation of angiotensin II receptor subtypes in rat cardiac fibroblasts and cardiomyocytes in culture. *J Clin Invest* **93**, 1592-601 (1994).

244. Kaiser, R.A. et al. Genetic inhibition or activation of JNK1/2 protects the myocardium from ischemia-reperfusion-induced cell death in vivo. *J Biol Chem* **280**, 32602-8 (2005).
245. Purcell, N.H. et al. Genetic inhibition of cardiac ERK1/2 promotes stress-induced apoptosis and heart failure but has no effect on hypertrophy in vivo. *Proc Natl Acad Sci U S A* **104**, 14074-9 (2007).
246. Patel, P.A., Tilley, D.G. & Rockman, H.A. Physiologic and cardiac roles of beta-arrestins. *J Mol Cell Cardiol* (2008).
247. Turu, G. et al. Differential beta-arrestin binding of AT1 and AT2 angiotensin receptors. *FEBS Lett* **580**, 41-5 (2006).
248. Buxton, I.L. & Brunton, L.L. Compartments of cyclic AMP and protein kinase in mammalian cardiomyocytes. *J Biol Chem* **258**, 10233-9 (1983).
249. Tasken, K. & Aandahl, E.M. Localized effects of cAMP mediated by distinct routes of protein kinase A. *Physiol Rev* **84**, 137-67 (2004).
250. Houslay, M.D. Underpinning compartmentalised cAMP signalling through targeted cAMP breakdown. *Trends Biochem Sci* **35**, 91-100 (2010).
251. Carnegie, G.K., Means, C.K. & Scott, J.D. A-kinase anchoring proteins: from protein complexes to physiology and disease. *IUBMB Life* **61**, 394-406 (2009).
252. Altarejos, J.Y. & Montminy, M. CREB and the CRTC co-activators: sensors for hormonal and metabolic signals. *Nat Rev Mol Cell Biol* **12**, 141-51 (2011).
253. Kvissel, A.K. et al. Involvement of the catalytic subunit of protein kinase A and of HA95 in pre-mRNA splicing. *Exp Cell Res* **313**, 2795-809 (2007).
254. Martin, B.R., Deerinck, T.J., Ellisman, M.H., Taylor, S.S. & Tsien, R.Y. Isoform-specific PKA dynamics revealed by dye-triggered aggregation and DAKAP1alpha-mediated localization in living cells. *Chem Biol* **14**, 1031-42 (2007).
255. Harootunian, A.T. et al. Movement of the free catalytic subunit of cAMP-dependent protein kinase into and out of the nucleus can be explained by diffusion. *Mol Biol Cell* **4**, 993-1002 (1993).
256. Mayr, B. & Montminy, M. Transcriptional regulation by the phosphorylation-dependent factor CREB. *Nat Rev Mol Cell Biol* **2**, 599-609 (2001).
257. Meoli, E. et al. Protein kinase A effects of an expressed PRKAR1A mutation associated with aggressive tumors. *Cancer Res* **68**, 3133-41 (2008).
258. Zippin, J.H. et al. Bicarbonate-responsive "soluble" adenylyl cyclase defines a nuclear cAMP microdomain. *J Cell Biol* **164**, 527-34 (2004).
259. Jarnaess, E. et al. Splicing factor arginine/serine-rich 17A (SFRS17A) is an A-kinase anchoring protein that targets protein kinase A to splicing factor compartments. *J Biol Chem* **284**, 35154-64 (2009).
260. Rich, T.C. et al. Cellular mechanisms underlying prostaglandin-induced transient cAMP signals near the plasma membrane of HEK-293 cells. *Am J Physiol Cell Physiol* **292**, C319-31 (2007).
261. Xin, W., Tran, T.M., Richter, W., Clark, R.B. & Rich, T.C. Roles of GRK and PDE4 activities in the regulation of beta2 adrenergic signaling. *J Gen Physiol* **131**, 349-64 (2008).

262. Burnham, K.P. & Anderson, D.R. *Model selection and multimodel inference : a practical information-theoretic approach*, xxvi, 488 p. (Springer, New York, 2002).
263. Sugiura, N. Further Analysis of Data by Akaikes Information Criterion and Finite Corrections. *Communications in Statistics Part a-Theory and Methods* **7**, 13-26 (1978).
264. Greenberg, M.E. & Bender, T.P. Identification of newly transcribed RNA. *Curr Protoc Mol Biol* **Chapter 4**, Unit 4 10 (2007).
265. Steegborn, C., Litvin, T.N., Levin, L.R., Buck, J. & Wu, H. Bicarbonate activation of adenylyl cyclase via promotion of catalytic active site closure and metal recruitment. *Nat Struct Mol Biol* **12**, 32-7 (2005).
266. Chen, Y. et al. Soluble adenylyl cyclase as an evolutionarily conserved bicarbonate sensor. *Science* **289**, 625-8 (2000).
267. Buck, J., Sinclair, M.L., Schapal, L., Cann, M.J. & Levin, L.R. Cytosolic adenylyl cyclase defines a unique signaling molecule in mammals. *Proc Natl Acad Sci U S A* **96**, 79-84 (1999).
268. DiPilato, L.M. & Zhang, J. The role of membrane microdomains in shaping beta2-adrenergic receptor-mediated cAMP dynamics. *Mol Biosyst* **5**, 832-7 (2009).
269. DiPilato, L.M., Cheng, X. & Zhang, J. Fluorescent indicators of cAMP and Epac activation reveal differential dynamics of cAMP signaling within discrete subcellular compartments. *Proc Natl Acad Sci U S A* **101**, 16513-8 (2004).
270. Allen, M.D. & Zhang, J. Subcellular dynamics of protein kinase A activity visualized by FRET-based reporters. *Biochem Biophys Res Commun* **348**, 716-21 (2006).
271. Hagiwara, M. et al. Coupling of hormonal stimulation and transcription via the cyclic AMP-responsive factor CREB is rate limited by nuclear entry of protein kinase A. *Mol Cell Biol* **13**, 4852-9 (1993).
272. Shimojo, M., Paquette, A.J., Anderson, D.J. & Hersh, L.B. Protein kinase A regulates cholinergic gene expression in PC12 cells: REST4 silences the silencing activity of neuron-restrictive silencer factor/REST. *Mol Cell Biol* **19**, 6788-95 (1999).
273. Lynch, M.J. et al. RNA silencing identifies PDE4D5 as the functionally relevant cAMP phosphodiesterase interacting with beta arrestin to control the protein kinase A/AKAP79-mediated switching of the beta2-adrenergic receptor to activation of ERK in HEK293B2 cells. *J Biol Chem* **280**, 33178-89 (2005).
274. McCahill, A. et al. In resting COS1 cells a dominant negative approach shows that specific, anchored PDE4 cAMP phosphodiesterase isoforms gate the activation, by basal cyclic AMP production, of AKAP-tethered protein kinase A type II located in the centrosomal region. *Cell Signal* **17**, 1158-73 (2005).
275. Terrin, A. et al. PGE(1) stimulation of HEK293 cells generates multiple contiguous domains with different [cAMP]: role of compartmentalized phosphodiesterases. *J Cell Biol* **175**, 441-51 (2006).
276. de Rooij, J. et al. Mechanism of regulation of the Epac family of cAMP-dependent RapGEFs. *J Biol Chem* **275**, 20829-36 (2000).

277. Beavo, J.A., Bechtel, P.J. & Krebs, E.G. Activation of protein kinase by physiological concentrations of cyclic AMP. *Proc Natl Acad Sci U S A* **71**, 3580-3 (1974).
278. Wong, W. & Scott, J.D. AKAP signalling complexes: focal points in space and time. *Nat Rev Mol Cell Biol* **5**, 959-70 (2004).
279. Michel, J.J. & Scott, J.D. AKAP mediated signal transduction. *Annu Rev Pharmacol Toxicol* **42**, 235-57 (2002).
280. Ellis-Davies, G.C. Caged compounds: photorelease technology for control of cellular chemistry and physiology. *Nat Methods* **4**, 619-28 (2007).
281. Stierl, M. et al. Light modulation of cellular cAMP by a small bacterial photoactivated adenylyl cyclase, bPAC, of the soil bacterium Beggiatoa. *J Biol Chem* **286**, 1181-8 (2011).
282. Schroder-Lang, S. et al. Fast manipulation of cellular cAMP level by light in vivo. *Nat Methods* **4**, 39-42 (2007).
283. Chuang, H.Y., Hofree, M. & Ideker, T. A decade of systems biology. *Annu Rev Cell Dev Biol* **26**, 721-44 (2010).
284. Ni, Q. et al. Signaling diversity of PKA achieved via a Ca2+-cAMP-PKA oscillatory circuit. *Nat Chem Biol* **7**, 34-40 (2011).
285. Tay, S. et al. Single-cell NF-kappaB dynamics reveal digital activation and analogue information processing. *Nature* **466**, 267-71 (2010).
286. Paliwal, S. et al. MAPK-mediated bimodal gene expression and adaptive gradient sensing in yeast. *Nature* **446**, 46-51 (2007).
287. Prasad, K.M., Xu, Y., Yang, Z., Acton, S.T. & French, B.A. Robust cardiomyocyte-specific gene expression following systemic injection of AAV: in vivo gene delivery follows a Poisson distribution. *Gene Ther* **18**, 43-52 (2011).
288. Chen, Y. & Periasamy, A. Intensity range based quantitative FRET data analysis to localize protein molecules in live cell nuclei. *J Fluoresc* **16**, 95-104 (2006).
289. Yang, J.H. & Saucerman, J.J. Phospholemman is a negative feed-forward regulator of Ca(2+) in beta-adrenergic signaling, accelerating beta-adrenergic inotropy. *J Mol Cell Cardiol* (2012).
290. De Arcangelis, V., Liu, S., Zhang, D., Soto, D. & Xiang, Y.K. Equilibrium between adenylyl cyclase and phosphodiesterase patterns adrenergic agonist dose-dependent spatiotemporal cAMP/protein kinase A activities in cardiomyocytes. *Mol Pharmacol* **78**, 340-9 (2010).
291. Goldspink, P.H. & Russell, B. The cAMP response element binding protein is expressed and phosphorylated in cardiac myocytes. *Circ Res* **74**, 1042-9 (1994).
292. Wadzinski, B.E. et al. Nuclear protein phosphatase 2A dephosphorylates protein kinase A-phosphorylated CREB and regulates CREB transcriptional stimulation. *Mol Cell Biol* **13**, 2822-34 (1993).
293. Dalton, G.D. & Dewey, W.L. Protein kinase inhibitor peptide (PKI): a family of endogenous neuropeptides that modulate neuronal cAMP-dependent protein kinase function. *Neuropeptides* **40**, 23-34 (2006).
294. Bagley, S., Goldberg, M.W., Cronshaw, J.M., Rutherford, S. & Allen, T.D. The nuclear pore complex. *J Cell Sci* **113 (Pt 22)**, 3885-6 (2000).

295. Finlay, D.R., Newmeyer, D.D., Price, T.M. & Forbes, D.J. Inhibition of in vitro nuclear transport by a lectin that binds to nuclear pores. *J Cell Biol* **104**, 189-200 (1987).
296. Soto, D., De Arcangelis, V., Zhang, J. & Xiang, Y. Dynamic protein kinase a activities induced by beta-adrenoceptors dictate signaling propagation for substrate phosphorylation and myocyte contraction. *Circ Res* **104**, 770-9 (2009).
297. Woo, A.Y. & Xiao, R.P. beta-Adrenergic receptor subtype signaling in heart: From bench to bedside. *Acta Pharmacol Sin* **33**, 335-41 (2012).
298. Di Benedetto, G. et al. Protein kinase A type I and type II define distinct intracellular signaling compartments. *Circ Res* **103**, 836-44 (2008).
299. Zaccolo, M. Phosphodiesterases and compartmentalized cAMP signalling in the heart. *Eur J Cell Biol* **85**, 693-7 (2006).
300. Dodge-Kafka, K.L., Langeberg, L. & Scott, J.D. Compartmentation of cyclic nucleotide signaling in the heart: the role of A-kinase anchoring proteins. *Circ Res* **98**, 993-1001 (2006).
301. Sample, V. et al. Regulation of nuclear PKA revealed by spatiotemporal manipulation of cyclic AMP. *Nat Chem Biol* **8**, 375-82 (2012).
302. Tilemann, L., Ishikawa, K., Weber, T. & Hajjar, R.J. Gene therapy for heart failure. *Circ Res* **110**, 777-93 (2012).
303. Leenen, F.H., White, R. & Yuan, B. Isoproterenol-induced cardiac hypertrophy: role of circulatory versus cardiac renin-angiotensin system. *Am J Physiol Heart Circ Physiol* **281**, H2410-6 (2001).
304. Hill, J.A. & Olson, E.N. Cardiac plasticity. *N Engl J Med* **358**, 1370-80 (2008).
305. Metrich, M. et al. Epac activation induces histone deacetylase nuclear export via a Ras-dependent signalling pathway. *Cell Signal* **22**, 1459-68 (2010).
306. Metrich, M. et al. Epac mediates beta-adrenergic receptor-induced cardiomyocyte hypertrophy. *Circ Res* **102**, 959-65 (2008).
307. Morel, E. et al. cAMP-binding protein Epac induces cardiomyocyte hypertrophy. *Circ Res* **97**, 1296-304 (2005).
308. Anderson, M.E., Brown, J.H. & Bers, D.M. CaMKII in myocardial hypertrophy and heart failure. *J Mol Cell Cardiol* **51**, 468-73 (2011).
309. Mishra, S. et al. Cardiac hypertrophy and heart failure development through Gq and CaM kinase II signaling. *J Cardiovasc Pharmacol* **56**, 598-603 (2010).
310. Houser, S.R. & Molkentin, J.D. Does contractile Ca2+ control calcineurin-NFAT signaling and pathological hypertrophy in cardiac myocytes? *Sci Signal* **1**, pe31 (2008).
311. Wilkins, B.J. & Molkentin, J.D. Calcium-calcineurin signaling in the regulation of cardiac hypertrophy. *Biochem Biophys Res Commun* **322**, 1178-91 (2004).
312. Ha, C.H. et al. PKA phosphorylates histone deacetylase 5 and prevents its nuclear export, leading to the inhibition of gene transcription and cardiomyocyte hypertrophy. *Proc Natl Acad Sci U S A* **107**, 15467-72 (2010).
313. Backs, J. et al. Selective repression of MEF2 activity by PKA-dependent proteolysis of HDAC4. *J Cell Biol* **195**, 403-15 (2011).
314. Zaccolo, M. & Pozzan, T. Discrete microdomains with high concentration of cAMP in stimulated rat neonatal cardiac myocytes. *Science* **295**, 1711-5 (2002).

315. Mongillo, M. et al. Fluorescence resonance energy transfer-based analysis of cAMP dynamics in live neonatal rat cardiac myocytes reveals distinct functions of compartmentalized phosphodiesterases. *Circ Res* **95**, 67-75 (2004).
316. Kapiloff, M.S. et al. An adenylyl cyclase-mAKAPbeta signaling complex regulates cAMP levels in cardiac myocytes. *J Biol Chem* **284**, 23540-6 (2009).
317. Stangherlin, A. et al. cGMP signals modulate cAMP levels in a compartment-specific manner to regulate catecholamine-dependent signaling in cardiac myocytes. *Circ Res* **108**, 929-39 (2011).
318. Liu, S., Zhang, J. & Xiang, Y.K. FRET-based direct detection of dynamic protein kinase A activity on the sarcoplasmic reticulum in cardiomyocytes. *Biochem Biophys Res Commun* **404**, 581-6 (2011).
319. Tomita, H. et al. Inducible cAMP early repressor (ICER) is a negative-feedback regulator of cardiac hypertrophy and an important mediator of cardiac myocyte apoptosis in response to beta-adrenergic receptor stimulation. *Circ Res* **93**, 12-22 (2003).
320. Fentzke, R.C., Korcarz, C.E., Lang, R.M., Lin, H. & Leiden, J.M. Dilated cardiomyopathy in transgenic mice expressing a dominant-negative CREB transcription factor in the heart. *J Clin Invest* **101**, 2415-26 (1998).
321. Gusterson, R.J., Jazrawi, E., Adcock, I.M. & Latchman, D.S. The transcriptional co-activators CREB-binding protein (CBP) and p300 play a critical role in cardiac hypertrophy that is dependent on their histone acetyltransferase activity. *J Biol Chem* **278**, 6838-47 (2003).
322. Matus, M. et al. Cardiomyocyte-specific inactivation of transcription factor CREB in mice. *FASEB J* **21**, 1884-92 (2007).
323. Isner, J.M. Myocardial gene therapy. *Nature* **415**, 234-9 (2002).
324. Vinge, L.E., Raake, P.W. & Koch, W.J. Gene therapy in heart failure. *Circ Res* **102**, 1458-70 (2008).
325. Cho, H.C. & Marban, E. Biological therapies for cardiac arrhythmias: can genes and cells replace drugs and devices? *Circ Res* **106**, 674-85 (2010).
326. Leiden, J.M. Human gene therapy: the good, the bad, and the ugly. *Circ Res* **86**, 923-5 (2000).
327. Williams, M.L. & Koch, W.J. Viral-based myocardial gene therapy approaches to alter cardiac function. *Annu Rev Physiol* **66**, 49-75 (2004).
328. Sheridan, C. Gene therapy finds its niche. *Nat Biotechnol* **29**, 121-8 (2011).
329. Corporation, C. A Phase 1/2 Trial of Intracoronary Administration of MYDICAR® (AAV1/SERCA2a) in Subjects With Heart Failure Divided Into Two Stages: Stage One Open-Label, Sequential Dose-Escalation Cohorts and Stage Two Randomized, Double-Blind, Placebo-Control, Parallel Cohorts. Vol. 2011 (Bethesda (MD): National Library of Medicine (US), 2007).
330. London, I.C. & Foundation, L. Investigation of the Safety and Feasibility of SERCA Gene Transfer in the Human Failing Heart Using an Adeno-associated Viral Vector. Vol. 2011 (Bethesda (MD): National Library of Medicine (US), 2009).
331. Hajjar, R.J. et al. Design of a phase 1/2 trial of intracoronary administration of AAV1/SERCA2a in patients with heart failure. *J Card Fail* **14**, 355-67 (2008).

332. Jaski, B.E. et al. Calcium upregulation by percutaneous administration of gene therapy in cardiac disease (CUPID Trial), a first-in-human phase 1/2 clinical trial. *J Card Fail* **15**, 171-81 (2009).
333. Horowitz, J.D., Rosenson, R.S., McMurray, J.J., Marx, N. & Remme, W.J. Clinical Trials Update AHA Congress 2010. *Cardiovasc Drugs Ther* (2011).
334. Jessup, M. et al. Calcium Upregulation by Percutaneous Administration of Gene Therapy in Cardiac Disease (CUPID): a phase 2 trial of intracoronary gene therapy of sarcoplasmic reticulum Ca2+-ATPase in patients with advanced heart failure. *Circulation* **124**, 304-13 (2011).
335. Posner, J.B., Hammermeister, K.E., Bratvold, G.E. & Krebs, E.G. The Assay of Adenosine-3' ,5'-Phosphate in Skeletal Muscle. *Biochemistry* **3**, 1040-4 (1964).
336. Posner, J.B., Stern, R. & Krebs, E.G. Effects of Electrical Stimulation and Epinephrine on Muscle Phosphorylase, Phosphorylase B Kinase, and Adenosine 3',5'-Phosphate. *J Biol Chem* **240**, 982-5 (1965).
337. Gyorke, I. & Gyorke, S. Regulation of the cardiac ryanodine receptor channel by luminal Ca2+ involves luminal Ca2+ sensing sites. *Biophys J* **75**, 2801-10 (1998).
338. Dell'Italia, L.J. et al. Compartmentalization of angiotensin II generation in the dog heart. Evidence for independent mechanisms in intravascular and interstitial spaces. *J Clin Invest* **100**, 253-8 (1997).
339. Hojo, Y. et al. Inhibition of angiotensin converting enzyme cannot prevent increases in angiotensin II production in coronary circulation. *Heart* **83**, 574-6 (2000).
340. Fujioka, A. et al. Dynamics of the Ras/ERK MAPK cascade as monitored by fluorescent probes. *J Biol Chem* **281**, 8917-26 (2006).
341. Lenzen, C., Cool, R.H., Prinz, H., Kuhlmann, J. & Wittinghofer, A. Kinetic analysis by fluorescence of the interaction between Ras and the catalytic domain of the guanine nucleotide exchange factor Cdc25Mm. *Biochemistry* **37**, 7420-30 (1998).
342. Stites, E.C., Trampont, P.C., Ma, Z. & Ravichandran, K.S. Network analysis of oncogenic Ras activation in cancer. *Science* **318**, 463-7 (2007).
343. Hatakeyama, M. et al. A computational model on the modulation of mitogen-activated protein kinase (MAPK) and Akt pathways in heregulin-induced ErbB signalling. *Biochem J* **373**, 451-63 (2003).
344. Huang, C.Y. & Ferrell, J.E., Jr. Ultrasensitivity in the mitogen-activated protein kinase cascade. *Proc Natl Acad Sci U S A* **93**, 10078-83 (1996).
345. Yamada, S., Shiono, S., Joo, A. & Yoshimura, A. Control mechanism of JAK/STAT signal transduction pathway. *FEBS Lett* **534**, 190-6 (2003).
346. Yasukawa, H. et al. The JAK-binding protein JAB inhibits Janus tyrosine kinase activity through binding in the activation loop. *EMBO J* **18**, 1309-20 (1999).
347. Chen, H.E., Chang, S., Trub, T. & Neel, B.G. Regulation of colony-stimulating factor 1 receptor signaling by the SH2 domain-containing tyrosine phosphatase SHPTP1. *Mol Cell Biol* **16**, 3685-97 (1996).
348. Bhalla, U.S. Signaling in small subcellular volumes. I. Stochastic and diffusion effects on individual pathways. *Biophys J* **87**, 733-44 (2004).
349. Fukunaga, K. et al. Decreased protein phosphatase 2A activity in hippocampal long-term potentiation. *J Neurochem* **74**, 807-17 (2000).

350. Kikuchi, S. et al. Kinetic simulation of signal transduction system in hippocampal long-term potentiation with dynamic modeling of protein phosphatase 2A. *Neural Netw* **16**, 1389-98 (2003).
351. Rich, T.C. et al. A uniform extracellular stimulus triggers distinct cAMP signals in different compartments of a simple cell. *Proc Natl Acad Sci U S A* **98**, 13049-54 (2001).
352. Magakian Iu, A. et al. [Multiparametric study and cluster-analysis of the transformed cultures of human cells]. *Tsitologiia* **51**, 20-5 (2009).

Curriculum Vitae

JASON HUNG-YING YANG
University of Virginia
PO Box 800759
Charlottesville, VA 22908
jhyang@virginia.edu

CITIZENSHIP USA

EDUCATION

- Ph.D., Biomedical Engineering 2006 – 2012
  University of Virginia, Charlottesville, VA
  Advisor: Jeffrey J. Saucerman, Ph.D.
- B.S., Biomedical Engineering and Electrical Engineering 2000 – 2005
  Johns Hopkins University, Baltimore, MD
  Advisor: Raimond L. Winslow, Ph.D.

INDUSTRIAL WORK EXPERIENCE

- Visiting Scientist, Structure-Activity Relationship Screening, Discovery Sciences Fall 2011
  AstraZeneca Pharmaceuticals, Götenborg, Sweden

TEACHING

- August Teaching Workshop (Invited Instructor, Teaching Resource Center, UVA) Fall 2011
- August Teaching Workshop (Invited Instructor, Teaching Resource Center, UVA) Fall 2010
- BIMS 8064: Special Topics in Cardiovascular Research (Invited Lecturer, Robert M. Berne Cardiovascular Research Center, UVA) Spring 2010
- TRC-TPT Pedagogy Seminar (Instructor, Teaching Resource Center, UVA) Spring 2010
- August Teaching Workshop (Invited Instructor, Teaching Resource Center, UVA) Fall 2009
- BME 3310: BME Systems Analysis (Guest Lecturer, BME, UVA) Fall 2009
- BME 4063: BME Capstone Design (Invited Lecturer, BME, UVA) Fall 2009
- BME 3315: Computational Biomedical Engineering (TA, Lecturer, BME, UVA) Spring 2009
- BME 4417: Tissue Engineering (TA, Biomedical Eng., UVA) Spring 2008

PEER REVIEWED PUBLICATIONS (* denotes equal contribution)

- **Yang JH**, Smith JS, Shields CW, Polanowska-Grabowska RK, Saucerman JJ. *PKA catalytic subunit compartmentation regulates contractile and hypertrophic responses to β-adrenergic signaling*. (*in preparation*)

- **Yang JH**, Saucerman JJ. *Phospholemman is a negative feed-forward regulator of Ca^{2+} in β-adrenergic signaling, accelerating β-adrenergic inotropy*. J Mol Cell Cardiol. 2012; 52(5):1048-55.
- Sample V*, DiPilato LM*, **Yang JH***, Ni Q, Saucerman JJ, Zhang J. *Regulation of nuclear PKA revealed by spatiotemporal manipulation of cAMP*. Nat Chem Biol. 2012; 8(4):375-82.
- Benedict KF, Mac Gabhann F*, Amanfu RK*, Chavali AK*, Gianchandani EP*, Glaw LS*, Oberhardt MA*, Thorne BC*, **Yang JH***, Papin JA, Peirce SM, Saucerman JJ, Skalak TC. *Systems analysis of bounded signaling modules generates experimental roadmap for eight major diseases*. Ann Biomed Eng. 2011; 39(2):621-35
- **Yang JH**, Saucerman JJ. *Computational models reduce complexity and accelerate insight into cardiac signaling networks*. Circ Res. 2011; 108(01):85-97.
- Gurewitsch ED, Kim EJ, **Yang JH**, Outland KE, McDonald MK, Allen RH. *Comparing McRoberts' and Rubin's maneuvers for initial management of shoulder dystocia: An objective evaluation*. Am J Obstet Gynecol. 2005; 192(1):153-160.
- Kim EJ, Allen RH, **Yang JH**, McDonald MK, Tam W, Gurewitsch ED. *Simulating complicated human birth for research and training.* Conf Proc IEEE Eng Med Biol Soc. 2004; 4:2762-6.

ABSTRACTS

- Gurewitsch E, Kim E, **Yang J**, Outland K, Allen R. *An objective evaluation of McRoberts' and Rubin's maneuvers for shoulder dystocia*. Am J Obstet Gynecol. 2003; 189(6):S208.

LETTERS

- **Yang J**. *Science Careers: Where does advocacy fit?* Science. 2009; 323(5911):208-209.

PLATFORM PRESENTATIONS (*presenter* italicized)

Regional / National / International Meetings

- *Yang JH*, Saucerman JJ. *PKA catalytic subunit compartmentation regulates contractile and hypertrophic responses to β-adrenergic signaling*. Cardiac Regulatory Mechanisms, Gordon Research Seminar. 2012.
- *Yang JH*, Saucerman JJ. *Phospholemman is a negative feed-forward regulator of Ca^{2+} in β-adrenergic signaling, accelerating β-adrenergic inotropy*. 90th Annual Meeting of the Virginia Academy of Science. 2012.
- *Yang JH*, Saucerman JJ. *Spatial Compartmentation of PKA Activity Regulates Contractility and Hypertrophy in Cardiac Myocytes*. 2009 Annual Fall Meeting of the Biomedical Engineering Society. 2009.
- *Yang JH*, Saucerman JJ. *Modeling Opposing Angiotensin II Receptor Subtype Behaviors in Cardiovascular Disease and Therapy*. 2009 Annual Fall Meeting of the Biomedical Engineering Society. 2009.
- *Benedict KF*, MacGabhann F*, Amanfu RK*, Chavali AK*, Gianchandani EP*, Glaw LS*, Oberhardt MA*, Yang JH*, Thorne BC, Papin JA, Peirce SM, Saucerman JJ, Skalak TC. *Systems Analysis of Bounded Signaling Modules Generates Novel Insight into Eight Major Diseases*. 2009 Annual Fall Meeting of the Biomedical Engineering Society. 2009.
- Yang JH, *Saucerman JJ*. *Multi-Scale Model of Phospholamban Mutations in the Mouse Heart*. 2nd International Symposium on Bio- and Medical Informatics and Cybernetics (BMIC 2008). 2008.
- *Yang JH*, Saucerman JJ. *Phospholamban Mutations in the Murine Heart*. 2007 Annual Fall Meeting of the Biomedical Engineering Society. 2007.
- *Kim EJ*, Allen RH, Yang JH, McDonald MK, Tam W, Gurewitsch ED. *Simulating complicated human births for research and training*. 26th Annual International Conference of the IEEE Engineering in Medicine and Biology Society (EMBS 2004). 2004.

University of Virginia

- ***Yang JH***, Saucerman JJ. *PKA Catalytic Subunit Compartmentation Regulates Contractile and Hypertrophic Responses to β-Adrenergic Signaling*. UVA Graduate Biosciences Society Spring Symposium. 2012.
- ***Yang JH***, Saucerman JJ. *PKA Catalytic Subunit Compartmentation Regulates Contractile and Hypertrophic Responses to β-Adrenergic Signaling*. 2012 Robert J. Huskey Graduate Research Exhibition. 2012.
- ***Yang JH***, Saucerman JJ. *Regulation of Nuclear PKA Revealed by cAMP Manipulation and Model-Based Inference* . GBS4 Graduate Biosciences Society Student Seminar Series. 2012.
- ***Yang JH***, Saucerman JJ. *Spatial Compartmentation of PKA Activity Regulates Contractility and Hypertrophy in Cardiac Myocytes*. 2010 Robert J. Huskey Graduate Research Exhibition. 2010.
- ***Yang JH***, Saucerman JJ. *Spatial Compartmentation of PKA Activity Regulates Contractility and Hypertrophy in Cardiac Myocytes*. UVA BMES Annual Graduate Student Symposium. 2009.
- ***Yang JH***, Saucerman JJ. *Multi-Scale Model of Phospholamban Mutations in the Mouse Heart*. 2008 Robert J. Huskey Graduate Research Exhibition. 2008.

POSTER PRESENTATIONS (*presenter* italicized)

Regional / National / International Meetings

- ***Yang JH***, Saucerman JJ. *PKA catalytic subunit compartmentation regulates contractile and hypertrophic responses to β-adrenergic signaling*. Cardiac Regulatory Mechanisms, Gordon Research Conference. 2012.
- ***Yang JH***, Saucerman JJ. *Understanding How Stress Causes Broken Hearts*. Seventh Annual Graduate Student Research Forum, Virginia Council of Graduate Schools. 2012.
- ***Yang JH***, Saucerman JJ. *Nuclear PKA Compartmentation Manages Hypertrophic Responses to β-Adrenergic Signaling*. AHA Basic Cardiovascular Sciences 2011 Scientific Sessions. 2011.
- *Benedict K*, MacGabhann F*, Amanfu R*, Chavali A*, Gianchandani E*, Glaw L*, Oberhardt M*, Thorne B*, **Yang J***, Papin J, Peirce S, Saucerman J, Skalak T. *Systems Analysis of Bounded Signaling Modules Generates Novel Insights into Eight Major Diseases*. 10th International Conference on Systems Biology. 2009.
- **Yang J**, *Saucerman J*. *PKA Activity Compartmentation Requires Slow Nuclear Transport Kinetics in Cardiac Myocytes*. Experimental Biology 2008. 2008.
- ***Yang JH***, Helm PA, Winslow RL. *Ex vivo 3D DTMRI of Human Myocardium*. 2005 Annual Fall Meeting of the Biomedical Engineering Society (BMES 2005). 2005.

University of Virginia

- ***Yang JH***, Saucerman JJ. *Nuclear PKA Compartmentation Manages Hypertrophic Responses to β-Adrenergic Signaling*. UVA BMES Annual Graduate Student Symposium. 2011.
- ***Yang JH***, Saucerman JJ. *Modeling Therapeutic Options for Manipulating Nuclear PKA Compartmentation in Heart Disease*. UVA Biotechnology Training Program Symposium 2011. 2011.
- ***Yang JH***, Saucerman JJ. *PKA Activity Compartmentation Requires Slow Nuclear Transport Kinetics in Cardiac Myocytes*. UVA Graduate Biosciences Society Spring Symposium. 2008.
- ***Yang JH***, Vandsburger MH, Xu Y, French BA, Epstein FH, Saucerman JJ. *Multi-Scale Integration from Signaling Networks to Cardiac MRI*. UVA Engineering Research Symposium. 2007.

Johns Hopkins University

- *Helm PA*, Scollan DF, Baumgartner WA, **Yang JH**, Tseng HJ, Winslow RL. *3D Diffusion Tensor Imaging*. Center for Cardiovascular Bioinformatics and Modeling. 2004.

FUNDING

- University of Virginia, Biotechnology Training Grant ($42,156; NIH 5-T32-GM08715; 2009 – 2011)
- American Heart Association, Predoctoral Fellowship Grant. “Systems Analysis of CREB Activation.” ($40,000; Award #0715283U; 2007 – 2009)
- University of Virginia, Robert M. Berne Basic Cardiovascular Research Center Training Grant ($40,000; Declined; 2007)

AWARDS

- Jill E. Hungerford Biomedical Sciences Prize ($3000; 2012)
- Biomedical Engineering Outstanding Graduate Student Award ($500; 2012)
- 2nd Place, 2012 Robert J. Huskey Graduate Research Exhibition ($150; 2012)
- Mary and Otis Updike Professional Development Award in Biomedical Engineering ($500; 2011)
- All-University Graduate Teaching Assistant Award ($250; 2011)
- 3rd Place, 2010 Robert J. Huskey Graduate Research Exhibition ($100; 2010)
- University of Virginia, Teaching Pedagogy Seminar, Teaching Resource Center ($300; 2010)
- University of Virginia, Office of the Vice President for Research and Graduate Studies, Graduate Student Travel Grant ($500; 2007)
- 1st Place, Student Paper Design Competition, 26th Annual IEEE-EMBS International Conference ($300; 2004)

HONORS
- Selected Representative, Virginia Council of Graduate Schools (2012)
- 2nd Place, UVA BMES Annual Graduate Student Symposium (2011)
- Semi-Finalist, University of Virginia Engineering Research Symposium (University of Virginia; 2007)
- Dean's List (Johns Hopkins University; 2002)
- Hopkins Trustee Scholar (Johns Hopkins University; 2000 – 2004)
- Lockheed-Martin National Merit Scholar (Johns Hopkins University; 2000 – 2004)
- National Forensics League Degree of Excellence (2000)

EDITORIAL ACTIVITIES
- Ad Hoc Reviewer, *Mathematical Biosciences*

LEADERSHIP
- Co-chair, University of Virginia Biotechnology Training Program Symposium 2011 (2010 – 2011)
- Secretary, Executive Committee, Virginia Rugby Football Club (2009 – 2011)
- Leader, University of Virginia Center for Systems Bioengineering Journal Club (2009 – 2010)

SERVICE / SCIENCE POLICY
- University of Virginia Biotechnology Training Program Admissions Committee (2012)
- Invited Participant, AAAS Workshop on Advocacy in Science (2011)
- Congressional Advocate, American Institute for Medical and Biological Engineering 4th Annual Council of Societies Federal Symposium (2009)
- Invited Participant, University of Virginia All-University Retreat on Research, Science and Technology (2008)
- Staff Coordinator, 6th Annual FRET Microscopy Workshop, W.M. Keck Center for Cellular Imaging (2007)

OUTREACH
- Invited Speaker, Century High School Science and Technology Career Fair (2011)
- Graduate Reviewer, SPECTRA: The Virginia Engineering and Science Undergraduate Research Journal (2011)
- Judge, Virginia Piedmont Regional Science Fair (2010, 2011)
- Invited Panel Speaker, UVA Biomedical Engineering Society Career Panel (2008)

AFFILIATIONS
- American Society for Engineering Education (2010 – Present)
- American Association for the Advancement of Science (2007 – Present)
- American Heart Association (2006 – Present)
- Biomedical Engineering Society (2004 – Present)
- Tomorrow's Professor Today, University of Virginia Teaching Resource Center (2008 – 2010)
- IEEE Engineering in Medicine and Biology Society (2003 – 2006)
- Institute of Electrical and Electronics Engineering (IEEE) (2003 – 2006)

ADVISING / MENTORSHIP

Undergraduate Students (Years; Post-Graduate Activities)
- C. Wyatt Shields IV, UVA (2010 – 2011; Biomedical Engineering Ph.D. Student, Duke University)
- Jeff Smith, UVA (2010 – 2011; Chemist, Merck & Co.)
- Greg Bass, UVA (2009 – 2010; Bioengineering Ph.D. Student, University of Auckland, New Zealand)
- Anthony Soltis, UVA (2007 – 2010; Bioengineering Ph.D. Student, Mass. Institute of Technology)
- Brooks Taylor, UVA (2007 – 2009; Bioengineering Ph.D. Student, UC San Diego)
- Lulu Chu, UVA (2006 – 2009; Biomedical Engineering Ph.D. Student, Johns Hopkins University)